Dynamical description of relativistic heavy-ion collisions out-of equilibrium

Dissertation zur Erlangung des Doktorgrades der Naturwissenschaften

vorgelegt beim Fachbereich Physik der Johann Wolfgang Goethe-Universität in Frankfurt am Main

von
Pierre Moreau
aus La Roche sur Yon, Frankreich

Frankfurt am Main (2019)
(D 30)

vom Fachbereich Physik der
Johann Wolfgang Goethe-Universität als Dissertation angenommen.

Dekan:

Prof. Dr. Michael Lang

Gutachter:

Prof. Dr. Elena Bratkovskaya, Prof. Dr. Marcus Bleicher

Datum der Disputation: 12.08.2019

"Il faut faire de la vie un rêve et faire d'un rêve une réalité."

Pierre Curie

Zusammenfassung

* * *

Die vorliegende Dissertation untersucht die Nichtgleichgewichtsdynamik von relativistischen Schwerionenkollisionen ausgehend von der anfänglichen Produktion von Teilchen durch den Zerfall von Strings, der Bildung eines Quark-Gluon-Plasmas (QGP), dessen kinetische und chemische Äquilibrierung als Funktion der Zeit sowie seine Transporteigenschaften im Gleichgewicht bei endlicher Temperatur und endlichem chemischen Potential. Ein Verständnis der frühen Phase der Schwerionenkollisionen ist insbesondere von großen Interesse, da letztere eine Verbindung zwischen den ersten Nukleon-Nukleon Kollisionen und der Quark-Gluon-Plasma Phase herstellen, die zu einem späteren Zeitpunkt ein gewisses Maß an Thermalisierung zeigt. Allerdings können nur Nichtgleichgewichts-Theorien eine Verbindung zwischen dem anfänglichen QGP und seiner - zumindest partiellen - Thermalisierung herstellen. Um die Dynamik eines stark wechselwirkenden Mediums wie des Quark-Gluon-Plasmas zu beschreiben, reichen übliche Transportgleichungen (basierend auf der Boltzmann-Gleichung) nicht aus und es müssen komplexere Theorien, die auch für stark korrelierte Medien geeignet sind, angewendet werden. Hier kommen hydrodynamische Simulationen oder Transportrechnungen - basierend auf verallgemeinerten Transportgleichungen - zum Einsatz. Solche verallgemeinerte Transportgleichungen, wie die Kadanoff-Baym-Gleichungen, ergeben sich aus der quantenmechanischen Nichtgleichgewichts-Vielteilchentheorie, in der Green's-Funktionen in Minkowski Raum-Zeit die interessierenden Größen sind, um die Dynamik des betrachteten Mediums zu beschreiben. Mit geeigneten Näherungen kann man so kinetische Transportgleichungen erhalten, die eine einheitliche Behandlung von stabilen und instabilen Teilchen auch außerhalb des Gleichgewichts ermöglichen. Diese Bestandteile bilden die Basis des Transportmodells Parton-Hadron-String Dynamics (PHSD), welches daher ein geeignetes 'Instrument' ist um die verschiedenen Phasen einer Schwerionenkollision zu analysieren, egal ob die verschiedenen Formen der Materie im Gleichgewicht sind oder nicht.

In dieser Arbeit wird zunächst die Quantenchromodynamik (QCD) vorgestellt und erklärt, wie diese Theorie im Laufe der Jahre entwickelt wurde um ein wichtiger Bestandteil des Standardmodells der Teilchenphysik zu werden. Eine Definition der Theorie der Quantenchromodynamik, deren grundlegende Eigenschaften und Symmetrien und Methoden zur Lösung auf einem euklidischen Raum-Zeit Gitter folgen

sodann. Die primäre Möglichkeit zur experimentellen Untersuchung der Eigenschaften der QCD besteht in der Analyse von Schwerionenkollisionen. Es wird erläutert, welche Observablen insbesondere geeignet sind zum Nachweis eines QGP in relativistischen Schwerionenkollisionen. Wir werden weiterhin die verbleibenden Herausforderungen in unserem Verständnis der QCD vorstellen, die sich primär auf das Phasendiagramm der stark wechselwirkenden Materie konzentrieren.

Im zweiten Kapitel untersuchen wir die Nichtgleichgewichts-Feldtheorie und die damit verbundenen Techniken - wie die Keldysh-Kontur - zur Beschreibung der Green'schen Funktionen als wesentlichen Freiheitsgrade. Wir leiten die Evolutionsgleichung für die Green'schen Funktionen her, d. h. die Kadanoff-Baym-Gleichungen am Beispiel einer skalaren Feldtheorie. Mit Hilfe einer unitären Wigner-Transformation und einer Gradientenentwicklung im Phasenraum erhalten wir sodann die spektrale Informationen von 'Teilchen' sowie verallgemeinerte Transportgleichungen für deren Zeitentwicklung. In einer weiteren Quasiteilchen-Näherung erhält man die Boltzmann-Gleichung für schwach wechselwirkende Freiheitsgrade, bei der man die Dämpfungsrate des Teilchens mit seiner Wechselwirkungsrate und damit der Äquilibrierungszeit des Systems unmittelbar in Beziehung setzen kann.

Im nächsten Kapitel wird das Transportmodell Parton-Hadron-String Dynamics (PHSD), welches die Anwendung der verallgemeinerten Transportgleichungen zur Beschreibung relativistischer Schwerionenkollisionen darstellt, vorgestellt. Wir präsentieren die Hauptbestandteile, die zur Beschreibung einer Schwerionenkollision erforderlich sind, d.h. die Wechselwirkung der anfänglichen Kerne bis zu den finalen Teilchenspektren, die experimentelle Meßgrößen darstellen. Insbesondere beschreiben wir die Initialisierung der Kerne, die hadronischen Wechselwirkungen, den String-Fragmentierungsprozess, die Streuung der Partonen in der Quark-Gluon-Plasma Phase und den Hadronisierungsprozess. Letztendlich werden einige chrakteristische Ergebnisse der PHSD im Vergleich zu experimentellen Daten präsentiert um die Mechanismen der Teilchenproduktion und das Baryonen-Stopping zu veranschaulichen.

Wir beginnen im Kapitel 4 mit der Untersuchung der Nichtgleichgewichtseigenschaften des Quark-Gluon-Plasmas, welches bei relativistischen Schwerionenkollisionen erzeugt wird. Zu diesem Zweck vergleichen wir die Quark-Gluon-Plasmaentwicklung aus dem PHSD mit einem viskosen hydrodynamischen Modell, bei dem ein lokales kinetisches und chemisches Gleichgewicht angenommen wird. Ausgehend von den gleichen Anfangsbedingungen der frühen QGP Phase wie im PHSD Modell, unter Verwendung einer äquivalenten Gitter-QCD-Zustandsgleichung, den gleichen Transportkoeffizienten (Scheer- und Volumenviskositäten) im hydro-

dynamischen Modell, vergleichen wir die zeitliche Entwicklung der Systeme in Bezug auf Energiedichte, Fourier-transformierte Energiedichte, Strömungsgeschwindigkeit, räumliche und Impuls-Exzentrizität und Elliptizität zur Quantifizierung der Spuren von Nichtgleichgewichtsphänomenen. Wir werden feststellen, dass aufgrund von Nichtgleichgewichtseffekten die Transportrechnungen von "event-by-event" Simulationen große Schwankungen in den kollektiven Eigenschaften aufweisen, während die gemittelten Ensemble-Observablen nahe an den hydrodynamischen Ergebnissen liegen.

Im Kapitel 5 konzentrieren wir uns auf das frühe Vorgleichgewichtsstadium ultra-relativistischer Schwerionenkollisionen und insbesondere auf die Freiheitsgrade der QGP-Phase in diesem Stadium. Wir untersuchen die Auswirkungen eines QGP, welches anfänglich entweder aus einem System aus massiven Gluonen (Szenario I) oder alternativ aus Quarks und Antiquarks (Szenario II) besteht. Wir werden feststellen, dass diese beiden Szenarien zu unterschiedlichen hadronischen Observablen führen, wenn der gleiche anfängliche Energie-Impuls-Tensor $T^{\mu\nu}(x)$ benutzt wird, d.h. kurz nach dem Durchfluß der kollidierenden Kerne. Im Falle der gluonischen Ausgangsbedingung (Szenario I) verläuft die Bildung seltsamer Quarkpaare (s, $\bar{s}$) im Quark-Gluon-Plasma langsamer als im Szenario II, was zu deutlichen Unterschieden in den Hadronenspektren mit Strangeness führt.

Das nächste Kapitel wird ebenfalls die Produktion von Teilchen im Frühstadium von Schwerionenkollisionen behandeln, jedoch bei niedrigeren Kollisionsenergien. Hier wird eine mikroskopische Beschreibung des K^+/π^+-Verhältnisses im Vordergrund stehen, d. h. die Erklärung des Maximums in diesem Verhältnis bei etwa 30 A GeV ("Horn") in zentralen Au+Au (oder Pb+Pb) Kollisionen. Insbesonders werden wir die Modifikation des String-Fragmentierungsprozesses (über den Schwinger-Mechanismus) in einer Umgebung mit hoher hadronischer Dichte aufgrund der teilweisen Wiederherstellung der chiralen Symmetrie untersuchen. Wir werden herausstellen, dass die Verhältnisse K^+/π^+ und $(\Lambda + \Sigma^0)/\pi^-$ bei zentralen Au+Au-Kollisionen Aufschluss geben über die relative Bedeutung der Wiederherstellung der chiralen Symmetrie und des Deconfinements. Die Modellierung der Wiederherstellung der chiralen Symmetrie basiert sich auf dem Pion-Nukleon Σ-Term bei der Berechnung des skalaren Quarkkondensats $< \bar{q}q >$. Letzteres dient als Ordnungsparameter für die Wiederherstellung der chiralen Symmetrie und ist mit den effektiven Quarkmassen m_s und m_q unmittelbar verknüpft. Weiterhin wird die skalare Nukleonendichte ρ_s, die ebenfalls in die Berechnung von $< \bar{q}q >$ eingeht, im nichtlinearen $\sigma - \omega$ Modell ausgewertet. Wir verwenden verschiedene Parametrisierungen der nuklearen Zustandsgleichung (zur Ermittlung von ρ_s) um die Unsicherheit in unseren Berechnungen abzuschätzen. Der

Schwinger-Mechanismus (für den String-Zerfall) legt sodann das Verhältnis der Produktion von seltsamen zu leichten Quarks im hadronischen Medium fest. Wir weisen darauf hin, dass oberhalb von $\sim$ 80 A GeV die Reaktionsdynamik schwerer Kerne in erster Linie von partonischen Freiheitsgraden bestimmt wird, sodass Spuren der Wiederherstellung der chiralen Symmetrie bei hohen Energien schwer zu identifizieren sind. Unsere Ergebnisse liefern eine mikroskopische Erklärung für das "Horn" -Phänomen in der Anregungsfunktion des K^+/π^+-Verhältnisses: Die Wiederherstellung der chiralen Symmetrie in der hadronischen Phase führt zu einem steilen Anstieg dieses Teilchenverhältnisses bis zu $\sqrt{s_{NN}} \approx 7$ GeV, während der Abfall bei höheren Energien mit dem Auftreten eines partonischen Mediums verbunden ist. Weiterhin wird das Erscheinen/Verschwinden des 'Horn'-Maximums in Abhängigkeit von der Systemgröße und der Kollisionszentralität untersucht.

In Kapitel 7 erweitern wir das Parton-Hadron-String Dynamics (PHSD) - Transportmodell im partonischen Sektor, indem wir explizit die totalen und differentiellen partonischen Streuungsquerschnitte als Funktion der Temperatur T und des baryochemischen Potentials μ_B berechnen auf der Basis der effektiven Propagatoren und Kopplungen des Dynamical QuasiParticle Models (DQPM), welches auch die generelle Zeitentwicklung der partonischen Freiheitsgrade beschreibt. Wir berechnen insbesondere die Kollisionsbreiten für die partonischen Freiheitsgrade bei endlichen T und μ_B im zeitlichen Sektor und schließen daraus, dass die partonischen Freiheitsgrade hinreichend gute Quasiteilchen sind. Weiterhin wird das Verhältnis der Scheer- und Volumenviskosität zur Entropiedichte, d. h. η/s und ζ/s, unter Verwendung dieser Kollisionsbreiten berechnet und für $\mu_B = 0$ mit Gitter-QCD-Rechnungen verglichen. Wir stellen fest, dass das neue Verhältnis η/s nicht sehr stark von dem im ursprünglichen DQPM - auf der Grundlage des Kubo-Formalismus - abweicht. Außerdem gibt es nur eine sehr bescheidene Änderung von η/s mit dem baryonchemischen Potential μ_B in Abhängigkeit von der skalierten Temperatur $T/T_c(\mu_B)$. Dies gilt auch für eine Vielzahl von hadronischen Observablen aus zentralen A+A-Kollisionen im Energiebereich von 5 GeV $\leq \sqrt{s_{NN}} \leq$ 200 GeV bei der Implementierung der differentiellen Querschnitte in das PHSD-Modell. Wir beobachten nur kleine Unterschiede im Antibaryon-Sektor ($\bar{p}, \bar{\Lambda} + \bar{\Sigma}^0$) bei $\sqrt{s_{NN}} = 17.3$ GeV und 200 GeV mit praktisch keiner Empfindlichkeit der Rapiditäts und p_T-Spektren auf die μ_B-Abhängigkeit der partonischen Querschnitte. In allen untersuchten Kollisionssystemen (A + A und C + Au) ergeben sich nur kleine Veränderungen im Strange-Teilchen Sektor. Es wird daher sehr schwierig sein, ein robustes Signal experimentell zu extrahieren. Da wir in Schwerionen-Observablen nur kleine Spuren einer μ_B -Abhängigkeit finden - obwohl die effektiven Partonenmassen und Kollisionsbreiten sowie deren Partonenquerschnitte eindeutig von μ_B abhängen - impliziert dies, dass man eine beträchtliche Partonendichte und ein

großes Raum-Zeit-QGP-Volumen zur Untersuchung der Dynamik in der partonischen Phase benötigt. Diese Bedingungen sind nur bei hohen Kollisionsenergien erfüllt, bei denen μ_B jedoch eher niedrig ist. Wenn andererseits die Kollisionsenergie verringert und somit μ_B erhöht wird, wird die hadronische Phase dominant und dementsprechend wird es zunehmend schwieriger, Signale aus der Partonendynamik auf der Basis von "Bulk"-Observablen zu extrahieren.

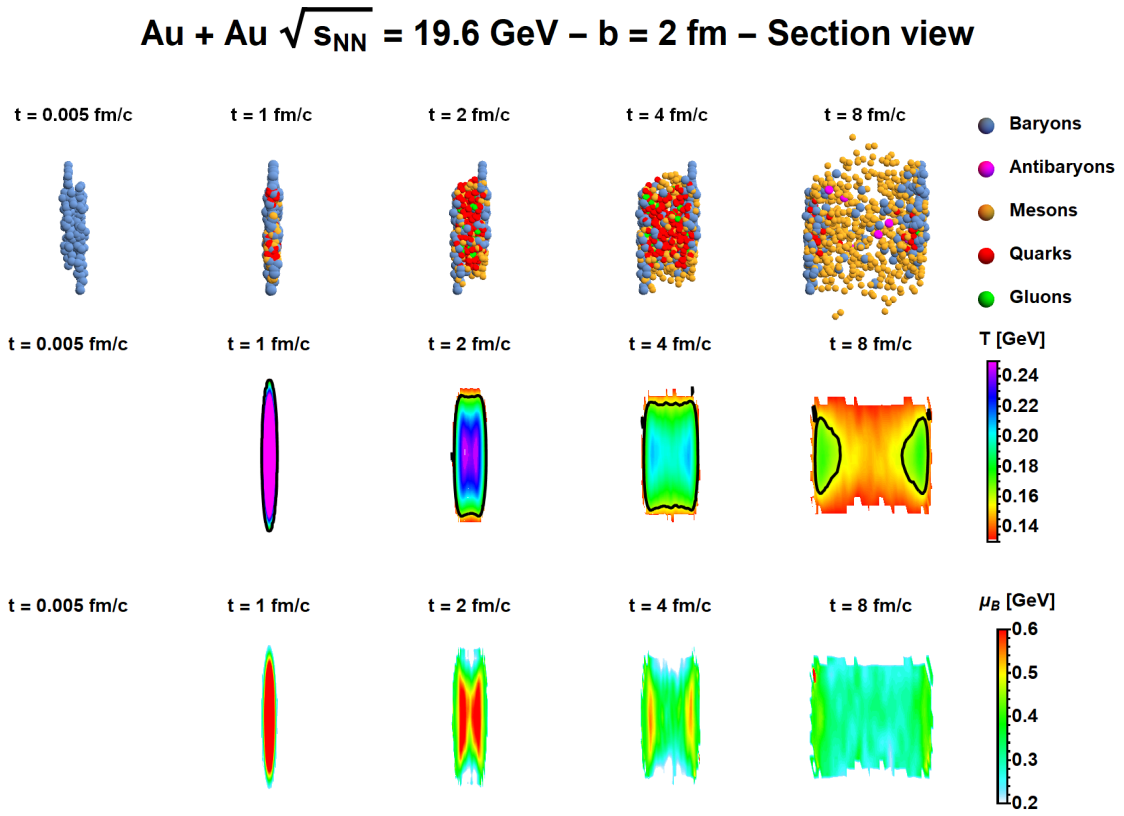

Figure 0.1 – Abbildung einer PHSD-Simulation für eine zentrale Au+Au-Kollision bei einer Kollisionsenergie von $\sqrt{s_{NN}} = 19.6$ GeV sowie die Raum-Zeit Entwicklung der mittleren Temperatur T und des baryochemischen Potentials μ_B.

Preface

* * *

This dissertation is submitted to the Department of Physics of the Johann Wolfgang Goethe University Frankfurt to achieve the Ph.D. degree of Natural Sciences. The research presented here was carried out from October 2014 until May 2019 under the supervision of Prof. Dr. Elena Bratkovskaya and led to the following publications:

Publications in Peer-Reviewed Physics Journals

[1] **P. Moreau**, O. Soloveva, L. Oliva, T. Song, W. Cassing, and E. Bratkovskaya, "Exploring the partonic phase at finite chemical potential within an extended off-shell transport approach", Phys. Rev. **C100**, 014911 (2019), arXiv:1903.10257 [nucl-th]

[2] T. Song and **P. Moreau**, "Low-energy Bremsstrahlung photon in relativistic nucleon+nucleon collisions", Phys. Rev. **D98**, 116007 (2018), arXiv:1810.08013 [nucl-th]

[3] Y. Xu, S. A. Bass, **P. Moreau**, T. Song, M. Nahrgang, E. Bratkovskaya, et al., "Resolving discrepancies in the estimation of heavy quark transport coefficients in relativistic heavy-ion collisions", Phys. Rev. **C99**, 014902 (2019), arXiv:1809.10734 [nucl-th]

[4] T. Song, W. Cassing, **P. Moreau**, and E. Bratkovskaya, "Discrepancy in low transverse momentum dileptons from relativistic heavy-ion collisions", Phys. Rev. **C98**, 041901 (2018), arXiv:1806.09377 [nucl-th]

[5] T. Song, W. Cassing, **P. Moreau**, and E. Bratkovskaya, "Open charm and dileptons from relativistic heavy-ion collisions", Phys. Rev. **C97**, 064907 (2018), arXiv:1803.02698 [nucl-th]

[6] Y. Xu, **P. Moreau**, T. Song, M. Nahrgang, S. A. Bass, and E. Bratkovskaya, "Traces of nonequilibrium dynamics in relativistic heavy-ion collisions", Phys. Rev. **C96**, 024902 (2017), arXiv:1703.09178 [nucl-th]

[7] A. Palmese, W. Cassing, E. Seifert, T. Steinert, **P. Moreau**, and E. L. Bratkovskaya, " Chiral symmetry restoration in heavy-ion collisions at intermediate energies", Phys. Rev. **C94**, 044912 (2016), arXiv:1607.04073 [nucl-th]

[8] **P. Moreau**, O. Linnyk, W. Cassing, and E. Bratkovskaya, "Examinations of the early degrees of freedom in ultrarelativistic nucleus-nucleus collisions", Phys. Rev. **C93**, 044916 (2016), arXiv:1512.02875 [nucl-th]

[9] W. Cassing, A. Palmese, **P. Moreau**, and E. L. Bratkovskaya, "Chiral symmetry restoration versus deconfinement in heavy-ion collisions at high baryon density", Phys. Rev. **C93**, 014902 (2016), arXiv:1510.04120 [nucl-th]

Conference proceedings

[1] T. Song, E. Bratkovskaya, W. Cassing, and **P. Moreau**, "Electromagnetic probes of the quark-gluon plasma", Astronomische Nachrichten **340**, 157–162 (2019), eprint: https://onlinelibrary.wiley.com/doi/pdf/10.1002/asna.201913580

[2] T. Song, E. L. Bratkovskaya, W. Cassing, and **P. Moreau**, "Electromagnetic emissivity of hot and dense matter", J. Phys. Conf. Ser. **1070**, 012006 (2018)

[3] E. L. Bratkovskaya, W. Cassing, **P. Moreau**., and A. Palmese, "Chiral Symmetry Restoration and Deconfinement in Heavy-Ion Collisions", in *Chapter of the book "Walter Greiner Memorial Volume", edited by Peter O Hess and Horst Stöcker, World Scientific, Singapore, 2018, p. 71-89 (ISBN: 978-981-3234-27-7)* (2018), pp. 71–89

[4] E. L. Bratkovskaya, W. Cassing, A. Palmese, and **P. Moreau**, "Chiral Symmetry Restoration in Heavy-ion Collisions at High Baryon Density", Acta Phys. Polon. Supp. **10**, 507 (2017)

[5] **P. Moreau**, Y. Xu, T. Song, M. Nahrgang, S. Bass, and E. Bratkovskaya, "Traces of non-equilibrium dynamics in relativistic heavy-ion collisions", PoS **CPOD2017**, 042 (2018), arXiv:1711.10223 [nucl-th]

[6] E. L. Bratkovskaya, W. Cassing, **P. Moreau**, and T. Song, "Review of the theoretical heavy-ion physics", in Proceedings, 3rd International Conference on Particle Physics and Astrophysics (ICPPA 2017): Moscow, Russia, October 2-5, 2017 (2017), arXiv:1711.01976 [nucl-th]

[7] E. L. Bratkovskaya, A. Palmese, W. Cassing, E. Seifert, T. Steinert, and **P. Moreau**, "Chiral symmetry restoration versus deconfinement in heavy-ion collisions at high baryon density", J. Phys. Conf. Ser. **878**, 012018 (2017)

[8] **P. Moreau**, A. Palmese, W. Cassing, E. Seifert, T. Steinert, and E. L. Bratkovskaya, "Evidence for chiral symmetry restoration in heavy-ion collisions", Nucl. Phys. **A967**, 836–839 (2017), arXiv:1704.05946 [nucl-th]

[9] **P. Moreau**, W. Cassing, A. Palmese, and E. L. Bratkovskaya, "(Anti-) strangeness in heavy-ion collisions", J. Phys. Conf. Ser. **742**, 012016 (2016)

[10] E. L. Bratkovskaya, W. Cassing, **P. Moreau**, and A. Palmese, "Observables and open problems for NICA", Eur. Phys. J. **A52**, 219 (2016)

[11] **P. Moreau**, W. Cassing, A. Palmese, and E. Bratkovskaya, "Hadron Production within PHSD", Acta Phys. Polon. Supp. **9**, 279 (2016), arXiv:1603.02832 [nucl-th]

[12] **P. Moreau**, F. Li, C.-M. Ko, W. Cassing, and E. Bratkovskaya, "Antistrangeness production in heavy-ion collisions", J. Phys. Conf. Ser. **668**, 012072 (2016), arXiv:1509.04455 [nucl-th]

Table of contents

* * *

Introduction

* * *

Modern physics is composed of two fundamental theories: the Standard Model of Particle Physics which classifies and describes the interactions between elementary particles, and the Big Bang scenario which relies on General Relativity and describes the "birth" of our universe and its evolution until this day. The key questions with respect to these two theories is to understand the matter of our universe and how it was initially created. In the XX$^{\text{th}}$ century, the building blocks of matter were progressively revealed thanks to experimental evidences. Furthermore, in the 1950s more "exotic" particles were discovered in high energy collisions from cosmic rays entering the earth atmosphere or in particle accelerators. The latter have particularly provided a lot of information about elementary particles and also compelling evidences in favor of the Standard Model which by example describes the proton or neutrons as composite particles of smaller constituents: the quarks and gluons. At very high energies, heavy-ion collisions (HICs) and the Big Bang scenario are connected by an extreme state of matter known as the Quark-Gluon Plasma (QGP). It corresponds to a deconfined state of quarks and gluons and can be described by the theory of strong interactions: the Quantum-ChromoDynamics (QCD).

A theoretical understanding of relativistic heavy-ion collisions necessary involves the use of a nonequilibrium many-body theory or transport theory, which are also of interest in the context of cosmological as well as condensed matter physics. In these different areas the ultimate goals are to understand how a quantum system reacts and evolves in extreme conditions, how it equilibrates chemically and kinetically with time, what are its transport coefficients in equilibrium, and what is the nature of its different phases and transitions. Within relativistic heavy-ion collisions, strongly interacting matter is created under extreme and nonequilibrium conditions and therefore it is a perfect experimental opportunity to test and investigate the properties of QCD and more generally nonequilibrium quantum-field theories. The characterization of the QGP in relativistic heavy-ion collisions led to the conclusion that it behaves almost as a strongly interacting perfect fluid which is well described by hydrodynamical models employing the assumption of local equilibrium. However, only nonequilibrium transport approaches can provide the link between the initial extreme conditions of the QGP and its apparent thermalization

at later times, by describing the whole evolution of heavy-ion collisions in terms of microscopic degrees-of-freedom.

Furthermore, as we will see in this dissertation, QCD cannot be solved by using a perturbative expansion (unless considering the extremely high-energy limit) and therefore non-perturbative effects should necessarily be incorporated in order to describe the behavior of the matter produced in heavy-ion collisions. One way to directly solve QCD is by using lattice QCD calculations which provide information about strongly interacting matter in equilibrium and at vanishing chemical potential, but are computationally expensive. To describe the dynamics of heavy-ion collisions, one needs to use effective approaches which can reproduce the basic properties of QCD in equilibrium and which can also provide the correct degrees-of-freedom. In this work we employ the Dynamical Quasi-Particle Model (DQPM) which treats the partons as interacting quasiparticles with medium-dependent complex self-energies. The latter are fitted in order to reproduce lattice QCD results in equilibrium and therefore provide a simple approach which incorporates the non-perturbative nature of QCD. In order to describe the dynamics of a strongly interacting medium such as the Quark-Gluon Plasma, usual transport equations (based on the Boltzmann equation) are not sufficient and one needs to employ more sophisticated approaches such as hydrodynamic simulations or generalized transport equations which are suited for such a strongly correlated medium. Such transport equations, i.e. the Kadanoff-Baym equations, result from the nonequilibrium quantum many-body theory, where the real-time Green's function is the essential quantity of interest, in order to understand the dynamics of the medium under consideration. With suitable approximations one can obtain kinetic transport equations which offer a unified treatment of stable and unstable particles also out-of-equilibrium. All these ingredients are incorporated into the Parton-Hadron-String Dynamics (PHSD) which is therefore the ideal tool to dissect and understand the different stages of a heavy-ion collision, whether the matter is in equilibrium or not.

The aim of this dissertation is to study and shed light on the nonequilibrium nature of the medium as created in the beginning of heavy-ion collisions, including the initial production of particles through string fragmentation and the Quark-Gluon Plasma state by studying its kinetic and chemical equilibration as a function of time as well as its description and characterization at finite chemical potential. We will first introduce the Quantum-ChromoDynamics (QCD) and explain how this theory has been developed throughout the years to become an important part of the Standard Model of Particle Physics. We will present how the theory of QCD is defined and what are its basic properties and symmetries,

and also how it can be solved by using lattice techniques. The only way to experimentally investigate the properties of QCD is by means of heavy-ion collisions and in particular we will detail which probes confirm that a Quark-Gluon Plasma has been produced in heavy-ion collisions. We will present the remaining challenges in our understanding of QCD which are focused around the QCD phase diagram. In the second chapter, we study the nonequilibrium field theory and the associated techniques such as the Keldysh contour where the Green's functions are the essential degrees-of-freedom. From the evolution equation for the Green's functions, i.e. the Kadanoff-Baym equations, we apply a gradient expansion in order to obtain generalized transport equations. In the quasiparticle approximation we recover the Boltzmann equation where one can relate the damping rate of the particle to its interaction rate and to the equilibration time of the system. In the next chapter we introduce the Parton-Hadron-String Dynamics (PHSD) which applies the generalized transport equation to the description of relativistic heavy-ion collisions. We present the main ingredients which are used to describe a heavy-ion collision from the collision of the initial nuclei up to the final particle spectra. We close this chapter by presenting a few results from the PHSD in comparison with experimental data to briefly illustrate the mechanisms of particle production and baryon stopping.

We start our investigations in chapter 4 about the nonequilibrium properties of the QGP as produced in relativistic heavy-ion collisions. For that purpose, we compare the evolution from the PHSD to a hydrodynamical model where local equilibrium is assumed and assess the differences between these two descriptions. In chapter 5 we focus on the very early pre-equilibrium stage of ultra-relativistic heavy-ion collisions and especially on the content of the QGP phase at this stage. We study the implications of a QGP being initially populated by exclusively gluons or quarks and antiquarks on final experimental observables such as rapidity spectra of bulk particles or photon and dilepton spectra. The next chapter will also discuss the production of particles in the early stage of heavy-ion collisions but at lower collisional energies where a microscopic explanation of the strangeness enhancement, i.e. the "horn", will be addressed. In particular we will study the modification of the string fragmentation process in a high-density environment due to the partial restoration of chiral symmetry.

In chapter 7 we will present the Dynamical QuasiParticle model in detail and will investigate the properties of strongly interacting matter at finite temperature and chemical potential by evaluating the QCD equation of state, the partonic interaction rates and the associated transport coefficients, in comparison with the available lattice QCD data. Secondly, we will incorporate the ingredients from

the DQPM such as the parton masses and the interaction cross sections into the PHSD transport approach in order to study the QGP phase at finite baryon chemical potential as produced in heavy-ion collisions. After illustrating the different regions of the QCD phase diagram which are probed in heavy-ion collisions, we will compare our results for bulk observables such as rapidity and p_T spectra with experimental data and conclude on the effect of the finite μ_B dynamics of the QGP.

Throughout this thesis, we will use the natural units $\hbar = c = k_B = 1$. With this prescription, values of length and time will generally be expressed in $(\text{GeV})^{-1}$. In order to come back to ordinary units (fm for length, fm/c for time, Kelvin for temperature), we recall the value of the constants $\hbar c = 0.197$ GeV fm, $(\hbar c)^2 = 0.389$ GeV^2 mb and $k_B = 8.617385 \times 10^{-14}$ GeV K^{-1}.

Chapter 1

Basics of Quantum ChromoDynamics

* * *

"The universe is not only queerer than we suppose, but queerer than we can suppose."

J. B. S. Haldane

The starting point of this dissertation is an introduction to the physics that we will discuss in the next chapters, with a brief history on the Standard Model of particle physics, which is the fundamental background of this study. Afterwards we will focus on the theory governing the dynamics of strongly interacting matter, i.e. the Quantum ChromoDynamics (QCD), its symmetries and how to solve this theory in equilibrium by lattice QCD simulations. The behavior of strongly interacting matter under extreme conditions will be discussed and especially the Quark-Gluon Plasma (QGP) phase is of particular interest. We will show that this state of matter can be studied in the theory of QCD as well as experimentally by heavy-ion collisions. We will describe the goals of actual heavy-ion experiments and how they relate to this work and to the unsolved questions of QCD.

1.1 History of the Standard Model of Particle Physics

The quest for understanding the matter inside and around us has a very long history and starts in the Ancient Greek civilization. In the Vth century before common era, Democritus gave rise to the **Atomism** philosophy, arguing that the matter should be composed of tiny indivisible pieces. However, there was no experimental evidence for this idea and the thought that predominated was from Aristotle who considered four elements: fire, air, water and earth. It's only in the end of the XVIIIth century that the Atomism philosophy came to light again in the study of chemical reactions by Lavoisier who stated that mass is neither created nor destroyed. At the beginning of the XIXth century, Dalton presented the first theory of atoms and introduced the notion of atomic weight for different elements. In the same spirit, Mendeleev made in 1869 another step forward in the comprehension of atomic matter with his **periodic table of the chemical elements** [22]. Even if he didn't join the philosophical thought of the Atomism, Mendeleev believed that a relationship between the chemical properties of the elements and their atomic weights would be the key to understand their chemistry. Concerning the chemistry we can also mention the works related to the electrolysis, where by example Faraday emphasized for the first time an universal unit of charge and popularized terms as ions, anions or cations.

In 1860, Maxwell published his work on the **kinetic theory of gases** where he describes the distribution of the particle velocities in a gas based on molecular collisions [25]. Later in 1872, Boltzmann generalized the distribution found by Maxwell when he studies the behavior of gases out-of equilibrium by the **Boltzmann equation** [28]. He explains that the collisions between the particles are responsible for the equilibrium and that the equilibrium distribution is unique: the Maxwell-Boltzmann distribution. In 1897, Thomson showed that the cathode rays in Crookes tubes were in fact composed of negative particles much smaller than an atomic scale: the electron [29]. This discovery completely changed the view that atomists had since the electron seemed to be a constituent of the atom, the latter thus not being a fundamental particle. The proof that molecules exist came in 1905 by Einstein where he gave an explanation for the **Brownian motion** [30] which is due to collisions of the atoms and molecules of the liquid. The Brownian motion is called after Robert Brown who observed the random movement of pollen particles in a liquid in 1827.

Concurrently, the fact that matter was composed of individual particles turned

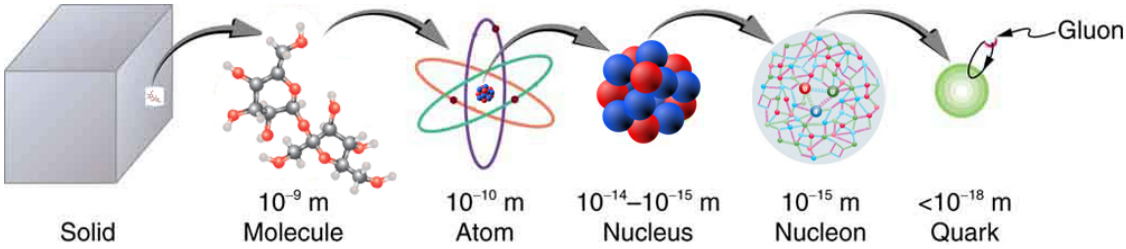

Figure 1.1 – Schematic view of the matter as we understand it nowadays for different scales, starting from a solid to the quarks and gluons composing the nucleons.

out to be true also for light, despite the success of Maxwell's equations that considered light as an electromagnetic radiation [31]. The revolution started with Planck in 1900 who found that the black-body radiation could be explained by considering that the energy can only be absorbed or emitted in specific amounts [32]: the **quantum**. A few years later, Einstein followed Planck's reasoning and explained in 1905 the **photoelectric effect** [35] that definitely proved that light was made of individual particles: the **photons**. However, the discovery of x-rays made before in 1895 by Röntgen (caused by the Bremsstrahlung radiation of electrons in the Crookes tube) and its identification by Max von Laue in 1912 as an electromagnetic radiation, reinforced Maxwell's statement that invisible radiations of different wavelengths can exist.

The discovery of the nucleus came in 1909 by Rutherford using radioactive elements previously found by Becquerel in 1886 and confirmed later on by Maria Skłodowska-Curie and Pierre Curie. Rutherford characterized these radioactive radiations into three categories, the α-rays, β-rays and γ-rays, that happened to be helium nuclei, electrons and high-energy photons, respectively. In his experiment, he used α-particles to probe gold atoms and proved that the atom mass and its positive charge were concentrated in a very small volume [36]. In 1919 he proves experimentally the existence of the **proton** [37] and speculates in the 1920s that a neutral particle should also be part of the nucleus, the **neutron**, which was later on discovered by Chadwick in 1932. Following Rutherford's and Planck's discoveries, Bohr developed the first quantum model of the atom in 1913 [38] where the electrons rotates around the nucleus in circular orbits. Even after several improvements of Bohr's model, the correct description of the atom came after the work of Heisenberg, de Broglie and Schrödinger [41–43] who developed a quantum mechanical description of the electron which is considered both as a wave and a particle (**wave-particle duality**). This theory describes an electron with an unique set of quantum numbers according to the **Pauli Exclusion Principle** [44].

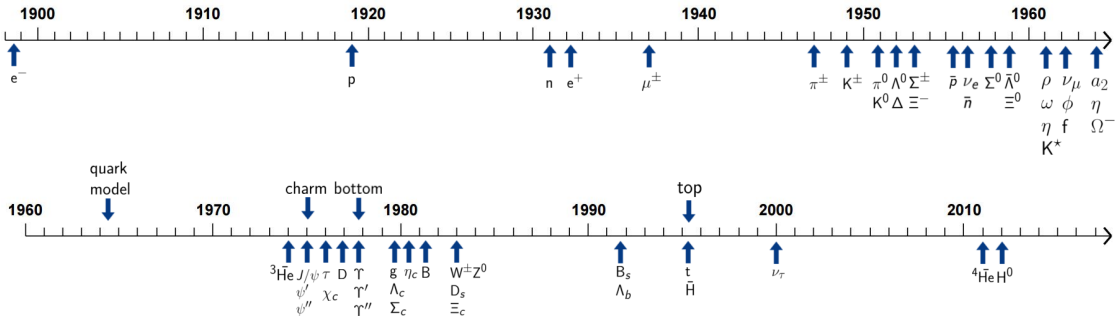

Figure 1.2 – Chronology of some of the particle discoveries before (top panel) and after (bottom panel) the quark model in 1964.

For the sake of finding a complete description of the electron, Dirac in 1928 combined quantum mechanics and relativity in his eponymous equation [45], and even predicted the positron, electron's antiparticle, that would annihilate with the latter to form at least two photons with an energy corresponding to the particle masses as given by Einstein's equation $E = mc^2$ in 1905 [46]. The positron was discovered in 1932 by Anderson in cosmic rays passing through a cloud chamber. In order to explain all the variety of particles discovered through cosmic rays and the development of particle accelerators between the 1930s and the 1960s (see fig. 1.2), Gell-Mann [47] and Zweig [48] proposed the **quark model** in 1964 where hadrons are actually composite particles.

The experimental proof that protons and neutrons were made of composite particles came in 1969 at the Stanford Linear Accelerator Center (SLAC) [50], but still the identification of these particles as the quarks predicted by Gell-Mann and Zweig was not evident for the scientific community. The discovery of the charm quark through the J/ψ bound state in 1974 at the SLAC [53] and at the Brookhaven National Laboratory (BNL) [54] convinced of the reality of the quark model. The discovery of the heavier bottom [55] and top [56] quarks at the Fermi National Accelerator Laboratory (Fermilab) concluded the completion of the quark model. In addition, the search in a gauge boson describing the interactions between quarks was of great interest since theories were developing in the 1970s around the comprehension of the hadron structure. The two first experimental signatures of the gluon were found in 1979 at the Deutsches Elektronen-Synchrotron (DESY) in the decay of the Υ into three gluons [59], and in the quark pair production and bremsstrahlung process $e^+e^- \to q\bar{q}g$ [60]. Since this discovery, more fundamental particles have been added to what is called the Standard Model of Particle Physics which describes the interaction of fundamental particles through three fundamental forces: electromagnetic, weak and strong interactions (Fig. 1.3). The last particle

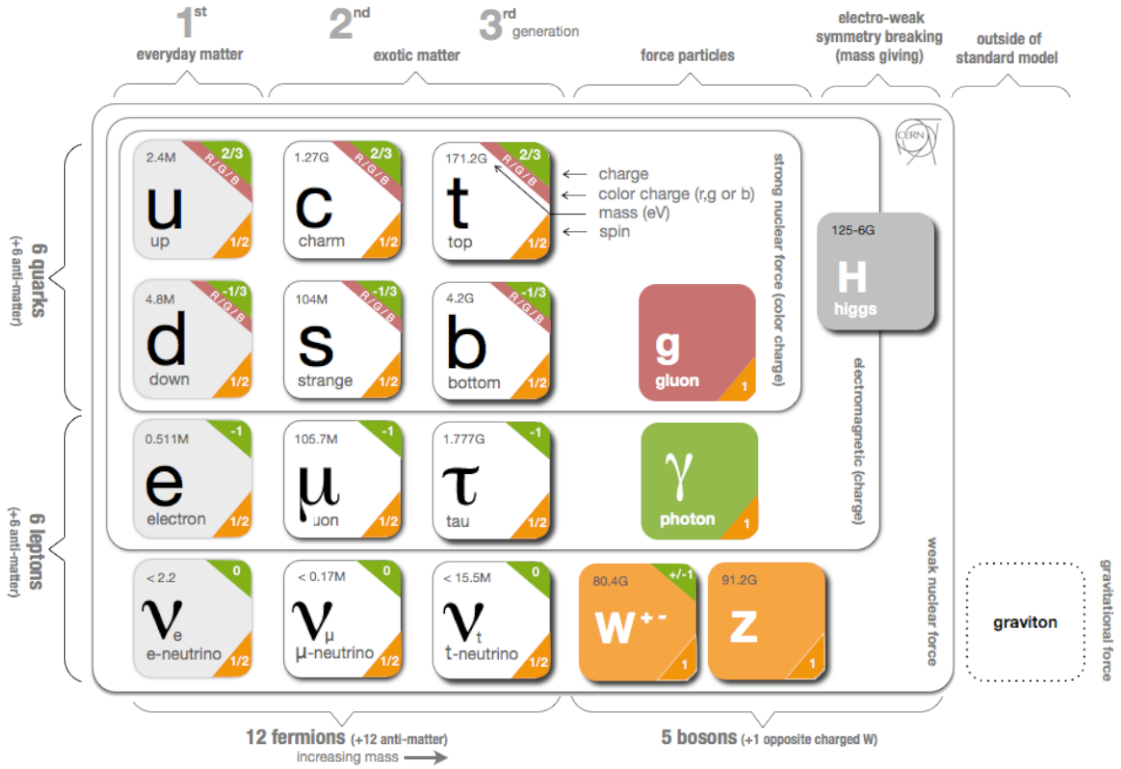

Figure 1.3 – Standard model of particle physics showing the mass, charge, color charge and spin of the different fundamental particles as well as their interaction through the different bosons (taken from Ref. [49]).

added to the standard model was found in 2012 by the discovery of the Higgs boson by the ATLAS and CMS experiments at the Large Hadron Collider (LHC) [61].

1.2 Quantum ChromoDynamics

In this thesis, we will concentrate on the theory that describes the (strong) interactions between colored objects which are quarks and gluons: the **Quantum ChromoDynamics (QCD)**. The color charge was first suggested to remedy the problem of the Ω^- and the Δ^{++} baryons, which, according to the quark model, would be composed of three identical quarks (s and u respectively) with aligned spins. This configuration is forbidden by the Pauli exclusion principle, except if there would be an additional quantum degree-of-freedom with at least three distinct values [64]. This problem was solved in 1964-65 by Greenberg [65], and Han and Nambu [66], who suggested that each of the quarks can have a 3-valued color charge

which would be responsible for the interactions between them through a $SU(3)_c$ gauge vector boson, the gluon. The classical Lagrangian density of QCD describes the dynamics of the quark-field spinors $\psi_q(x)$ and the gluon fields $A^a_\mu(x)$ by:

$$\mathcal{L}_{QCD} = \sum_q \bar{\psi}_{q,i} \left(i \not{D}_{ij} - m\delta_{ij} \right) \psi_{q,j} - \frac{1}{4} F^a_{\mu\nu} F^{\mu\nu}_a, \tag{1.1}$$

with $\bar{\psi} \equiv \psi^\dagger \gamma^0$ being the Dirac adjoint of ψ. The sum over q runs over the different quark flavors, i represents the quark color which runs from $i = 1$ to $N_c = 3$, and a is the combination of color charges carried by the gluon, running from $a = 1$ to $N_c^2 - 1 = 8$. The QCD Lagrangian is **gauge invariant**, meaning that gauge fields (the gluons) are introduced such that the Lagrangian is invariant under the local group transformation $\psi(x) \to e^{i\alpha_a(x)T^a}\psi(x)$, where T^a are the generators of the $SU(3)$ group (see more details in Appendix B). These generators are 3×3 matrices which encode the fact that a gluon interacting with a quark will rotate the color of the latter in $SU(3)_c$ space [67]. To ensure gauge invariance, the gauge covariant derivative is used in Eq. (1.1):

$$\not{D}_{ij} := \gamma^\mu (D_\mu)_{ij} = \gamma^\mu \partial_\mu \delta_{ij} - i g_s \gamma^\mu T^a_{ij} A^a_\mu, \tag{1.2}$$

with γ^μ being the Dirac gamma matrices, and g_s the QCD **coupling constant**. The first term of the Lagrangian (1.1) describes the quark propagation in a gauge field, whereas the second term corresponds to the so-called **Yang-Mills** [68] Lagrangian describing the gluon dynamics which contains the field strength tensor:

$$F^{\mu\nu}_a = \partial_\mu A^a_\nu - \partial_\nu A^a_\mu + g_s f^{abc} A^b_\mu A^c_\nu, \tag{1.3}$$

with f^{abc} being the structure constants of $SU(3)$ (see more details in Appendix B). The fact that this theory has non-vanishing structure constants indicates that the gluons can interact with each other (since they carry themselves color), which defines QCD as a **non-abelian gauge theory**.

Note

QCD being a non-abelian gauge theory leads to two characteristics which are **asymptotic freedom** and **confinement**. The asymptotic freedom was discovered in 1973 by Gross and Wilczek [69], and Politzer [70], and translates into the fact that at very high energies (or very short distances), the interactions between quarks and gluons become weaker. On the contrary at low energies (or large distances), the anti-screening of color charges leads to highly nonperturbative interactions which confine quarks into colorless bound states known as hadrons. These characteristics are opposite to QED which is an abelian gauge theory with the symmetry group $U(1)$ (see figure below). Due to asymptotic freedom, one can think that by heating or compressing hadrons up to very high energies, a new state of matter can be produced where quarks and gluons are not confined anymore into hadrons: this is the **Quark-Gluon Plasma** (QGP).

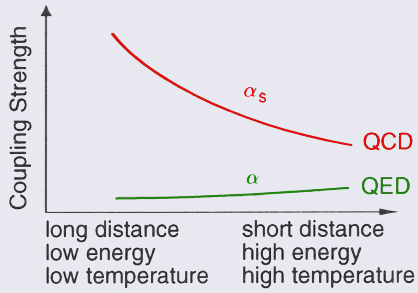

Figure 1.4 – Behavior of the QED and QCD coupling constant as a function of the distance scale (adapted from Ref. [71]).

1.2.1 Symmetries of QCD

In addition of the local color symmetry, the QCD Lagrangian has several other global symmetries associated to the quark flavors. Symmetries are very important because they define the conservation laws of the theory by the **Noether's theorem** [72] which states that [73]:

"If a Lagrangian has a continuous symmetry then there exists a current associated with that symmetry that is conserved when the equations of motion are satisfied".

We start by considering the general transformation

$$\psi(x) \to \psi'(x) = e^{-i\alpha_a \Gamma^a} \psi(x), \tag{1.4}$$

with real constants α_a, and with Γ^a being the generators of a possible $U(N)$ or $SU(N)$ group. The **Noether currents** associated with the QCD Lagrangian are then found to be:

$$J^a_\mu = \frac{\partial \mathcal{L}_{QCD}}{\partial(\partial_\mu \psi)} \frac{\delta \psi}{\delta \alpha_a} = \bar{\psi}(x) \gamma_\mu \Gamma^a \psi(x). \tag{1.5}$$

These currents are conserved (i.e. $\partial_\mu J^\mu_a(x) = 0$) if the QCD Lagrangian is invariant under the transformation (1.4). To each conserved current J_a a conserved charge is associated, which is given by:

$$Q_a = \int d^3x J^0_a(x) = \int d^3x \ \psi^\dagger(x) \Gamma_a \psi(x), \tag{1.6}$$

and satisfies

$$\partial_t Q_a = \int d^3x \ \partial_t J^0_a(x) = \int d^3x \ \vec{\nabla} \cdot \vec{J}_a(x) = 0. \tag{1.7}$$

In order to study the symmetries of QCD, we will concentrate on the low energy domain (with only the u and d quarks), and it is therefore useful to separate the Lagrangian into different quark flavor contributions:

$$\mathcal{L}_{ud} = \mathcal{L}_{QCD} - \mathcal{L}_{scbt} = \mathcal{L}_{\text{chiral}} - \left(m_u \ \bar{u}u + m_d \ \bar{d}d \right), \tag{1.8}$$

where $\mathcal{L}_{ud}$ and $\mathcal{L}_{scbt}$ are the contribution to the QCD Lagrangian from the light quarks u, d and from heavier quarks s, c, b, t, respectively. $\mathcal{L}_{\text{chiral}}$ is the remaining part of the Lagrangian which doesn't contain the mass terms associated to the light quarks u and d.

The different symmetries, which are associated to the 2-flavor QCD Lagrangian $\mathcal{L}_{ud}$, are summarized in table 1.1 [74, 75]. The first symmetry is **isospin symmetry** and is conserved if one assumes equal masses $m_u = m_d$. If this condition would be exactly fulfilled in Nature, the three pions, or the proton and neutron, would have exactly same mass (see also Fig. 1.3 for the quark masses). The generators of the associated $SU(2)_f$ group are $\tau^k = \sigma^k/2$ with σ^k being the **Pauli matrices** in flavor space. If one extends to the three flavor case (including the s quark), the so-called flavor $SU(3)_f$ symmetry is broken due to the larger

strange quark mass, but still can be useful to categorize hadrons according to their strangeness content and charge [76, 77]. The second global symmetry $U_V(1)$ manifests itself as **baryon number conservation** and is always conserved.

Symmetry	Transformation	Current	Name	Manifestation
$SU_V(2)$	$\psi \to e^{-i\tau^k \omega_k}\psi$	$J^k_\mu = \bar{\psi}\gamma_\mu \tau^k \psi$	isospin	approx. conserved
$U_V(1)$	$\psi \to e^{-i\alpha}\psi$	$j_\mu = \bar{\psi}\gamma_\mu \psi$	baryonic	always conserved
$SU_A(2)$	$\psi \to e^{-i\tau^k \theta_k \gamma_5}\psi$	$J^k_{5,\mu} = \bar{\psi}\gamma_\mu\gamma_5 \tau^k \psi$	chiral	Breaking
$U_A(1)$	$\psi \to e^{-i\beta\gamma_5}\psi$	$j_{5,\mu} = \bar{\psi}\gamma_\mu\gamma_5 \psi$	axial	axial anomaly

Table 1.1 – The different symmetries, associated transformations, current and manifestations, of the two flavor QCD Lagrangian [74, 75]. The subscript V and A refers to vector and axial-vector, respectively. The variables ω, α, θ, β are arbitrary real numbers.

The two other symmetries are the **chiral** and **axial symmetries** which involve the $\gamma_5 = i\gamma^0\gamma^1\gamma^2\gamma^3$ matrix and are conserved in the massless case, i.e. only for the $\mathcal{L}_{\text{chiral}}$ part of the classical QCD Lagrangian. To study in more detail the symmetries of the Lagrangian density $\mathcal{L}_{\text{chiral}}$, it is useful to introduce left- and right-handed quark states which are eigenstates of the **chirality operator** γ_5:

$$q_L = P_L\, q = \frac{1}{2}(1-\gamma_5)\, q \quad \text{with} \quad \gamma_5\, q_L = -q_L, \tag{1.9}$$

$$q_R = P_R\, q = \frac{1}{2}(1+\gamma_5)\, q \quad \text{with} \quad \gamma_5\, q_R = +q_R, \tag{1.10}$$

with $q^T = (u, d)$. $P_{L/R}$ are the (orthogonal) chirality operators with the following properties: $\bar{\psi}_L = \bar{\psi}P_R$ and $\bar{\psi}_R = \bar{\psi}P_L$. The 2-flavor Lagrangian can then be written as:

$$\begin{aligned}\mathcal{L}_{ud} &= \bar{q}_L\, i\not{D}\, q_L + \bar{q}_R\, i\not{D}\, q_R - (\bar{q}_L\, \mathbf{m}\, q_R + \bar{q}_R\, \mathbf{m}\, q_L) + \mathcal{L}_{\text{gluons}} \\ &= \mathcal{L}_{\text{chiral}} - (\bar{q}_L\, \mathbf{m}\, q_R + \bar{q}_R\, \mathbf{m}\, q_L)\end{aligned} \tag{1.11}$$

with $\mathbf{m}$ being the matrix containing the quark masses in flavor space. One can see that the Lagrangian $\mathcal{L}_{\text{chiral}}$ is invariant under the separate rotations:

$$q_L \to e^{-i\lambda_k \theta_L^k}\, q_L, \qquad q_R \to e^{-i\lambda_k \theta_R^k}\, q_R, \tag{1.12}$$

where $\theta_{L/R}$ are real parameters. If left- and right-handed fields transform in the same way, the symmetry is called **vector symmetry**, whereas if they transform differently, the symmetry is called axial-vector or **chiral symmetry**. To connect with the transformations and subscripts V and A in table 1.1, one can define vector and axial-vector transformations:

$$q \to e^{-i\lambda_k \theta_V^k}\, q, \qquad q \to e^{-i\lambda_k \theta_A^k \gamma_5}\, q, \tag{1.13}$$

with $\theta_V = \theta_L = \theta_R$ and $\theta_A = -\theta_L = \theta_R$. As an example, the conserved charges related to the $U(1)$ symmetries in table 1.1 are the baryon number B and axial charge Q_A:

$$B \equiv \frac{1}{3} Q_V = \frac{1}{3} \int d^3x\ \bar{\psi}\psi = \frac{1}{3} \int d^3x\ \left[\bar{q}_R(x) q_R(x) + \bar{q}_L(x) q_L(x)\right], \tag{1.14}$$

$$Q_A = \int d^3x\ \bar{\psi}\ \gamma_5\ \psi = \int d^3x\ \left[\bar{q}_R(x) q_R(x) - \bar{q}_L(x) q_L(x)\right]. \tag{1.15}$$

Note

For massless fermions, the chirality is the same quantity as the **helicity**: if the spin of the particle is aligned (opposite) with its momentum, the particle has a positive (negative) helicity, as shown in the figure below. When dealing with massive particles, the helicity becomes frame-dependent and therefore, chirality and helicity must be distinguished.

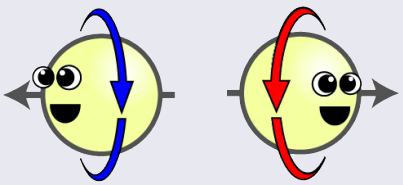

Figure 1.5 – Particles having a negative (left-hand side) and positive (right-hand side) helicity (from Ref. [78]).

Finally, we give the overall symmetries of the 2-flavor chiral Lagrangian $\mathcal{L}_{chiral}$ which can be written in the following form:

$$SU_V(2) \times SU_A(1) \times U_V(1) \times U_A(1) = [SU(2) \times U(1)]_L \times [SU(2) \times U(1)]_R. \tag{1.16}$$

Note

Due to the finite light quark masses, the chiral and axial symmetries are **explicitly broken**, but by comparing these masses to the scale of QCD $\Lambda_{QCD} \approx 200$ MeV, one can naively think that the chiral and axial symmetries can be approximately realized in Nature. This implies for the symmetry $SU_A(2)$ ($U_A(1)$) that each isospin multiplet (all hadrons) should have a so-called chiral partner, with the exact same mass and opposite chirality, which is however not observed in the hadronic spectrum. This suggests that the axial and chiral symmetries could be **spontaneously broken** due to temperature or density effects. The **Goldstone's theorem** [79] states that:

"The spontaneous breaking of a continuous global symmetry implies the existence of associated massless spinless particles",

and is realized in Nature for the chiral symmetry but not for the axial symmetry:

- Pions, due to their small mass, are identified to the pseudo-Goldstone bosons associated with the explicit and spontaneous breaking of the chiral symmetry $SU_A(2)$ at low temperatures and densities. An other hint for the spontaneous breaking of chiral symmetry is the mass difference between the vector ρ and pseudo-vector a_1 mesons. These mesons are good candidates to be chiral partners since their quantum numbers match the ones from the vector and axial-vector current, respectively. In a chiral restored phase, one expects chiral partners to have exactly the same mass since, by example, the ρ-meson can be rotated into the a_1 state by a chiral transformation [80].

- The $U_A(1)$ symmetry is explicitly broken not only by the current quark mass in the QCD Lagrangian, but also by the quantum effect called axial or Adler-Bell-Jackiw anomaly [81, 82]. This originates from the non-invariance of the path integral measure under the $U_A(1)$ transformation [74, 83, 84]. An other manifestation of the axial anomaly is the large η' mass compared to other pseudoscalar mesons, according to the Witten-Veneziano mechanism [85, 86].

1.2.2 Lattice QCD

As we have seen, the physics of hadrons and their possible transition to a plasma state is highly nonperturbative since it corresponds to the low energy regime of QCD. In this case, one cannot rely on an expansion in power series of the strong coupling constant as in perturbative approaches, but rather one should find a "brute-force" method to solve QCD directly. The lattice QCD (lQCD) approach initially developed by Wilson [87] overcomes these difficulties by discretizing the theory of QCD on a space-time lattice. The matter fields (quarks) are situated at the lattice points called sites, whereas gauge fields (gluons) connect the sites on the so-called link variables or links $U_\mu = \exp(iaA_\mu(x))$ with a being the lattice spacing (see Fig. 1.6). As we will see later, QCD has to be discretized on an Euclidean space-time in order to be solved by Monte-Carlo algorithms. One usually considers a 4-dimensional hyper-cubic lattice of $N_s^3 \times N_t$ points, with N_s (N_t) being the number of points in the spatial (temporal) dimension. To calculate quantities at finite temperature T, one can relate the latter to the temporal extension of the lattice as $T = (N_t \times a)$ [88]. Applying the Wick's rotation [89], one can express the theory from Minkowski to Euclidean space-time and in particular, time is substituted by the imaginary time $t \to -ix_4$.

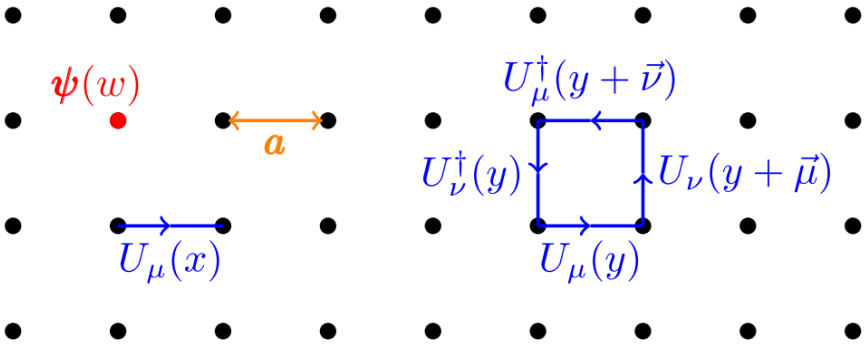

Figure 1.6 – Illustration of the lattice discretization, where ψ is the fermion field defined on the sites, U is the link variable, and on the right-hand side the plaquette product of links (taken from Ref. [90]).

To study a quantized version of the theory, one employs the functional integral formulation over quark and gluon fields, which gives the partition function of QCD

as [67]:

$$
\begin{aligned}
Z &= \int \mathcal{D}U \prod_f \mathcal{D}q_f \, \mathcal{D}\bar{q}_f \, e^{-S_E[U]} \\
&= \int \mathcal{D}U \prod_f \mathcal{D}q_f \, \mathcal{D}\bar{q}_f \, e^{-S_g[U]-\sum_f \bar{q}_f(D[U]+m_f)q_f} \\
&= \int \mathcal{D}U \, e^{-S_g[U]} \prod_f \det\left(D[U]+m_f\right),
\end{aligned}
\tag{1.17}
$$

with the Euclidean action

$$
S_E = -\int_0^{1/T} dx_4 \int_V d^3x \, \mathcal{L}_E, \tag{1.18}
$$

and $\mathcal{L}_E$ being the Lagrangian in Euclidean space-time. The symbol $\mathcal{D}$ represents the functional sum over all field configurations, meaning the sum over all possible choices of the field values on the lattice. The gluon action S_g can be calculated on the lattice using a product of the link variables U_μ around closed loops (plaquette), which is a discretized version of the **Wilson loop**. Concerning the quark action, $D[U]$ is the chosen Dirac operator on the lattice, and det is the determinant of the fermion matrix $(D[U]+m_f)$. The so-called **fermion determinant** induces very high computational costs (which are inversely proportional to the quark mass) since it should be taken over all indices of the quark fields (color, flavor, spin and space-time coordinates). The replacement of the fermion determinant by a constant, thus ignoring the effects of dynamical quarks, is called the **quenched approximation**.

The integration in Eq. (1.17) can only be performed using Monte-Carlo techniques due to the very large number of variables. With this method, a Markov chain of configurations is generated in accordance to the probability $\propto \exp(-S_g[U])$. These Monte-Carlo techniques induce statistical as well as systematics errors due to the finite lattice spacing. However, lattice QCD results can be evaluated at different lattice spacings and extrapolated to the limit $a \to 0$ to obtain the correct continuum results. The thermal expectation value of a physical observable $\mathcal{O}$ can for example be evaluated on the lattice as:

$$
\langle \mathcal{O}(U,q,\bar{q}) \rangle = \frac{1}{Z} \int \mathcal{D}U \prod_f \mathcal{D}q_f \mathcal{D}\bar{q}_f \, \mathcal{O}(U,q,\bar{q}) \, e^{-S_g[U]-\sum_f \bar{q}_f(D[U]+m_f)q_f}. \tag{1.19}
$$

One can evaluate two- or three-point functions on the lattice; for example this

method has been very successful in describing the hadron spectroscopy, and can also be used to predict the content and masses of hypothetic hadrons by choosing the appropriate operators [91]. Thermodynamic quantities can be evaluated on the lattice by evaluation of the QCD partition function [88] and lead to very precise results at vanishing chemical potential $\mu = 0$. For example, the left-hand side of Fig. (1.7) shows the latest results for the (2+1)-flavor QCD Equation of State (EoS) as a function of the temperature. One can see a rapid crossover transition from a hadron-gas below T_c to a Quark-Gluon Plasma (QGP) above T_c, with $T_c \approx 155$ MeV ($\approx 1.8 \times 10^{12}$ K) being the **critical temperature**. In lattice QCD calculations, one can also study the restoration of chiral symmetry as a function of temperature. The order parameter for the restoration of chiral symmetry, i.e. the **chiral condensate**, is shown on the right-hand side of Fig. 1.7 as a function of temperature and shows a pseudo-critical temperature which is similar to the one for the deconfinement temperature [92]. A lot of interests in the lattice QCD community focus on the understanding of the interplay between the chiral and deconfinement transitions. These findings are summarized in the so-called **Columbia plot** [93] (Fig. 1.8) which indicates the nature of the thermal QCD transition as a function of the light and strange quark masses, thus varying the degree of chiral symmetry restoration. When the quark masses are zero, chiral symmetry is fully restored whereas when they are infinitely massive, one recovers the pure Yang-Mills theory.

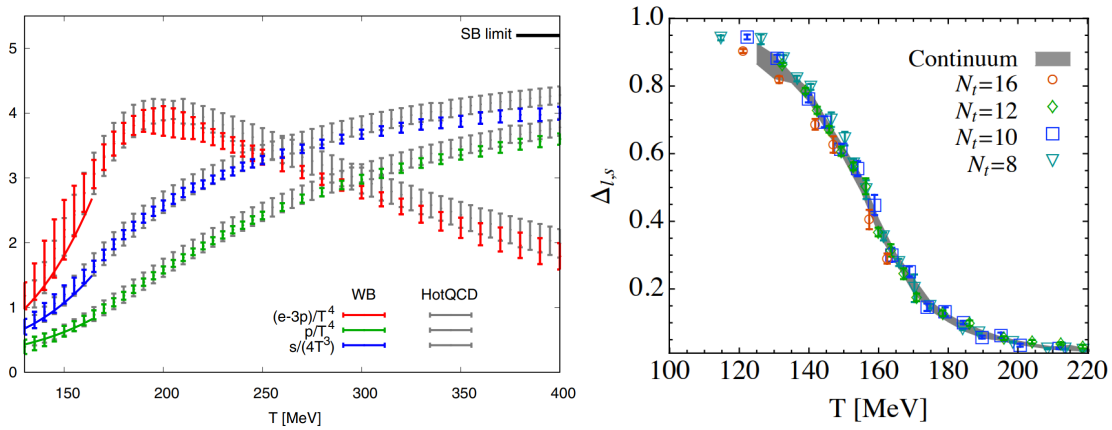

Figure 1.7 – Left: Continuum extrapolated results of the $2+1$ flavor interaction measure, pressure and entropy density from the HotQCD collaboration [94] and the WB collaboration [95] (taken from Ref. [88]). The Stefan-Boltzmann limit is indicated for the pressure and the scaled entropy. Right: Results for the continuum extrapolated "subtracted" chiral condensate as a function of the temperature (from Ref. [96]).

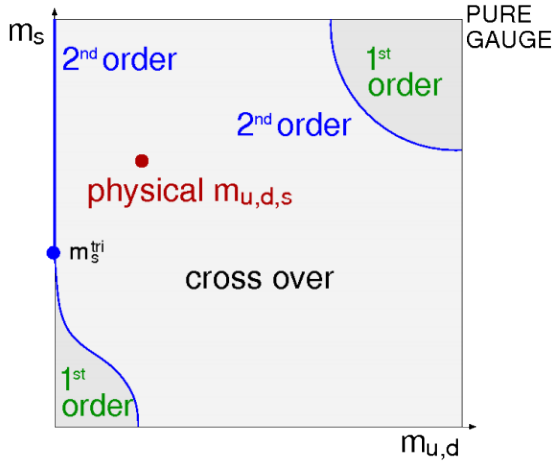

Figure 1.8 – Columbia plot showing the current expectations on the order of the thermal phase transition in QCD (including the $U_A(1)$ anomaly) as a function of the light and strange quark masses (from Ref. [97]).

Note

An **order parameter** is a measure of how much a transtion is realized in a system. This number usually ranges between 0 after the transition and a finite number below. For the case of QCD, the order parameter associated to the deconfinement is the Polyakov loop, and for the chiral symmetry the chiral condensate. The behavior of the order parameter depends on the type of phase transition:

- **1$^{\text{st}}$ order**: the order parameter is discontinuous at the transition, meaning that thermal energy can be absorbed or released by the system while the temperature remains constant. During the transition, the two phases coexist, a famous example being the melting of ice or the boiling of water.
- **2$^{\text{nd}}$ order**: the order parameter has no discontinuity (it is a "continuous phase transition") but its first derivative does. This transition is characterized by an infinite correlation length, where one can not distinguish in which phase the sytem is, leading to the phenomemon of critical opalescence. The end point of the region where two phases can coexist, i.e. of a 1$^{\text{st}}$ order transition, is a 2$^{\text{nd}}$ order transition denoted as a **critical point**.
- **crossover**: this is not a real phase transition since it presents no discontinuities in the order parameter or thermodynamic observables between the two phases.

The evaluation of thermodynamic quantities at finite chemical potential μ can not be performed by using the Monte-Carlo algorithms mentioned above due to the so-called **sign problem**. This problem is already present at vanishing chemical potential where the fermion determinant can become negative for light quarks, and thus prohibiting the evaluation of the QCD partition function by Monte-Carlo techniques. However, this problem can be overcome when considering an even number of degenerate light quarks since we then obtain in Eq. (1.17) $\left(\det\left(D[U]+m_f\right)\right)^{N_f}$. At finite chemical potential, the fermion determinant becomes complex and the evaluation of the partition function can not be performed by Monte-Carlo algorithms. Different techniques are nowadays used to access the QCD EoS at finite baryon chemical μ_B including a Taylor expansion around $\mu_B = 0$, or an analytic continuation of the results obtained at imaginary chemical potential, where the sign problem does not appear. One should note that these techniques are limited to low chemical potential $\mu_B/T < 2$, where until now, no indication of a possible QCD critical point has been found in this region [101]. The QCD phase diagram and properties of QCD as a function of the chemical potential (Fig. 1.9) can only be accessed through effective models as we will see in the next chapters of this thesis,

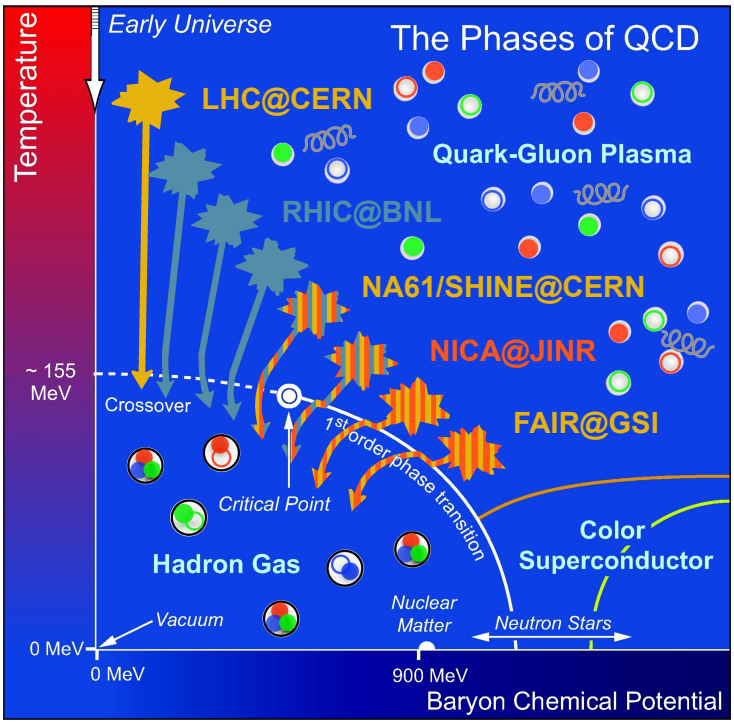

Figure 1.9 – Current status of the conjectured QCD phase diagram in the temperature T - chemical potential μ_B plane (adapted from Refs. [98–100]).

or experimentally, as we will see in the next section, through heavy-ion collisions where extremely hot and dense matter can be achieved.

1.3 Heavy-ion collisions

The main motivation of relativistic heavy-ion experiments is to study the Quark-Gluon Plasma (QGP) state of matter which can only be produced at very high temperatures or densities. The QGP was motivated by the theory of QCD as we have seen in the previous section, and has a lot of implications through different fields of physics like astrophysics. Indeed, our entire universe was in a QGP state at the very beginning of its history according the to **Big Bang theory** (see Fig. 1.10). In this description, the universe was initially a very dense fireball consisting of quarks, gluons, photons and other leptons, which expanded and cooled down to form nucleons, ions, atoms, until our actual universe consisting of stars and galaxies. To understand the history of our universe, it is therefore mandatory to understand what are the properties of the QGP as a function of temperature and density, and how does it lead to confined matter as we know it. Moreover, objects of our universe, which have a very high density, could also contain a QGP state, such as white dwarfs, neutron stars and quark stars.

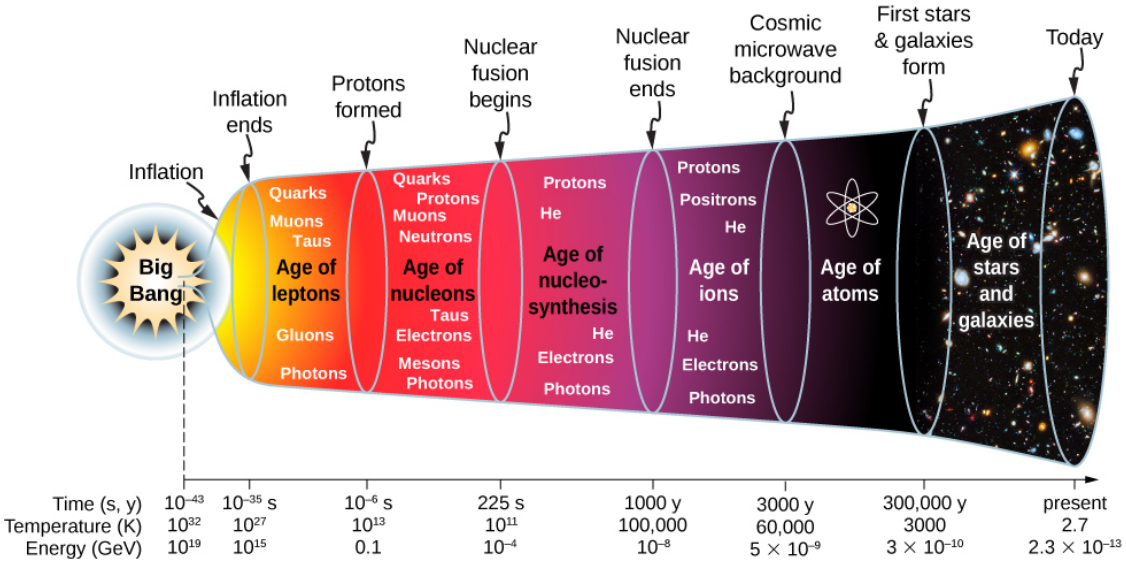

Figure 1.10 – History of our universe according to the Big Bang theory (taken from Ref. [102]).

In heavy-ion experiments, the possible formation of a QGP can only be accessed through the theoretical understanding of the final spectra of detected particles. Among others, several probes (see also the illustration in Fig. 1.11) can signal the appearance of a QGP in heavy-ion collisions:

- **Bulk particles**: the production and momentum of low p_T hadrons can be modified due to the appearance of the QGP. Examples are: a plateau and a rise of the mean transverse momentum as a function of the collisional energy can indicate a first-order phase transition [103]; increase of the elliptic flow [104]; enhanced production of strangeness in the QGP [105]; multi-strange antibaryons become easier to produce from the QGP than from hadronic interactions [106].

- **Quarkonia**: They are flavorless mesons formed by a quark and its antiquark. Bound states of heavy quarks (charmonium $c\bar{c}$ and bottomonium $b\bar{b}$) are of special interest to study the appearance of the QGP since they are produced at the very beginning of the heavy-ion collision. Moreover, they are expected to survive in the deconfined phase up to a certain temperature known as their dissociation temperature T_d. For example, the survival of the J/ψ ($T_d \approx 2T_c$) and its excited state ψ' ($T_d \approx 1.1T_c$) can ideally be associated to the temperature reached in the QGP phase: this is known as the **sequential suppression** [107].

- **Jet quenching**: Jets are very energetic partons which are produced through hard scatterings at the very beginning of heavy-ion collisions, and therefore, they can probe the matter created in the latter and lose a significant amount of energy into the QGP. Back to back jets are then observed in heavy-ion experiments as hadronic showers which are produced by fragmentation of the initial energetic parton, and their energy can be compared to reveal a possible attenuation.

- **Electromagnetic probes**: An enhancement of thermal photons and dileptons is expected during a QGP phase due to the collisions between partons (Drell-Yann process, gluon Compton scattering, quark annihilation with gluon bremsstrahlung). They are in theory excellent probes since they practically do not interact with the matter created in heavy-ion collisions, and therefore they keep their energy from their production until their detection. However, many other sources of photons and dileptons are present in heavy-ion collisions (by example the Dalitz decay of the pseudoscalar mesons π^0 and η, and the decay of vector mesons like the ρ, ω, ϕ, J/Ψ etc.).

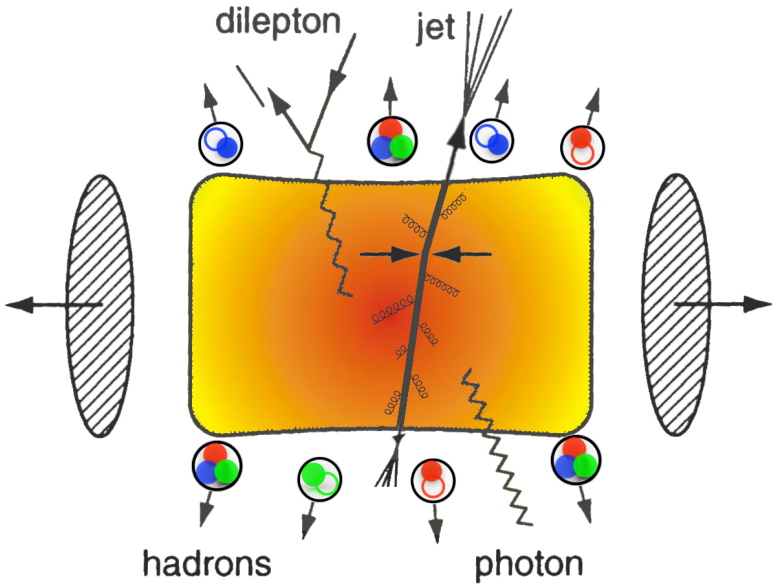

Figure 1.11 – Different particles produced in a heavy-ion collision which can be used as probes of the Quark-Gluon Plasma (adapted from Ref. [71]).

Several of these probes have been successfully observed at the Super Proton Synchrotron (SPS) and later on at higher collisional energies at the Relativistic Heavy Ion Collider (RHIC), which undoubtedly announced the production of a QGP in their heavy-ion collisions. A surprise in this discovery was that the QGP formed in heavy-ion collisions behaved almost like a perfect fluid, requiring it to be a strongly coupled plasma with a very low viscosity [108]. Also, flow patterns were additionally observed in charm and bottom quarks [109], implying that even these heavy quarks are dragged along by the collective expansion of the QGP. However, the properties of strongly interacting matter are far from being precisely known at this day, especially at high densities, and heavy-ion experiments are trying to accumulate experimental data at different collisional energies to answer the following questions:

- **Onset of deconfinement**: At which collisional energy or density is the QGP precisely produced in heavy-ion collisions? To this purpose, one can study different collisional energies and different system sizes and look if the signatures of a QGP appear or not in the experimental data.
- **First-order phase transition**: To address the question whether there is a 1^{st} order phase transition or not, one should find observables that can signal this behavior. The directed flow, which is related to the pressure in the system, is a promising observable.

- **Critical end point**: The existence of the critical end point is directly linked to the 1st order phase transition, finding one of these phenomena implies the existence of the other. It could be detected by analyzing the fluctuations on some observables as a function of the system size and the collisional energy.

- **Chiral symmetry restoration**: As explained in the previous subsection, vector mesons like the ρ, ω, ϕ, are sensitive to the restoration of chiral symmetry and a change in their properties (mass and width) is looked for in heavy-ion experiments. Vector mesons present the advantage that they can be studied via dilepton decays.

The quest for these unsolved questions aims to complete our understanding of the QCD phase diagram, where the different states and transitions of strongly interacting matter are represented as a function of the temperature T and baryon chemical potential μ_B (see Fig. 1.9). Experiments which can or intend to explore different regions of the QCD phase diagram are the Beam Energy Scan (BES) [110] program at the Relativistic Heavy Ion Collider (RHIC), the NA61/SHINE experiment [111] at the European Organization for Nuclear Research (CERN), the Nuclotron-based Ion Collider fAcility (NICA) [112] at the Joint Institute for Nuclear Research (JINR), and the Facility for Antiproton and Ion Research (FAIR) [113–115] at the GSI Helmholtz Centre for Heavy Ion Research. More information about the research programs that will be studied in this work can be found in table 1.2.

Unfortunately, the temperature and chemical potential, which are reached in a heavy-ion collision, are not directly accessible, especially if the system is out of equilibrium. To obtain an estimate on these quantities, **statistical models** are employed and fixed in order to reproduce the observed particle yields given by experimental data. In the Grand Canonical (GC) description of a system in thermal and chemical equilibrium, the partition function reads [116]:

$$Z^{GC}(T,V,\mu_Q) = \mathrm{Tr}\left[\exp\left(-\beta(H-\sum_i \mu_{Q_i} Q_i)\right)\right], \tag{1.20}$$

with V being the volume of the system, H the Hamiltonian, and μ_{Q_i} the chemical potential associated to the conserved charge Q_i. To constrain these models on heavy-ion collision data, one should include the conservation of electric charge Q, baryon number B and strangeness S. To obtain the full partition function of the system, one can sum the individual contributions from the non-interacting hadron or resonance i as [116]:

$$\ln Z_i(T,V,\vec{\mu}) = \frac{V g_i}{2\pi^2}\int_0^\infty \pm p^2 \; dp \; \ln\left[1 \pm \lambda_i \exp(-\beta E_i)\right], \tag{1.21}$$

with $\vec{\mu} = (\mu_B, \mu_S, \mu_Q)$, g_i the degeneracy factor associated with particle i, the sign (+) is for fermions and (-) for bosons, and the fugacity reads

$$\lambda_i(T, \vec{\mu}) = \exp\left(\frac{B_i\mu_B + S_i\mu_S + Q_i\mu_Q}{T}\right). \tag{1.22}$$

For the case of a heavy-ion collision, the net strangeness is zero and the electric charge is fixed by the content of the initial nuclei. From this statistical analysis, one then calculates the density of particles which leads to the extraction of the baryon chemical potential μ_B, and the **chemical freeze-out** temperature which is the temperature after which the system ideally does not change its chemical composition. This extraction is shown in the left-hand side of Fig. 1.12 for Au-Au collisions at different centralities and energies. On the right-hand side of Fig. 1.12, one can see the collisional energy dependence on the chemical as well as **kinetic freeze-out** temperature, the latter corresponding to the temperature where the momentum of the particles is fixed. It is found that the chemical and kinetic freeze-out are very similar at low collisional energies, whereas this difference increases at high energies. The chemical freeze-out temperature saturates at high energies and indicates that the chemical composition of the system seems to be decided around the transition temperature T_c. After the hadronization process, hadrons interact until the kinetic freeze-out temperature which becomes lower at higher energies, indicating that the effect of hadronic interactions seems to be more important in this energy region.

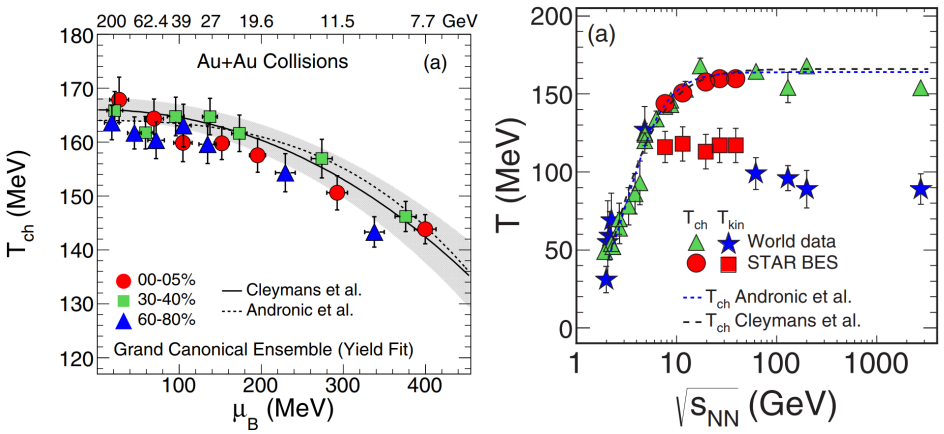

Figure 1.12 – Left: Evaluation of the chemical freeze-out temperature T_{ch} and the baryon chemical potential μ_B for Au+Au collisions at different collisional energies and centralities. Right: Energy dependence of the chemical and kinetic freeze-out temperature for central heavy-ion collisions. Both figures are from Ref. [117].

Research center	Facility / accelerator	Year	Beam	E_{kin}[A GeV] (E_{beam})	$\sqrt{s_{NN}}$ [GeV]
Brookhaven National Laboratory (BNL)	Alternating Gradient Synchrotron (AGS)	(1959) 1992	$^{197}_{79}$Au	2 4 6 8 10.7	2.70 3.32 3.84 4.30 4.86
European Organization for Nuclear Research (CERN[1])	Super Proton Synchrotron (SPS)	(1976) 1994	$^{208}_{82}$Pb	20 30 40 80 158	6.27 7.62 8.76 12.32 17.27
BNL	Relativistic Heavy Ion Collider (RHIC)	2000	$^{197}_{79}$Au	29.73 43.24 68.62 110.20 202.90 386.72 808.89 2.07×10^3 9.00×10^3 21.32×10^3	7.7 9.2 11.5 14.5 19.6 27 39 62.4 130 200
CERN	Large Hadron Collider (LHC)	2008	$^{208}_{82}$Pb	4.06×10^6 1.34×10^7	2.76×10^3 5.02×10^3
Joint Institute for Nuclear Research (JINR)	Nuclotron-based Ion Collider fAcility (NICA)	2019	$^{208}_{82}$Pb	6.65-62.62	4-11
GSI Helmholtz Centre for Heavy Ion Research	Facility for Antiproton and Ion Research (FAIR)	2025	$^{208}_{82}$Pb	6.65-41.30	4-9

Table 1.2 – Summary of the different heavy-ion collision experiments that will be studied in this thesis, with the starting year of the heavy-ion collisions (and in parenthesis of the facility), and with the energy range expressed in the laboratory frame and in the center-of-mass frame.

[1] From the French: Conseil Européen pour la Recherche Nucléaire

1.4 Summary

In this chapter, we gave a brief summary about the history of the Standard Model of Particle Physics, including the major discoveries which led to the quark-model or the theory of strong interactions known as the Quantum ChromoDynamics. This theory was introduced with its Lagrangian and the properties associated with the latter such as gauge invariance and global symmetries which lead to the conservation of conserved currents. By example we have seen that the chiral symmetry breaking has particularly noticeable implications in the hadronic spectrum. The only way to exactly solve QCD is by employing lattice QCD simulations which obtain very successful results for the properties of QCD at vanishing chemical potential. However, regions with a larger chemical potential are at this day not accessible with the current lattice QCD techniques. Properties of strongly interacting matter can however be tested in the laboratory by means of heavy-ion collisions. A new state of matter was discovered and characterized, the Quark-Gluon Plasma (QGP), which was also predicted by the theory of QCD. We listed the probes of the QGP as produced in heavy-ion collisions and also the remaining challenges in our understanding of QCD. Among these is the exploration of the QCD phase diagram as a function of the temperature T and the baryon chemical potential μ_B which is currently or will be performed in facilities such as the RHIC, NICA or FAIR. In Chapter 7 of this dissertation we will precisely investigate which regions of the $T-\mu_B$ phase diagram are probed in heavy-ion collisions, but before we will explain how heavy-ion collisions can be described by using nonequilibrium quantum field theory.

Chapter 2

Nonequilibrium Quantum Field Theory

* * *

"When the system is fairly dense, the particles never get away from the other particles in the system. Therefore, we cannot ever really think of the particles as being "in between collisions"."

Leo P. Kadanoff, Gordon Baym [118].

2.1 Representations and Keldysh Contour

In order to study a system consisting of relativistic quantum particles, one employs the framework of quantum field theory, a combination of quantum mechanics, special relativity and classical field theory. This theory was initially developed in the 1920's in order to find a quantized description of the electromagnetic field. In that context, creation and annihilation of particles is essential as well as the

The notations and structure of this section is inspired from Ref. [119, 120] to be consistent with the concepts and definitions of Chapter 3.

description of antiparticles, or multi-particle interactions.

In the context of nonequilibrium dynamics, one generally deals with an initially equilibrated state which suffers some time-dependent external perturbation. In the following, we will therefore consider time-dependent Hamiltonians and operators defined in second quantization. Unlike the Schrödinger description where the time dependence of the system is carried by the quantum state, we will use the Heisenberg picture where the field operators themselves carry the space-time dependence. The time-evolution of a many-body quantum system is determined by the Schrödinger equation which describes the evolution of the many-body wave function $|\Psi(t)\rangle$ [121]:

$$i\partial_t |\Psi(t)\rangle = \hat{H}(t) |\Psi(t)\rangle . \tag{2.1}$$

This equation can be solved by introducing a time-evolution operator defined as $|\Psi(t)\rangle = \hat{\mathcal{S}}(t,t_0)|\Psi(t_0)\rangle$ also known as the $\mathcal{S}-$**matrix** [73] where t_0 is some initial time. The evolution equation of the $\mathcal{S}-$matrix is:

$$i\partial_t \, \hat{\mathcal{S}}(t,t_0) = \hat{H}(t) \, \hat{\mathcal{S}}(t,t_0) \tag{2.2}$$

and has the formal solution

$$\hat{\mathcal{S}}(t,t_0) = T\left[\exp\left(-i\int_{t_0}^{t} dt' \hat{H}(t')\right)\right] = \sum_{n=0}^{\infty} \frac{T\left[-i\int_{t_0}^{t} dt' \hat{H}(t')\right]^n}{n!}, \tag{2.3}$$

where the symbol T orders the operators chronologically from the right to the left according to their time arguments. Moreover, the time-evolution operator has the following properties:

$$\hat{\mathcal{S}}^{-1}(t,t_0) = \hat{\mathcal{S}}^{\dagger}(t,t_0) = \hat{\mathcal{S}}(t_0,t). \tag{2.4}$$

The expectation value of an Hermitian operator $\hat{\mathcal{O}}(t)$ corresponding to the quantum state in Eq. (2.1) can be expressed as a function of the time-evolution operator as:

$$\langle\Psi(t)|\hat{\mathcal{O}}|\Psi(t)\rangle = \langle\Psi(t_0)|\hat{\mathcal{O}}_H(t)|\Psi(t_0)\rangle \tag{2.5}$$

where the left-hand side corresponds to the Schrödinger picture and the right-hand side defines the operator in the **Heisenberg representation**:

$$\hat{\mathcal{O}}_H(t) = \hat{\mathcal{S}}^\dagger(t,t_0)\ \hat{\mathcal{O}}\ \hat{\mathcal{S}}(t,t_0) \tag{2.6}$$

which obeys the Heisenberg equations of motion:

$$i\partial_t\ \hat{\mathcal{O}}_H(t) = \left[\hat{\mathcal{O}}_H(t), \hat{H}(t)\right]. \tag{2.7}$$

One can go further by separating the Hamiltonian $\hat{H}(t) = \hat{H}_0(t) + \hat{V}(t)$ in a noninteracting and interacting part, denoted as $\hat{H}_0(t)$ and $\hat{V}(t)$, respectively. The **interaction picture** for an Hermitian operator $\hat{\mathcal{O}}$, which will be evolved in time by only taking into account the noninteracting part of the Hamiltonian $\hat{H}_0(t)$, is defined as:

$$\hat{\mathcal{O}}_I(t) = \hat{\mathcal{S}}_0^\dagger(t,t_0)\ \hat{\mathcal{O}}\ \hat{\mathcal{S}}_0(t,t_0), \tag{2.8}$$

where the time-evolution operator $\hat{\mathcal{S}}_0(t,t_0)$ is also given by Eq. (2.3) but only contains the noninteracting part of the Hamiltonian $\hat{H}_0(t)$. One can express again Eq. (2.6) as a function of the newly introduced operator in the interaction picture as:

$$\hat{\mathcal{O}}_H(t) = \hat{U}^\dagger(t,t_0)\ \hat{\mathcal{O}}_I(t)\ \hat{U}(t,t_0), \tag{2.9}$$

where $\hat{U}(t,t_0)$ relates the full Heisenberg picture operators to the "free" one defined in the interaction picture, and obeys the evolution equation:

$$i\partial_t\ \hat{\mathcal{U}}(t,t_0) = \hat{V}_I(t)\ \hat{\mathcal{U}}(t,t_0) \tag{2.10}$$

which can be solved, similarly as Eq. (2.2), in two different ways:

$$\hat{\mathcal{U}}(t,t_0) = \hat{\mathbb{1}} - i\int_{t_0}^{t} dt'\ \hat{V}_I(t')\ \hat{\mathcal{U}}(t',t_0), \tag{2.11}$$

$$\hat{\mathcal{U}}(t,t_0) = T\left[\exp\left(-i\int_{t_0}^{t} dt'\ \hat{V}_I(t')\right)\right] = \sum_{n=0}^{\infty} \frac{T\left[-i\int_{t_0}^{t} dt'\ \hat{V}_I(t')\right]^n}{n!}, \tag{2.12}$$

where $\hat{V}_I(t)$ denotes the interaction representation of $\hat{V}(t)$. The two latter equations are also denoted as **Dyson series** [122] (as for Eq. (2.3)), and relate the time-dependent perturbation theory to Feynman's method, where each order of this series corresponds to a set of Feynman diagrams.

Using the time-evolution operator, one can deduce the evolution of any operator $\hat{O}$. Suppose we have an initial state (pure or mixed) given by a density matrix $\hat{\rho}$, one can show that the **expectation value** of this operator is given by:

$$\left\langle \hat{\mathcal{O}}_H(t) \right\rangle = \mathrm{Tr}\left\{ \hat{\rho}\ \hat{\mathcal{O}}_H(t) \right\} = \mathrm{Tr}\left\{ \hat{\rho}\ \hat{S}^\dagger(t,t_0)\ \hat{\mathcal{O}}\ \hat{S}(t,t_0) \right\} \tag{2.13}$$

$$= \mathrm{Tr}\left\{ \hat{\rho}\ \hat{U}^\dagger(t,t_0)\ \hat{\mathcal{O}}_I\ \hat{U}(t,t_0) \right\}. \tag{2.14}$$

We can simplify further this equation for the expectation value by expressing the conjugate transpose of $\hat{\mathcal{S}}$ (and similarly for $\hat{\mathcal{U}}$) as:

$$\hat{\mathcal{S}}^\dagger(t,t_0) = T^a\left[\exp\left(-i \int_t^{t_0} dt' \hat{H}(t') \right) \right], \tag{2.15}$$

where we used the anticausal time-ordering operator T^a. Eq. (2.13-2.14) can then be expressed in the compact form

$$\begin{aligned} \left\langle \hat{\mathcal{O}}_H(t) \right\rangle &= \left\langle \hat{\mathcal{S}}_C\ \hat{\mathcal{O}} \right\rangle = \mathrm{Tr}\left\{ \hat{\rho}\ \hat{\mathcal{S}}_C\ \hat{\mathcal{O}} \right\} \\ &= \left\langle \hat{\mathcal{U}}_C\ \hat{\mathcal{O}}_I(t) \right\rangle = \mathrm{Tr}\left\{ \hat{\rho}\ \hat{\mathcal{U}}_C\ \hat{\mathcal{O}}_I(t) \right\} \end{aligned}, \tag{2.16}$$

where T_C orders the operators according to the so-called **Keldysh contour** (see also Fig. 2.1) and where $\hat{\mathcal{S}}_C$ and $\hat{\mathcal{U}}_C$ are the time-evolution operators defined on the contour as:

$$\hat{\mathcal{S}}_C = T_C\left[\exp\left(-i \int_C dt' \hat{H}(t') \right) \right], \tag{2.17}$$

$$\hat{\mathcal{U}}_C = T_C\left[\exp\left(-i \int_C dt' \hat{V}_I(t') \right) \right]. \tag{2.18}$$

Note

When dealing with an initial density matrix obeying a canonical distribution as $\hat{\rho} = 1/Z \exp\left(-\beta \hat{H}\right)$, with Z being the canonical partition function $Z = \mathrm{Tr}\left(\exp\left(-\beta \hat{H}\right)\right)$ and $\beta = 1/T$ being the inverse temperature, the Keldysh contour in Eq. (2.16) can be extended to an imaginary time $(t_0 - i\beta)$. This extension permits to mathematically treat the statistical average of the initial state as the time evolution of the operator.

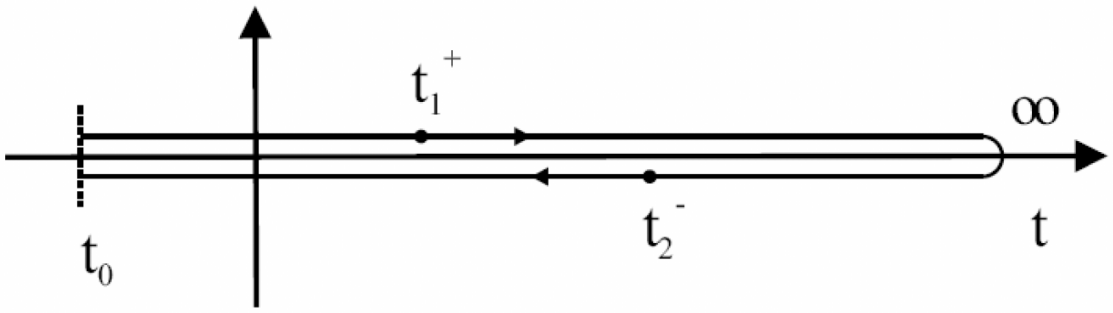

Figure 2.1 – The closed time contour in the Keldysh formalism. The figure is taken from Ref. [120].

2.2 Green's functions on the contour

In this section we will focus on the derivation of 2-point correlation functions and Green's functions which contain both statistical and dynamical information about the many-body system (see Ref. [118] concerning the case of quantum mechanics). n-point correlation functions are defined as the expectation value of field operator products and can be computed in the nonequilibrium case using the ingredients of the previous section like the Keldysh formalism. In the context of a scalar field theory, the **contour Green's function** reads:

$$iG(x,y) = \left\langle T_C\left(\hat{\phi}(x)\hat{\phi}^\dagger(y)\right)\right\rangle = \left\langle \hat{\mathcal{U}}_C\left(\hat{\phi}_I(x)\hat{\phi}_I^\dagger(y)\right)\right\rangle \tag{2.19}$$

where $\hat{\phi}$ denotes the scalar field operator in the Heisenberg representation for bosons, and $x = (x^0, \mathbf{x})$ and $y = (y^0, \mathbf{x})$ are the space-time coordinates. An important characteristic of this Green's function is that it can systematically be expanded perturbatively in terms of Feynman diagrams due to the operator $\hat{\mathcal{U}}_C$ containing the interactions. As a result of the Wick decomposition [123], only entirely **connected Feynman diagrams** actually contribute to the expectation value in Eq. (2.19), whereas disconnected vacuum diagrams do not.

Equation (2.19) can be decomposed into four different Green's functions: the causal (time-ordered), the anticausal, the lesser ($<$) and the greater ($>$) which read [124–126]

$$iG^c\ (x,y) = iG^{++}(x,y) = \left\langle T^c\left(\hat{\phi}(x)\hat{\phi}^\dagger(y)\right)\right\rangle \tag{2.20}$$

$$iG^<(x,y) = iG^{+-}(x,y) = \left\langle \hat{\phi}^\dagger(y)\hat{\phi}(x)\right\rangle \tag{2.21}$$

$$iG^>(x,y) = iG^{-+}(x,y) = \left\langle \hat{\phi}(x)\hat{\phi}^\dagger(y)\right\rangle \tag{2.22}$$

$$iG^a\ (x,y) = iG^{--}(x,y) = \left\langle T^a\left(\hat{\phi}(x)\hat{\phi}^\dagger(y)\right)\right\rangle, \tag{2.23}$$

where T^c and T^a are, respectively, the causal and anticausal time-ordering operators used in the previous section. The $\pm$ signs in Eq. (2.20-2.23) indicate whether the time argument of x and y are situated on the upper or lower branch of the Keldysh contour in Fig. 2.1. The set of Green's function in Eq. (2.19) can also be written as a 2×2 matrix:

$$G(x,y) = \begin{array}{c} \\ + \\ - \end{array} \begin{array}{c} \begin{array}{cc} + & - \end{array} \\ \begin{pmatrix} G^c\ (x,y) & G^<(x,y) \\ G^>(x,y) & G^a\ (x,y) \end{pmatrix} \end{array} . \tag{2.24}$$

One can notice that the Green's functions in Eq. (2.20-2.23) are not independent and verify the following relations:

$$G^c\ (x,y) = \theta(x^0-y^0)\ G^>(x,y) + \theta(y^0-x^0)\ G^<(x,y) \tag{2.25}$$

$$G^a\ (x,y) = \theta(y^0-x^0)\ G^>(x,y) + \theta(x^0-y^0)\ G^<(x,y), \tag{2.26}$$

where θ is the Heaviside step function. $G^<(x,y)$ and $G^>(x,y)$ are the so-called **Wightman functions** and contain information about observables or kinetic properties like e.g. the particle density $\langle n(x)\rangle = -iG^<(x,x)$.

Note

Considering an equilibrium state described by the canonical density operator:

$$\hat{\rho} = \frac{e^{-\beta \hat{H}}}{Z} = \sum_n e^{-\beta E_n} |n\rangle \langle n|, \tag{2.27}$$

we can evaluate the traces in Eq. (2.21-2.22) as:

$$\begin{aligned} G^{>}(t) &= \mathrm{Tr}\left\{\hat{\rho}\ \phi(t)\ \phi^{\dagger}(0)\right\} = \frac{1}{Z}\mathrm{Tr}\left\{e^{-\hat{H}(\beta - it)}\phi\ e^{-it\hat{H}}\phi^{\dagger}\right\} \\ &= \frac{1}{Z}\sum_{m,n} e^{-\beta E_n} |\langle n|\phi|m\rangle|^2\ e^{it(E_n - E_m)} \end{aligned} \tag{2.28}$$

$$\begin{aligned} G^{<}(t) &= \mathrm{Tr}\left\{\hat{\rho}\ \phi^{\dagger}(0)\ \phi(t)\right\} = \frac{1}{Z}\mathrm{Tr}\left\{e^{-\hat{H}\beta}\phi^{\dagger}\ e^{it\hat{H}}\phi\ e^{-it\hat{H}}\right\} \\ &= \frac{1}{Z}\sum_{m,n} e^{-\beta E_m} |\langle n|\phi|m\rangle|^2\ e^{it(E_n - E_m)}. \end{aligned} \tag{2.29}$$

One can see that these series converge as long as $0 \leq \mathrm{Im}\, t \leq \beta$, and in that case $G^{<}$ and $G^{>}$ are connected by the **Kubo-Martin-Schwinger** (KMS) condition [127, 128]:

$$G^{<}(t) = G^{>}(t - i\beta) \tag{2.30}$$

One can also define retarded and advanced propagators, which can be useful to calculate a physical response, as:

$$\begin{aligned} G_R(x,y) &= \quad \theta(x^0 - y^0)\,(G^{>}(x,y) - G^{<}(x,y)) &&= \quad \theta(x^0 - y^0)\ A(x,y) \\ G_A(x,y) &= -\theta(y^0 - x^0)\,(G^{>}(x,y) - G^{<}(x,y)) &&= -\theta(y^0 - x^0)\ A(x,y), \end{aligned} \tag{2.31}$$

where A is denoted as the **spectral function** and is more conveniently used in momentum space since it contains information about spectral properties of states.

2.3 Kadanoff-Baym equations

This section aims to describe the time evolution of a relativistic many-body system and therefore to find the equation of motion for the contour Green's function. In quantum field theory, a Lagrangian description is preferentially used because of its Lorentz invariance, contrary to the Hamiltonian one. In the case of a **scalar field theory** for $\hat{\phi} = \hat{\phi}^\dagger$, the Lagrangian density reads:

$$\mathcal{L} = \frac{1}{2}\partial^\mu \hat{\phi}\partial_\mu \hat{\phi} - \frac{m^2}{2}\hat{\phi}^2 - \mathcal{V}(\hat{\phi}) \tag{2.32}$$

where $\mathcal{V}$ is called a potential density or the interaction Lagrangian. The field operators obey the equal-time commutation relations:

$$\left[\hat{\phi}(t,\mathbf{x}),\hat{\phi}(t,\mathbf{y})\right] = 0, \qquad \left[\partial_t\hat{\phi}(t,\mathbf{x}),\partial_t\hat{\phi}(t,\mathbf{y})\right] = 0, \qquad \left[\hat{\phi}(t,\mathbf{x}),\partial_t\hat{\phi}(t,\mathbf{y})\right] = i\delta^{(3)}(\mathbf{x}-\mathbf{y}). \tag{2.33}$$

We first derive the field equation of motions by using the Euler-Lagrange equations. We obtain a **Klein-Gordon** [129, 130] type of equation [131, 132]:

$$\boxed{\left(-\Box_x - m^2\right)\hat{\phi}(x) = \frac{\partial \mathcal{V}}{\partial \hat{\phi}}(x) = \hat{j}(x)} \tag{2.34}$$

where $\Box_x = \partial_x^\mu \partial_\mu^x = \partial_{x^0}^2 - \nabla_{\mathbf{x}}^2$ is the d'Alembert operator, and $\hat{j}(x)$ is the source term describing the local interaction between the fields and $\hat{\phi}(x)$.

Note

One can also verify the above Klein-Gordon equation by using the Heisenberg evolution equation for the field operator in Eq. (2.7). In this case one needs to derive first the Hamiltonian corresponding to the Lagrangian in Eq. (2.32) by making use of Noether's theorem [132, 133].

With these prerequisites, we can derive the evolution equation for the contour Green's function by applying two time derivatives to Eqs. (2.19) or equivalently to Eq. (2.20)-(2.23). By using the commutation relations for the field operators and their evolution equations, one arrives to the **Dyson equations** [124, 125]:

$$(-\partial_x^\mu \partial_\mu^x - m^2)G(x,y) = \delta_C^{(4)}(x,y) + \left\langle T_C\left(\hat{j}(x)\hat{\phi}(y)\right)\right\rangle$$

$$(-\partial_x^\mu \partial_\mu^x - m^2)G(x,y) = \delta_C^{(4)}(x,y) + \int_C d^4z\ \Sigma(x,z)\ G(z,y), \tag{2.35}$$

where $\delta_C^{(4)}(x-y)$ is the Delta function defined on the contour, which has the following properties [124]:

$$\delta_C^{(4)}(x,y) = \delta^{(3)}(\mathbf{x}-\mathbf{y}) \begin{cases} \delta^{++}(x^0-y^0) = \delta(x^0-y^0) \\ \delta^{+-}(x^0-y^0) = 0 \\ \delta^{-+}(x^0-y^0) = 0 \\ \delta^{--}(x^0-y^0) = -\delta(x^0-y^0). \end{cases} \tag{2.36}$$

The quantity Σ in Eq. (2.35) is called the **proper** (or irreducible) **self-energy** and encodes the changes in the particle properties due to its interactions. Since the expectation value should only contain connected diagrams, this constrains the proper self-energy to be one-particle irreducible (1PI), which means that it cannot be broken into two unconnected diagrams by opening a particle line.

Note

In practice, the complexity of solving self-consistent equations for the Green's functions (as well as for the self-energies) is reduced by applying certain truncation schemes. An important restriction is that they should be conserving, meaning that charge and energy-momentum conservation laws as well as thermodynamic consistency should be satisfied. The **Φ-derivable scheme** [125, 134, 135] is used in order to obtain self-consistent and conserving equations for the self-energy as:

$$\Sigma(x,y) = 2i\frac{\delta\Phi[G]}{\delta G(y,x)}, \tag{2.37}$$

where the functional Φ is the sum of all closed two-particle irreducible (2PI) diagrams built up by full propagators G. The advantage is that any truncation applied to the level of Φ, a so-called Φ-derivable approximation, will be conserving and thermodynamically consistent.

We can separate the self-energy defined on the contour in the same way as for the Green's functions in Eqs. (2.25)-(2.26). By introducing a lesser $\Sigma^<$ and greater $\Sigma^>$ self-energy and adding a local contribution, we obtain for the causal Σ^c and acausal Σ^a self-energies:

$$\Sigma^c\ (x,y) = \Sigma^\delta\ \delta_C^{(4)}(x-y) + \theta(x^0-y^0)\ \Sigma^>(x,y) + \theta(y^0-x^0)\ \Sigma^<(x,y) \tag{2.38}$$

$$\Sigma^a\ (x,y) = \Sigma^\delta\ \delta_C^{(4)}(x-y) + \theta(y^0-x^0)\ \Sigma^>(x,y) + \theta(x^0-y^0)\ \Sigma^<(x,y). \tag{2.39}$$

Note

By multiplying Eq. (2.35) by the Green's function $G_0(x,y)$ of the free fields, which satisfies $(-\partial_x^\mu \partial_\mu^x - m^2)G_0(x,y) = \delta_C(x-y)$, one obtains the Dyson equation in matrix representation [136]:

$$\begin{pmatrix} G^c(x,y) & G^<(x,y) \\ G^>(x,y) & G^a(x,y) \end{pmatrix} = \begin{pmatrix} G_0^c(x,y) & G_0^<(x,y) \\ G_0^>(x,y) & G_0^a(x,y) \end{pmatrix} + \tag{2.40}$$

$$\begin{pmatrix} G_0^c(x,x') & G_0^<(x,x') \\ G_0^>(x,x') & G_0^a(x,x') \end{pmatrix} \odot \begin{pmatrix} \Sigma^c(x',y') & -\Sigma^<(x',y') \\ -\Sigma^>(x',y') & \Sigma^a(x',y') \end{pmatrix} \odot \begin{pmatrix} G^c(y',y) & G^<(y',y) \\ G^>(y',y) & G^a(y',y) \end{pmatrix},$$

where $\odot$ stands for the intermediate integration over space-time on the contour, or in the usual compact form:

$$G = G_0 + G_0 \Sigma G. \tag{2.41}$$

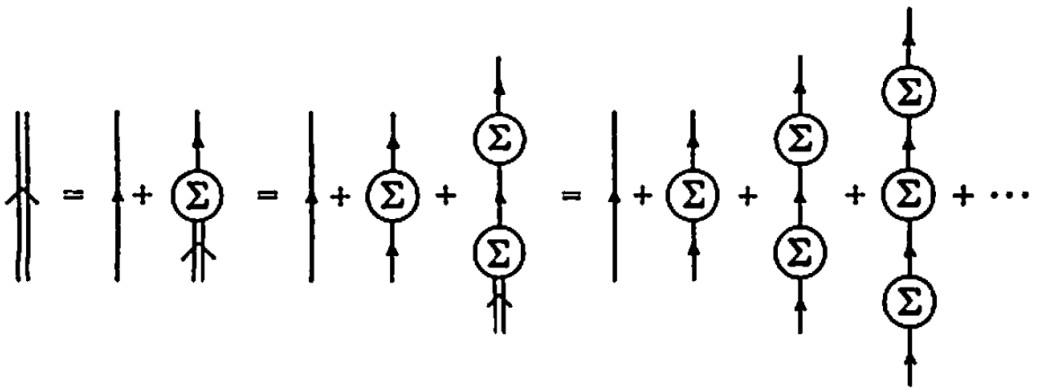

Figure 2.2 – Illustration of the Dyson equation (2.41), where the full propagator is expressed iteratively with the bare and full propagator, and the proper self-energy. The figure is taken from Ref. [137].

If we now decompose the Dyson equation (2.35) for each branch of the Keldysh contour by making use of the Langreth theorem [138–140], we obtain equations for the different Green's functions known as the **Kadanoff-Baym equations**:

$$(-\partial_x^\mu \partial_\mu^x - m^2 - \Sigma^\delta(x))G^{\lessgtr}(x,y) = \int_{t_0}^{x^0} dz^0 \int d^3z \ \left(\Sigma^>(x,z) - \Sigma^<(x,z)\right) \ G^{\lessgtr}(z,y) - \int_{t_0}^{y^0} dz^0 \int d^3z \ \Sigma^{\lessgtr}(x,z) \ \left(G^>(z,y) - G^<(z,y)\right), \tag{2.42}$$

$$(-\partial_y^\mu \partial_\mu^x - m^2 - \Sigma^\delta(y))G^{\lessgtr}(x,y) = \int_{t_0}^{x^0} dz^0 \int d^3z \ \left(G^>(x,z) - G^<(x,z)\right) \ \Sigma^{\lessgtr}(z,y) - \int_{t_0}^{y^0} dz^0 \int d^3z \ G^{\lessgtr}(x,z) \ \left(\Sigma^>(z,y) - \Sigma^<(z,y)\right). \tag{2.43}$$

These equations can be simplified by making use of the retarded/advanced Green's functions defined in Eq. (2.31) as well as retarded/advanced self-energies as:

$$\begin{aligned}(-\partial_x^\mu \partial_\mu^x - m^2 - \Sigma^\delta(x))G^{\lessgtr}(x,y) &= \int_{t_0}^{\infty} dz^0 \int d^3z \ \left(\Sigma^R(x,z) \ G^{\lessgtr}(z,y) + \Sigma^{\lessgtr}(x,z) \ G^A(z,y)\right) \\ (-\partial_y^\mu \partial_\mu^x - m^2 - \Sigma^\delta(y))G^{\lessgtr}(x,y) &= \int_{t_0}^{\infty} dz^0 \int d^3z \ \left(G^R(x,z) \ \Sigma^{\lessgtr}(z,y) + G^{\lessgtr}(x,z) \ \Sigma^A(z,y)\right).\end{aligned} \tag{2.44}$$

Similarly from the Dyson equation (2.35), we can obtain equations of motion for the retarded (advanced) Green's functions:

$$\begin{aligned}(-\partial_x^\mu \partial_\mu^x - m^2 - \Sigma^\delta(x))G^{R/A}(x,y) &= \delta^{(4)}(x,y) + \int d^4z \ \Sigma^{R/A}(x,z) \ G^{R/A}(z,y) \\ (-\partial_y^\mu \partial_\mu^y - m^2 - \Sigma^\delta(y))G^{R/A}(x,y) &= \delta^{(4)}(x,y) + \int d^4z \ G^{R/A}(x,z) \ \Sigma^{R/A}(z,y),\end{aligned} \tag{2.45}$$

which depend solely on retarded (advanced) quantities and where the integration extends here to the full space and time.

2.4 Spectral information in Wigner space

In the context of transport theory, phase-space coordinates are used to describe the space-time evolution of the system. In order to use the ingredients derived in the previous section, we apply the **Wigner transform** [141] to the Kadanoff-Baym equations (2.44-2.45). For that purpose, we introduce the relative and central coordinates

$$s^\mu = x^\mu - y^\mu, \qquad X^\mu = \frac{x^\mu + y^\mu}{2}, \tag{2.46}$$

which define the Wigner transformation as the Fourier transform of 2-point functions with respect to the relative coordinates as:

$$\bar{F}(P,X) = \int_{-\infty}^{+\infty} d^4s \; e^{is_\mu P^\mu} \; F(x = X + \frac{s}{2}, y = X - \frac{s}{2}) \,. \tag{2.47}$$

In order to apply the Wigner transform to the convolutions in the right hand-side of Eq. (2.44), we make use of the following identity:

$$\begin{aligned} &\int_{-\infty}^{\infty} d^4s \; e^{is_\mu P^\mu} \int_{-\infty}^{\infty} d^4z \; F(x,z) \; G(z,y) \\ &\qquad = e^{\frac{i}{2}\left(\partial_\mu^P \cdot \partial_{X'}^\mu - \partial_\mu^X \cdot \partial_{P'}^\mu\right)} \; \bar{F}(P,X) \; \bar{G}(P',X')\Big|_{X'=X,P'=P} \\ &\qquad = \bar{F}(P,X) \; \bar{G}(P,X) + \frac{i}{2}\Big\{\bar{F}(P,X), \; \bar{G}(P,X)\Big\} + \mathcal{O}\Big(\partial_X^2\Big), \end{aligned} \tag{2.48}$$

where we used the relativistic **Poisson bracket** defined as:

$$\Big\{\bar{F}(P,X), \bar{G}(P,X)\Big\} = \partial_\mu^P \bar{F}(P,X) \; \partial_X^\mu \bar{G}(P,X) - \partial_X^\mu \bar{F}(P,X) \; \partial_\mu^P \bar{G}(P,X). \tag{2.49}$$

The last line of Eq. (2.48) corresponds to a first order gradient approximation which is usually used in transport theory. In that context it is assumed that the considered medium suffers only slowly-varying perturbations in space and time, justifying the use of a gradient expansion. To perform the gradient expansion, we need to express the derivative of Eq. (2.44-2.45) in terms of the relative and central coordinates X and s as:

$$\partial_x = \partial_s + \frac{1}{2}\partial_X \qquad \partial_y = -\partial_s + \frac{1}{2}\partial_X \qquad \partial_x^2 - \partial_y^2 = 2\partial_s \cdot \partial_X \tag{2.50}$$

and also the Wigner transform of the Klein-Gordon operator:

$$(-\partial_x^\mu \partial_\mu^x - m^2)F(x,y) \to \left(P^2 + iP^\mu \partial_\mu^X - \frac{1}{4}\partial_X^2 - m^2\right)\bar{F}(P,X), \tag{2.51}$$

$$(-\partial_y^\mu \partial_\mu^y - m^2)F(x,y) \to \left(P^2 - iP^\mu \partial_\mu^X - \frac{1}{4}\partial_X^2 - m^2\right)\bar{F}(P,X). \tag{2.52}$$

We start by applying the Wigner transform to Eq. (2.45) for the retarded and advanced Green's functions, only keeping the derivatives up to first order. The sum of the two equations (2.45) gives:

$$\left[P_0^2 - \mathbf{P}^2 - m^2 - \bar{\Sigma}^\delta(X) - \bar{\Sigma}^R(P,X)\right]\ \bar{G}^R(P,X) = 1. \tag{2.53}$$

To proceed further, we decompose the Green's functions and the self-energies in terms of real quantities:

$$\boxed{\bar{G}^{R/A} = \mathrm{Re}\,\bar{G}^R \pm i\ \mathrm{Im}\,\bar{G}^R = \mathrm{Re}\,\bar{G}^R \mp i\bar{A}/2} \quad \text{with} \quad \bar{A} = \mp\ 2\ \mathrm{Im}\,\bar{G}^{R/A}, \tag{2.54}$$

$$\boxed{\bar{\Sigma}^{R/A} = \mathrm{Re}\,\bar{\Sigma}^R \pm i\ \mathrm{Im}\,\bar{\Sigma}^R = \mathrm{Re}\,\bar{\Sigma}^R \mp i\bar{\Gamma}/2} \quad \text{with} \quad \bar{\Gamma} = \mp\ 2\ \mathrm{Im}\,\bar{\Sigma}^{R/A}. \tag{2.55}$$

The real parts for these retarded and advanced quantities are the same in Wigner space, while the imaginary parts have opposite signs and are proportional to the **spectral function** $\bar{A}$ and the **width** $\bar{\Gamma}$. The latter can themselves be expressed in terms of the lesser and greater Green's functions as:

$$\boxed{\bar{A} = i\bar{G}^> - i\bar{G}^<}, \qquad \boxed{\bar{\Gamma} = i\bar{\Sigma}^> - i\bar{\Sigma}^<}. \tag{2.56}$$

Note

For an equilibrium state, the Fourier transform of the KMS condition (2.30) leads to:

$$\bar{G}^{>}_{\rm eq}(P) = \int d^4s\; e^{is_\mu P^\mu} G^{>}_{\rm eq}(s) = e^{\beta p_0} \bar{G}^{<}_{\rm eq}(P), \tag{2.57}$$

with $\bar{G}^{\lessgtr}$ being purely imaginary since the real (imaginary) part of $G^{\lessgtr}$ is anti-symmetric (symmetric) with respect to the coordinate s [120]. This boundary condition can be expressed in terms of the distribution function $\bar{N}(p_0)$ and the spectral function $\bar{A}(P)$ as:

$$i\bar{G}^{>}_{\rm eq}(P) = \bar{A}(P)\Big(1+\bar{N}(P_0)\Big)\ , \qquad i\bar{G}^{<}_{\rm eq}(P) = \bar{A}(P)\bar{N}(P_0). \tag{2.58}$$

An interpretation of the above formulae is that for positive (negative) energies p_0, $\bar{G}^{<}$ ($\bar{G}^{>}$) is proportionnal to the density of states, while $\bar{G}^{>}$ ($\bar{G}^{<}$) evaluates the density of states available for the addition of a particle with 4-momentum P to the medium [118, 142]. One can show that the lesser and greater self-energies obey the KMS condition $\Sigma^{<}(t) = \Sigma^{>}(t - i\beta)$ (for $0 \leq \mathrm{Im}\, t \leq \beta$), which leads by Fourier tranform to the following equilibrium expressions in momentum space:

$$i\bar{\Sigma}^{>}_{\rm eq}(P) = \bar{\Gamma}(P)\Big(1+\bar{N}(P_0)\Big)\ , \qquad i\bar{\Sigma}^{<}_{\rm eq}(P) = \bar{\Gamma}(P)\bar{N}(P_0). \tag{2.59}$$

By separating the real and imaginary parts of Eq. (2.53) using Eq. (2.54-2.55), we obtain two equations for the real part of the retarded Green's function $\mathrm{Re}\bar{G}^R$ and the spectral function $\bar{A}$ in terms of the real part of the retarded self-energy $\mathrm{Re}\bar{\Sigma}^R$ and the width $\bar{\Gamma}$:

$$\Big[P_0^2 - \mathbf{P}^2 - m^2 - \bar{\Sigma}^\delta - \mathrm{Re}\bar{\Sigma}^R\Big]\,\mathrm{Re}\bar{G}^R \;=\; 1 - \frac{1}{4}\,\bar{\Gamma}\;\bar{A}, \tag{2.60}$$

$$\Big[P_0^2 - \mathbf{P}^2 - m^2 - \bar{\Sigma}^\delta - \mathrm{Re}\bar{\Sigma}^R\Big]\,\bar{A} \;=\; \bar{\Gamma}\;\mathrm{Re}\bar{G}^R, \tag{2.61}$$

which implies a direct relation between the real and imaginary part of the retarded/advanced Green's function, which reads (for $\bar{\Gamma} \neq 0$):

$$\mathrm{Re}\bar{G}^R = \frac{P_0^2 - \mathbf{P}^2 - m^2 - \bar{\Sigma}^\delta - \mathrm{Re}\bar{\Sigma}^R}{\bar{\Gamma}}\bar{A}. \tag{2.62}$$

These relations also provide explicit expressions for $\mathrm{Re}\bar{G}^R$ and $\bar{A}$ in terms of the real and imaginary parts of the self-energy:

$$\bar{A} = \frac{\bar{\Gamma}}{\left[P_0^2 - \mathbf{P}^2 - m^2 - \bar{\Sigma}^\delta - \mathrm{Re}\,\bar{\Sigma}^R\right]^2 + \bar{\Gamma}^2/4} = \frac{\bar{\Gamma}}{\bar{M}^2 + \bar{\Gamma}^2/4} \equiv \frac{-2\,\mathrm{Im}\,\bar{\Sigma}^R}{\bar{M}^2 + (\mathrm{Im}\,\bar{\Sigma}^R)^2}\,, \tag{2.63}$$

$$\mathrm{Re}\,\bar{G}^R = \frac{P_0^2 - \mathbf{P}^2 - m^2 - \bar{\Sigma}^\delta - \mathrm{Re}\,\bar{\Sigma}^R}{\left[P_0^2 - \mathbf{P}^2 - m^2 - \bar{\Sigma}^\delta - \mathrm{Re}\,\bar{\Sigma}^R\right]^2 + \bar{\Gamma}^2/4} = \frac{\bar{M}}{\bar{M}^2 + \bar{\Gamma}^2/4}\,, \tag{2.64}$$

where the mass-function $\bar{M}$ in Wigner-space has been introduced. The spectral function in Eq. (2.63) shows a typical Breit-Wigner shape with energy- and momentum-dependent self-energy. Even if these relations contain no derivative, they are valid up to first order in the gradients. Note also that the off-equilibrium nature of the above equations only enters in their dependence on the space-time coordinate X.

If one applies the same procedure, but by taking the difference of the Eq. (2.45), we obtain the following evolution equation for the spectral function and the real part of the retarded Green's function:

$$p^\mu \partial_\mu^X \ \bar{A} = \frac{1}{2}\left\{\bar{\Sigma}^\delta + \mathrm{Re}\,\bar{\Sigma}^R,\ \bar{A}\right\} + \frac{1}{2}\left\{\bar{\Gamma},\ \mathrm{Re}\,\bar{G}^R\right\}, \tag{2.65}$$

$$p^\mu \partial_\mu^X \ \mathrm{Re}\,\bar{G}^R = \frac{1}{2}\left\{\bar{\Sigma}^\delta + \mathrm{Re}\,\bar{\Sigma}^R,\ \mathrm{Re}\,\bar{G}^R\right\} - \frac{1}{8}\left\{\bar{\Gamma},\ \bar{A}\right\}. \tag{2.66}$$

2.5 Off-shell Transport equations

In order to derive the transport equations for the lesser and greater Green's functions, which will describe the evolution of the system, we apply the same method (as in the previous subsection) to the Kadanoff-Baym equations (2.44). In the latter, we change the initial time for the integration to $t_0 \to -\infty$ for convenience. With this simplification, the initial Green's functions reduce to the equilibrium ones, implying that initial correlations are not taken into account. After applying these procedures and subtracting the two Eq. (2.44), we obtain the following generalized transport equation [118, 126, 143–148]:

$$2P^\mu\partial_\mu^X\; i\bar{G}^{\lessgtr} - \left\{\bar{\Sigma}^\delta + \mathrm{Re}\,\bar{\Sigma}^R,\; i\bar{G}^{\lessgtr}\right\} - \left\{i\bar{\Sigma}^{\lessgtr},\; \mathrm{Re}\,\bar{G}^R\right\} = i\bar{\Sigma}^< i\bar{G}^> - i\bar{\Sigma}^> i\bar{G}^<, \tag{2.67}$$

where we used Eq. (2.56) and the identity $i\bar{\Sigma}^{\lessgtr}\bar{A} - \bar{\Gamma} i\bar{G}^{\lessgtr} = i\bar{\Sigma}^< i\bar{G}^> - i\bar{\Sigma}^> i\bar{G}^<$. We obtain as well by summing the Eq. (2.44) a generalized mass-shell equation:

$$\underbrace{\left[P_0^2 - \mathbf{P}^2 - m^2 - \bar{\Sigma}^\delta - \mathrm{Re}\,\bar{\Sigma}^R\right]}_{\bar{M}}\; i\bar{G}^{\lessgtr} = i\bar{\Sigma}^{\lessgtr}\,\mathrm{Re}\,\bar{G}^R + \frac{1}{4}\left\{i\bar{\Sigma}^>,\; i\bar{G}^<\right\} - \frac{1}{4}\left\{i\bar{\Sigma}^<,\; i\bar{G}^>\right\}, \tag{2.68}$$

where the mass function $\bar{M}$ has been introduced in Eq. (2.63). The transport equation (2.67) can be seen as a quantum generalization of the Boltzmann equation (cf. Appendix A.2). On the l.h.s of Eq. (2.67) one recognizes a drift term $P^\mu\partial_\mu^x\; i\bar{G}^{\lessgtr}$, as well as a contribution from the real part of the self-energy, known as the Vlasov term. As we will see later, the real part of the self-energy acts as an effective potential whose space-time derivative provides a "force" term. The Poisson bracket $\left\{i\bar{\Sigma}^{\lessgtr},\; \mathrm{Re}\,\bar{G}^R\right\}$ governs the evolution of the off-shell dynamics and actually vanishes in the on-shell Boltzmann limit [118, 126, 145–148]. On the r.h.s one finds the typical collision term, where the loss term $i\bar{\Sigma}^> i\bar{G}^<$ represents the scattering out of the corresponding phase-space cell, whereas the gain term $i\bar{\Sigma}^< i\bar{G}^>$ takes into account the scattering into the actual cell.

Even if the two equations (2.67)-(2.68) have been derived by a first order gradient expansion, they differ from each other since the term $\left\{i\bar{\Sigma}^{\lessgtr},\; \mathrm{Re}\,\bar{G}^R\right\}$ contains second order derivatives [126, 144, 148]. To remedy this discrepancy, we introduce out-of-equilibrium distribution functions in the Green's functions and self-energies of the following form [120]:

$$i\bar{G}^<(P,X) = \bar{N}(P,X)\bar{A}(P,X), \qquad i\bar{G}^>(P,X) = \left[1 + \bar{N}(P,X)\right]\bar{A}(P,X), \tag{2.69}$$

$$i\bar{\Sigma}^<(P,X) = \bar{N}^\Sigma(P,X)\bar{\Gamma}(P,X), \qquad i\bar{\Sigma}^>(P,X) = \left[1 + \bar{N}^\Sigma(P,X)\right]\bar{\Gamma}(P,X). \tag{2.70}$$

The self-energy can be written as:

$$i\bar{\Sigma}^{<} = \bar{\Gamma}\bar{N}^{\Sigma} = \bar{\Gamma}\bar{N} + \bar{K} \tag{2.71}$$

where the correction term:

$$\bar{K} = \bar{\Gamma}(\bar{N}^{\Sigma} - \bar{N}) = (i\bar{\Sigma}^{<} i\bar{G}^{>} - i\bar{\Sigma}^{>} i\bar{G}^{<})\bar{A}^{-1} \tag{2.72}$$

is proportional to the collision term of Eq. (2.67) which is itself of order 1 in the gradients. By replacing the self-energy in the Poisson bracket $\left\{i\bar{\Sigma}^{<},\ \mathrm{Re}\bar{G}^{R}\right\}$, one can deduce that this correction term $\bar{K}$ will result in terms of 2^{nd} order in the gradients which should be discarded for consistency. Therefore, we can simply replace the self-energy in the Poisson brackets as $i\bar{\Sigma}^{<} = i\bar{G}^{<}\bar{\Gamma}/\bar{A}$ to find the generalized transport equation within the Botermans-Malfliet form [120, 144]:

$$\frac{1}{2}\bar{A}\bar{\Gamma}\left[\left\{\bar{M}, iG^{<}\right\} - \frac{1}{\bar{\Gamma}}\left\{\bar{\Gamma}, \bar{M}\cdot iG^{<}\right\}\right] = i\bar{\Sigma}^{<} i\bar{G}^{>} - \bar{\Sigma}^{>} i\bar{G}^{<}. \tag{2.73}$$

Note

The Wigner transformation in Eq. (2.47) actually contains a $\hbar$ factor in the exponential as $\exp(is_{\mu}P^{\mu}/\hbar)$. This means that the gradient expansion in Eq. (2.48) also corresponds to an expansion in powers of $\hbar$. The transport equations are therefore obtained in the so-called **semiclassical approximation** by keeping only the first derivatives in space and time.

2.6 Damping rate and Quasiparticle limit

The collision term I_{coll} on the right-hand side of Eqs. (2.67)-(2.73) can be evaluated assuming small deviations from equilibrium for the Green's functions and the self-energies as:

$$\begin{aligned} I_{\mathrm{coll}}(P,X) &= \left(i\bar{\Sigma}^{<}(P,X) i\bar{G}^{>}(P,X) - i\bar{\Sigma}^{>}(P,X) i\bar{G}^{<}(P,X)\right) \\ &\approx \left(i\bar{\Sigma}^{<}_{\mathrm{eq}} i\delta\bar{G}^{>} - i\bar{\Sigma}^{>}_{\mathrm{eq}} i\delta\bar{G}^{<}\right) + \left(i\delta\bar{\Sigma}^{<} i\bar{G}^{>}_{\mathrm{eq}} - i\delta\bar{\Sigma}^{>} i\bar{G}^{<}_{\mathrm{eq}}\right), \end{aligned} \tag{2.74}$$

where the definitions $\bar{G}^{\lessgtr} = \bar{G}^{\lessgtr}_{\mathrm{eq}} + \delta\bar{G}^{\lessgtr}$ and $\bar{\Sigma}^{\lessgtr} = \bar{\Sigma}^{\lessgtr}_{\mathrm{eq}} + \delta\bar{\Sigma}^{\lessgtr}$ have been used. The

Green's functions and self-energies can be approximated by the equilibrium ones which, using Eq. (2.56), leads to $\delta\bar{G}^< \approx \delta\bar{G}^> \equiv \delta\bar{G}$ and $\delta\bar{\Sigma}^< \approx \delta\bar{\Sigma}^> \equiv \delta\bar{\Sigma}$. The collision term can then be linearized in the following form [149]:

$$I_{\rm coll}(P,X) \approx -\bar{\Gamma}_{\rm eq}(P)\ i\delta\bar{G}(P,X) + \bar{A}_{\rm eq}(P)\ i\delta\bar{\Sigma}(P,X), \tag{2.75}$$

where the width in equilibrium is identified with $\bar{\Gamma}_{\rm eq} = i\bar{\Sigma}^>_{\rm eq} - i\bar{\Sigma}^<_{\rm eq}$ from Eq. (2.56).

In the **quasiparticle limit**, it is assumed that the particles interact weakly enough so that the width $\bar{\Gamma}(P,X)$ of the spectral function (2.63) is found to be small compared to the real part of the self-energy. As a consequence, the spectral function from Eq. (2.63) becomes sharply peaked around the pole energy $E_{\mathbf{P}}$ as:

$$\lim_{\bar{\Gamma}\to 0} \bar{A} = 2\pi\delta\left(P_0^2 - \mathbf{P}^2 - m^2 - \bar{\Sigma}^\delta - {\rm Re}\,\bar{\Sigma}^R(P,X)\right) = 2\pi\delta\left(P_0^2 - E_{\mathbf{P}}^2\right) \equiv \bar{A}_0. \tag{2.76}$$

In the quasiparticle approximation, the collision term can be expressed in terms of the scattering matrix element $|\mathcal{M}|^2$ as [149]:

$$\begin{aligned} I_{\rm coll} = & -\int \frac{d^4P_2}{(2\pi)^4}\int \frac{d^4P_3}{(2\pi)^4}\int \frac{d^4P_4}{(2\pi)^4}\ (2\pi)^4\delta^{(4)}\left(P+P_2-P_3-P_4\right)\ \left|\mathcal{M}_{P+P_2\to P_3+P_4}\right|^2 \\ & \times\Big[\bar{G}^<(P,X)\bar{G}^<(P_2,X)\bar{G}^>(P_3,X)\bar{G}^>(P_4,X) \\ & -\bar{G}^>(P,X)\bar{G}^>(P_2,X)\bar{G}^<(P_3,X)\bar{G}^<(P_4,X)\Big]. \end{aligned} \tag{2.77}$$

By replacing in the previous formula the Green's functions for particles 2, 3 and 4, by their equilibrium expressions (2.58) and neglecting the gain term, one can identify the collisional width $\bar{\Gamma}_{\rm eq}$ as the multiplicative term of $i\delta\bar{G}$ as:

$$\begin{aligned} \bar{\Gamma}_{\rm eq}(\mathbf{P}) = & \int \frac{d^4P_2}{(2\pi)^4}\int \frac{d^4P_3}{(2\pi)^4}\int \frac{d^4P_4}{(2\pi)^4}\ \bar{A}(P_2)\ \bar{A}(P_3)\ \bar{A}(P_4) \\ & \times (2\pi)^4\delta^{(4)}\left(P+P_2-P_3-P_4\right)\ \left|\mathcal{M}_{P+P_2\to P_3+P_4}\right|^2 \\ & \times N(P_2)(1+N(P_3))(1+N(P_4)). \end{aligned} \tag{2.78}$$

To recover the Boltzmann equation, one should also approximate the drift term of the transport equations (2.67-2.73) within the quasiparticle approximation, leading to:

$$\left(2P^\mu - \partial_P^\mu \operatorname{Re}\bar{\Sigma}^R\right)\partial_\mu^X iG^< + \left(\partial_X^\mu \operatorname{Re}\bar{\Sigma}^R\right)\left(\partial_\mu^P iG^<\right) = I_{\text{coll}}, \tag{2.79}$$

where the contribution to the self-energy from $\bar{\Sigma}^\delta$ has been incorporated into $\operatorname{Re}\bar{\Sigma}^R$. By using a similar form for the Green's functions as the equilibrium ones in Eq. (2.58) and by separating into positive and negative energy contributions:

$$\begin{aligned} i\bar{G}^<(P,X) &= \bar{A}_0(P,X)\bar{N}(P,X) \\ &= 2\pi\delta\left(P_0^2 - E_{\mathbf{P}}^2\right)\left[\theta(P_0)\bar{N}(\mathbf{P},X) + \theta(-P_0)(\bar{N}(\mathbf{P},X)+1)\right], \end{aligned} \tag{2.80}$$

one arrives, by making use of the evolution equation for the spectral function (2.65), to the following transport equation for the distribution function $\bar{N}(\mathbf{P},X)$:

$$\begin{aligned} &\left(2E_{\mathbf{p}}\partial_t + 2\mathbf{P}\cdot\nabla_{\mathbf{X}} - \nabla_{\mathbf{X}}\operatorname{Re}\bar{\Sigma}^R(\mathbf{P},X)\cdot\nabla_{\mathbf{P}}\right)\bar{N}(\mathbf{P},X) \\ &\qquad = -\bar{\Gamma}_{\text{eq}}(\mathbf{P})\ \delta\bar{N}(\mathbf{P},X) + i\delta\bar{\Sigma}(\mathbf{P},X), \end{aligned} \tag{2.81}$$

where the energy of the particle is now fixed and defined as the pole energy $E_{\mathbf{P}}^2 = \mathbf{P}^2 + m^2 + \operatorname{Re}\bar{\Sigma}(\mathbf{P},X)$ and where the equilibrium distribution function is given by $\bar{N}(E_{\mathbf{P}}) \equiv \bar{N}(\mathbf{P},X) - \delta\bar{N}(\mathbf{P},X)$. Furthermore, it is assumed here that the self-energy is independent of the momentum $\mathbf{P}$. To further simplify the collision term, we neglect the deviations from equilibrium for the self-energies ($\delta\bar{\Sigma}^{\lessgtr} = 0$) to obtain the Boltzmann equation in the relaxation time approximation [142, 150–153]:

$$(\partial_t + \mathbf{v}_{\mathbf{P}}\cdot\nabla_{\mathbf{X}} - \nabla_{\mathbf{X}}E_{\mathbf{P}}\cdot\nabla_{\mathbf{P}})\bar{N}(\mathbf{P},X) = -\frac{\bar{\Gamma}_{\text{eq}}(\mathbf{P})}{2E_{\mathbf{P}}}\delta\bar{N}(\mathbf{P},X) \equiv -\frac{\delta\bar{N}(\mathbf{P},X)}{\tau}. \tag{2.82}$$

One can recognize the same structure as for the Boltzmann equation (A.16) with the drift term on the left-hand side containing a force term proportional to $\nabla_{\mathbf{X}}E_{\mathbf{P}}$, and the collision term I_{coll} on the right-hand side which linearly depends on the relaxation time τ.

This expression (as well as Eq. (2.75)) directly connects the imaginary part of the self-energy through $\bar{\Gamma}(\mathbf{P}) = \mp\ 2\ \mathrm{Im}\bar{\Sigma}^{R/A}$ to the equilibration time τ of the particle's distribution function [142, 145, 149, 154–160]. By replacing in Eq. (2.78) the spectral functions for particles (2, 3 and 4) by their on-shell values (2.76), one can deduce the expression for the well-known quasiparticle **interaction rate** Γ^{int} (inverse relaxation time) as:

$$\begin{aligned}\Gamma^{\mathrm{int}}(\mathbf{P}) = \frac{1}{2E_{\mathbf{P}}}\int\frac{d^3P_2}{(2\pi)^3 2E_{\mathbf{P_2}}}\int\frac{d^3P_3}{(2\pi)^3 2E_{\mathbf{P_3}}}\int\frac{d^3P_4}{(2\pi)^3 2E_{\mathbf{P_4}}} \\ \times(2\pi)^4\ \delta^{(4)}\left(P+P_2-P_3-P_4\right)\ \left|\mathcal{M}_{P+P_2\to P_3+P_4}\right|^2 \\ \times N(\mathbf{P_2})(1\pm N(\mathbf{P_3}))(1\pm N(\mathbf{P_4})).\end{aligned} \tag{2.83}$$

where $\pm$ stands for bosons (+) and fermions (-). The interaction rate of the particle is also connected to the so-called **damping rate** γ which is defined as the imaginary part of the dispersion relation P_0 as [155, 161]:

$$P_0 = \omega_{\mathbf{P}} - i\gamma, \tag{2.84}$$

where $\omega_{\mathbf{P}}$ is the frequency of the oscillation. The retarded propagator from Eq. (2.53) reads:

$$\bar{G}^R(P) = \frac{1}{P_0^2 - \mathbf{P}^2 - m^2 - \mathrm{Re}\,\bar{\Sigma}^R - i\,\mathrm{Im}\,\bar{\Sigma}^R}, \tag{2.85}$$

whose poles define the dispersion relation of the particle and therefore its frequency and damping through the medium as [142, 156–163]:

$$\omega_{\mathbf{P}} = \pm\left(\mathbf{P}^2 + m^2 + \mathrm{Re}\,\bar{\Sigma}^R\right)^{1/2}\ ; \qquad \gamma_{\mathbf{P}} = -\frac{\mathrm{Im}\,\bar{\Sigma}^R}{2\omega_{\mathbf{P}}} = \frac{\bar{\Gamma}}{4\omega_{\mathbf{P}}} = \frac{\Gamma^{\mathrm{int}}}{2}, \tag{2.86}$$

where the quasiparticle condition $\gamma_{\mathbf{P}} < \mathrm{Re}\,\bar{\Sigma}^R/2\omega_{\mathbf{P}}$ - corresponding to no over-damping - is assumed. This leads to the following retarded propagator:

$$\bar{G}^R(\omega,\mathbf{p}) \approx \frac{1}{\omega^2 - \mathbf{p}^2 - m^2 - \mathrm{Re}\,\bar{\Sigma}^R + 2i\omega\gamma_{\mathbf{P}}}, \tag{2.87}$$

whose Fourier transform $G^R(x) = \int\frac{d^4p}{(2\pi)^4}\ e^{-ipx}\ \bar{G}^R(\omega,\mathbf{p})$ is found to be similar to

the one of a damped harmonic oscillator and indeed leads to a damping $\propto e^{-\gamma t}$ after performing the energy integration (by applying the residue theorem [164]).

The spectral function in the quasiparticle approximation [160, 165] – corresponding to the propagator (2.87) – can be calculated via $\bar{A} = -2\,\mathrm{Im}\,\bar{G}^R$ and reads:

$$\begin{aligned}\bar{A}(\omega,\mathbf{p}) &= \frac{4\omega\gamma_{\mathbf{P}}}{(\omega^2-\mathbf{p}^2-m^2-\mathrm{Re}\,\bar{\Sigma}^R)^2+4\gamma_{\mathbf{P}}^2\omega^2} \\ &\equiv \frac{\gamma_{\mathbf{P}}}{E}\left(\frac{1}{(\omega_{\mathbf{P}}-E)^2+\gamma_{\mathbf{P}}^2}+\frac{1}{(\omega+E)^2+\gamma_{\mathbf{P}}^2}\right),\end{aligned} \tag{2.88}$$

with $E^2 = \mathbf{p}^2 + m^2 + \mathrm{Re}\,\bar{\Sigma}^R - \gamma_{\mathbf{P}}^2$. This spectral function has a Lorentzian shape and is an often used *Ansatz* to describe the distribution of off-shell particles as in the Dynamical QuasiParticle Model (see next sections).

2.7 Summary

In this chapter, I started by introducing the tools which are used in the study of quantum fields out-of equilibrium. We have seen that the time evolution of any operator can be calculated by means of different evolution operators which correspond to Dyson series. These evolution operators, whether they are calculated from the full Hamiltonian or only its interacting part, are expressed in the so-called Heisenberg or interaction representation, respectively. The expectation values of any time-dependent operator can also be calculated using the evolution operators which are then defined on the Keldysh contour. This allows to calculate the expectation values of the 2-point Green's functions which are of particular interest to study the properties and dynamics of a medium. By decomposing the Keldysh contour, one can define four different Green's functions as well as retarded and advanced propagators which contain information about the spectral properties of states. In the case of a scalar field theory, we study the evolution equations for the different Green's functions which are called the Kadanoff-Baym equations. By applying a Wigner transform to the evolution equations of the retarded/advanced Green's functions, we were able to obtain information about the spectral function and its evolution equation valid up to first order in the gradients. Performing the same procedure to the Kadanoff-Baym equations for the lesser and greater Green's functions, we obtain generalized off-shell transport equations. In the last part of this chapter, we have seen that these transport equations reduce to the well-known Boltzmann equation in the quasiparticle limit. In this limit, one finds a direct connection between the quasiparticle damping rate (which is related to the width

or imaginary part of the self-energy) and its interaction rate (inverse relaxation time). In the next chapter, we will see how to numerically solve the off-shell transport equations and apply them to the description of heavy-ion collisions.

Chapter 3

The Parton-Hadron-String Dynamics (PHSD)

* * *

3.1 Test-particle representation

In order to solve the generalized transport equation in consistent first order gradient expansion, i.e. in the Botermans-Malfliet form (2.73), we employ the test-particle *Ansatz* [166] which approximates the (real and positive semi-definite) Green's function $i\bar{G}^<$ as a sum of point-like particles:

$$i\bar{G}^<(P_0,\mathbf{P},t,\mathbf{X}) \sim \sum_{i=1}^{N} \frac{1}{2P_0}\delta^{(3)}\left(\mathbf{X}-\mathbf{X}_i(t)\right)\delta^{(3)}\left(\mathbf{P}-\mathbf{P}_i(t)\right)\delta\left(P_0-\epsilon_i(t)\right) \qquad (3.1)$$

where the position of the test-particle i at time t is denoted by $\mathbf{X}_i(t)$, and its 4-momentum by $(\epsilon_i(t),\mathbf{P}_i(t))$. We first study the free propagation of particles in between collisions, i.e. by neglecting the collision terms I_{coll} in the generalized transport equation (2.73), which we can rewrite in the form [126, 145, 167]:

$$2P^\mu \partial_\mu^X i\bar{G}^< - \partial_\mu^X \left[\left(\partial_P^\mu \,\mathrm{Re}\,\bar{\Sigma}^R + \frac{P^2 - m^2 - \mathrm{Re}\,\bar{\Sigma}^R}{\bar{\Gamma}} \partial_P^\mu \bar{\Gamma} \right) i\bar{G}^< \right] \tag{3.2}$$
$$+ \partial_P^\mu \left[\left(\partial_\mu^X \,\mathrm{Re}\,\bar{\Sigma}^R + \frac{P^2 - m^2 - \mathrm{Re}\,\bar{\Sigma}^R}{\bar{\Gamma}} \partial_\mu^X \bar{\Gamma} \right) i\bar{G}^< \right] = 0 \ ,$$

where the contribution of the self-energy $\bar{\Sigma}^\delta$ has been incorporated into $\mathrm{Re}\,\bar{\Sigma}^R$. By replacing $i\bar{G}^<$ in the previous equation by the test-particle approximation (3.1), one can separate the contributions from similar coefficients of delta functions in order to obtain equations of motion for the test-particles as [120, 145, 167, 168]:

$$\frac{d\mathbf{X}_i}{dt} = \frac{1}{1 - C_{(i)}} \frac{1}{2\epsilon_i} \left[2\mathbf{P}_i + \nabla_{\mathbf{P}_i} \mathrm{Re}\,\bar{\Sigma}^R_{(i)} + \frac{\epsilon_i^2 - \mathbf{P}_i^2 - m^2 - \mathrm{Re}\,\bar{\Sigma}^R_{(i)}}{\bar{\Gamma}_{(i)}} \nabla_{\mathbf{P}_i} \bar{\Gamma}_{(i)} \right] \tag{3.3}$$

$$\frac{d\mathbf{P}_i}{dt} = \frac{-1}{1 - C_{(i)}} \frac{1}{2\epsilon_i} \left[\nabla_{\mathbf{X}_i} \mathrm{Re}\,\bar{\Sigma}^R_{(i)} + \frac{\epsilon_i^2 - \mathbf{P}_i^2 - m^2 - \mathrm{Re}\,\bar{\Sigma}^R_{(i)}}{\bar{\Gamma}_{(i)}} \nabla_{\mathbf{X}_i} \bar{\Gamma}_{(i)} \right] \tag{3.4}$$

$$\frac{d\epsilon_i}{dt} = \frac{1}{1 - C_{(i)}} \frac{1}{2\epsilon_i} \left[\partial_t \,\mathrm{Re}\,\bar{\Sigma}^R_{(i)} + \frac{\epsilon_i^2 - \mathbf{P}_i^2 - m^2 - \mathrm{Re}\,\bar{\Sigma}^R_{(i)}}{\bar{\Gamma}_{(i)}} \partial_t \bar{\Gamma}_{(i)} \right] \tag{3.5}$$

with the multiplication factor $C_{(i)}$ which contains energy derivatives of the self-energy as:

$$C_{(i)} = \frac{1}{2\epsilon_i} \left[\partial_{\epsilon_i} \mathrm{Re}\,\bar{\Sigma}^R_{(i)} + \frac{\epsilon_i^2 - \mathbf{P}_i^2 - m^2 - \mathrm{Re}\,\bar{\Sigma}^R_{(i)}}{\bar{\Gamma}_{(i)}} \partial_{\epsilon_i} \bar{\Gamma}_{(i)} \right] , \tag{3.6}$$

and yields a shift of the system time t to the 'eigentime' of the particle i defined by $\tilde{t}_i = t/(1 - C_{(i)})$. This correction factor is a generalization of the quasiparticle renormalization factor appearing for finite width particles [144]. One can see that the evolution equation for $d\mathbf{X}_i/d\tilde{t}_i$, $d\mathbf{P}_i/d\tilde{t}_i$ and $d\epsilon_i/d\tilde{t}_i$, are the same as Eqs. (3.3)-(3.4)-(3.5) without this normalization factor $1 - C_{(i)}$. For the case of a momentum independent width $\bar{\Gamma}_{(i)}(X)$, one can take as an independent variable $M^2 = P^2 - \mathrm{Re}\,\bar{\Sigma}^R$ instead of the energy P_0, which is then fixed as:

$$P_0^2 = \mathbf{P}^2 + M^2 + \mathrm{Re}\,\bar{\Sigma}^R. \tag{3.7}$$

Eq. (3.5) can be written as an evolution equation for the function M:

$$\frac{d\Delta M_i^2}{dt} = \frac{\Delta M_i^2}{\bar{\Gamma}_{(i)}} \frac{d\bar{\Gamma}_{(i)}}{dt} \quad \leftrightarrow \quad \frac{d}{dt} \ln \left(\frac{\Delta M_i^2}{\bar{\Gamma}_{(i)}} \right) = 0 \tag{3.8}$$

where $\Delta M_i^2 = M_i^2 - m^2$ is a measure of the off-shellness of the particle i, whose evolution is found to be directly proportional to the ratio $\bar{M}/\bar{\Gamma}$. This ratio also appears in Eq. (3.2) as a weighting factor for the changes induced by the variation of the imaginary part of the self-energy $\bar{\Gamma} = -2\,\mathrm{Im}\,\bar{\Sigma}^R$. This off-shell contribution can also be traced back to the 2$^{\mathrm{nd}}$ Poisson bracket on the left-hand sides of Eqs. (2.67)-(2.73).

Similar expressions have also been derived in the non-relativistic case in Ref. [146], where the off-shell masses obey a similar evolution determined by the non-relativistic width and mass function. In the on-shell limit $\bar{\Gamma} \to 0$, Hamilton's equations (A.1) for stable particles are recovered [169].

3.2 Application to heavy-ion collisions

The test-particle *Ansatz* (3.1) is used in the Parton-Hadron-String Dynamics (PHSD) in order to evaluate the left-hand side (drift term) of the transport equation. Concerning the right-hand side (collision term) of the transport equations, a stochastic method is commonly employed in order to find collision partners within the same time step of the computation. In PHSD, the **parallel ensemble** method is used meaning that the computation is divided into N ensembles, each of them containing a similar number of particles. Collisions can only happen between particles within the same ensemble, but macroscopic quantities like the density of particles are averaged over the parallel ensembles. An other method to solve a transport equation is to consider the evolution of the test-particles in one single ensemble, known as the **full-ensemble** method, where N test-particles are used to describe one real particle and where collisions between test-particles can happen with the rescaled cross-section σ/N. In both methods, the Pauli-blocking probability for final particles has to be taken into account which may forbid scattering to happen if the final states are already filled.

PHSD is using a space-time grid which evolves in time for describing heavy-ion collisions: at the beginning of the reaction, a large number of interactions are expected due to high densities implying that the time step has to be sufficiently small (less than the inverse interaction rate of the particles) in order to catch the whole dynamics; at later times the density of particles decreases, allowing to use a

larger time step for the sake of efficiency. The PHSD lattice is also contracted in the axis parallel to the beam direction (commonly referred to the $z-$axis): due to the highly-Lorentz-contracted initial nuclei at high collisional energies (see Fig. 3.1), a precise grid is necessary according to the typical length-scale of the system which is inversely proportional to the Lorentz gamma factor γ_N. This gamma factor can be calculated from the energy available in the collision of a nucleon pair $\sqrt{s_{NN}}$ or in the laboratory frame (where a target at rest is used) from the kinetic energy of the accelerated nucleus E_{kin} as:

$$\gamma_N = \frac{\sqrt{s_{NN}}}{2M_N} \quad \text{with} \quad \sqrt{s_{NN}} = \sqrt{2M_N(E_{\text{kin}} + 2M_N)}, \tag{3.9}$$

with M_N being the mass of a nucleon ≈ 0.938 GeV and the beam energy being $E_{beam} = E_{kin} + m_N$. We mention that in PHSD, E_{kin} is the input for the collisional energy of the heavy-ions. The production of particles in heavy-ion collisions is examined through inclusive spectra as well as differential spectra which are usually expressed as a function of different quantities like their rapidity y or transverse momentum p_T defined as:

$$y = \frac{1}{2}\ln\left(\frac{E+p_z}{E-p_z}\right) \quad ; \quad p_T = \sqrt{p_x^2 + p_y^2}. \tag{3.10}$$

One can see in Fig. 3.1 that particles with a high rapidity are generally close to the remnants of the initial nuclei, whose initial rapidity is:

$$y_N = \frac{1}{2}\ln\left(\frac{1+\beta_z}{1-\beta_z}\right) \quad \text{with} \quad \beta_z = \sqrt{1 - \frac{1}{\gamma_N^2}} \tag{3.11}$$

which gives $y_N \approx 3$ for $\sqrt{s_{NN}} = 19.6$ GeV. The initial baryons (contained in the nuclei) are also mostly present in this high rapidity region, but some of them are also found at lower rapidities (as also seen in the net baryon density): this effect is measured by the **baryon stopping** and will be discussed later. It is also seen that most of the particles at midrapidity ($|y| < 0.5$) are produced by the hadronization process occurring when the Quark-Gluon Plasma (QGP) phase approaches the crossover temperature (or energy density ≈ 0.5 GeV.fm^{-3}). Concerning the momentum of these particles, one can see that the "fireball" or "bulk" produced by the heavy-ion collisions contains predominantly low transverse momentum particles. High momentum particles are rare and usually produced in the hard initial nucleon-nucleon scatterings. Due to their high momentum, these particles are able to go through and leave the "fireball" faster than the "bulk" particles: for this reason they are called "hard-probes" since they can probe the matter created in heavy-ion collisions from the very beginning. Tables 3.1-3.2 contain the different mesons and

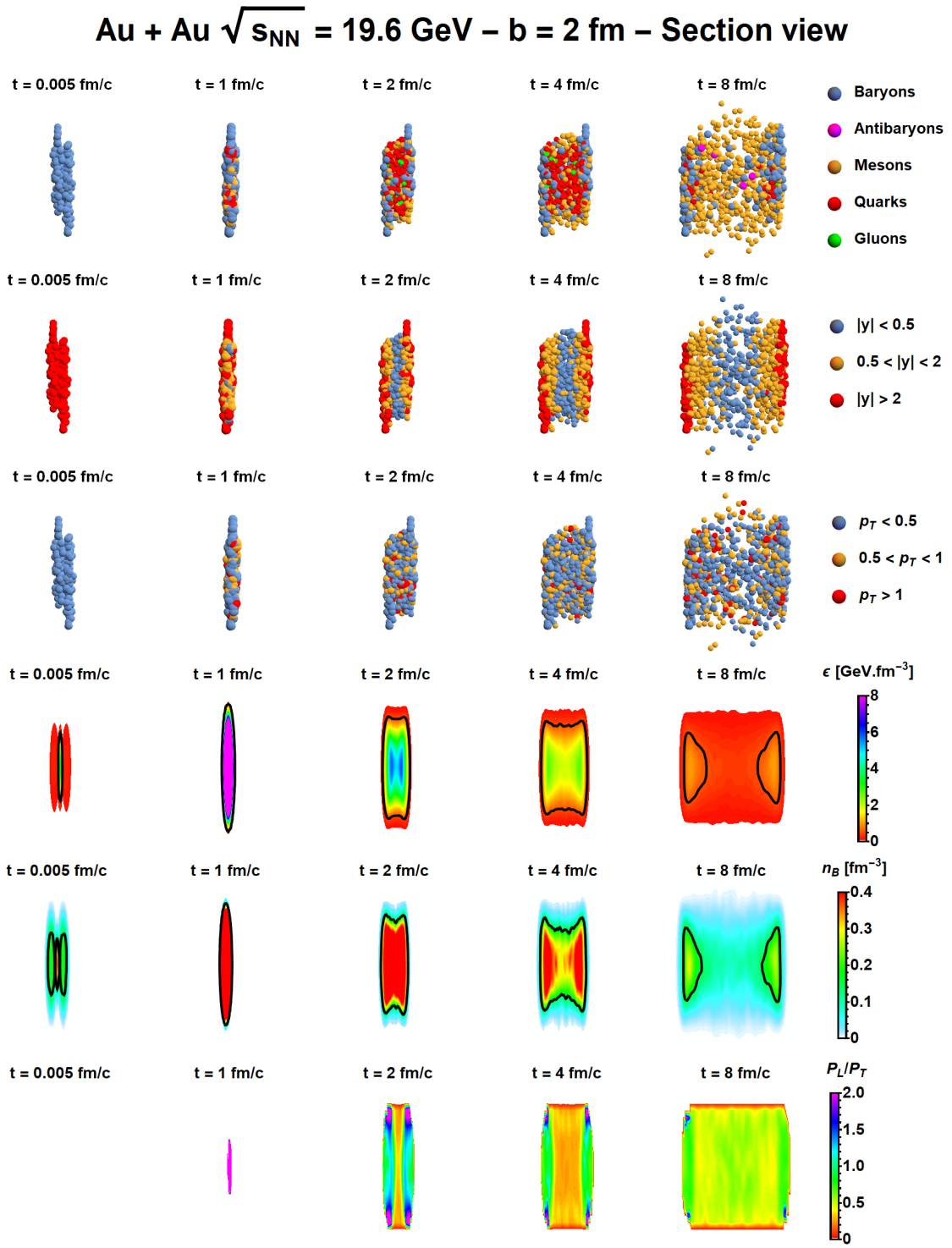

Figure 3.1 – Illustration of a PHSD simulation for a central Au+Au collision at a collisional energy of $\sqrt{s_{NN}} = 19.6$ GeV. The initial nuclei have a rapidity $y_N \approx 3$ and are Lorentz contracted by a factor $\gamma_N = 10.45$. The local energy density ϵ, net baryon density n_B, and the ratio of longitudinal over transverse pressure P_L/P_T, were extracted from the PHSD in the region where $y \approx 0$. The black lines indicate the critical energy density $\epsilon_c = 0.5$ GeV/fm^3 and the density of normal nuclear matter $\rho_0 = 0.15$ fm^{-3}.

baryons included in the PHSD transport code where the particles made of light quarks mostly constitute the "bulk" produced in heavy-ion collisions, whereas rare particles containing several strange quarks or a charm quark are, as well as high p_T particles, considered as specific probes. The lightest particles are contained in the bulk since they are cheaper to produce, while the production of heavier quarks or particles is suppressed as we will see in the following subsection about hadronic interactions.

3.2.1 Initialization

In PHSD, the two initial nuclei are initialized in such a way that they will collide with the specified energy and impact parameter. The distribution of the initial nucleons in coordinate and momentum space is crucial for the description of heavy-ion observables since all the following dynamics depend on it. For heavy-ions, it is common to use the Woods-Saxon distribution [170] which gives the nuclear density profile $\rho(r)$ as a function of the radius of the nucleus r:

$$\rho(r) = \rho_0 \frac{1+\omega(r/R)}{1+\exp\left(\frac{r-R}{a}\right)}, \tag{3.12}$$

with ρ_0 being the density of the nucleus in its center (≈ 0.15 fm^{-3} which is indicated by the black line in the fifth panel of Fig. 3.1), ω the deviation from a spherical shape, R is the radius of the nucleus and a is the skin depth. The radius and the skin depth can be parametrized as a function of the mass number A as:

$$R = R_0\ A^{1/3}\ , \qquad a = 0.02444\ A^{1/3} + 0.2864\ [\text{fm}], \tag{3.13}$$

with $R_0 = 1.096$ fm. In our case we will only study spherical heavy-ions such that $\omega = 0$. In the rest frame of the nucleus, the momentum of the nucleons is choosen according to the semiclassical Thomas-Fermi model [171, 172], i.e. as $0 < |\mathbf{p}| < p_F$ with p_F denoting the Fermi momentum:

$$p_F(r) = \sqrt[3]{\frac{3}{2}\pi^2\rho(r)}. \tag{3.14}$$

Particle	Quark content	Mass [GeV]	$I^G(J^{PC})$	$c\tau$
$\pi^{\pm}$	$u\bar{d}$	0.140	$1^-(0^-)$	7.80 m
π^0	$(u\bar{u}-d\bar{d})/\sqrt{2}$	0.135	$1^-(0^{-+})$	25.05 nm
η	$c_1(u\bar{u}-d\bar{d})+c_2(s\bar{s})$	0.548	$0^+(0^{-+})$	0.15 nm
$\rho^{\pm}$	$u\bar{d}$	0.775	$1^+(1^{--})$	1.32 fm
ρ	$(u\bar{u}-d\bar{d})/\sqrt{2}$	0.775	$1^+(1^{--})$	1.32 fm
ω	$c_1(u\bar{u}-d\bar{d})+c_2(s\bar{s})$	0.783	$0^-(1^{--})$	23.20 fm
η'	$c_1(u\bar{u}-d\bar{d})+c_2(s\bar{s})$	0.958	$0^+(0^{-+})$	1.00 pm
ϕ	$c_1(u\bar{u}-d\bar{d})+c_2(s\bar{s})$	1.020	$0^-(1^{--})$	46.36 fm
$a_1^{\pm}$	$u\bar{d}$	1.230	$1^-(1^{++})$	0.33-0.79 fm
a_1^0	$(u\bar{u}-d\bar{d})/\sqrt{2}$	1.230	$1^-(1^{++})$	0.33-0.79 fm
$K^{\pm}$	$u\bar{s}$	0.494	$1/2(0^-)$	3.71 m
$K^0(\bar{K}^0)$	$d\bar{s}$	0.498	$1/2(0^-)$	2.68 cm (S) / 15.34 m (L)
$K^{*\pm}$	$u\bar{s}$	0.892	$1/2(1^-)$	3.92 fm
$K^{*0}(\bar{K}^{*0})$	$d\bar{s}$	0.896	$1/2(1^-)$	4.17 fm
$D^{\pm}$	$c\bar{d}$	1.870	$1/2(0^-)$	311.80 μm
$D^0(\bar{D}^0)$	$c\bar{u}$	1.865	$1/2(0^-)$	122.90 μm
$D^{*\pm}$	$c\bar{d}$	2.010	$1/2(1^-)$	2.36 pm
$D^{*0}(\bar{D}^0)$	$c\bar{u}$	2.007	$1/2(1^-)$	$>$ 93.80 fm
J/Ψ	$c\bar{c}$	3.097	$0^-(1^{--})$	2.12 pm
Ψ'	$c\bar{c}$	3.686	$0^-(1^{--})$	0.67 pm
η_c	$c\bar{c}$	2.984	$0^+(0^{-+})$	6.16 fm
$D_s^{\pm}$	$c\bar{s}$	1.968	$0(0^-)$	151.20 μm
$D_s^{*\pm}$	$c\bar{s}$	2.112	$0(?^?)$	$>$ 103.7 fm

Table 3.1 – List of mesons considered in PHSD. The data about quark content, mass, isospin I, $G-$parity, spin J, parity P, $C-$parity, and lifetime τ (or width) are taken from Ref. [67].

Particle	Quark content	Mass [GeV]	$I(J^P)$	$c\tau$
p	uud	0.938	$1/2(1/2^+)$	-
n	udd	0.940	$1/2(1/2^+)$	2.64×10^8 km
$N(1440)$	$uud-udd$	≈ 1.440	$1/2(1/2^+)$	≈ 0.56 fm
$N(1535)$	$uud-udd$	≈ 1.530	$1/2(1/2^-)$	≈ 1.31 fm
Δ^{++}	uuu	≈ 1.232	$3/2(3/2^+)$	≈ 1.68 fm
Δ^{+}	uud	≈ 1.232	$3/2(3/2^+)$	≈ 1.68 fm
Δ^{0}	udd	≈ 1.232	$3/2(3/2^+)$	≈ 1.68 fm
Δ^{-}	ddd	≈ 1.232	$3/2(3/2^+)$	≈ 1.68 fm
Λ^0	uds	1.115	$0(1/2^+)$	7.89 cm
Σ^+	uus	1.189	$1(1/2^+)$	2.40 cm
Σ^0	uds	1.197	$1(1/2^+)$	22.20 pm
Σ^-	dds	1.193	$1(1/2^+)$	4.43 cm
Σ^{*+}	uus	1.383	$1(3/2^+)$	5.47 fm
Σ^{*0}	uds	1.384	$1(3/2^+)$	5.47 fm
Σ^{*-}	dds	1.387	$1(3/2^+)$	5.00 fm
Ξ^0	uss	1.315	$1/2(1/2^+)$	8.71 cm
Ξ^-	dss	1.322	$1/2(1/2^+)$	4.91 cm
Ξ^{*0}	uss	1.532	$1/2(3/2^+)$	21.65 fm
Ξ^{*-}	dss	1.535	$1/2(3/2^+)$	19.90 fm
Ω^-	sss	1.673	$0(3/2^+)$	2.46 cm
Λ_c^+	udc	2.286	$0(1/2^+)$	59.9 μm
Σ_c^{++}	uuc	2.454	$1(1/2^+)$	104.23 fm
Σ_c^{+}	udc	2.453	$1(1/2^+)$	$>$ 42.83 fm
Σ_c^{0}	ddc	2.454	$1(1/2^+)$	107.65 fm
Σ_c^{*++}	uuc	2.518	$1(3/2^+)$	13.33 fm
Σ_c^{*+}	udc	2.518	$1(3/2^+)$	$>$ 11.59 fm
Σ_c^{*0}	ddc	2.518	$1(3/2^+)$	12.88 fm
Ξ_c^{+}	usc	2.468	$1/2(1/2^+)$	132.00 μm
Ξ_c^{0}	dsc	2.471	$1/2(1/2^+)$	33.60 μm
$\Xi_c^{\prime+}$	usc	2.576	$1/2(1/2^+)$	?
$\Xi_c^{\prime0}$	dsc	2.578	$1/2(1/2^+)$	?
Ξ_c^{*+}	usc	2.646	$1/2(3/2^+)$	92.06 fm
Ξ_c^{*0}	dsc	2.646	$1/2(3/2^+)$	83.83 fm
Ω_c^{0}	ssc	2.695	$0(1/2^+)$	21 μm
Ω_c^{*0}	ssc	2.766	$0(3/2^+)$	?

Table 3.2 – List of baryons considered in PHSD. The data about quark content, mass, isospin I, spin J, parity P, and lifetime τ (or width) are taken from Ref. [67]. Their respective antiparticles are incorporated, too.

3.2.2 Hadronic interactions

As explained in the previous subsection, the parallel ensemble method is used in PHSD meaning that the test-particles can interact within the same ensemble and the same time step. To decide whether a collision between two test-particles can happen or not, one needs to know the impact parameter b of the possible collision, and the total cross section $\sigma_{tot} = \sum_i \sigma_i$ that, when given a geometrical interpretation, defines an area of interaction. The collision is accepted when the impact parameter is less than the maximum given by the geometrical cross section as [173] (see more details in Appendix C):

$$b \leq b_{max} = \sqrt{\frac{\sigma}{\pi}}. \tag{3.15}$$

If a collision is accepted, the reaction channel i has to be choosen by Monte-Carlo with a probability $P_i = \sigma_i/\sigma$.

Primary high energy scatterings between nucleons are described in PHSD by the FRITIOF Lund model [174, 175] which assumes the production of excited color-neutral objects called **strings**. PYTHIA 6.4 [176] and JETSET 7.3 [177] are also incorporated to describe the production and fragmentation of jets.

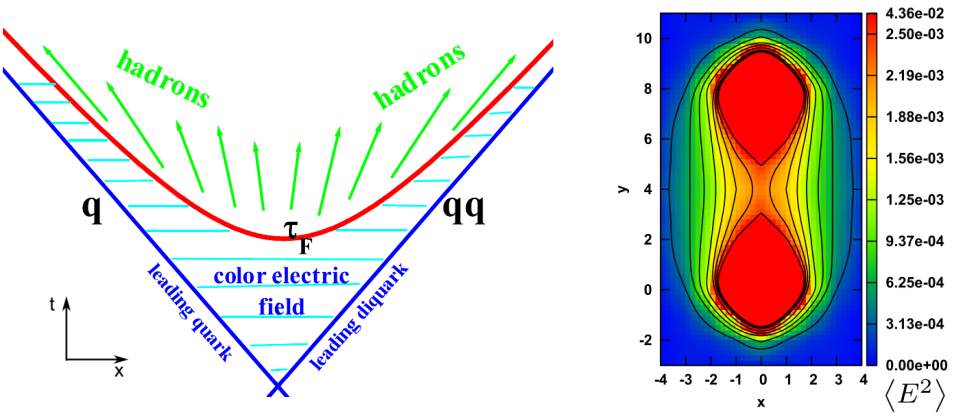

Figure 3.2 – (Left) Illustration of a string formation and decay from an initial baryon. The string ends - constituted of a quark and diquark - drift apart while being connected by a color electric field, which produces hadrons after the formation time τ_F. (Right) Values of the color electric field in a static quark-antiquark system evaluated from lattice QCD in units of the lattice spacing $a = 2718 \pm 32$ MeV (taken from Ref. [178]).

As shown in Fig. 3.2 for the case of an initial baryon, the string ends are composed of **leading particles** which, when drifting apart, stretch the color electric field in between them. The color electric field describes phenomenologically the low energy gluon dynamics between colored objects. On the right-hand side of Fig. 3.2, one can see that the color electric field for a static quark-antiquark system from lattice QCD simulations [178] looks indeed like a "flux tube" or a string. At large separation distances between the hadron constituents, the potential is known (from lattice QCD [179]) to increase linearly with the distance as $V(r) \sim \kappa r$ with κ being the string tension $\kappa \approx 0.176$ GeV$^2 \approx 0.9$ GeV/fm. The color electric field is stretched until enough energy is available to produce color-neutral $q\bar{q}$ pairs from the vacuum: this is the so-called **string breaking** which was also confirmed by lattice QCD calculations [180]. The newly produced q (or $\bar{q}$) will recombine with an other q (or $\bar{q}$) from a different string breaking to produce a color dipole with (possibly) different flavor content. These newly produced particles are called pre-hadrons and lead to the formation of color-neutral leading particles at the string ends, as well as non-leading **secondary (pre-)hadrons** (shown in Fig. 3.2 by the green color). The secondary pre-hadrons are only allowed to interact with the surrounding matter after a formation time $\tau_F \approx 0.5 - 0.8$ fm/c from the string formation. Due to time dilation, the formation of leading hadrons can be long compared to the inverse interaction rate. Until the complete formation of leading hadrons, reduced cross sections are used to describe the interactions of the leading quarks/diquarks as:

$$\begin{aligned} \sigma(q-B) &= 1/3\ \sigma(B-B) \approx 10\ \text{mb} \\ \sigma(qq-B) &= 2/3\ \sigma(B-B) \approx 20\ \text{mb} \\ \sigma(qq-q) &= 2/9\ \sigma(B-B) \approx 6.6\ \text{mb}, \end{aligned} \tag{3.16}$$

where $\sigma(B-B)$ denotes the baryon-baryon cross section. The leading particles do not necessarily correspond to the initial valence quarks, but are in practice chosen to be the particles with the highest momentum in the center of mass of the string.

In order to distribute the energy - accumulated in the string - to the secondary hadrons, one needs a so-called **fragmentation function** which corresponds to the probability for a hadron with a transverse mass $m_\perp$ to acquire the energy fraction x of the fragmented string. The LUND fragmentation function reads:

$$f(x, m_\perp) \approx \frac{(1-x)^a}{x} \exp\left(\frac{-b\ m_\perp^2}{x}\right) \tag{3.17}$$

with the parameters $a = 0.23$ and $b = 0.34$ GeV^{-2} which are used in HSD [182].

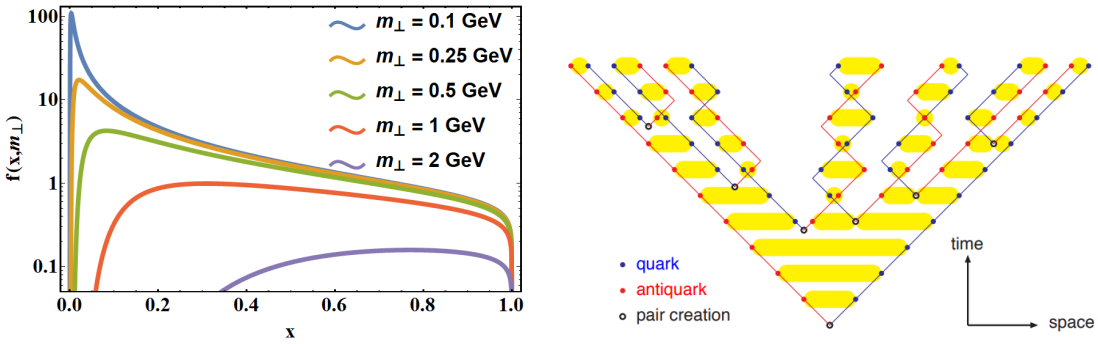

Figure 3.3 – (Left) LUND fragmentation function $f(x, m_\perp)$ from Eq. (3.17) as a function of the energy fraction x for different values of the transverse mass $m_\perp$. (Right) Illustration corresponding to the space-time evolution of hadron production in the Lund string model (from Ref. [181]).

This fragmentation function is shown in Fig. 3.3 as a function of the energy fraction x for different values of the transverse mass $m_\perp$. One can see that particles with a low traverse mass are predominantly produced, especially at low momentum energy fraction x, while the probability to produce high transverse mass particles is enhanced at large x.

On the right hand side of Fig. 3.3 the production of n hadrons is shown from the creation of $n-1$ massless quark-antiquark pairs from an initial $q\bar{q}$ pair creation. One can see that the string energy (in yellow) is converted into successive pair creation according to the available energy (or equivalently to the distance) between the $q\bar{q}$ pairs. At the end of this process, massless $q\bar{q}$ pairs traveling on the light cone are bound together by the string energy, giving rise to the so-called "yo-yo" trajectories. In this simple picture, each breakup point of the strings is found iteratively according to the distribution (3.17) since space-time trajectories can be converted into energy-momentum quantities as explained in Refs. [183, 184]. In particular, each enclosed area on the right hand side of Fig. 3.3 is proportional to $\propto m_i^2/\kappa^2$ with m_i being the mass of the secondary hadron i.

In the general case of massive quarks, the flavor of the produced quarks is determined by the **Schwinger formula** according to the following tunneling amplitude [185]:

$$J = \exp\left(-\frac{\pi m_\perp^2}{2\kappa}\right). \tag{3.18}$$

In the string decay process, only the relative probability to produce either a $u\bar{u}$,

$d\bar{d}$, $s\bar{s}$, etc... is important and can be calculated in vacuum by using the corresponding constituent quark masses. For example, the production probability of a $s\bar{s}$ compared to a light quark pair is:

$$\frac{P(s\bar{s})}{P(u\bar{u})} = \frac{P(s\bar{s})}{P(d\bar{d})} = \gamma_s = \exp\left(-\pi \frac{m_s^2 - m_{u,d}^2}{2\kappa}\right), \tag{3.19}$$

where $m_{u,d}$ denotes the dressed or constituent mass of a light quark u or d taken as equal. In the vacuum, the relative factors used in PHSD are [182]:

$$u : d : s : \text{diquark} = \begin{cases} 1:1:0.3:0.07 \text{ for } \sqrt{s_{NN}} \geq 37 \text{ GeV} \\ 1:1:0.4:0.07 \text{ for } \sqrt{s_{NN}} \leq 8 \text{ GeV} \ . \end{cases} \tag{3.20}$$

As we will see in Chapter 6, these relative probabilities - to produce quarks of different flavor - can be modified in a high density environment due to the restoration of chiral symmetry.

Concerning low energy hadronic collisions (below $\sqrt{s} = 2.6$ GeV for baryon-baryon collisions and below $\sqrt{s} = 2.2$ GeV for meson-baryon collisions), no strings are formed and the interactions can be described by elastic or inelastic cross sections, using the principle of detailed balance for backward channels. The HSD model [186, 187] describes the evolution of a hadronic medium, and incorporates 2-particle interactions ($2 \leftrightarrow 2$), the formation of resonances and their decay ($1 \leftrightarrow 2$), and the annihilation of baryons-antibaryons by means of three mesons ($2 \leftrightarrow 3$) [188–190].

3.2.3 Quark-gluon plasma

When in the PHSD space-time grid the local energy density is found to be larger than the critical one $\epsilon_c = 0.5$ GeV fm^{-3}, the newly produced hadrons from the strings are dissolved into quarks, gluons and mean-field energy, in the proportions defined by the Dynamical QuasiParticle Model (DQPM) [191]. For the sake of energy, momentum, and charge conservations, the initial hadrons are dissolved according to their mass and (anti-)quark content into the corresponding DQPM partons. Therefore, the mass of the produced quarks/gluons is directly influenced by the mass of the hadron they originate from. During the evolution of the Quark-Gluon Plasma (QGP), the parton mass is then dynamically actualized and distributed according to its spectral function defined by the DQPM as a function

of the temperature and baryon chemical potential of the medium. In PHSD, only the timelike contribution to thermodynamic quantities can be propagated in terms of particles, whereas the spacelike part can be associated to a potential energy U_j. The space-derivatives of this potential energy will change the momentum of the particle j according to the force term $-\nabla U_j(x) = -dU_j(\rho_p)/d\rho_p \nabla\rho_p(x)$, with ρ_p being the parton scalar density.

One can see in Fig. 3.1 that initially the energy density inside the nuclei ($\approx$ 0.15 GeV fm^{-3}) is well below the critical energy density. But as soon as the nuclei pass through each other, the energy density drastically increases and therefore the newly produced particles from the string decay dissolve into a Quark-Gluon Plasma (QGP). During the QGP phase, quarks and gluons can interact according to the following (quasi-)elastic channels:

$$qq \to qq, \qquad q+\bar{q} \to q+\bar{q}, \qquad \bar{q}+\bar{q}, \to \bar{q}+\bar{q} \tag{3.21}$$

$$gg \to gg, \qquad g+q \to g+q, \qquad g+\bar{q} \to g+\bar{q}, \tag{3.22}$$

and inelastic channels,

$$q+\bar{q} \leftrightarrow g. \tag{3.23}$$

During the collisions, partons can change their mass according to their spectral function, and therefore according to the temperature and chemical potential of the corresponding cell. By default, all the cross sections for the aforementioned processes are derived from the DQPM in accordance with the parton widths (or interaction rates), except for the $q+\bar{q} \leftrightarrow g$ process which is described by a Breit-Wigner cross section [192]. Further improvements on the partonic cross sections will be discussed in Chapter 7. We specify that partonic channels such as $g \to g+g$ and $q+\bar{q} \to g+g$ should in principle be taken into account, but are suppressed due the large gluon mass in the DQPM.

As the system expands and cools down, the energy density drops until hadronization occurs implying that the colored off-shell partons are then combined into off-shell colorless hadrons. The hadronization process is described in PHSD by covariant transition rates which, for the fusion of a quark-antiquark pair into a meson m of energy-momentum $p = (\omega, \mathbf{p})$ at space-time point x, reads:

$$\frac{dN_m(x,p)}{d^4x d^4p} = \mathrm{Tr}_q\,\mathrm{Tr}_{\bar{q}}\ \delta^{(4)}\left(p-p_q-p_{\bar{q}}\right)\delta^{(4)}\left(\frac{x_q+x_{\bar{q}}}{2}-x\right)\ \omega_q\rho_q(p_q)\ \omega_{\bar{q}}\rho_{\bar{q}}(p_{\bar{q}}) \quad (3.24)$$

$$\times\,|v_{q\bar{q}}|^2\ W_m\left(x_q-x_{\bar{q}},\frac{p_q-p_{\bar{q}}}{2}\right)\ f_q(x_q,p_q)\ f_{\bar{q}}(x_{\bar{q}},p_{\bar{q}})\ \delta(\text{flavor,color}).$$

In this equation, the shorthand notation was used:

$$\mathrm{Tr}_i\,....=\sum_i\int d^4x_i\int\frac{d^4p_i}{(2\pi)^4}....., \quad (3.25)$$

where the sum over i is over discrete discrete quantum number (spin, flavor, color). In Eq. (3.24), f_i and ρ_i represent the distribution and spectral function of particle i, respectively, and $v_{q\bar{q}}$ is the effective quark-antiquark interaction from the DQPM (see Ref. [191]). The quantity W_m represents the dimensionless phase-space distribution of the formed meson:

$$W_m(x,p)=\exp\left(\frac{x^2}{2b^2}\right)\ \exp\left(2b^2\left(p^2-\frac{(M_q-M_{\bar{q}})^2}{4}.\right)\right) \quad (3.26)$$

The parameter b is fixed in accordance with the root mean square radius of mesons which is taken to be $b=\sqrt{\langle r^2\rangle}=0.66$ fm (in the rest frame).

By varying the collisional energy of the initial nuclei, more or less particles are produced in the heavy-ion collisions, resulting in a lesser or larger QGP phase. We illustrate this by showing in Fig. 3.4 the QGP energy fraction for different collisional energies. One can see that for high energies the QGP fraction is indeed large compared to lower collisional energies where the proportion of QGP is small and present only for a short time. The QGP phase appears very suddenly after the initial collision at high energies whereas this appearance is smoother at lower energies since the passing time of the nuclei is longer. The same statements can be applied by looking at the QGP fraction only in the midrapidity region (right hand-side of Fig. 3.4), where one can see that at very high energies the production of particles is dominated by the QGP phase. At lower energies, the QGP lifetime is shifted to larger times since its appearance takes longer. Also, at lower energies, the rapidity window $|y|<0.5$ covers more of the total dynamics of the heavy-ion collision than at higher energies, leading to a longer duration of the QGP in this region.

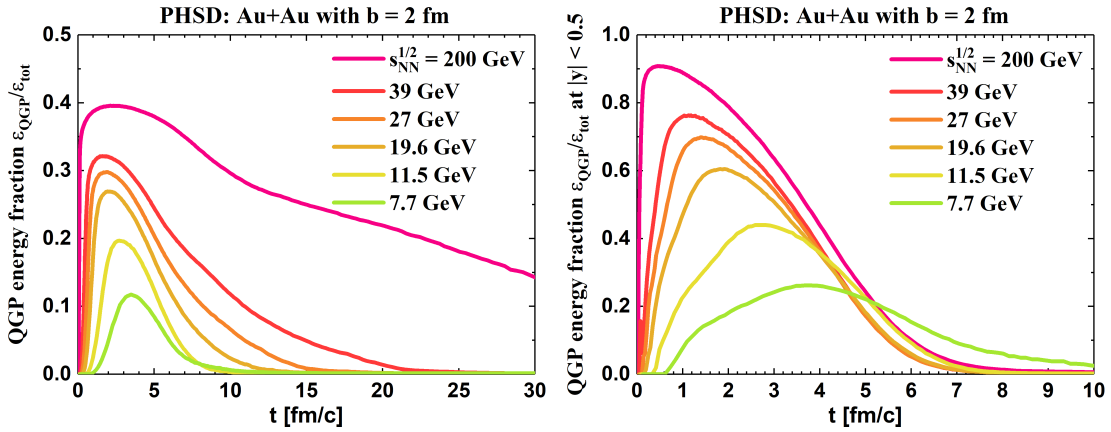

Figure 3.4 – The QGP energy fraction as a function of time t in central (impact parameter b = 2 fm) Au+Au collisions for different collisional energies $\sqrt{s_{NN}}$, taking into account all rapidities (left) and only the midrapidity region $|y| < 0.5$ (right).

3.3 Baryon stopping and excitation functions

The production of particles in a heavy-ion collision is directly influenced by the content of the initial nuclei which contain protons and neutrons. We have seen in the previous section that a large amount of energy is converted into a QGP state at high collisional energies, whereas at lower collisional energies the QGP region is subdominant. Therefore at high collisional energies, most of the final hadrons are produced after hadronization of the QGP phase, whereas at lower energies secondary hadronic collisions play an important role. An additional mechanism, which dictates the content of the final hadrons, is the baryon stopping which measures how much the initial nuclei (and their baryons) are slowed down by the collision. Since baryon number is conserved, the net-baryon number remains constant during the whole evolution of the collision and the spread of the net-baryon number $N_{B-\bar{B}}$ along the longitudinal direction can tell us about the stopping of the initial baryons. In the left-hand side of Fig. 3.5 we show a qualitative illustration of the net-baryon distribution $dN_{B-\bar{B}}/dy$ as a function of the rapidity y from the PHSD. The vertical lines indicate for each collisional energy the corresponding initial rapidity of the nuclei y_N for orientation. We mention that the nucleons which did not interact are not counted here. In the case of a small stopping, the net-baryon distribution should be close to the initial rapidity y_N whereas for a large stopping most of the baryons should be stopped in the midrapidity region. One can see in Fig. 3.5 that at the top RHIC energies ($\sqrt{s_{NN}} = 200$ GeV) the net-baryon

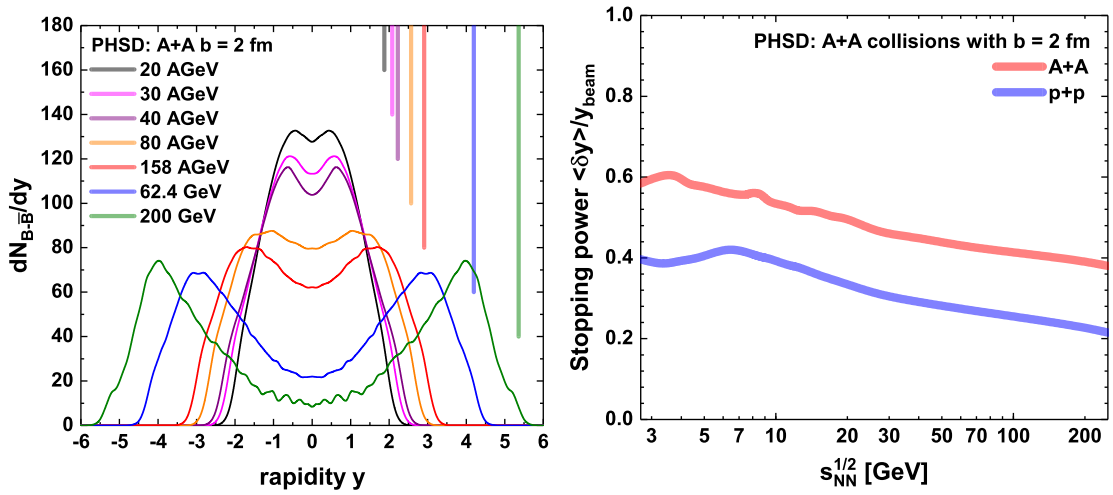

Figure 3.5 – (Left:) Net-baryon rapidity distributions for different collisional energies $\sqrt{s_{NN}}$. The vertical lines show the rapidity of the initial nuclei for orientation. (Right:) Stopping power $\langle \delta y \rangle / y_N$ as a function of the collisional energy $\sqrt{s_{NN}}$.

distribution is close to the initial rapidity $y_N \approx 5.4$ and only a small fraction of the net baryons are present at midrapidity indicating that the baryon stopping is small in that case. When looking at lower collisional energies, one can see that the parabola shape of the net-baryon distribution at high energies changes progressively to a Gaussian shape centered at midrapidity, indicating that the baryon stopping is larger in that regime. More observables can be studied to assess the baryon stopping at lower energies such as the baryon directed flow ($v_1 \sim p_x/p_T$) and elliptic flow ($v_2 \sim (p_x^2 - p_y^2)/p_T^2$) which can provide constraints on the nuclear equation of state and its stiffness [193–195]. At higher energies, the shape of the net-baryon distribution function is found to be sensitive to the type of transition to a Quark-Gluon Plasma [196] and to the baryon diffusion [197].

To quantify the baryon-stopping, we calculate the average change in rapidity $\langle \delta y \rangle$ with respect to the initial rapidity y_N of the initial baryons as [198, 199]:

$$\langle \delta y \rangle = y_N - \frac{2}{N_{part}} \int_0^{y_N} y \, \frac{dN_{B-\bar{B}}}{dy} \, dy, \tag{3.27}$$

where N_{part} is the number of participating nucleons in the collision and y_N is taken from Eq. (3.11). We show the corresponding results from the PHSD in the right-hand side of Fig. 3.5 as a function of the collisional energy $\sqrt{s_{NN}}$. One can see that at the AGS-SPS energies the change in rapidity $\langle \delta y \rangle$ of the initial baryons is more than half of the initial rapidity y_N, and that the stopping power $\langle \delta y \rangle / y_N$

monotonically decreases with increasing energy as expected from the net-baryon distributions: the nuclei become almost "transparent" in very energetic collisions. This comes from the fact that with increasing energy the **parton distribution function** $f(x,Q^2)$, which describes the probability of finding a particle inside a nucleus with a longitudinal momentum fraction x at a specific resolution scale (or momentum transfer Q), becomes more and more populated at low x. The nucleons can be seen as composed of three valence quarks surrounded by wee partons (gluons and sea-quarks), the latter having a much smaller momentum fraction x compared to the valence quarks [71]. Especially at very high collisional energies the density of low x gluons becomes so large that the nucleus can be described as a coherent classical field called the **color glass condensate** (CGC) [200–202]. We mention that the baryon stopping can also be studied within the CGC framework (see Refs. [203–206]).

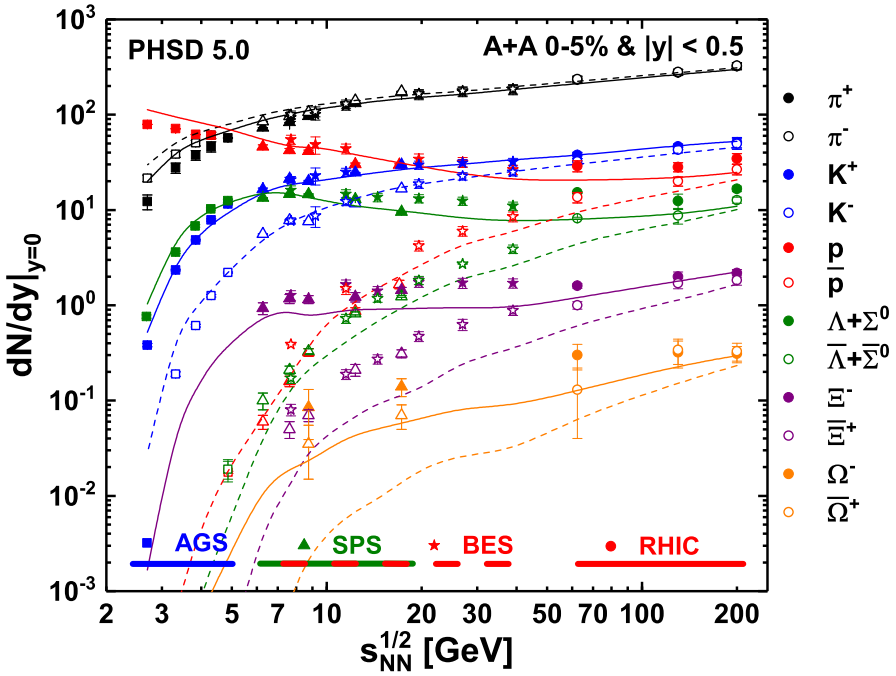

Figure 3.6 – Excitation function dN/dy of particles produced in central heavy-ion collisions at midrapidity from the PHSD in comparison with the experimental data from the E895 [207, 208], E866-E917 [209–211], E896 [212] and E895 [213] collaborations at the AGS energies, from the NA49 [214–218] and the NA57 [219] collaborations for the SPS energies, and from the STAR collaboration for the Beam-Energy-Scan [117, 220] and top RHIC regimes [221–223].

We now illustrate the production of particles in heavy-ion collisions in Fig.

3.6 by showing the excitation function $dN/dy|_{y=0}$ as a function of the collisional energy $\sqrt{s_{NN}}$. As expected from our previous comments on the baryon stopping, the production of particles at high energies is practically symmetric with respect to particles-antiparticles and mainly originates from the hadronization process of the Quark-Gluon Plasma. With decreasing energy one can see a separation between baryons and antibaryons which comes from baryon stopping, from possible $B-\bar{B}$ annihilations, and from the fact that antibaryons (especially multi-strange baryons) are preferentially produced by the hadronization process from the QGP. In the context of this Ph.D. project, the production of multi-strange baryons and antibaryons has been studied with the PHSD in Ref. [21] but will not be detailed here. Concerning the mesons, the pion production is nearly identical while one observes a large difference between the K^+ and the K^- at low energies which comes from the fact that strange quarks are preferentially contained in the $\Lambda+\Sigma^0$ baryons due to the high baryon concentration. The production of strange mesons and baryons within the PHSD will be thoroughly studied and explained in Chapter 6.

3.4 Summary

We described the Parton-Hadron-String Dynamics (PHSD) transport approach [120, 224–226], which is a microscopic covariant dynamical model for strongly interacting systems formulated on the basis of Kadanoff-Baym equations [118, 227, 228] for Green's functions in phase-space representation (introduced in the previous chapter). We explained how this approach consistently describes the full evolution of a relativistic heavy-ion collision from the initial hard scatterings and string formation through the dynamical deconfinement phase transition to the strongly-interacting quark-gluon plasma (sQGP) as well as hadronization and the subsequent interactions in the expanding hadronic phase as in the Hadron-String-Dynamics (HSD) transport approach [187, 229]. The transport theoretical description of quarks and gluons in the PHSD is based on the Dynamical Quasi-Particle Model (DQPM) for partons that is constructed to reproduce lattice QCD results for the QGP in thermodynamic equilibrium [120, 230] on the basis of effective propagators for quarks and gluons (more details can be found in Chapter 7). It is important to emphasize that the PHSD differs from conventional Boltzmann approaches in a couple of essential aspects:

1. it incorporates dynamical quasiparticles due to the finite width of the spectral functions (imaginary part of the propagators);

2. it involves scalar mean-fields that substantially drive the collective flow in

the partonic phase;

3. it is based on a realistic equation of state from lattice QCD and thus describes the speed of sound $c_s(T)$ reliably;

4. the hadronization is described by the fusion of off-shell partons to off-shell hadronic states (resonances or strings) and does not violate the second law of thermodynamics since the number of final hadronic states is larger than the number of partons, i.e. there is a production of entropy in the hadronization process [120];

5. all conservation laws (energy-momentum, flavor currents etc.) are fulfilled in the hadronization contrary to coalescence models [231–234];

6. the effective partonic cross sections are not given by pQCD but are self-consistently determined within the DQPM and probed by transport coefficients (correlators) in thermodynamic equilibrium.

Chapter 4

Nonequilibrium properties

* * *

As we have explained in the previous chapters, relativistic heavy-ion collisions produce a hot, dense phase of strongly interacting matter known as the Quark-Gluon Plasma (QGP). As we will see, its lifetime is of the order of 10 fm/c at RHIC energies and when approaching the critical temperature T_c, this plasma hadronizes into discrete particles [235–241]. A lot of information can be extracted from the final heavy-ion observables, however, to investigate the properties of the QGP itself, present research relies on dynamical models whose output are analogous to experimental measurements as they provide final-state particle distributions. The advantage of using dynamical models to describe heavy-ion collisions is that the entire space-time evolution can be dissected and used to study rare probes, such as jets, heavy quarks and electromagnetic radiation that are sensitive to the properties of the "bulk" medium. A variety of models have been successful in describing current experimental data measured at RHIC and LHC, but they strongly differ in their assumptions concerning the production of the QGP. The problem is to find out which of these model features really reflect the actual properties of the hot and dense QCD matter, how to compare these models, and how sensitive final observables are from one model to another.

In this chapter, we investigate the nonequilibrium effects on the QGP dynamics produced in relativistic heavy-ion collisions, by comparing the nonequilibrium

This work has been performed in collaboration with the QCD group at Duke University. All the results obtained from the PHSD have been analyzed and illustrated by myself, whereas the results from the hydrodynamical model have been produced by Yingru Xu.

PHSD transport approach to the 2D+1 viscous hydrodynamic VISHNew model [242, 243], which is based on the assumption of local equilibrium and conservation laws. Nonequilibrium effects are considered to be strongest at the beginning of the heavy-ion reactions since, as we will see, the created medium is highly anisotropic at this stage. These characteristics are especially expected to affect the properties of hard probes which are produced during the initial nucleon scatterings, such as heavy quarks, jets, or electromagnetic radiation. However, we will concentrate here only on studying the bulk dynamics, which have also been found to retain traces of nonequilibrium effects in observables such as correlation functions and higher-order anisotropy coefficients [244–246]. In particular, event-by-event fluctuations, and their impact on the collective observables, have been studied by Kodama et. al [245]. Based on the comparison of the coarse-grained hydrodynamical evolution with the PHSD dynamics, they find that in spite of large fluctuations on event-by-event basis in the PHSD, the ensemble averages are close to the hydrodynamical limit. A similar behavior has been pointed out before within the PHSD study in Ref. [224] where a linear correlation of the elliptic flow v_2 with the initial spatial eccentricity ε_2 has been obtained for the model study of an expanding partonic fireball (cf. Fig. 7 in Ref. [224]). Such correlations of v_2 versus ε_2 are expected in the ideal hydrodynamical case [247]. The large event-by-event fluctuations of the charge distributions has been addressed also in another PHSD study [248].

This chapter focuses on isolating differences in the dynamical evolution of the system that can be attributed to nonequilibrium dynamics, on quantifying how far in equilibrium the system actually is, and on possibly finding new observables which are sensitive to the nonequilibrium evolution of the QGP.

4.1 2D+1 viscous hydrodynamics

Relativistic hydrodynamical models calculate the space-time evolution of the QGP medium via the conservation equations

$$\partial_\mu T^{\mu\nu} = 0 \tag{4.1}$$

for the energy-momentum tensor

$$T^{\mu\nu} = e\, u^\mu u^\nu - \Delta^{\mu\nu}(P + \Pi) + \pi^{\mu\nu}, \tag{4.2}$$

provided a set of initial conditions for the fluid flow velocity u^μ, energy density e, pressure P, shear stress tensor $\pi^{\mu\nu}$, and bulk viscous pressure Π. For our analysis, VISH2+1 [242] has been used, which is an extensively tested implementation of

boost-invariant viscous hydrodynamics that has been updated to handle fluctuating event-by-event initial conditions [243]. The method from Ref. [249] is used for the calculation of the shear stress tensor $\pi^{\mu\nu}$.

This particular implementation of viscous hydrodynamics calculates the time evolution of the viscous corrections through the second-order Israel-Stewart equations [250, 251] in the 14-momentum approximation, which yields a set of relaxation-type equations [252]

$$\begin{aligned}\tau_\Pi \dot{\Pi} + \Pi = &-\zeta\theta - \delta_{\Pi\Pi}\Pi\theta + \phi_1\Pi^2 \\ &+ \lambda_{\Pi\pi}\pi^{\mu\nu}\sigma_{\mu\nu} + \phi_3\pi^{\mu\nu}\pi_{\mu\nu}, \qquad (4.3a)\\ \tau_\pi \dot{\pi}^{\langle\mu\nu\rangle} + \pi^{\mu\nu} = &\, 2\eta\sigma^{\mu\nu} + 2\pi_\alpha^{\langle\mu} w^{\nu\rangle\alpha} - \delta_{\pi\pi}\pi^{\mu\nu}\theta \\ &+ \phi_7\pi_\alpha^{\langle\mu}\pi^{\nu\rangle\alpha} - \tau_{\pi\pi}\pi_\alpha^{\langle\mu}\sigma^{\nu\rangle\alpha} \\ &+ \lambda_{\pi\Pi}\Pi\sigma^{\mu\nu} + \phi_6\Pi\pi^{\mu\nu}. \qquad (4.3b)\end{aligned}$$

Here, η and ζ are the shear and bulk viscosities. For the remaining transport coefficients, analytic results derived for a gas of classical particles in the limit of small but finite masses [252] are used.

The hydrodynamical equations of motion must be closed by an equation of state (EoS), $P = P(e)$, which is based on continuum extrapolated lattice calculations at zero baryon density published by the HotQCD collaboration [94] and blended into a hadron resonance gas EoS in the interval $110 \leq T \leq 130$ MeV using a smooth step interpolation function [253]. While not identical, this EoS is compatible with the one that the DQPM model (underlying the PHSD approach) is tuned to reproduce.

In order to start the hydrodynamical calculation, an initial condition needs to be specified. Initial condition models provide the outcome of the collision's pre-equilibrium evolution at the hydrodynamical thermalization time, at approximately 0.5 fm/c. This pre-equilibrium stage is the least understood phase of a heavy-ion collision. While some hydrodynamical models explicitly incorporate pre-equilibrium dynamics [254] starting from a full initial state calculation, others sidestep the uncertainty associated with this early regime by generating parametric initial conditions directly at the materialization time [255–257].

For our study here, we will initialize the hydrodynamical calculation with an initial condition extracted from PHSD that provides us with a common starting

configuration for both models regarding our comparison of the dynamical evolution of the system.

4.2 Nonequilibrium initial conditions

In this section we explain how we constructed the initial condition for the hydrodynamical evolution from the nonequilibrium PHSD evolution. Since in PHSD no equilibrium assumptions is made regarding the nature of the QGP during its evolution until the final hadronic freeze-out, we have to select the earliest possible stage when a hydrodynamical evolution is feasible, i.e. when viscous corrections are small (note that this criterion is less stringent than assuming full momentum isotropization or local thermal equilibrium).

4.2.1 Evaluation of the energy-momentum tensor $T^{\mu\nu}$ in PHSD

In order to calculate $T^{\mu\nu}$ in PHSD, which fully describes the medium in every space-time coordinate, the space-time is divided into cells of size $\Delta x = 1$ fm, $\Delta y = 1$ fm (which is comparable to the size of a hadron) and $\Delta z \propto 0.5 \times t/\gamma_{NN}$ scaled by γ_{NN} to account for the expansion of the system. We note that choosing a higher resolution has been shown in Ref. [248, 258–261] to lead to very similar results. In each cell, we can obtain $T^{\mu\nu}$ in the computational frame from:

$$T^{\mu\nu}(x) = \sum_i \int \frac{d^3p_i}{(2\pi)^3} \, f_i(E_i) \, \frac{p_i^\mu p_i^\nu}{E_i}. \tag{4.4}$$

where $f_i(E)$ is the distribution function corresponding to the particle i, p_i^μ the 4-momentum and $E_i = p_i^0$ is the energy of the particle i. In the case of an ideal fluid, if the matter is at rest ($u^\mu = (1,0,0,0)$) $T^{\mu\nu}(x)$ should only have diagonal components and the energy density in the cell can be identified with the T^{00} component. However, in heavy-ion collisions the matter is viscous, anisotropic and relativistic, thus the different components of the pressure are not equal and it becomes more difficult to extract the relevant information. This especially holds true for the early time at which the initial conditions for the hydrodynamical model are taken.

The needed quantities for the hydrodynamical evolution are the local energy density e, the cell 4-velocity $u^\mu = \gamma \, (1, \beta_x, \beta_y, \beta_z)$ with $\vec{\beta}$ being the cell velocity,

the shear stress tensor $\pi^{\mu\nu}$, and the bulk viscous pressure Π. As we will see, all these quantities can be extracted from the energy momentum tensor, expressed in the local rest frame (LRF) of the space-time cell. In the general case, the energy-momentum tensor can always be diagonalized, i.e presented as

$$T^{\mu\nu}\ (x_\nu)_i = \lambda_i\ (x^\mu)_i = \lambda_i\ g^{\mu\nu}\ (x_\nu)_i, \tag{4.5}$$

with $i = 0, 1, 2, 3$, where its eigenvalues are λ_i and the corresponding eigenvectors $(x_\nu)_i$. When $i = 0$, the local energy density e is identified to the eigenvalue of $T^{\mu\nu}$ (Landau matching condition) and the corresponding time-like eigenvector is defined as the 4-velocity u_ν (multiplying Eq. (4.2) by u_ν):

$$T^{\mu\nu}u_\nu = eu^\mu = (eg^{\mu\nu})u_\nu \tag{4.6}$$

using the normalization condition $u^\mu u_\mu = 1$. In order to solve this equation, we have to calculate the determinant of the corresponding matrix which is the 4^{th} order characteristic polynomial associated to the eigenvalues λ:

$$P(\lambda) = \begin{vmatrix} T^{00}-\lambda & T^{01} & T^{02} & T^{03} \\ T^{10} & T^{11}+\lambda & T^{12} & T^{13} \\ T^{20} & T^{21} & T^{22}+\lambda & T^{23} \\ T^{30} & T^{31} & T^{32} & T^{33}+\lambda \end{vmatrix}. \tag{4.7}$$

The procedure to find the solution to this 4^{th} order polynomial is described in detail at the end of Appendix D. Having the four solutions for this polynomial, we can identify the energy density being the larger and positive solution, and the 3 other solutions are $(-P_i)$ the pressure components expressed in the LRF. To obtain the 4-velocity of the cell, we use (4.6) which gives the set of equations:

$$\begin{cases} (T^{00}-e) + T^{01}X + T^{02}Y + T^{03}Z = 0 \\ T^{10} + (T^{11}+e)X + T^{12}Y + T^{13}Z = 0 \\ T^{20} + T^{21}X + (T^{22}+e)Y + T^{23}Z = 0 \\ T^{30} + T^{31}X + T^{32}Y + (T^{33}+e)Z = 0 \end{cases} \tag{4.8}$$

Rearranging these equations, we can obtain the solutions which are actually for the vector $u_\nu = \gamma\ (1, X, Y, Z) = \gamma\ (1, -\beta_x, -\beta_y, -\beta_z)$. To obtain the physical 4-velocity u^μ, we have to multiply by $g^{\mu\nu}u_\nu = u^\mu$.

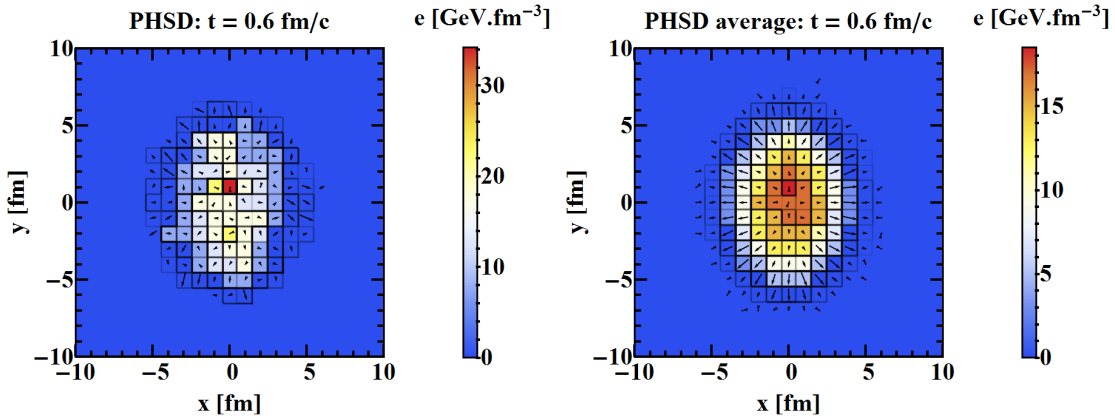

Figure 4.1 – Initial conditions for hydrodynamics: the energy density profiles from a single PHSD event (left panel) and averaged over 100 PHSD events (right panel) taken at $t = 0.6$ fm/c for a peripheral ($b = 6$ fm) Au+Au collision at $\sqrt{s_{NN}} = 200$ GeV.

4.2.2 PHSD initial conditions for hydrodynamics

By applying the Landau matching procedure to the energy momentum tensor evaluated on the space-time grid of the PHSD, we obtain the initial conditions for the hydrodynamical evolution such as the local energy density e and the initial flow velocity $\vec{\beta}$. As explained in Chapter 3, the parallel ensemble algorithm is used in the PHSD for the test-particle method, implying that thermodynamic quantities are averaged over a certain number of ensembles. From a hydrodynamical point of view, gradients should not be too large and therefore a relatively smooth profile needs to be obtained by varying the number of parallel events (NUM) in the PHSD. Here, we choose NUM= 30, which provides the same level of smoothing of the initial energy density as in typical PHSD simulations at RHIC energies. In Fig. 4.1 we show the initial condition at time $\tau = 0.6$ fm/c extracted from a single PHSD event averaged over (NUM = 30) parallel events (left panel) and averaged over 100 parallel events (right panel); the color maps represent the local energy density while the arrows shows the initial flow at each of the cells. Even though the initial profiles are averaged over NUM= 30 parallel events, the distribution still captures the feature of event-by-event initial state fluctuations.

In Fig. 4.2 we investigate the dependence of the PHSD initial conditions on the equilibration time τ_0, at which the nonequilibrium evolution is switched to a hydrodynamical evolution in local thermal equilibrium. As expected, for larger initial times τ_0, the local initial flow increases and the local energy density decreases.

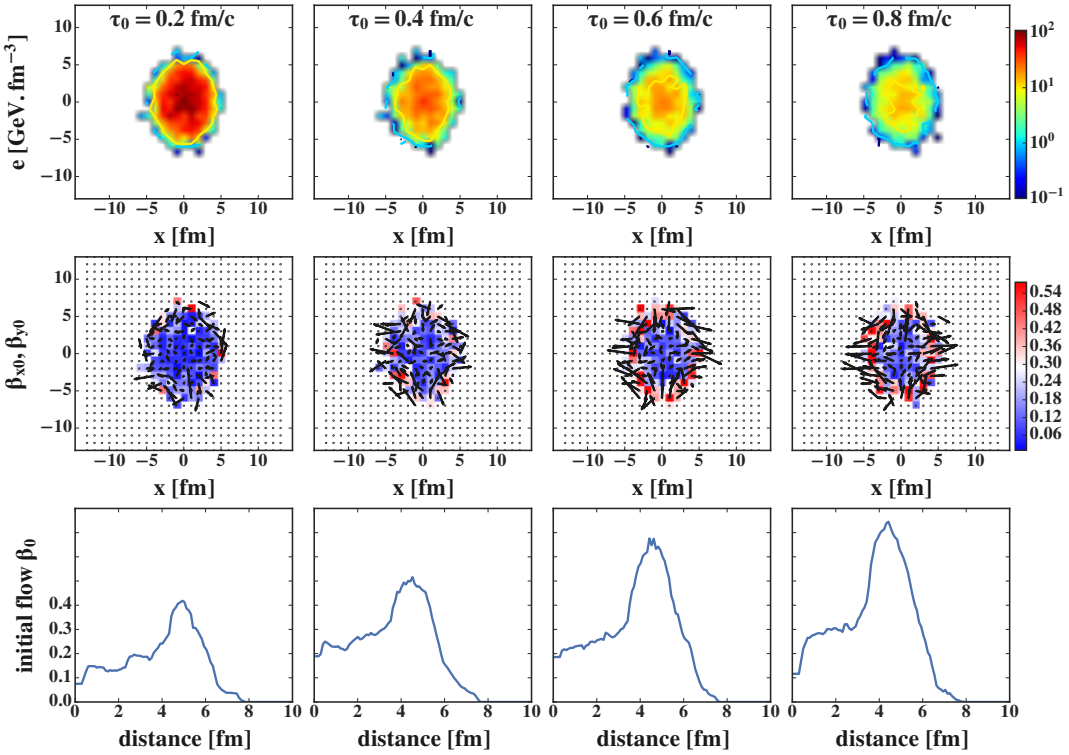

Figure 4.2 – Initial conditions of a peripheral Au+Au collision (b = 6fm) at $\sqrt{s_{NN}}$ = 200 GeV (calculated within the PHSD): **upper** contour: the local energy density in the transverse plane; **middle**: quiver plot of initial flow v_x, v_y in the transverse plane (colormap indicate the magnitude of local initial flow); **lower**: initial flow with respect to the distance of the cell from the center.

4.3 Medium evolution: hydrodynamics versus PHSD

In this section we compare the response of the hydrodynamical long-wavelength evolution with the PHSD initial conditions to the nonequilibrium PHSD evolution itself. To ensure a fair comparison, the temperature-dependent shear viscosity, which was determined in PHSD simulations [262], has been incorporated in the hydrodynamical model. This shear viscosity is shown in the left panel of Fig. 4.3: the blue and red symbols correspond to η/s obtained from the Kubo formalism and from the relaxation time approximation method, respectively. The black line

in Fig. 4.3 shows the parametrization of the PHSD $\eta/s(T)$, which is used in the viscous hydrodynamics for the present study. We note that the parametrized curve is very similar to the recently determined temperature dependence of η/s via Bayesian analysis of the available experimental data [263].

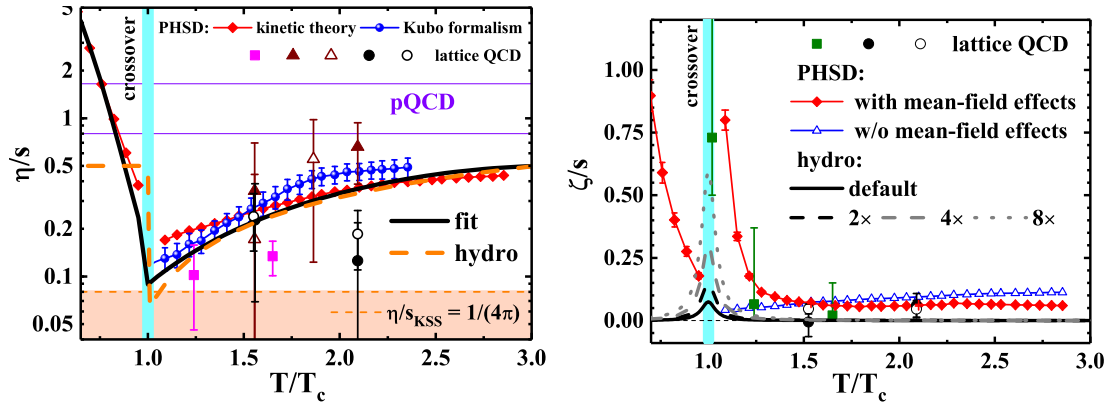

Figure 4.3 – η/s and ζ/s versus scaled temperature T/T_C: **Left:** The symbols indicate the PHSD results of η/s from Ref. [262], calculated using different methods: the relaxation-time approximation (red line+diamonds) and the Kubo formalism (blue line+dots); the black line corresponds to the parametrization of the PHSD results for η/s. The orange short dashed line demonstrates the Kovtun-Son-Starinets bound [264, 265] $(\eta/s)_{KSS} = 1/(4\pi)$. For comparison, the results from the virial expansion approach (green line) [266] are shown as a function of temperature, too. The orange dashed line is the η/s of the VISHNU hydrodynamical model that has been recently determined by Bayesian analysis; **Right:** ζ/s from PHSD simulation from Ref. [262] and the ζ/s that is adapted in the hydrodynamical simulations.

While the effect of shear viscosity on the hydrodynamical evolution has been studied extensively for simulations of heavy-ion collisions, the bulk viscosity has not been treated as carefully so far. This is because at higher temperatures the bulk viscosity should be very small, and vanish in the conformal limit. Moreover, an enhanced bulk viscosity at the pseudo-critical temperature causes problems for the applicability for hydrodynamics itself. Studies conducted for dynamical quasiparticle models, like the one used in PHSD, show that the magnitude and temperature behavior of the bulk viscosity depend on details of the parametrization of the equation of state and properties of the underlying degrees-of-freedom [230, 262]. For the relaxation time approximation in quasiparticle models slightly different values for the bulk viscosity are obtained [267, 268]. Given these uncertainties for the values of the bulk viscosity, we decided to use the bulk viscosity that has recently been determined by the Bayesian analysis of experimental data in the hydrodynamical simulations [263]. In the right panel of Fig. 4.3 we compare the ratio of bulk vis-

cosity to entropy density ζ/s that is adapted in the hydrodynamical simulations and the one extracted from PHSD simulations. It should be noted that the maximum ζ/s, that hydrodynamical model can handle, is much smaller than the bulk viscosity from PHSD simulations, and its effect on the momentum anisotropy will be discussed at the end of this section.

4.3.1 Pressure isotropization

In order to justify the choice of the initial time $\tau_0 = 0.6$ fm, we first check the evolution of the different pressure components extracted from the PHSD. This is illustrated in Fig. 4.4 which shows the evolution of the transverse and longitudinal pressures divided by the local energy density e in different cells along the x-axis extracted from PHSD as a function of time for a peripheral Au+Au collision at $\sqrt{s_{NN}} = 200$ GeV. These pressure components correspond to the eigenvalues of $T^{\mu\nu}(x)$ where the latter have been averaged in this case over 100 PHSD events in order to get a smooth evolution. One can see that the early stage of the heavy-ion collisions is highly anisotropic since the pressure components differ substantially from the isotropic pressure given by the EoS, implying large viscous corrections to the energy-momentum tensor. While the longitudinal pressure dominates, the transverse pressure starts from zero, grows with time and approximately reaches the isotropic pressure within a range of 0.3 to 1 fm/c. On the other hand, the longitudinal pressure decreases to very low values and remains small for large times. One of the reasons for this behavior is that we took only a few cells on the z-axis which correspond to a pseudorapidty gap $\Delta\eta \approx \mathcal{O}(10^{-2})$. By taking into account more cells in the longitudinal direction, the longitudinal pressure increases but the collective expansion cannot be removed properly in this case (as it has already been studied in Section 7 of Ref. [244]). By looking at more peripheral cells (bottom panel of Fig. 4.4), we can see that the pressure components deviate more from the isotropic pressure given by the EoS compared to more central cells (top panel of Fig. 4.4).

We illustrate in Fig. 4.5 the (non-)equilibrated regions in the PHSD simulation in the full transverse plane. We evaluated the relative value between the transverse pressure extracted from PHSD P_T (see Fig. 4.4 for the pressure components) and the pressure P given by the EoS. One can see that the central region in grey is rather equilibrated for all times ($(P_T - P)/P$ is around 0). The peripheral cells have a higher pressure when the initial condition for the hydrodynamical model is taken ($t = 0.6$ fm/c), and then fluctuate around the isotropic pressure as depicted by the red and blue colors. As a further check, we evaluated the inverse

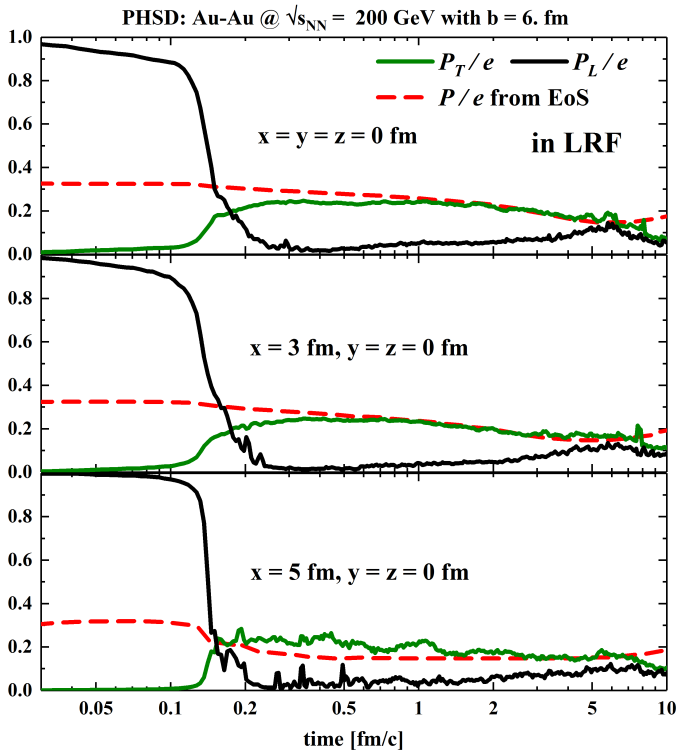

Figure 4.4 – Evolution of the ratio of the transverse P_T and longitudinal P_L pressures over the cell energy density e extracted from PHSD as a function of time for different cells along the x-axis in a peripheral ($b = 6$ fm) Au+Au collision at $\sqrt{s_{NN}} = 200$ GeV. Note that $T^{\mu\nu}$ has been averaged over 100 PHSD events.

Reynolds number in Fig. 4.6 defined as $R_\pi^{-1} = \sqrt{\pi^{\mu\nu}\pi_{\mu\nu}}/P$ which quantifies the applicability of fluid dynamics. One can see that at 0.6 fm/c the inverse Reynolds number is predominantly below 1 which reinforces this choice for the initialization time of the hydrodynamic simulation. We can therefore conclude that by averaging over the PHSD events, the medium reaches with time a transverse pressure comparable to the isotropic one as given by the lQCD EoS. This statement is of course not valid for a single PHSD event where the pressure components show a much more chaotic behavior and where the high fluctuations in density and velocity profiles indicate that the medium is in a nonequilibrium state, as we will see in the next section.

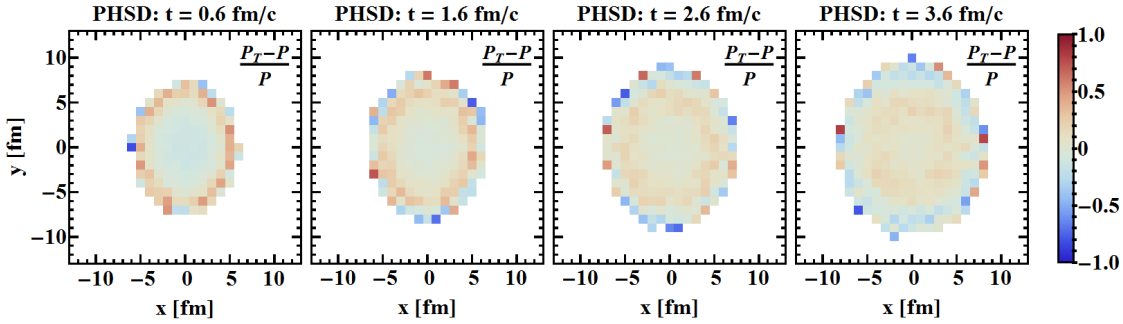

Figure 4.5 – Evolution of the relative value between the transverse pressure extracted from PHSD P_T (see also Fig. 4.4 for the pressure components) and the pressure P given by the EoS for different times in the transverse plane of a peripheral ($b = 6$ fm) Au+Au collision at $\sqrt{s_{NN}} = 200$ GeV. Note that $T^{\mu\nu}$ has been averaged over 100 PHSD events.

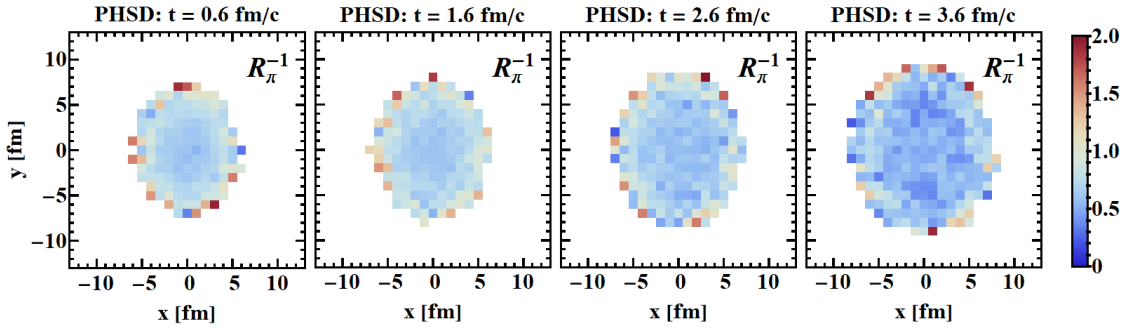

Figure 4.6 – Evolution of the inverse Reynolds number R_π^{-1} extracted from PHSD in the transverse plane of a peripheral ($b = 6$ fm) Au+Au collision at $\sqrt{s_{NN}} = 200$ GeV. Note that $T^{\mu\nu}$ has been averaged over 100 PHSD events.

4.3.2 Space-time evolution of energy density e and velocity $\vec{\beta}$

Starting with the same initial conditions (as discussed in section 4.2), the evolution of the QGP medium is now simulated by two different models: the nonequilibrium dynamics model – PHSD, and hydrodynamics – (2+1)-dimensional VISHNU. Fig. 4.7 shows the time evolution of the local energy density $e(x, y, z = 0)$ (from $T^{\mu\nu}$) (left) and the corresponding temperature T (right) as calculated using the lQCD EoS in the transverse plane from a single PHSD event (NUM = 30) at different times for a peripheral ($b = 6$ fm) Au+Au collision at $\sqrt{s_{NN}} = 200$ GeV.

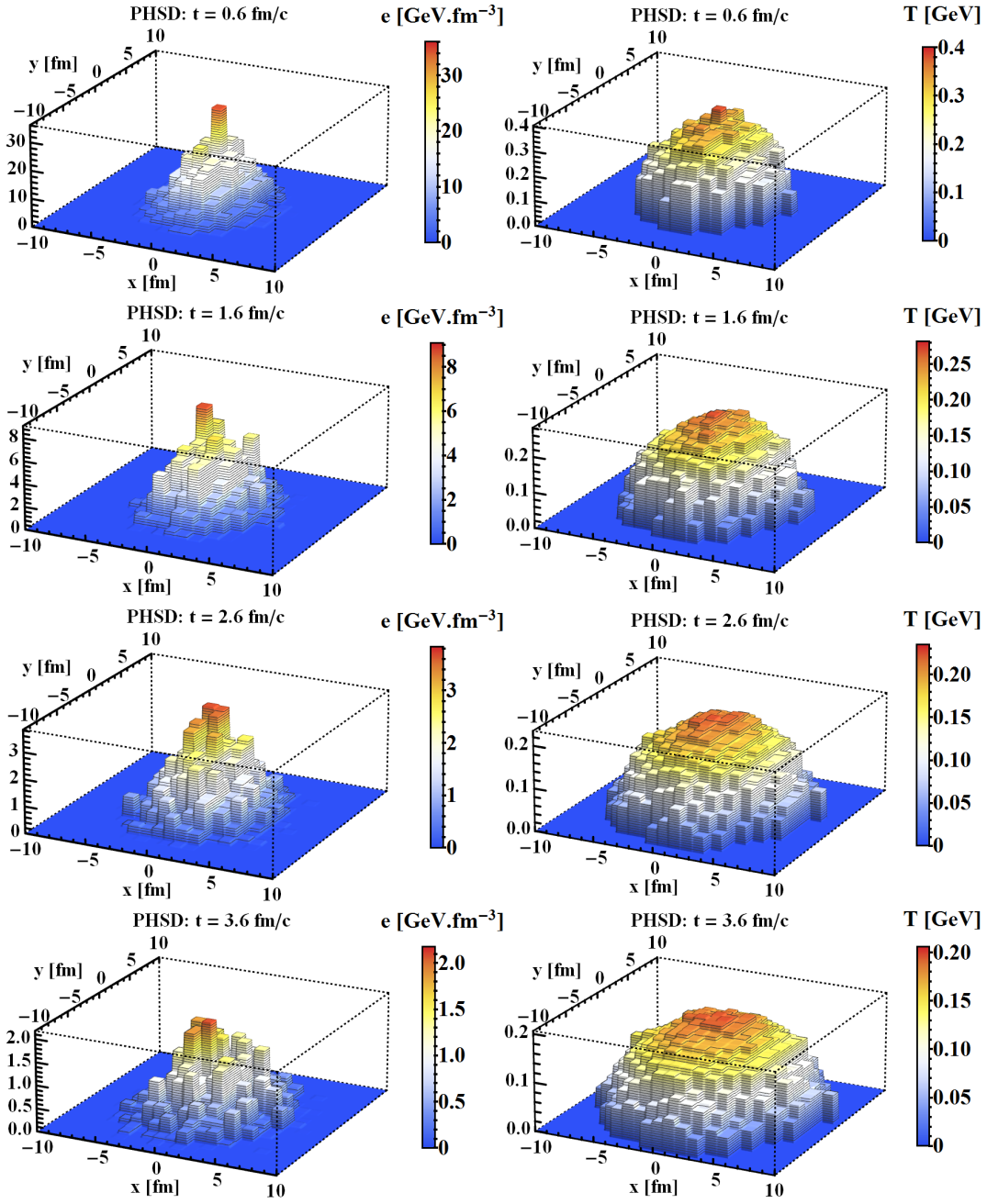

Figure 4.7 – Local energy density $e(x, y, z = 0)$ (left) and the corresponding temperature $T(x, y, z = 0)$ given by the EoS (right) in the transverse plane from a single PHSD event (NUM = 30) at different times for a peripheral (b = 6 fm) Au+Au collision at $\sqrt{s_{NN}} = 200$ GeV.

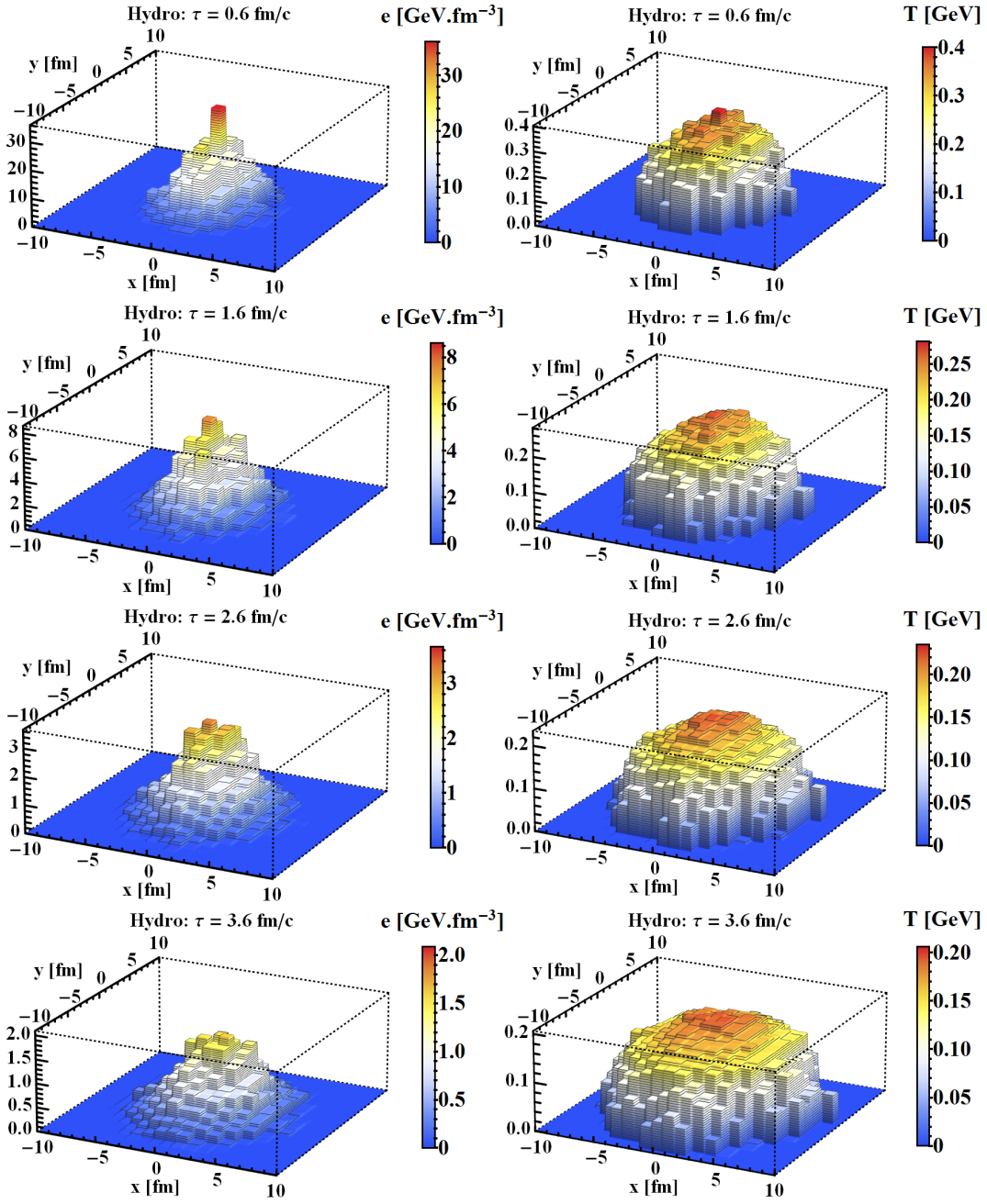

Figure 4.8 – Local energy density $e(x, y, z = 0)$ (left) and the corresponding temperature $T(x, y, z = 0)$ given by the EoS (right) in the transverse plane from a single hydrodynamical event at different proper times for a peripheral (b = 6 fm) Au+Au collision at $\sqrt{s_{NN}} = 200$ GeV.

As seen in figure 4.1 for $t = 0.6$ fm/c, the energy density profile is far from being smooth. Note also that the energy density decreases rapidly as the medium expands in the transverse and longitudinal directions. By converting the energy density to the temperature given by the lQCD EoS, we can see that the variations are less pronounced in that case. Fig. 4.8 shows the same quantities for a single event evolved through hydrodynamics. In particular for the energy density at later times one can already observe a significant smoothing compared to the PHSD evolution.

Fig. 4.9 shows the time evolution of the local energy density $e(x, y)$ in the transverse plane from a single PHSD event (NUM = 30) at different proper times for a peripheral Au+Au collision at $\sqrt{s_{NN}} = 200$ GeV, while Fig. 4.10 shows the same time evolution of $e(x, y)$ from a hydrodynamical evolution using the same initial condition as the PHSD event above. A comparison of the two medium evolutions shows distinct differences: in PHSD the energy density retains many small hot spots during its evolution due to its spatial non-uniformity. In hydrodynamics, the initial hot spots of energy density quickly dissolve and the medium becomes much smoother with increasing time. Moreover, as a result of the initial spatial anisotropy, the pressure gradient in x-direction is larger than that in y-direction, resulting in a slightly faster expansion in x-direction. We attribute these differences directly to the nonequilibrium nature of the PHSD evolution.

In Fig. 4.11 we show the time evolution of the velocity $\vec{\beta} = (\beta_x, \beta_y, \beta_z)$ in the transverse plane for the same PHSD initial condition evolved through PHSD and hydrodynamics. The longitudinal velocity β_z shown in the PHSD event remains on average approximately 0 and much smaller than the transverse flow since we only consider a narrow interval in the z-direction. At $\tau_0 = 0.6$ fm/c, the transverse flow has already developed and the transverse velocity can reach values of 0.5 at the edge of the profile. Even though the velocity increase with time in both PHSD and hydrodynamical events, it is clearly seen that the development of flow in a hydrodynamical event is much faster than in a PHSD event. In addition, local fluctuations in a single event are more visible in the PHSD event. Moreover, the velocities in x-direction is slightly larger than the one in y-direction in both events, as a result of the initial spatial anisotropy of the energy density, and that spatial anisotropy is converted into momentum anisotropy, which increases with time.

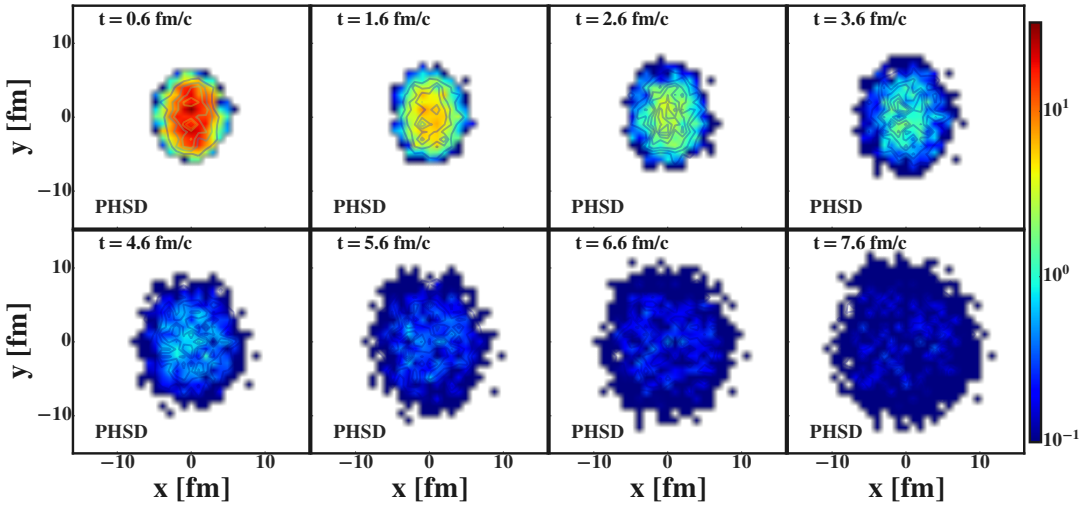

Figure 4.9 – Contour plots of the local energy density e in the transverse plane from the PHSD simulation of one event, for a peripheral Au+Au collision ($b = 6$ fm) at $\sqrt{s_{NN}}$ =200 GeV

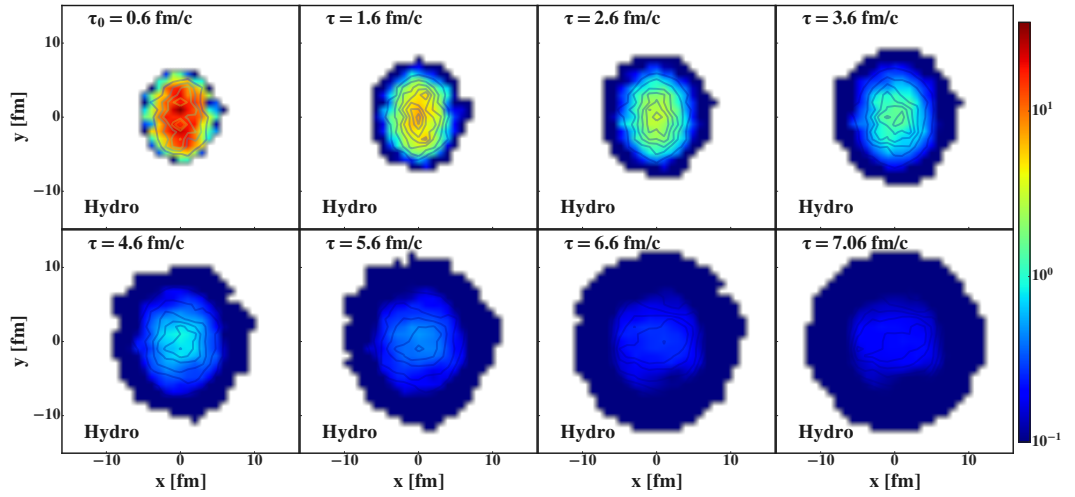

Figure 4.10 – Contour plots of the local energy density e in the transverse plane from the hydrodynamical simulation starting from the same initial conditions as in Fig. 4.9 including initial flow.

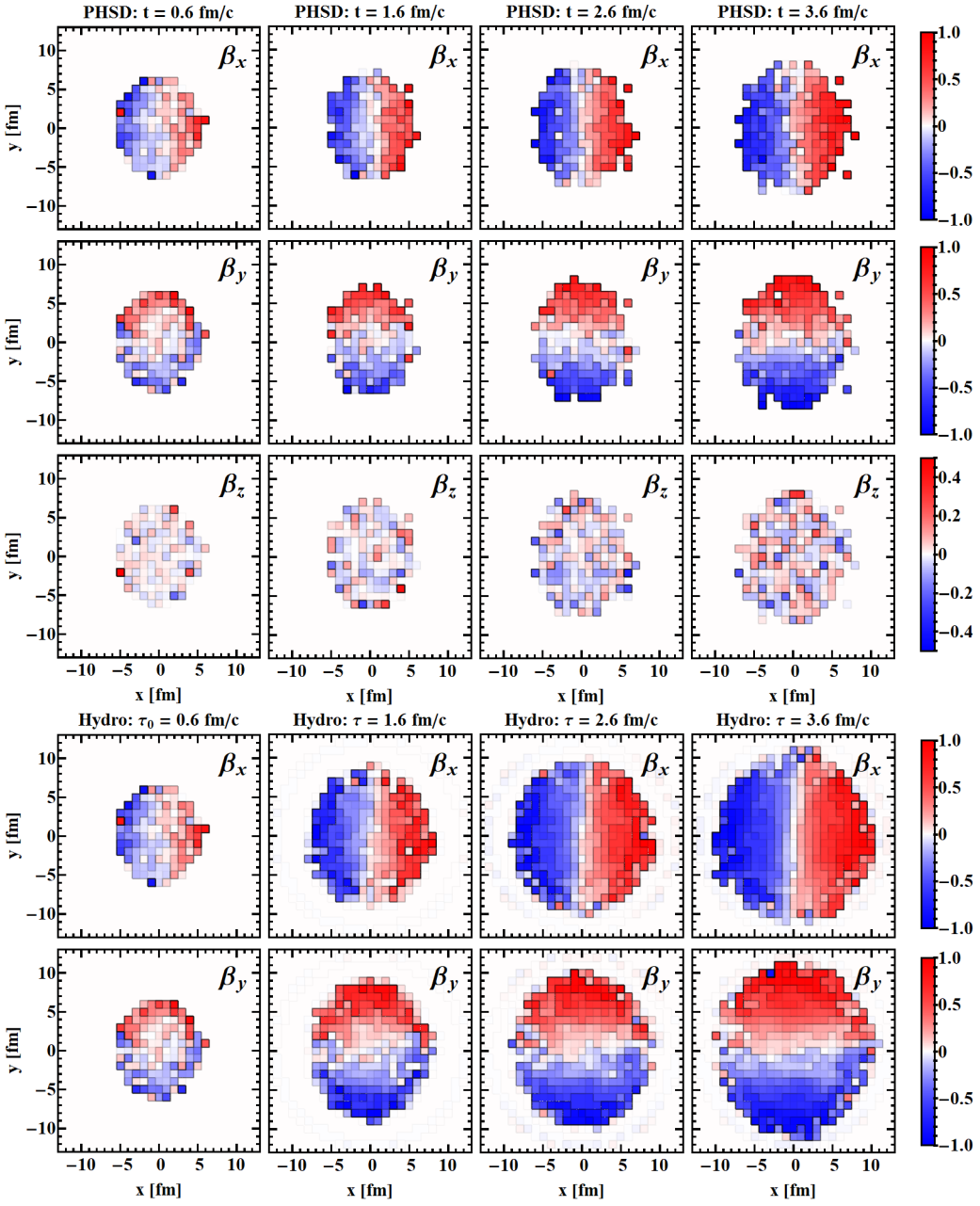

Figure 4.11 – Components of the 3-velocity $(\beta_x, \beta_y, \beta_z)$ in the transverse plane from a single PHSD event (NUM = 30) (top panel) and from a single hydrodynamical event (bottom panel) at different proper time for a peripheral (b = 6 fm) Au+Au collision at $\sqrt{s_{NN}} = 200$ GeV. β_z is scaled differently from β_x, β_y for better orientation.

4.3.3 Fourier images of energy density

The inhomogeneity of a medium can be quantified by the Fourier transform of the energy density, $\tilde{e}(k_x, k_y)$. For a discrete spatial grid with an energy distribution as $e(x, y)_{m\times n}$, the Fourier coefficients are given by

$$\tilde{e}(k_x, k_y) = \frac{1}{m}\frac{1}{n}\sum_{x=0}^{m-1}\sum_{y=0}^{n-1} e(x, y)e^{2\pi i(\frac{xk_x}{m}+\frac{yk_y}{n})}. \tag{4.9}$$

The zero mode $\tilde{e}_{k_x=0,k_y=0}$ is the total sum of the energy density, while higher order coefficients contain information about the correlations of the local energy density on different length scales. For a medium with large wave-length structures the higher-order coefficients should be suppressed and the typical global shape of the event should dominate. Given that our simulations in both PHSD and hydrodynamics are performed for the same centrality classes, we expect these structures to give similar Fourier coefficients for lower modes. However, if the structure of the fireball is dominated by smaller length scales, the higher Fourier modes are excited as well.

In Figs. 4.12 and 4.13 we present the Fourier transform $\tilde{e}(k_x, k_y)$ for a medium evolved by hydrodynamics and PHSD, respectively, for different stages of the evolution. For the hydrodynamical evolution only the dominant lower Fourier modes survive in the later stages (at the center of the plots) and shorter wavelength irregularities are washed out. On the other hand, short wavelength phenomena are seen at all times in the microscopic transport evolution of the PHSD; only the overall dilution of the medium reduces the strength.

This difference can be identified more easily in Fig. 4.14, where we plot the distribution of the Fourier coefficients $\langle\tilde{e}\left(\sqrt{k_x^2+k_y^2}\right)\rangle$ for different evolution times. For the lower order Fourier modes, which carry the information about the global event scale, the PHSD microscopically evolving medium and the hydrodynamical medium are identical. While the lower Fourier modes appear to be the same between the two approaches, we observe that the strength of the shorter wavelength modes rapidly decreases in the hydrodynamical evolution.

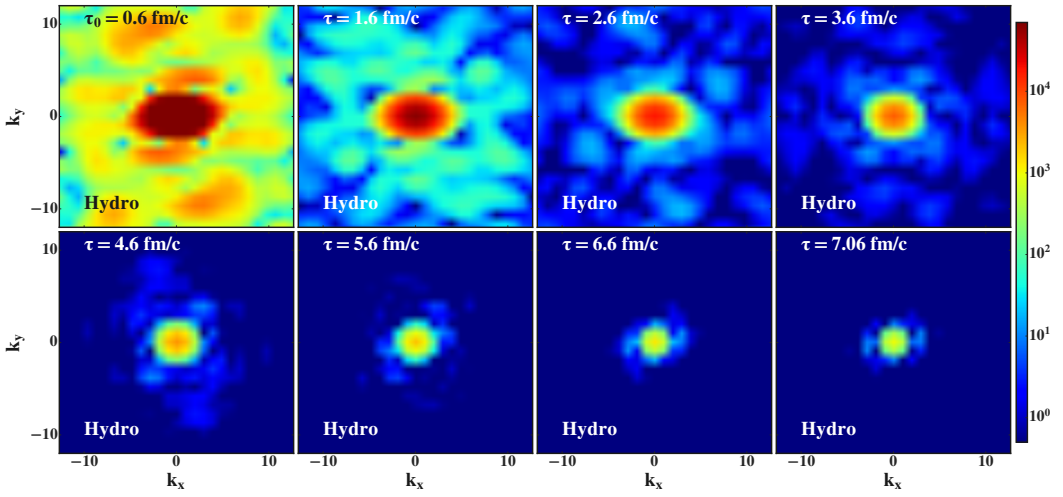

Figure 4.12 – Contour plots of the Fourier transform of the energy density $\tilde{e}(x, y, z = 0)$ for the simulation obtained within hydrodynamics as shown in Fig. 4.10.

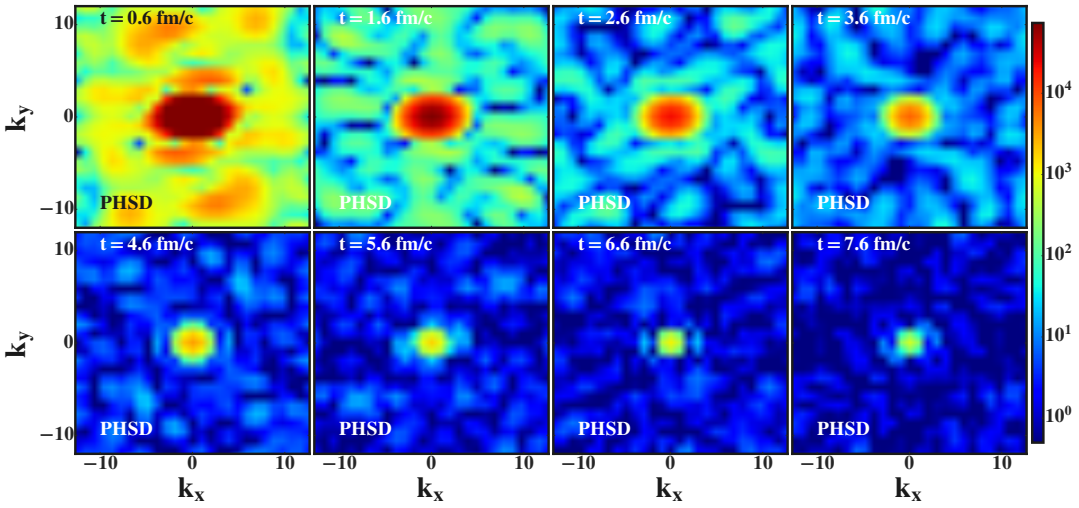

Figure 4.13 – Contour plots of the Fourier transform of the energy density $\tilde{e}(x, y, z = 0)$ for the simulation obtained within PHSD as shown in Fig. 4.9.

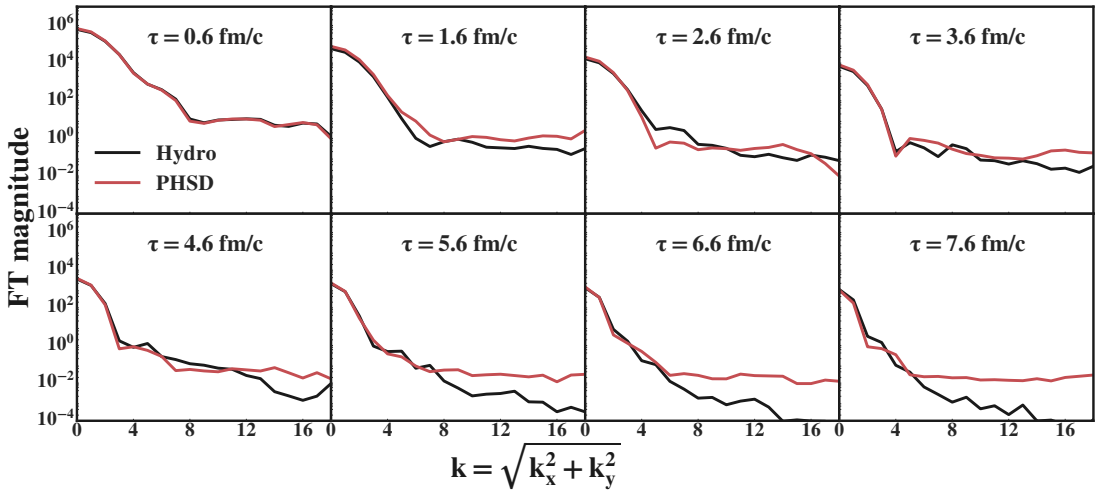

Figure 4.14 – Radial distribution of the Fourier modes of the energy density for different proper time in both PHSD and hydrodynamical events. The red lines correspond to the PHSD simulations and the black line corresponds to the hydrodynamical simulations.

4.3.4 Time evolution of the spatial and momentum anisotropy

Now we will focus on the medium's response to initial spatial anisotropies, which for the hydrodynamical models lead to substantial collective flow, measured by Fourier coefficients of the azimuthal particle spectra. Initial spatial gradients are transformed into momentum anisotropies via hydrodynamical pressure. While experimentally only the final state particle spectra are known, models for the space-time evolution of the medium can give insight into the evolution of the spatial and the momentum anisotropy. For hydrodynamical models the latter is directly related to the elliptic flow v_2. Similar statements apply to the PHSD transport approach where the initial spatial anisotropies are converted to momentum anisotropies [224].

The spatial anisotropy of the matter distribution is quantified by the eccentricity coefficients ϵ_n defined as

$$\epsilon_n \exp(in\Phi_n) = -\frac{\int r dr d\phi r^n \exp(in\phi) e(r,\phi)}{\int r dr d\phi r^n e(r,\phi)} \tag{4.10}$$

where $e(r,\phi)$ is the local energy density in the transverse plane. The second-order

coefficient ϵ_2 is also called ellipticity and to leading order is found to be the origin of the elliptic flow v_2. It can be simplified to

$$\epsilon_2 = \frac{\sqrt{\{r^2\cos(2\phi)\}^2 + \{r^2\sin(n\phi)\}^2}}{\{r^2\}} \tag{4.11}$$

where $\{...\} = \int dxdy(...)e(x,y)$ describes an event-averaged quantity weighted by the local energy density $e(x,y)$ [269].

The importance of event-by-event fluctuations in the initial state has been realized in particular for higher-order flow harmonics but also as a contribution to the elliptic flow and has been extensively investigated both experimentally and theoretically [270–272]. As shown earlier, the PHSD model naturally produces initial state fluctuations due to its microscopic dynamics. In the following, we apply event-by-event hydrodynamics implying that the hydrodynamic model has been initialized with individual PHSD events (100 for our case), and all subsequent quantities are averaged over many events.

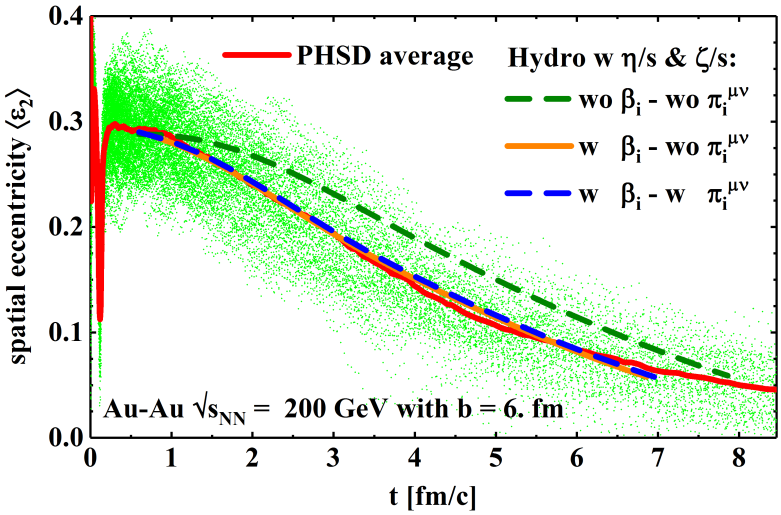

Figure 4.15 – Event-by-event averaged spatial eccentricity ϵ_2 of 100 PHSD events and 100 VISHNU events with respect to proper time, for a peripheral Au+Au collision ($b = 6$ fm) at $\sqrt{s_{NN}} = 200$ GeV. The green dots show the distribution of each of the 100 PHSD events used in this analysis. The solid red line is the average over all the green dots. The blue, yellow and black line correspond to hydrodynamical evolution taking different initial condition scenarios.

In Fig. 4.15 we show the time evolution of the ellipticity $\langle\epsilon_2\rangle$ for both medium

descriptions. One can see that for the PHSD simulations large oscillations in $\langle\epsilon_2\rangle$ are present at the beginning of the evolution due to the initialization geometries and formation times. After sufficient overlap of the colliding nuclei at the initial time τ_0 the average $\langle\epsilon_2\rangle$ is stabilized in PHSD. There are, however, still significant event-by-event fluctuations of this quantity at all times and strong variations between individual events. Moreover, we indicate that even if each individual hydrodynamical event deviates from the average, the ellipticity remains a smooth function of time. Due to the faster expansion in x-direction the initial spatial anisotropy decreases during the evolution for both medium descriptions. However, the spatial anisotropy decreases faster when initial pre-equilibrium flow β_i (extracted from the early PHSD evolution) is included in the hydrodynamical evolution. In this case, the time evolution of the event-by-event averaged spatial anisotropy is very similar in PHSD and in hydrodynamics. We mention that initializing with the shear-stress tensor $\pi_i^{\mu\nu}$ induced slight effects on the spatial eccentricity but not large enough to be visible.

A similar feature is also seen in the evolution of the momentum ellipticity, which is directly related to the integrated elliptic flow v_2 of light hadrons. The total momentum ellipticity is determined from the energy-momentum tensor as [249, 273]:

$$\epsilon_p = \frac{\int dxdy(T^{xx} - T^{yy})}{\int dxdy(T^{xx} + T^{yy})}. \tag{4.12}$$

Here the energy-momentum tensor includes the viscous corrections from the shear stress tensor $\pi^{\mu\nu}$ and the bulk viscous pressure Π.

In the upper panel of Fig. 4.16 we show the time evolution of the event-by-event averaged $\langle\epsilon(p)\rangle$ for the hydrodynamical medium description with and without pre-equilibrium flow in the initial conditions. Including the initial flow leads to a finite momentum anisotropy at τ_0 which subsequently increases as the pressure transforms the spatial anisotropy in collective flow. Consequently, ϵ_p is larger than in the scenario without initial flow throughout the entire evolution of the medium and an enhanced elliptic flow can be expected. Given the unresolved question of bulk viscosity in heavy-ion collisions, we investigate the effect of tuning the bulk viscosity from the standard value discussed at the beginning of this section to four times of this value, which comes closer to the bulk viscosity found in the DQPM. We see that for an enhanced bulk viscosity around T_c the momentum anisotropy develops a bump at later times, which is more pronounced for larger bulk viscosity.

In the lower panel of Fig. 4.16 the hydrodynamical simulation is compared to the results from PHSD, again for event-by-event averaged quantities and the

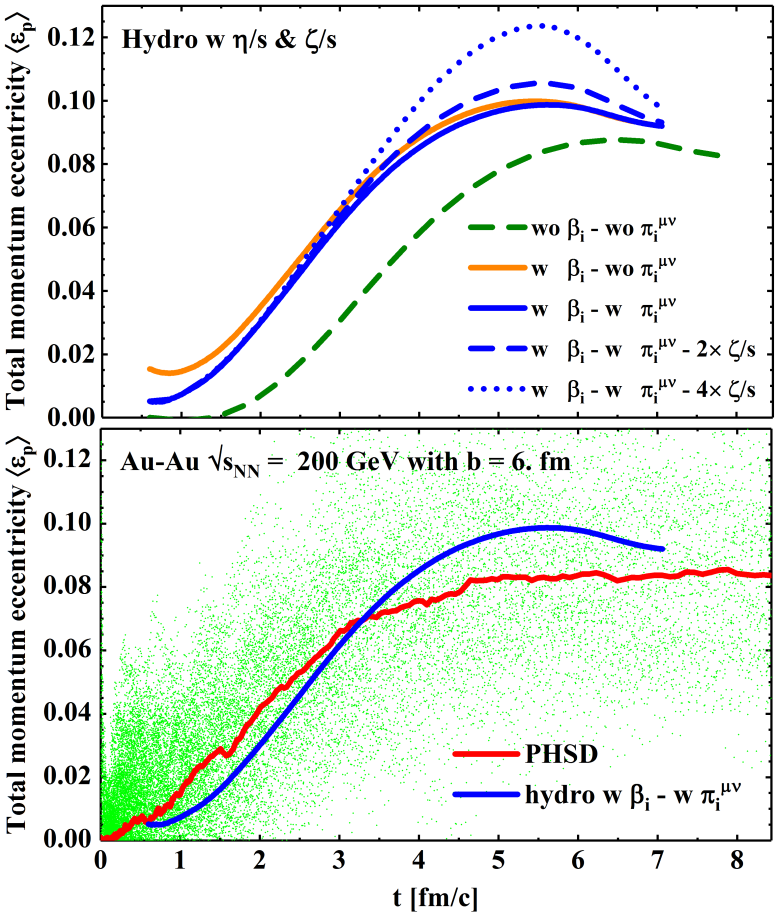

Figure 4.16 – Event-by-event averaged total momentum anisotropy of 100 PHSD events and 100 VISHNU events with respect to proper time, for a peripheral Au+Au collision ($b = 6$ fm) at $\sqrt{s_{NN}} = 200$ GeV. **Left:** the total momentum eccentricity of hydrodynamical evolution for different initial scenarios, as well as different bulk viscosity adapted in the hydrodynamical simulation. **Right:** comparison of the total momentum eccentricity from PHSD events compared with the standard hydrodynamical events. The green dots show the distribution of each of the 100 PHSD events used in this analysis. The solid red line is an average over the green dots. The black line corresponds to the standard hydrodynamical evolution taking the 100 initial conditions which are generated from PHSD events.

event-by-event fluctuations indicated by the spread of the green points. The PHSD momentum eccentricity is constructed by Eq. (4.12) where $T^{\mu\nu}$ is evaluated from Eq. (4.4). It can be observed that before τ_0 the averaged momentum anisotropy in PHSD develops continuously during the initial stage, before it reaches the value which is provided in the initial conditions for hydrodynamics. Despite the seemingly

large bulk viscosity, as discussed in the beginning of this section, the momentum anisotropy in PHSD does not show any hint of a bump like in the hydrodynamical calculation. The response to intrinsic bulk viscosity in a microscopic transport model does not seem to be as strong as in hydrodynamics.

4.4 Summary

In this chapter, we performed a comparison of two commonly used models for the evolution of a QGP medium in relativistic heavy-ion collisions, the microscopic off-shell transport approach PHSD and the macroscopic hydrodynamical VISHNew model. Both approaches give an excellent agreement with numerous experimental data, despite the very different assumptions inherent in these models. In PHSD, quasiparticles are treated in off-shell transport with thermal masses and widths which reproduce the lattice QCD equation of state. Hydrodynamics assumes local equilibrium to be reached in the initial stages of heavy-ion collisions and transports energy-momentum and charge densities according to the lattice QCD equation of state and transport coefficients such as the shear and bulk viscosity. We have tried to match the hydrodynamical evolution as closely as possible to these quantities as obtained within PHSD:

1. by construction the equation of state in PHSD is compatible with the lQCD equation of state used in the hydrodynamical evolution,
2. a new Landau-matching procedure was used to determine initial conditions for hydrodynamics from the PHSD simulation,
3. the hydrodynamical simulations utilize the same $\eta/s(T)$ as obtained within PHSD, in equilibrium,
4. different bulk viscosity parameterizations have been introduced in the hydrodynamical simulation that resemble those obtained in (dynamical) quasiparticle models, which are the basis for PHSD simulations.

In general we find that the ensemble averages over PHSD events follow closely the hydrodynamical evolution. The major differences between the macroscopic near-(local)-equilibrium and the microscopic off-equilibrium dynamics can be summarized as:

1. A strong short-wavelength spatial irregularity in PHSD at all times during the evolution versus a fast smoothing of initial irregularities in the hydrodynamical evolution such that only global long-wavelength structures survive.

These structures have been calculated on the level of the fluid velocity and energy density and quantified in terms of the Fourier modes of the energy density. Due to the QCD equation of state the irregularities imprinted in the temperature are smaller than in the energy density itself.

2. The hydrodynamical response to changing transport coefficients, especially the bulk viscosity, has a strong impact on the time evolution of the momentum anisotropy. In PHSD these transport coefficients can be determined but remain intrinsically linked to the interaction cross sections. Although there are indications for a substantial bulk viscosity in PHSD, it does not show the same sensitivity to the momentum space anisotropy as in hydrodynamical simulations.

3. Event-by-event fluctuations might be of similar magnitude in quantities like the spatial and momentum anisotropy but while they remain smooth functions of time in hydrodynamics significant variations are observed within in a single event in PHSD as a function of time.

Chapter 5

Initial condition for the Quark-Gluon Plasma

* * *

The theoretical modeling of heavy-ion collisions is based on effective approaches due to their nonperturbative and nonequlibrium nature. These approaches range from hydrodynamical models with different initial conditions [104, 242, 273–281] to various kinetic approaches [187, 225, 226, 234, 282–290] or different types of hybrid models [291–298], which involve the use of a hydrodynamical stage for the description of the Quark-Gluon Plasma (QGP). As we have seen in the previous chapter, hydrodynamical calculations need initial conditions for the energy-momentum tensor - given at some finite starting time of the order of 0.5 fm/c - to start the evolution of the QGP. These initial conditions are usually generated from the Glauber model or from other initial state scenarios such as the IP-glasma model [299, 300]. The latter includes characteristics of the color glass condensate (CGC) [301–303] - a classical configuration of low-x gluons - which is expected at relativistic energies and leads to structures of smaller scale compared to the Glauber model. However, during a hydrodynamical evolution of the QGP, nothing can be said about the nature of the microscopic degrees of freedom since only the equation of state and transport coefficients are needed. Only microscopic approaches can allow us to bridge the gap from $p-p$ to $p-A$ and $A-A$ collisions in

This work was done in collaboration with Olena Linnyk who calculated and illustrated the results for electromagnetic observables, whereas the remaining parts were performed by myself.

a unique way without introducing additional parameters.

In this chapter, we explore within the PHSD the sensitivity of hadronic and electromagnetic observables to the explicit initial degrees of freedom under the constraint of an identical energy-momentum tensor $T^{\mu\nu}(x)$ in the nonequilibrium phase just after the passage of the two nuclei (5% central Au-Au collisions at $\sqrt{s_{NN}} = 200$ GeV). For that purpose, we will investigate two different scenarios for the initial production of the QGP: the scenario I consists of a purely gluonic initial state as proposed more than two decades ago in Refs. [201, 304–307] since at that time a first-order phase transition from hadronic to partonic matter had been expected. This scenario was recently brought forward again in Ref. [308, 309] due to a possibly gluon dominated initial state. The scenario II describes the initial QGP stage with only quark and antiquark degrees of freedom (without gluons). We start this chapter by explaining the implementation of the initial gluonic degrees of freedom and then by studying the time evolution of the number of quarks and gluons in central Au+Au collisions at $\sqrt{s_{NN}} = 200$ GeV. After that, we will confront our two scenarios to various experimental data such as hadronic spectra, flow coefficients, and electromagnetic observables.

5.1 Extensions to gluonic initial states

To realize the initial gluonic state (scenario I) in the PHSD under the constraint of keeping the same energy-momentum tensor $T^{\mu\nu}$ as in the default PHSD simulations, we fuse the newly produced flavor neutral quark and antiquark pairs of closest distance in phase space to massive gluons. This gluonic fusion happens at the same time as the QGP is produced in conventional PHSD simulations, which is above the critical local energy denstity $\epsilon_c = 0.5$ GeV fm^{-3} according to unquenched lattice QCD simulations. We note that this conversion process from quark-antiquark pairs to the formation of gluons is the same as in the default PHSD, however, the proportion of quarks and antiquarks (as defined by the DQPM [120, 191]) is much larger compared to gluons due to their lighter masses, i.e. $M_q \approx 2/3 M_g$. Therefore, the default PHSD is much closer to the scenario II which only contains quark and antiquarks at the beginning of the QGP phase. To realize this second scenario the gluons, which are produced in the conventional PHSD, immediately decay to a quark and antiquark pair according to their spectral function from the DQPM.

5.1.1 Parton abundancies

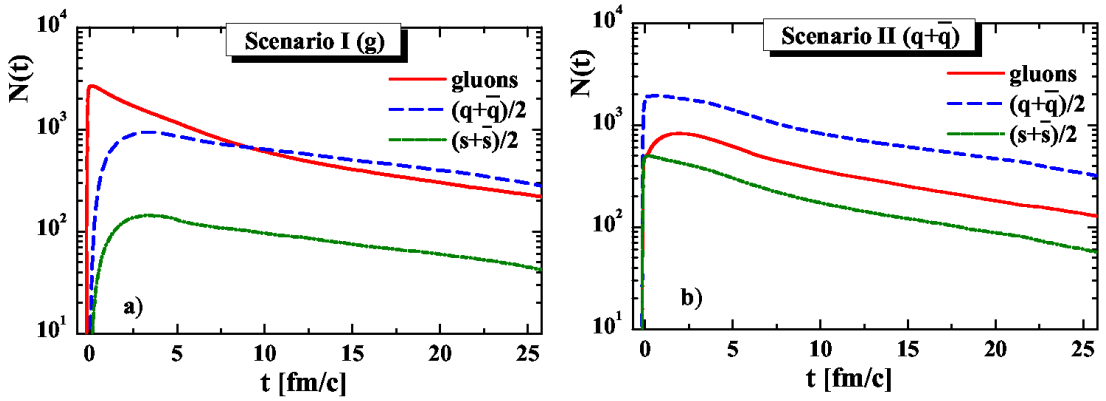

Figure 5.1 – (a) Time evolution of the gluon number (red solid line) as well as the total quark+antiquark number (divided by 2) (dashed blue line) and strange+antistrange quark number (divided by 2) (dot-dashed green line) as a function of time t for a central ($b = 2$ fm) Au-Au collision at $\sqrt{s_{NN}} = 200$ GeV in logarithmic representation for the scenario I (gluonic initial conditions). (b) Same quantities as in (a) but for the scenario II (fermionic initial conditions).

We illustrate our two different scenarios in Fig. 5.1 by the time evolution of the gluon number (solid red line) as well as the total quark+antiquark number (divided by 2) (dashed blue line) and strange+antistrange quark number (divided by 2) (dot-dashed green line) as a function of time t for a central ($b = 2$ fm) Au+Au collision at $\sqrt{s_{NN}} = 200$ GeV. One can see that in the first scenario the initial plasma stage is only populated by gluons, which then decay in time to quark-antiquark pairs produced by the gluon splitting. Consequently, the appearance of quarks is delayed and it takes approximately a time of 5 fm/c such that the population of quarks overtakes the one from the gluons. The early decrease of the gluon population is roughly exponential and one can therefore attribute a transition time τ_g to this decay which in our case appears to be around $\tau_g \approx 6-8$ fm/c, the latter being in line with the Boltzmann approach to multiparton scatterings (BAMPS) calculations from Ref. [288–290]. The second panel of Fig. 5.1 shows the parton evolution for the second scenario, where as expected, the early times are dominated by light and strange quarks, whereas gluons are formed with time during the first 2-3 fm/c.

In the scenario I the gluon decay to quark-antiquark pairs happens in accord with the gluon spectral function in PHSD that has a typical width of 100 to 150

MeV, implying that the decay rate is rather 'slow' (on timescales of 1.5 to 2 fm/c). Furthermore, the gluon decay depends on the final phase space and thus on the light or strange quark masses. For the initial times this leads to a ratio of strange to light quarks of about 1/3, however, the quarks appear with a delay time of 1.5-2 fm/c relative to the gluons (cf. Fig. 5.1) which is large compared to the average formation time of partons of 0.2-0.3 fm/c in the scenario II. We recall that the concept of string melting in the QGP also implies a ratio of the strange to light quarks of $\sim 1/3$ [9]. One might claim that these widths might be substantially underestimated in the DQPM (or PHSD) but for substantially larger widths the ratio of the shear viscosity over entropy density η/s or the electric conductivity σ would drop by the same factors and no longer be in accord with results from lattice QCD (cf. the review [136]).

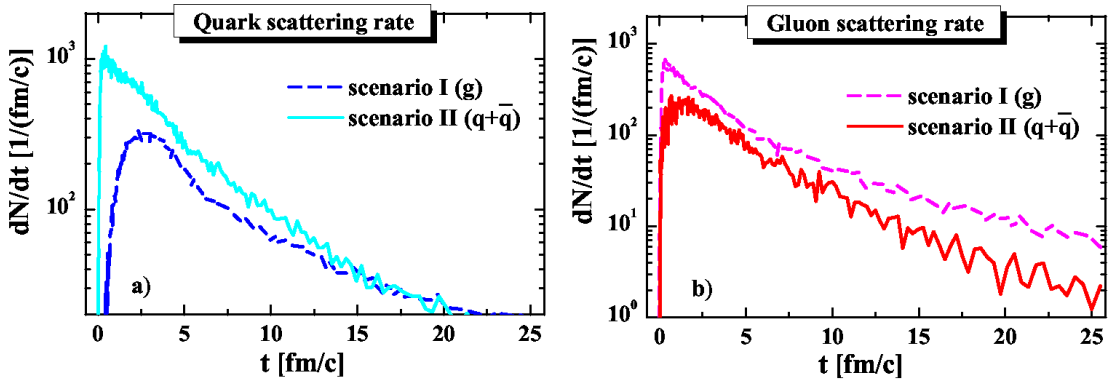

Figure 5.2 – (a) The quark interaction rate dN_q/dt from PHSD as a function of time t for a central ($b = 2$ fm) Au-Au collision at $\sqrt{s_{NN}} = 200$ GeV in the scenario I (lower dark blue dashed line) and scenario II (light blue upper line). (b) Same quantities as in (a) but for the gluon interaction rate dN_g/dt (see legend).

To further investigate the actual dynamics, we display the quark interaction rate dN_q/dt (a) and the gluon interaction rate dN_g/dt (b) for both scenarios in Fig. 5.2 for the same collisional system. As one can see, the quark interaction rate is substantially suppressed in the scenario I while the gluon interaction rate is suppressed in the scenario II. Without explicit representation we mention that the hadronization rate is slightly larger in the scenario II than in the gluonic scenario I.

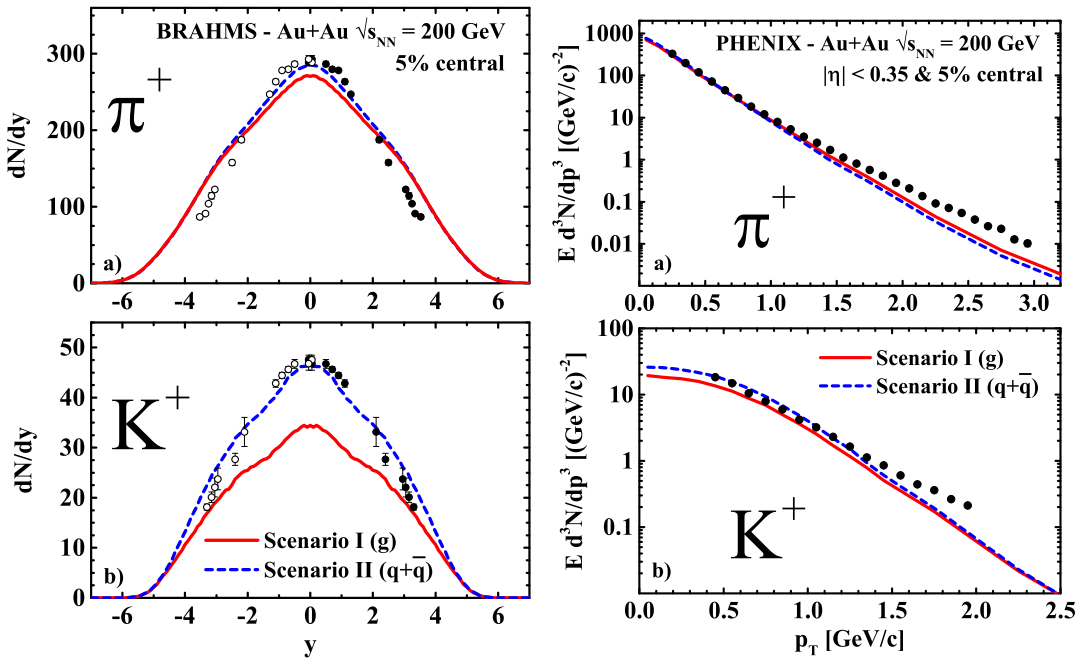

Figure 5.3 – Left: Rapidity distributions for π^+ (a) and K^+ (b) mesons from PHSD for the scenarios I and II in comparison to the results of the BRAHMS Collaboration [310] for 5% central Au-Au collisions at $\sqrt{s_{NN}} = 200$ GeV. Right: Transverse momentum spectra for π^+ (a) and K^+ (b) mesons from PHSD for the scenarios I and II in comparison to the results of the PHENIX Collaboration [311] for 5% central Au-Au collisions at $\sqrt{s_{NN}} = 200$ GeV.

5.2 Comparison to experimental data

In this Section we show the PHSD results employing the two different initial state scenarios (I with gluons and II with quarks and antiquarks), in comparison to experimental data from Au-Au collisions at $\sqrt{s_{NN}} = 200$ GeV. We mention that the results for the default PHSD, which can be found later in this dissertation, are closer to the ones obtained from the scenario II consisting of a quark-antiquark initial plasma stage.

5.2.1 Hadronic observables

We start with 5% central Au-Au collisions at $\sqrt{s_{NN}} = 200$ GeV and compare in the left-hand side of Fig. 5.3 the rapidity distributions for π^+ and K^+ mesons

from the scenarios I (red lines) and II (blue dashed lines) with the data from the BRAHMS collaboration [310]. As expected in the previous section, considering the very similar number of light quarks at late times in both scenarios, one only finds a small difference in the pion rapidity distribution. However, the K^+ distribution is sizeably underestimated in the scenario I since the strange and antistrange quarks are not present at all in the beginning of the collision. Considering that the strangeness equilibration time for the partonic energies of interest in the PHSD (of the order of 20-30 fm/c [192]) is long compared to the QGP lifetime, strange quarks cannot equilibrate in the system studied here. We show in the right-hand side of Fig. 5.3 the transverse momentum spectra of the same particles in comparison to the experimental data from Ref. [311]. One can see that the slopes are quite similar for both scenarios.

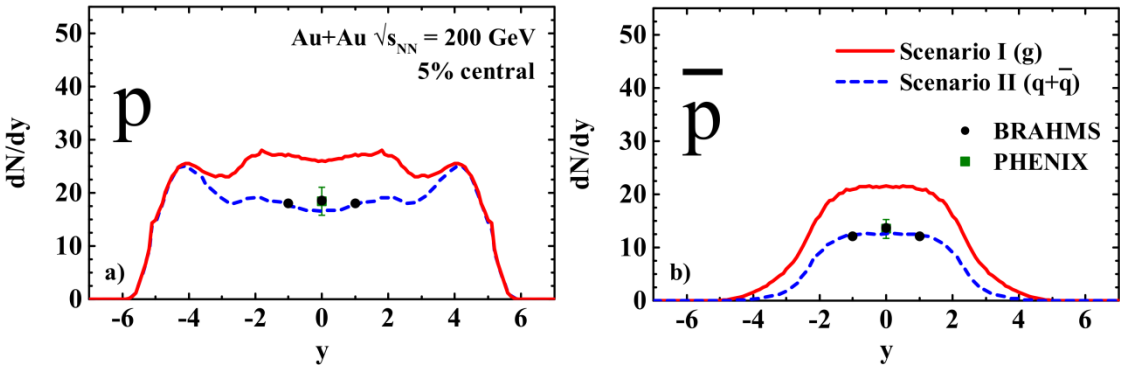

Figure 5.4 – The rapidity distribution of protons (a) and antiprotons (b) for 5% central Au-Au collisions at $\sqrt{s_{NN}} = 200$ GeV from the scenarios I and II in comparison to the experimental data from the BRAHMS [312] and PHENIX collaboration [311] (the data as well as calculations are without including the feeddown from strange baryons).

The results for the proton and antiproton rapidity distributions are displayed in Fig. 5.4 for 5% central Au+Au collisions at $\sqrt{s_{NN}} = 200$ GeV in the two scenarios and demonstrate that the scenario II with quarks and antiquarks in the initial state is clearly favored by the data from the BRAHMS [312] and PHENIX [311] collaborations.

The collective dynamics, however, might show a different picture since the elliptic flow v_2 is driven by collisions as well as the repulsive scalar partonic potential as defined by the DQPM. Fig. 5.5 shows the elliptic flow $v_2(p_T)$ and $v_2(y)$ of charged hadrons for Minimum Bias Au-Au collisions at $\sqrt{s_{NN}} = 200$ GeV in comparison with the results from the two scenarios. Unfortunately, almost no differences are

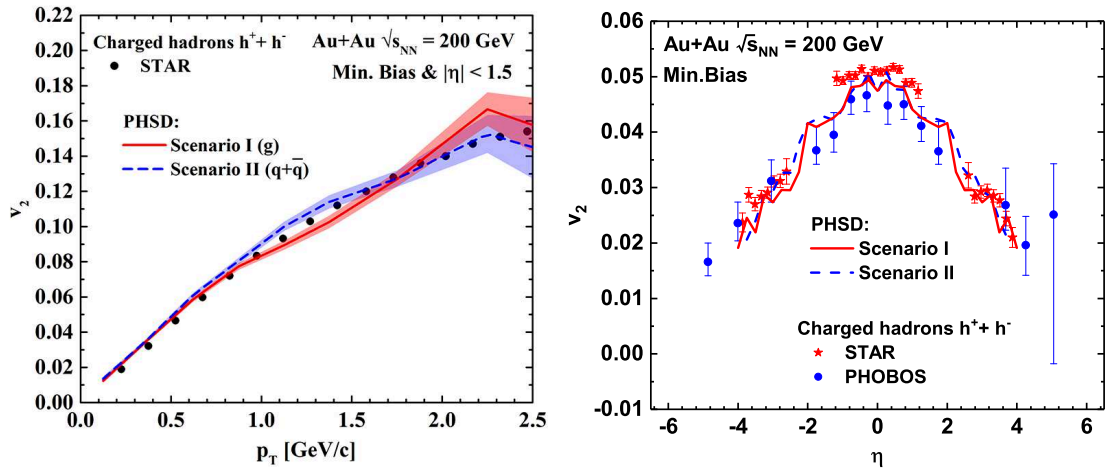

Figure 5.5 – The elliptic flow $v_2(p_T)$ (left) and $v_2(\eta)$ (right) of charged hadrons for Minimum Bias Au-Au collisions at $\sqrt{s_{NN}} = 200$ GeV from the scenarios I and II in comparison to the experimental data from the STAR collaboration [313, 314].

seen here and both results appear to be compatible with the STAR and PHOBOS data from Refs. [313, 314].

5.2.2 Electromagnetic observables

The electric field, which is generated by the spectator protons and therefore only present at the very early stage of heavy-ion collisions, can influence the trajectory of electric partonic charges. In particular, it was suggested in Ref. [315] by Voronyuk et al. that asymmetric nucleus-nucleus collisions can be studied to reveal the content of the initial plasma phase of heavy-ion collisions since in that case, the produced electric field leads to different directed flows of particles and antiparticles (of opposite electric charge). Unfortunately, in symmetric nucleus-nucleus collisions the electric field approximately cancels in the center of the partonic medium. However, electromagnetic observables such as dileptons or photons should be sensitive to the initial degrees of freedom of the QGP. Especially, the production of energetic photons by $q + \bar{q}$ annihilation should be substantially suppressed in the scenario I [316, 317] as compared to scenario II where quarks and antiquarks are present almost from the very beginning. Since also intermediate mass dileptons were found to be dominated by the $q + \bar{q}$ annihilation [318, 319], this expectation should also hold for the virtual photons. The quark–antiquark annihilation $q + \bar{q} \to g + \gamma$ and the gluon Compton scattering processes $q(\bar{q}) + g \to q(\bar{q}) + \gamma$ are diagrammatically presented in Fig. 5.6.

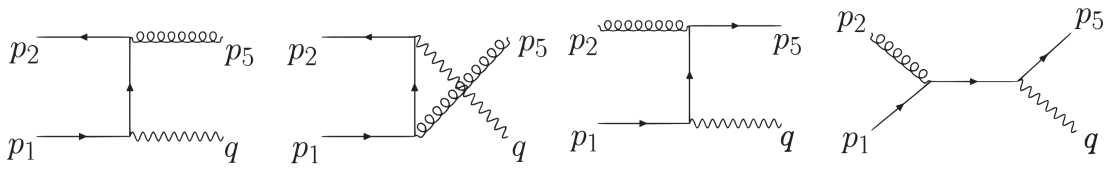

Figure 5.6 – Feynman diagrams for the leading partonic sources of thermal photons $q+\bar{q} \to g+\gamma$ (quark-antiquark annihilation) and $q(\bar{q})+g \to q(\bar{q})+\gamma$ (gluon Compton scattering) included in the PHSD calculations (from Ref. [320]).

In order to quantify this expectation we have performed PHSD calculations for the scenarios I and II following up the previous studies in Refs. [318, 319, 323–325] where all the details of the calculations are presented. We recall that also the computation of the electromagnetic radiation from partons has been evaluated with the DQPM propagators such that no new parameter enters these calculations (cf. Ref. [136] for a review). In Fig. 5.7 we show the corresponding PHSD results for the two scenarios in comparison to the thermal photon data from PHENIX [321, 322] for 0-20% centrality (a) and 20–40% centrality (b). The partonic photon contribution from $q-\bar{q}$ annihilation and Gluon Compton scattering is displayed in terms of the green dashed lines for scenario II and the dash-dot purple lines for the scenario I. The solid red lines reflect the thermal photon spectrum when adding the hadronic channels – dominated by mm and mB bremsstrahlung – for the scenario I while the dash-dotted blue line represents the same quantity for the scenario II. We find that the partonic contribution is about an order of magnitude larger in the scenario II than in the gluonic scenario I, however, when adding up all contributions only a moderate depletion of the spectrum is visible for $p_T > 2$ GeV/c which is below the PHENIX data at the largest transverse momenta. Note, however, that the thermal photon yield is slightly underestimated by the PHSD calculations for the most central collisions. Accordingly, the present photon data do not clearly differentiate between the two scenarios. In addition, the panel c) in Fig. 5.7 shows a comparison of the elliptic flow $v_2(p_T)$ for the scenario I (solid red line) and the scenario II (dashed blue line) with the PHENIX data. Here the hatched area displays the statistical uncertainty of the PHSD calculations. Nevertheless, there is a clear tendency for a larger photon v_2 in the scenario I which is readily understood in terms of a reduced and delayed production of photons in the QGP phase where the photons are emitted from quark and antiquark channels that have achieved a finite v_2 due to the strong gluon-gluon interactions before.

We now turn to dileptons where the virtuality (invariant mass) of the lepton pair serves as an additional degree of freedom. In the left-hand side of Fig. 5.8

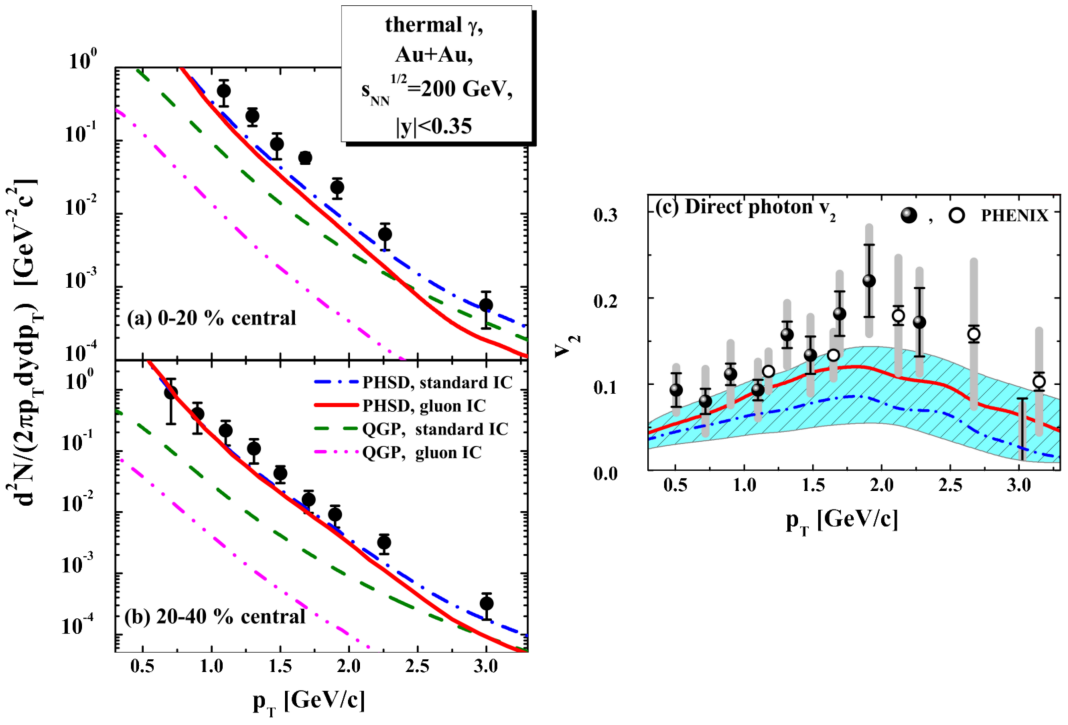

Figure 5.7 – The thermal photon yield from partonic channels versus transverse momentum p_T from PHSD (at midrapidity) in the scenarios I (lower dash-dot purple lines) and II (dashed green lines) for Au-Au reactions at $\sqrt{s_{NN}} = 200$ GeV for 0-20% centrality (a) and 20–40% centrality (b). The solid red lines reflect the thermal photon spectrum when adding the hadronic channels – dominated by mm and mB bremsstrahlung – for the scenario I while the dash-dotted blue lines represent the same quantity for the scenario II. The data for the thermal photons are from the PHENIX collaboration [321, 322]. The panel c) shows a comparison of the elliptic flow $v_2(p_T)$ for the scenario I (solid red line) and the scenario II (dashed blue line) with the PHENIX data. The hatched area displays the statistical uncertainty of the PHSD calculations.

we show a comparison of the QGP di-electron contribution as a function of the invariant mass for the scenario I (solid red line) and the scenario II (dash-dot blue line). Since the dilepton yield at higher masses (> 1 GeV) is dominated by $q - \bar{q}$ annihilation we find a large difference between the two scenarios which increases with the invariant mass M. Depending on the background yield and possible subtraction, the e^+e^- yield from 1.2 GeV $< M <$ 3 GeV should qualify as a proper observable to distinguish the two scenarios.

In the right-hand side of Fig. 5.8 we compare the mass spectra of e^+e^- pairs

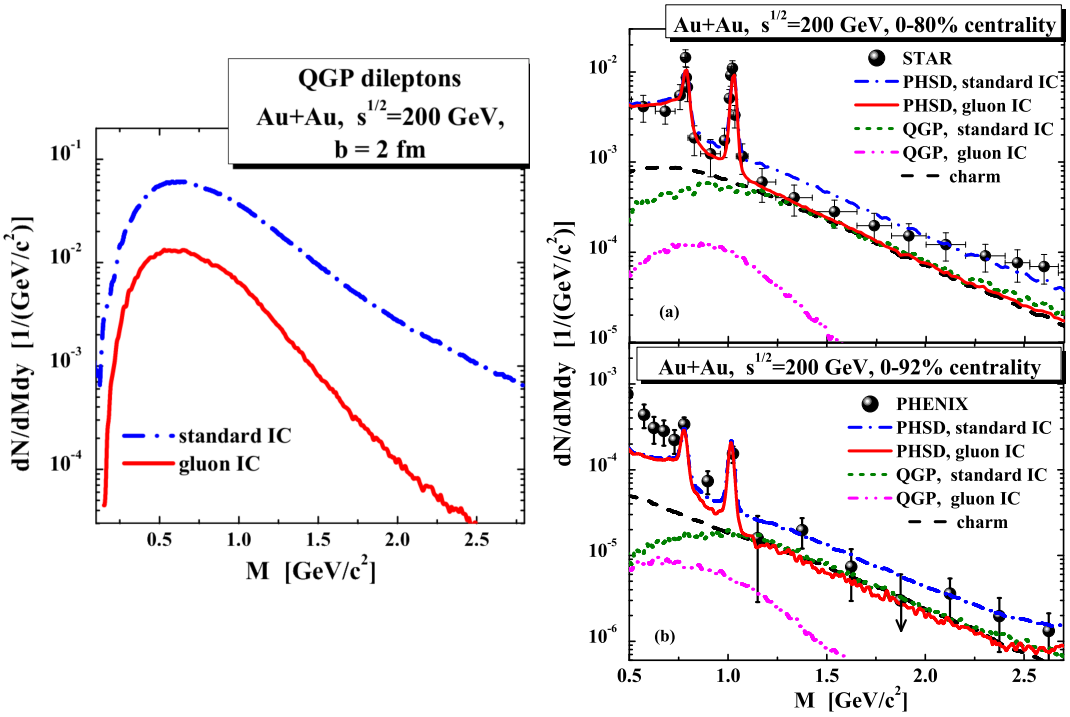

Figure 5.8 – Left: Comparison of the QGP di-electron contribution as a function of the invariant mass M for the scenario I (solid red line) and the scenario II (dash-dot blue line) for central Au+Au collisions at $\sqrt{s_{NN}} = 200$ GeV from the PHSD. Right: The transverse mass spectra of e^+e^- pairs from Au-Au reactions at $\sqrt{s_{NN}} = 200$ GeV for 0-80% centrality (a) and 0-92% (b). The thermal dilepton yield from partonic channels is displayed for the scenarios I (lower dash-dot purple lines) and II (dashed green lines). The solid red lines reflect the total dilepton spectrum when adding the residual channels – dominated by correlated D-meson decays – for the scenario I while the dash-dotted blue line represents the same quantity for the scenario II. The dilepton data are from the STAR Collaboration [326–328] (a) and from the PHENIX Collaboration [329–332] (b).

from Au-Au reactions at $\sqrt{s_{NN}} = 200$ GeV for 0-80% centrality from STAR [326–328] (a) and 0-92% from PHENIX [329–332] (b) to the PHSD results for the two scenarios. The thermal dilepton yield from partonic channels is displayed for the scenarios I (lower dash-dot purple lines) and II (dashed green lines) and shows again very large differences depending on the initial degrees of freedom. Whereas in case of scenario II the QGP contribution is roughly of the same size as the yield from correlated D-meson decays, the QGP yield from the scenario I is practically not visible in the total spectra. The solid red lines in Fig. 5.8 reflect the total dilepton spectrum when adding the residual channels – dominated by correlated

D-meson decays – for the scenario I while the dash-dotted blue line represents the same quantity for the scenario II. Whereas the present accuracy of the PHENIX data does not allow to differentiate the different initial degrees of freedom, the STAR data show a better agreement with the PHSD calculations for the scenario II. However, for a robust conclusion one needs to subtract the D-meson background as e.g. in the NA60 data [333].

5.3 Summary

In this chapter we employed the PHSD approach in order to explore the influence of the initial degrees of freedom on hadronic and electromagnetic observables at the top RHIC energy range for Au-Au collisions. For this purpose we have considered two initial state scenarios: (I) with only massive gluons in the initial state (after the passage of the impinging nuclei) and (II) with only quarks and antiquarks while keeping the local energy-momentum tensor $T^{\mu\nu}(x)$ unchanged. We point out that the default PHSD approach does not correspond to these limiting scenarios, however, is closer to scenario II due to the thermal suppression of the gluons which are heavier than the quarks/antiquarks in the DQPM. In PHSD the equilibration between the gluonic and fermionic degrees of freedom proceeds dominantly via the channel $g \leftrightarrow q + \bar{q}$ with an equilibration time of order 6-8 fm/c. We find that the total partonic collision rates (adding up quarks/antiquarks and gluons) as well as the hadronization rate are found to be similar in the two scenarios. However, the formation of $s, \bar{s}$ pairs in the gluon dominated QGP (scenario I) proceeds rather slow [192] such that the anti-strange quarks and accordingly the K^+ mesons do not achieve chemical equilibrium even in central Au+Au collisions at the top RHIC energy. Accordingly, the K^+ rapidity distribution is suppressed in the scenario I in conflict with the data from BRAHMS. The rapidity distributions for protons and antiprotons are overestimated in the gluonic scenario I, while a good agreement is achieved within the scenario II, in comparison to the data from the BRAHMS and STAR collaborations. The differential elliptic flow of charged particles (cf. Fig. 5.5) is not sensitive to the initial degrees of freedom, however, a drastic difference is seen in the photon and dilepton production from partonic sources since the initial gluonic degrees of freedom carry no electric charge. The actual comparison to the data from the PHENIX and STAR collaborations (cf. Figs. 5.7 and 5.8) slightly favor the scenario II, i.e. the early presence of quarks and antiquarks, however, a robust conclusion (from the photon data) will require more accurate measurements for transverse momenta of 2–3 GeV/c as well as a subtraction of the background from correlated D-meson decays in case of dileptons.

Chapter 6

Chiral symmetry restoration and strangeness production

* * *

We continue to investigate the early nonequilibrium phase of heavy-ion collisions and especially the production of strange particles, which has always been suggested as one of the most sensitive observables that could indicate the creation of a Quark-Gluon Plasma (QGP) in heavy-ion collisions (HIC) (for a complete review we refer the reader to Blume and Markert [106]). One of the first suggested signature results in an enhancement of the strangeness production in $A+A$ collisions with respect to $p+p$ collisions [105, 334]. Gazdzicki and Gorenstein [335] later on proposed that a sharp rise and drop in the excitation function of the K^+/π^+ ratio (the so-called "horn") should show up due to the appearance of a QGP phase at an energy of around $\sqrt{s_{NN}} \sim 7$ GeV. Statistical models [336–339] were able to reproduce the trend of experimental data for the K^+/π^+ ratio, but they can only provide a statistical description of what happens in heavy-ion collisions. On the other hand, conventional hadronic transport approaches [182, 340, 341], i.e. without including a QGP phase, could not describe the data. Especially, hadronic interaction rates were found to be too slow to reach chemical equilibrium in these nucleus-nucleus collisions [342]. Only within hybrid approaches [343] or three-fluid hydrodynamics [344, 345] a description of the "horn phenomenon" could

This work has been done in collaboration with Alessia Palmese (Gießen university) who illustrated the plots to assess the dependence of our results to the nuclear EoS, to the considered collisional system and centrality, whereas all other plots have been realized by myself.

be achieved due to the assumption of chemical equilibrium in the hydrodynamical phase. However, partonic rates were also found to be too slow to achieve a chemical equilibrium in heavy-collisions [192] (as we have also seen in the previous chapter), particularly at low collisional energies where the QGP phase is short-lived. Accordingly, the quest for a microscopic explanation of the K^+/π^+ horn remained.

Concurrently, the search for a possible chiral symmetry restoration (CSR) at high baryon density and/or high temperature is mainly focused on the study of dileptons in nucleus-nucleus collisions, where however, no clear evidence has been achieved so far [346, 347]. As we will see in this chapter, a linear decrease of the scalar quark condensate – the order parameter for chiral symmetry restoration – is expected with baryon density towards a chiral symmetric phase characterized by $\langle\bar{q}q\rangle \approx 0$ [348, 349]. Since $\langle\bar{q}q\rangle$ is not a measurable quantity, it is crucial to determine experimental observables which are sensitive to this condensate. It was found by a statistical analysis that a maximum net-baryon density can be achieved in heavy-ion collisions at low collisional energies around $\sqrt{s_{NN}} \approx 7$ GeV [350], which therefore appears to be a perfect energy region to probe the restoration of chiral symmetry.

In this chapter, we will relate the strangeness production in nucleus-nucleus collisions to the manifestation of chiral symmetry restoration. In particular, the horn in the K^+/π^+ ratio peaks at an energy of $\sqrt{s_{NN}} \approx 7$ GeV where precisely the restoration of chiral symmetry is expected. We will perform a systematic study within the PHSD on effects of the CSR on final particle distributions in HICs in the energy range $\sqrt{s_{NN}} = 2 - 200$ GeV. In the first section we will present the ingredients that we will use to realize the CSR in the string fragmentation of the PHSD, and their sensitivity to the nuclear Equation of State (EoS) within the non-linear $\sigma - \omega$ model. In section 6.2 we present the calculated results from PHSD – with and without the inclusion of CSR – for the particle rapidity spectra and excitation functions of strange particles, and confront them to available experimental data. Also, similar observables will be studied in different collisional systems and centralities.

6.1 Chiral symmetry restoration in PHSD

6.1.1 Theoretical framework

The starting point of this work is the evaluation of the scalar quark condensate as a function of the medium properties in the PHSD transport approach. This can be done following Ref. [351] by making use of the Feynman-Hellmann theorem [352, 353] which states that if $H(\lambda)$ is a Hermitian operator whose eigenvalue and normalized eigenvector are $E(\lambda)$ and $|\psi(\lambda)\rangle$, respectively, then the following identity is fulfilled:

$$\langle\psi(\lambda)|\frac{d}{d\lambda}H(\lambda)|\psi(\lambda)\rangle = \frac{d}{d\lambda}\langle\psi(\lambda)|H(\lambda)|\psi(\lambda)\rangle = \frac{d}{d\lambda}E(\lambda) \tag{6.1}$$

with λ being a parameter of the Hamiltonian. In this way, one can study the spontaneous chiral symmetry breaking of the QCD Hamiltonian $\mathcal{H}_{\rm QCD}$ by studying its variation with respect to the light quark mass $m_q \equiv 1/2(m_u + m_d)$. Only the part containing the quark masses $\mathcal{H}_{\rm mass}$ will be affected by a derivative with respect to m_q:

$$\begin{aligned}\mathcal{H}_{\rm mass} &= m_u\ \bar{u}u + m_d\ \bar{d}d + m_s\ \bar{s}s + ... \\ &= 2m_q\ \bar{q}q - \frac{1}{2}\ \delta m_q\ (\bar{u}u - \bar{d}d) + m_s\ \bar{s}s + ...\end{aligned} \tag{6.2}$$

with $\bar{q}q \equiv 1/2(\bar{u}u + \bar{d}d)$, and $\delta m_q = m_d - m_u$ denoting the difference between the u and d quarks which can be neglected assuming isospin symmetry (cf. chapter 1). By replacing the Hamiltonian (6.2) in Eq. (6.1) as $H \to \int d^3x\ \mathcal{H}_{QCD}$, we obtain:

$$2\,\langle\psi(m_q)|\int d^3x\ \bar{q}q\ |\psi(m_q)\rangle = \frac{d}{dm_q}E(m_q). \tag{6.3}$$

We consider now two different states: nuclear matter at rest $|\rho_N\rangle$ with a density ρ_N, and the vacuum state $|V\rangle$. By taking the difference between these two cases in the previous equation, we obtain:

$$2m_q\ \left(\langle\bar{q}q\rangle_{\rho_N} - \langle\bar{q}q\rangle_V\right) = m_q\ \frac{d}{dm_q}\epsilon(m_q) \approx\ \sigma_{\pi N}\ \rho_N\ , \tag{6.4}$$

where the energy density ϵ of nuclear matter is in first order $\epsilon \approx M_N\ \rho_N$. In Eq. (6.4), the pion-nucleon σ-term has been introduced:

$$\sigma_{\pi N} = m_q \frac{dM_N}{dm_q} \tag{6.5}$$

and measures how much of the nucleon mass can be attributed to the explicit chiral symmetry breaking introduced by the finite light quark masses m_q.

Note

Because of the explicit breaking of chiral symmetry by the quark masses, the divergence of the axial-vector current $J^k_{5,\mu} = \bar{\psi}\gamma_\mu\gamma_5\tau^k\psi$ is non-vanishing:

$$\partial^\mu J^k_{5,\mu} = i\bar{\psi}\left\{m, \tau^k\right\}\gamma_5\psi. \tag{6.6}$$

The pions $|\pi^k\rangle$ are found to have the same quantum numbers ($J^P = 0^-$, $I = 1$) as the divergence of the axial-vector current where $k = 1, 2, 3$ is the isospin index. The operator $J^k_{5,\mu}$ can annihilate a pion state and therefore connect the latter to the vacuum as [74, 133]:

$$\langle 0|J^k_{5,\mu}(x)|\pi^i(p)\rangle = i\delta^{ki} f_\pi \; p_\mu \; e^{-ip\cdot x}, \tag{6.7}$$

with $f_\pi \approx 93$ MeV being the pion decay constant. By taking the derivative of this expression, we obtain the PCAC (partially conserved axial current) relation:

$$\langle 0|\partial^\mu J^k_{5,\mu}(x)|\pi^i(p)\rangle = \delta^{ki} f_\pi m_\pi^2 e^{-ip\cdot x}, \tag{6.8}$$

which relates the fact that the axial-vector current is exactly conserved when the pion mass is vanishing. The previous identities also lead to the **Gell-Mann-Oakes-Renner** (GOR) relation [354–356]

$$f_\pi^2 m_\pi^2 = -\frac{1}{2}(m_u + m_d)\;\langle \bar{u}u + \bar{d}d\rangle_V = -2\; m_q\;\langle \bar{q}q\rangle_V\;, \tag{6.9}$$

which relates the current quark masses m_u and m_d of the QCD Lagrangian to the finite pion mass. The vacuum scalar condensate $\langle \bar{q}q\rangle_V \approx \langle \bar{u}u\rangle_V \approx \langle \bar{d}d\rangle_V$, which indicates the spontaneous breaking of chiral symmetry, has a value of $\langle \bar{q}q\rangle_V \approx -1.6$ fm^{-3} for the bare quark masses $m_u = m_d \approx 7$ MeV.

Equation (6.4) can be generalized to a mixture of mesons and baryons which reads in leading order [357]:

$$\frac{\langle \bar{q}q\rangle}{\langle \bar{q}q\rangle_V} = 1 - \frac{\sigma_{\pi N}}{f_\pi^2 m_\pi^2}\rho_S - \sum_h \frac{\sigma_h \rho_S^h}{f_\pi^2 m_\pi^2}\,, \tag{6.10}$$

where σ_h stands for the σ-commutator of the relevant mesons h. Note, however,

that the value of $\sigma_{\pi N}$ is not so accurately known; a recent analysis points towards a larger value of $\sigma_{\pi N} \approx 59$ MeV [358, 359] while actual lQCD results [360] suggest a substantially lower value. Accordingly, our following calculations – based on $\sigma_{\pi N} = 45$ MeV – have to be taken with some care although it corresponds to a 'world average' (cf. Fig. 5 in Ref. [361]). According to the light quark content, the σ-terms for other baryons can be calculated in this way [357]:

$$\sigma_h = \frac{N_q}{N_{\rm tot}} \sigma_{\pi N} \tag{6.11}$$

where N_q and $N_{\rm tot}$ are the number of light quarks and the total number of quarks inside the nucleon h , respectively. Thus the σ-term for hyperons is decreased by a factor of 2/3 for Λ and Σ hyperons and by a factor of 1/3 for Ξ baryons. From Eq. (6.5) and the GOR relation (6.9), one can find the pion σ-term $\sigma_h = m_\pi/2$. For mesons made out of light quarks and antiquarks, we will therefore use $\sigma_h = m_\pi/2$, whereas for mesons with a strange (antistrange) quark we consider $\sigma_h = m_\pi/4$ according to Eq. (6.11). We mention here that improved results for the sigma-commutator for kaons can be obtained from chiral perturbation theory as in Ref. [362] and alternative assumptions for non-pseudoscalar mesons can be employed as e.g. suggested by Cohen et al. in Ref. [351]. In view of the subleading contributions of these mesons to the ratio in Eq. (6.10) we keep the simple estimates noted above for our present study and look forward to a clarification of the present tension between the results from lQCD and dispersive approaches [363].

In Eq. (6.10), the quantities ρ_S and ρ_S^h denote the nucleon scalar density and the scalar density for a meson of type h, respectively. The scalar density of mesons h is evaluated in the independent-particle approximation as:

$$\rho_S^h(x) = \frac{(2s+1)(2\tau+1)}{(2\pi)^3} \int {\rm d}^3p \frac{m_h}{\sqrt{\mathbf{p}^2 + m_h^2}} f_h(x, \mathbf{p}) \,, \tag{6.12}$$

where $f_h(x, \mathbf{p})$ denotes the meson phase-space distribution ($x = (\mathbf{r}, t)$) and s, τ refer to the discrete spin and isospin quantum numbers, respectively.

6.1.2 The nuclear scalar density

The last quantity in Eq. (6.10) that still has to be determined is the nucleon scalar density ρ_S. The latter needs to be calculated in a suitable model with interacting degrees-of-freedom in order to match our knowledge on the nuclear EoS

at low temperature and finite density. A proper (and widely used) approach is the non-linear $\sigma-\omega$ model for nuclear matter where ρ_S is defined as:

$$\rho_S(x) = \frac{g_n}{(2\pi)^3}\int \mathrm{d}^3p \frac{m_N^*}{\sqrt{\mathbf{p}_N^{*2}+m_N^{*2}}} f_N(x,\mathbf{p})\,, \tag{6.13}$$

where m_N^* and p_N^* denote the effective mass and momentum, respectively, and $f_N(x,\mathbf{p})$ the phase-space occupation of a nucleon while the degeneracy factor is $g_n = 4$. In the non-linear $\sigma-\omega$ model the nucleon mass is modified due to the scalar interaction with the medium:

$$m_N^*(x) = m_N^V - g_s\sigma(x)\,, \tag{6.14}$$

where m_N^V denotes the nucleon mass in vacuum and $\sigma(x)$ is the scalar field which mediates the interaction between the nucleons and the medium with the coupling g_s. In order to calculate ρ_S in Eq. (6.13), we therefore have to determine the value of the scalar field $\sigma(x)$ at each space-time point x. This is done via the non-linear gap equation [364, 365]:

$$m_\sigma^2\sigma(x) + B\sigma^2(x) + C\sigma^3(x) = g_s\rho_S(x) = g_s g_n \int \frac{\mathrm{d}^3p}{(2\pi)^3}\frac{m_N^*(x)}{\sqrt{\mathbf{p}^2+m_N^{*2}}} f_N(x,\mathbf{p})\ , \tag{6.15}$$

since for matter at rest we have $\mathbf{p}^* = \mathbf{p}$. In Eq. (6.15) the self-interaction of the σ-field is included up to the fourth order. The parameters g_s, m_σ, B, C are fixed in order to reproduce the values of the nuclear matter quantities at saturation, i.e. the saturation density, the binding energy per nucleon, the compression modulus, and the effective nucleon mass. Actually, different sets for these quantities can be used, which differ from each other in the high density regime where sizable uncertainties remain. In Table 6.1 we display the values of g_s, m_s, B, C together with the vector coupling g_v, the vector meson mass m_v, the compression modulus K and the ratio between the effective and the bare nucleon mass m^*/m at saturation density for three sets commonly indicated as NL1, NL2 and NL3. The sets NL1 and NL3 have the same compression modulus K but differ in the effective mass m^*/m at saturation density whereas NL1 and NL2 have the same effective mass but differ in the compression modulus K. By comparing the results from NL1, NL2 and NL3 we will be able to explore separately the effects from the effective mass and compression modulus.

In Fig. 6.1 we show the dependence of the nucleon scalar density ρ_S on energy density ϵ in panel (a), and the ratio between the scalar quark condensate and its

	NL1	NL2	NL3
g_s	6.91	8.50	9.50
g_v	7.54	7.54	10.95
B (1/fm)	-40.6	50.57	1.589
C	384.4	-6.26	34.23
m_s (1/fm)	2.79	2.79	2.79
m_v (1/fm)	3.97	3.97	3.97
K (MeV)	380	210	380
m^*/m	0.83	0.83	0.70

Table 6.1 – Parameter sets NL1, NL2 and NL3 for the non-linear $\sigma-\omega$ model employed in the transport calculations from Ref. [365].

value in the vacuum $\langle\bar{q}q\rangle/\langle\bar{q}q\rangle_V$ in panel (b). Note that an analogous dependence is observed with respect to the baryon density ρ_B since the energy density ϵ in leading order is just the nucleon mass times the baryon density. The results shown in Fig. 6.1 are obtained at vanishing temperature $T=0$, i.e. there are no thermal mesons, but all the following considerations can be extended to a more realistic picture at finite temperature (meson density) and illustrate the consequences of CSR in the PHSD results for heavy-ion collisions. The energy density ϵ here is calculated within the non-linear $\sigma-\omega$ model by:

$$\epsilon = U(\sigma) + \frac{g_v^2}{2m_v^2}\rho_N^2 + g_n \int \frac{\mathrm{d}^3p}{(2\pi)^3}\; E^*(\mathbf{p})\left(N_f(\mathbf{p}) + N_{\bar{f}}(\mathbf{p})\right), \tag{6.16}$$

with

$$E^*(\mathbf{p}) = \sqrt{\mathbf{p}^2 + m_N^{*2}}\;, \tag{6.17}$$

$$U(\sigma) = \frac{m_s^2}{2}\sigma^2 + \frac{B}{3}\sigma^3 + \frac{C}{4}\sigma^4\;, \tag{6.18}$$

where ρ_N represents the nucleon density and $N_f(\mathbf{p})$ and $N_{\bar{f}}(\mathbf{p})$ are the particle/antiparticle occupation numbers at fixed momentum $\mathbf{p}$, respectively.

The scalar density ρ_S increases with increasing energy density ϵ as displayed in panel (a) of Fig. 6.1. We find a moderate sensitivity to the nuclear equation of state up to energy densities of ~ 0.5 GeV/fm^3 which are relevant for the hadronic phase. In fact, the lines referring to the parameter sets NL1/NL2 and NL3 show

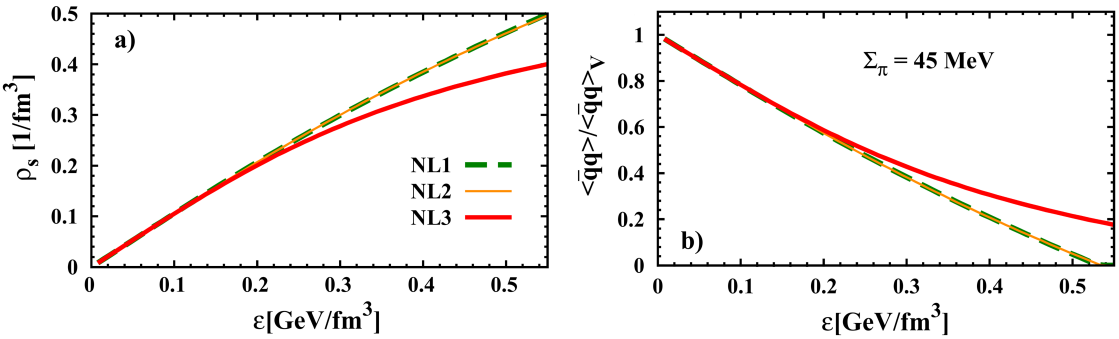

Figure 6.1 – The nucleon scalar density ρ_S (a), the ratio between the scalar quark condensate and its value in the vacuum $\langle\bar{q}q\rangle/\langle\bar{q}q\rangle_V$ (b) as a function of the energy density ϵ for the parameter sets NL3 (red solid lines), NL2 (thin orange lines) and NL1 (dashed green lines) at $T = 0$ and with $\sigma_{\pi N} = 45$ MeV.

a very similar behavior as a function of ϵ, but the NL3 (solid line) set is always characterized by lower values of the scalar density ρ_S relative to the NL1 or NL2 parametrization (dashed line). Since the scalar density ρ_S essentially depends on the effective nucleon mass m_N^*, this is attributed to the larger value of m_N^* in case of the NL1 and NL2 parameter sets. In panel (b) of Fig. 6.1 the ratio $\langle\bar{q}q\rangle/\langle\bar{q}q\rangle_V$ is presented as a function of ϵ. At $\epsilon = 0$ the scalar condensate corresponds to the vacuum value $\langle\bar{q}q\rangle_V$ and for fixed $\sigma_{\pi N} = 45$ MeV it decreases almost linearly with increasing energy density and almost vanishes for the critical energy density $\epsilon_c \approx 0.5$ GeV/fm^3. In this case, the order between NL1/NL2 and NL3 results is reversed: the NL3 parametrization for the nuclear EoS is associated to higher values of the scalar quark condensate with respect to the NL1 or NL2 sets.

6.1.3 The string decay in a hot and dense medium

As discussed in Chapter 3, the formation and decay of strings is described in PHSD by the Schwinger mechanism of quark-antiquark pair production [185]. In Eq. (3.19) for the strangeness fraction $P(s\bar{s})/P(u\bar{u}) = \gamma_s \sim s/u$, the string tension κ is determined experimentally (or by lattice QCD) as well as the effective masses m_q, m_s for the dressed quarks. This dressing is usually attributed to a scalar coupling to the vacuum condensate $\langle\bar{q}q\rangle_V$ which, as we have seen in the previous subsection, vanishes with increasing baryon density and/or temperature. In first order the dressed quark masses are expected to scale with the ratio (6.10) as:

$$m_s^* = m_s^0 + (m_s^V - m_s^0)\frac{\langle\bar{q}q\rangle}{\langle\bar{q}q\rangle_V}, \tag{6.19}$$

$$m_q^* = m_q^0 + (m_q^V - m_q^0)\frac{\langle\bar{q}q\rangle}{\langle\bar{q}q\rangle_V}\,, \tag{6.20}$$

with $m_s^0 \approx 100\,\mathrm{MeV}$ and $m_q^0 \approx 7\,\mathrm{MeV}$ for the bare quark masses. In the previous equations the effective masses decrease from the vacuum values with decreasing scalar condensate $\langle\bar{q}q\rangle$ to the constituent masses.

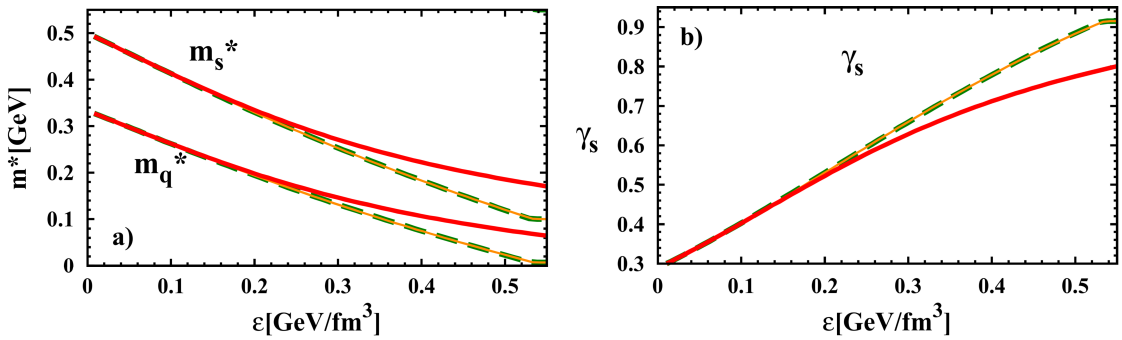

Figure 6.2 – The light and strange quark effective masses m_q^*, m_s^* (a), and the production probability of massive $s\bar{s}$ relative to light flavor production γ_s (b) as a function of the energy density ϵ for the parameter sets NL3 (red solid lines), NL2 (thin orange lines) and NL1 (dashed green lines) at $T = 0$ and with $\sigma_{\pi N} = 45$ MeV.

As in the previous subsection, we study the behavior of the light and strange quark effective masses m_q^*, m_s^*, and of the strangeness ratio γ_s in the panel (a) and (b) of Fig. 6.2, respectively, as a function of the energy density ϵ. When $\epsilon = 0$, the quark effective masses are equal to their vacuum values, $m_q \approx 0.33\,\mathrm{GeV}$ and $m_s \approx 0.5\,\mathrm{GeV}$; with increasing ϵ the quark masses decrease in line with the scalar quark condensate up to their bare values m_s^0 and m_q^0 for vanishing $\langle\bar{q}q\rangle/\langle\bar{q}q\rangle_V$. The decrease of both m_q and m_s is approximately linear in energy density where the slope associated to the light quark is flatter in comparison to the strange quark mass. Concerning the comparison between the different choices for the nuclear equation of state, we find also for these masses a non-negligible sensitivity and the same hierarchy as for the scalar quark condensate (the results associated to NL1/NL2 are always below the corresponding results for NL3). In the panel (b) of Fig. 6.2, the factor γ_s increases from the vacuum case ($\gamma_s \approx 0.3$) with increasing energy density up to values of 0.8 – 0.9 for $\epsilon \approx \epsilon_c$. Thus the production of a $s\bar{s}$ pair relative to a light quark pair is no longer suppressed close to the phase boundary for CSR as it is in vacuum. The reason of this increase is the steeper decrease of the effective strange quark mass (with energy density) in comparison to the effective light quark mass as mentioned above. Furthermore, the NL1 and NL2 parametrizations give larger values of γ_s compared to NL3 because of a faster

change of the masses with ϵ.

We note that this scheme for CSR in the string decay mechanism can be applied not only to the light and strange quarks, but also to diquark combinations that are additionally produced in the fragmentation of the string and lead finally to baryon-antibaryon pairs. Here the default JETSET ratios fix the diquark mass in the vacuum, e.g. a light diquark mass in vacuum of m^V_{uu}= 0.65 GeV leads to a suppression of a light diquark pair relative to a light quark-antiquark pair of

$$\frac{P(uu\bar{u}\bar{u})}{P(u\bar{u})} \approx 0.07\,. \tag{6.21}$$

For the creation of a diquark (su) one employs $m^V_{su} \approx 0.725$ GeV which leads to the ratio for a (su)-diquark pair relative to a light (uu)-diquark pair of

$$\frac{P(su\bar{s}\bar{u})}{P(uu\bar{u}\bar{u})} \approx 0.4\,. \tag{6.22}$$

Within the same line the vacuum mass of a ss-diquark can be determined from JETSET. The Schwinger mechanism of string decay in vacuum thus requires the following dressed vacuum masses: $m^V_u \approx 0.35$ GeV, $m^V_s \approx 0.5$ GeV, $m^V_{uu} \approx 0.65$ GeV, $m^V_{su} \approx 0.725$ GeV and $m^V_{ss} \approx 0.87$ GeV to comply with experimental observation in nucleon-nucleon collisions. The production probability of diquarks (su) relative to uu-diquarks (6.22) and (ss) relative to uu-diquarks does not change very much in the dense medium – in line with (indirect) experimental observation – and since $m^0_{su} - m^0_{uu} \approx m^0_s - m^0_u$, the 'bare' diquark masses m^0_{uu} can be fixed and give $m^0_{uu} \approx 0.5$ GeV, $m^0_{su} \approx 0.593$ GeV and $m^0_{ss} \approx 0.763$ GeV. The explicit variations of the flavor ratios with the energy density are displayed in Fig. 6.3 and show that the diquark ratios only very moderately change with the energy density whereas the s/u ratio steeply rises with ϵ. We specify once more that these results have been obtained within a pure hadronic system at vanishing temperature, but the conclusions are valid also for finite temperatures (meson densities).

We mention that in the hadronic phase, the ratio $s/u \sim \gamma_s$ in Fig. 6.3 increases with decreasing scalar quark condensate as long as the string tension κ remains approximately constant. In fact, lattice QCD results for the string tension below T_c show roughly a constant value, while it rapidly drops above T_c since no coherent electric color fields (strings) can be formed anymore. Accordingly, the Schwinger formula (3.19) no longer applies for the deconfined phase and the ratio s/u in PHSD is fixed to $\sim 1/3$ by comparison to the strangeness production at RHIC and LHC energies observed experimentally. Consequently we can identify a

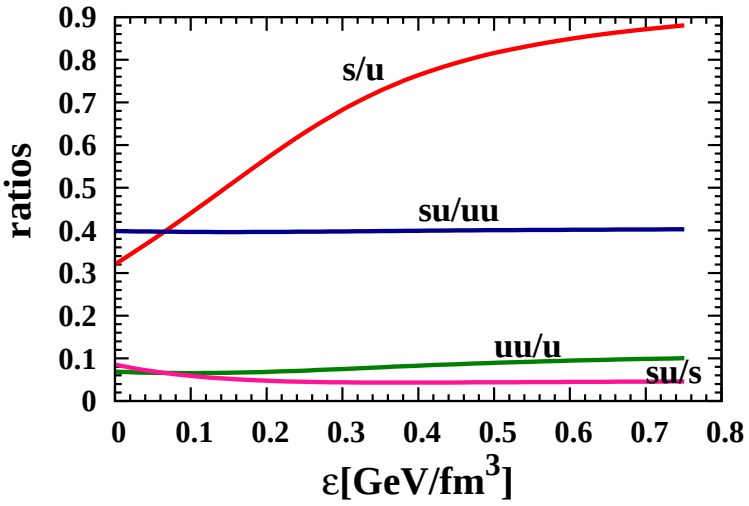

Figure 6.3 – The quark and diquark ratios in the string decay (hadronic environment) as a function of the energy density ϵ as evaluated within the non-linear $\sigma-\omega$ model for the parameter set NL3 for $T=0$.

"horn" structure in the s/u ratio as a function of ϵ, where the initial increase for $\epsilon < \epsilon_c$ is related to the chiral symmetry restoration in the hadronic phase and the subsequent sharp decrease is associated to the formation of the QGP for $\epsilon \geq \epsilon_c$.

To conclude this section, we list the features which are dynamically calculated in the PHSD for each cell in space-time:

- the scalar density ρ_S is determined by solving the gap equation (6.15) for the σ-field;
- the scalar condensate $\langle \bar{q}q \rangle$ is then computed via Eq. (6.10);
- the effective masses m_q^*, m_s^* are calculated according to Eqs. (6.19), (6.20) and plugged in the Schwinger formula (3.19) in order to compute the flavor production ratios for the string decay.

6.2 Application to nucleus-nucleus collisions

Numerical results for the space-time dependence of the scalar condensate ratio (6.10) are presented in Fig. 6.4 as a function of x and z (for $y=0$) at different times t for a central Au+Au collisions at 30 A GeV. Whereas in the approach

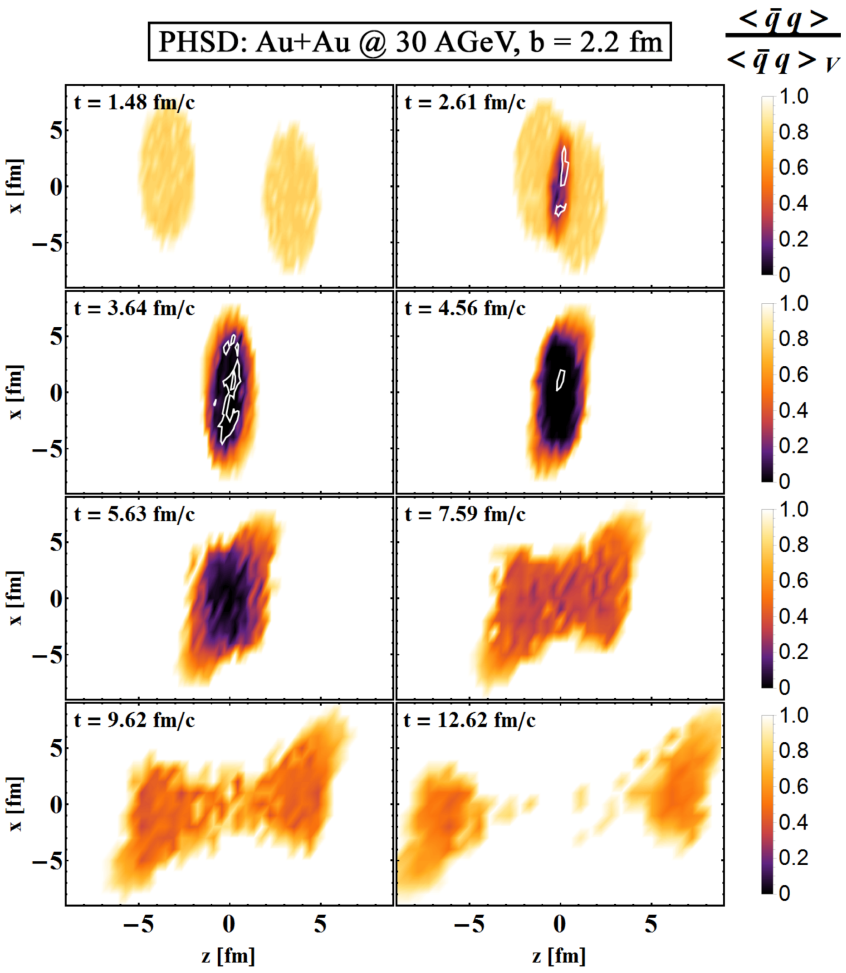

Figure 6.4 – The ratio (6.10) for the scalar quark condensate as a function of x and z (for $y = 0$) at different times t for a central Au+Au collisions at 30 A GeV employing the parameter set NL3 for the computation of the baryon scalar density. The white borderline separates the space-time regions of deconfined matter (ϵ_c) to hadronic matter.

phase the ratio drops to about 2/3 inside the impinging nuclei the scalar quark condensate practically vanishes in the full overlap phase from about 3 to 7 fm/c and regains the vacuum value only in the late expansion phase. This implies that the decay of strings in the hadronic environment is modified substantially in the hot and dense medium. The white borderlines in Fig. 6.4 separate the space-time regions of deconfined matter ($\epsilon \geq \epsilon_c$) to hadronic matter. It is clearly seen that although the chiral symmetry is approximately restored in the full overlap phase, some regions are occupied by deconfined partons in the PHSD. In these re-

gions, however, an enhanced production of strangeness should not occur since the Schwinger mechanism (3.19) no longer applies due to a vanishing string tension and a transformation of energy and momentum to massive partonic degrees-of-freedom.

6.2.1 Rapidity spectra at AGS and SPS energies

We present now our results for the rapidity distribution of the most abundant particles at AGS and SPS energies. We exclusively use the NL3 parameter set for the computation of the baryon scalar density (for now), and we consider the following four scenarios:

- The default HSD calculations without any CSR (and deconfinement transition) and a threshold in the local energy density of < 0.5 GeV/fm^3 for elastic and inelastic reactions of formed hadrons. For energy densities above 0.5 GeV/fm^3 a free streaming of the particles is assumed.
- HSD calculations with the modified string decay (describing CSR) for all local energy densities, however, keeping the free streaming of hadrons above 0.5 GeV/fm^3. Also in this scenario there is no deconfinement transition.
- The default PHSD calculations without any CSR, however, a crossover transition to the deconfined phase above the threshold in the local energy density of 0.5 GeV/fm^3.
- PHSD calculations with the modified string decay (describing CSR) for energy densities below 0.5 GeV/fm^3 and a crossover transition to the deconfined phase above the threshold in the local energy density of 0.5 GeV/fm^3.

The results for the rapidity distributions of pions, kaons, protons and $(\Lambda + \Sigma^0)$'s in these different scenarios are shown in Fig. 6.5 for 5% central Au+Au collisions at 10.7, 30 and 158 A GeV in comparison to the experimental data. Here the solid (red) lines show the results from PHSD (including CSR) while the blue solid lines result from HSD (including CSR) without partonic degrees-of-freedom. The dashed (red) line reflects the PHSD results without CSR while the dashed blue line results from HSD without CSR. One can see that the partonic degrees-of-freedom in PHSD – including a phase transition to the QGP in case of sufficient local energy density – do not change the rapidity distributions (red dashed lines) compared to HSD at the lower energies. Actually this rough equivalence also holds for PHSD and HSD when including CSR (red and dashed solid lines) at 10.7 A GeV, however, in this case the $K^{\pm}$ and $(\Lambda + \Sigma^0)$ distributions are better in line with the

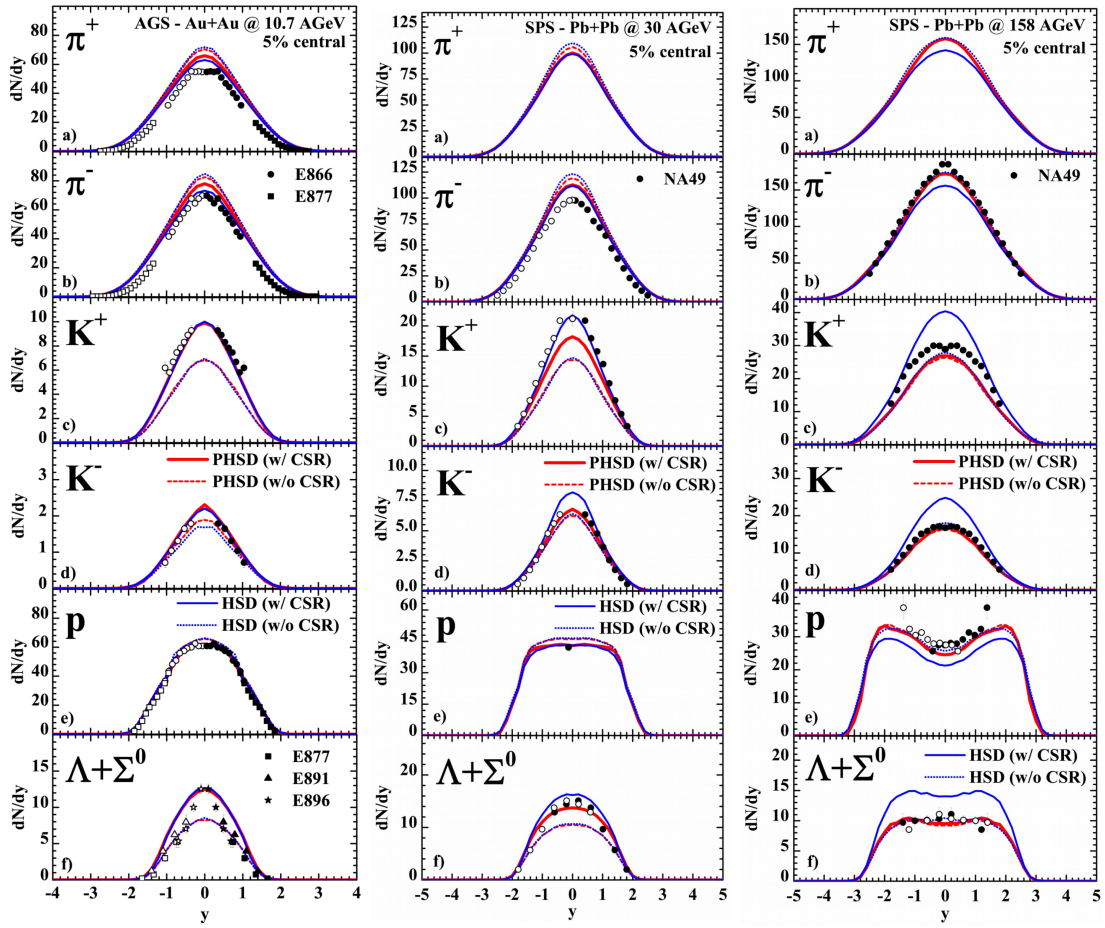

Figure 6.5 – The rapidity distribution of pions, kaons, protons and $(\Lambda + \Sigma^0)$'s for 5% central Au+Au collisions at 10.7 A GeV (left), 30 A GeV (middle) and 158 A GeV (right), in comparison to the experimental data from Refs. [212, 214–217, 366–372]. The parameter set NL3 for the computation of the baryon scalar density was used here.

experimental observations. Although the $\pi^{\pm}$ multiplicities are overestimated by the PHSD calculations (including CSR) at 10.7 and 30 A GeV a striking improvement is obtained with respect to the strangeness production at these energies for central Au+Au or Pb+Pb collisions.

6.2.2 Strange particle ratios

In order to summarize the findings of the previous subsection we show the ratios K^+/π^+, K^-/π^- and $(\Lambda+\Sigma^0)/\pi^-$ at midrapidity from 5% central Au+Au and Pb+Pb collisions in the left-hand side of Fig. 6.6 as a function of the invariant energy $\sqrt{s_{NN}}$ up to the top RHIC energies in comparison to the available experimental data. As before the solid (red) lines show the results from PHSD (including CSR) while the blue solid lines result from HSD (including CSR) without partonic degrees-of-freedom. The dashed (red) line reflects the PHSD results without CSR while the dashed blue line results from HSD without CSR. It is clearly seen from Fig. 6.6 that the results from HSD and PHSD merge for $\sqrt{s_{NN}} < 6$ GeV and fail to describe the data in the conventional scenario without incorporating the CSR. Especially the rise of the K^+/π^+ ratio at low bombarding follows closely the experimental excitation function when incorporating 'chiral symmetry restoration'. However, the drop in this ratio is due to deconfinement since there is no longer any string decay in a hadronic medium at higher bombarding energies. This is clearly seen in the case of HSD (with CSR) which overshoots the data substantially at high bombarding energy.

At AGS energies, the energy dependencies of the ratios K^+/π^+ and $(\Lambda+\Sigma^0)/\pi$ are closely connected, since K^+ and Λ (or Σ^0) are mostly produced in pairs due to strangeness conservation. On the other hand, the excitation function of the K^-/π^- ratio does not show any peak, but it smoothly increases as a function of $\sqrt{s_{NN}}$. In fact, especially at AGS energies, the antikaon production differs substantially from the production of K^+ and Λ, which occurs dominantly via string formation. In fact, the antikaons are produced mainly via secondary meson-baryon interactions by flavor exchange and their production is suppressed with respect to the Λ hyperons that carry most of the strange quarks. This is the reason why the inclusion of chiral symmetry restoration provides a substantial enhancement of the K^+/π^+ and $(\Lambda+\Sigma^0)/\pi$ excitation functions and a smaller change on the K^-/π^- ratio.

On the right-hand side of Fig. 6.6 we show the same observables but by studying now the dependence of our results on the parametrization of the nuclear equation of state in order to estimate the uncertainties of our approach. We show three scenarios: the default PHSD without CSR (blue dotted line) and PHSD including CSR with NL3 and NL1 as parameter sets for the nuclear EoS from the nonlinear $\sigma-\omega$ model (red solid and green dashed lines, respectively). The grey shaded area represents the results from PHSD including CSR taking into account

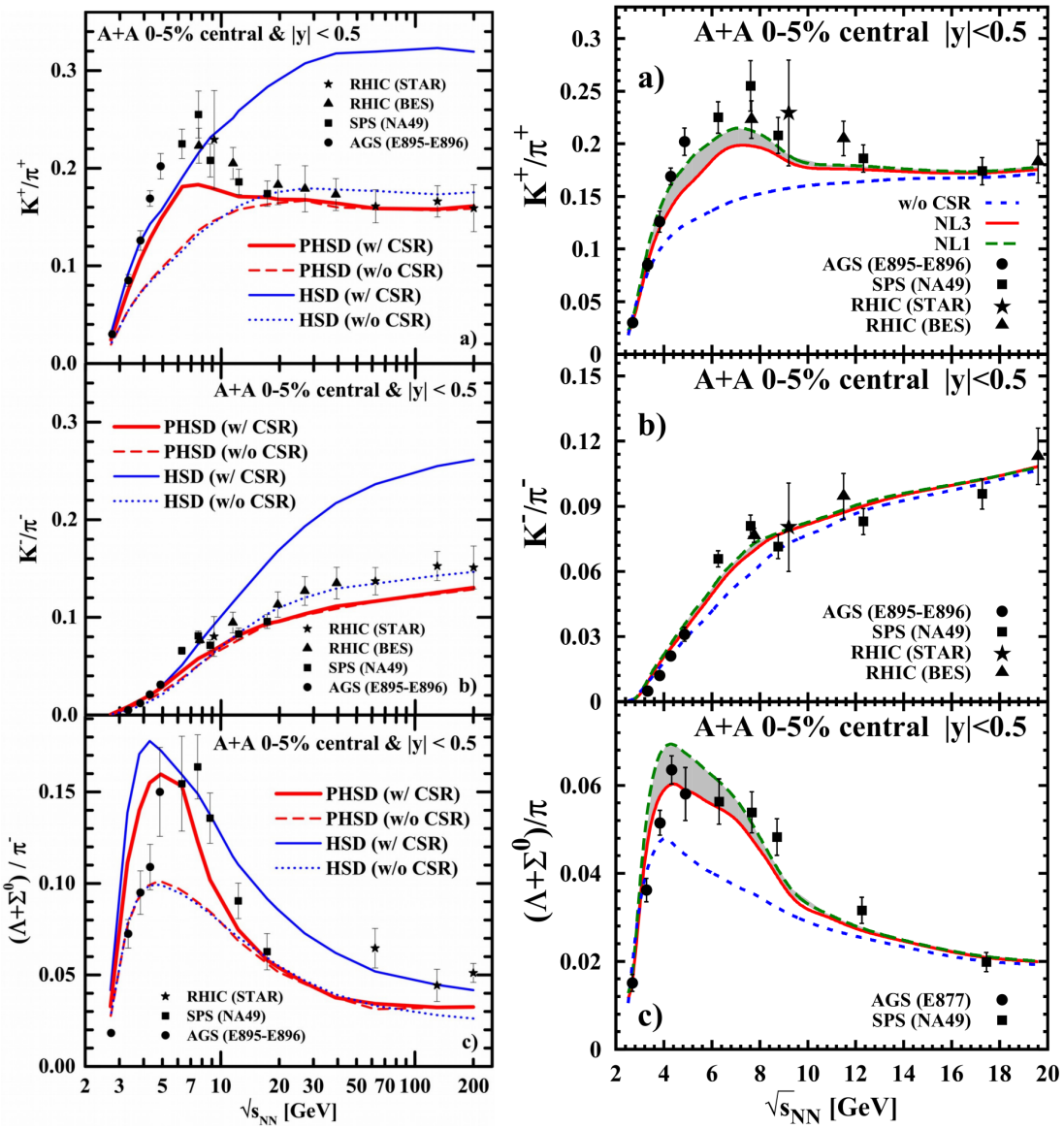

Figure 6.6 – The ratios K^+/π^+ (a), K^-/π^- (b) and Λ/π^- (c) at midrapidity from 5% central Au+Au collisions as a function of the invariant energy $\sqrt{s_{NN}}$ in comparison to the experimental data from [207, 217, 223, 373]. On the left-hand side, the parameter set NL3 for the computation of the baryon scalar density was exclusively used.

the uncertainty from the parameters of the $\sigma - \omega$ model for the EoS. The NL1 parameter set produces a sharper peak both in the K^+/π^+ and in the $(\Lambda + \Sigma^0)/\pi$ excitation functions with a slight maximum increase with respect to the NL3 re-

sults. At top SPS energies the strangeness is produced predominantly by the hadronization of partonic degrees-of-freedom, thus our results for all the ratios do not show an appreciable sensitivity to the nuclear EoS and the calculations with and without CSR tend to merge at $\sqrt{s_{NN}} \approx 20\,\text{GeV}$. Thus even adopting different parametrizations for the $\sigma - \omega$ model, we recover the same "horn" feature. This supports the reliability of the CSR mechanism as implemented in the PHSD model. Accordingly we attribute the experimental 'horn' in the excitation function to the approximate restoration of chiral symmetry at high baryon density but also deconfinement is essential to observe a drop in the K^+/π^+ ratio. We mention that the maximum in the K^+/π^+ ratio is not so pronounced in the PHSD calculations as in the data since the pion production is still overestimated by the PHSD.

Finally, in Fig. 6.7 we present the yields of $(\Lambda + \Sigma^0)$ and Ξ^- at midrapidity from 5% central Au+Au collisions as a function of the invariant energy $\sqrt{s_{NN}}$ in comparison to the available data from Refs. [212, 217]. We recover a "horn" structure, similar to that shown in Fig. 6.6 for the energy dependence of the strange to non-strange particle ratios. A sensitivity on the nuclear model parametrizations persists at low energy, while in the top SPS energy regime the results corresponding to the different scenarios merge. The comparison with the available data at $\sqrt{s_{NN}} < 8\,\text{GeV}$ supports the validity of the CSR picture, while at larger energies we under-estimate the experimental observations. We mention that this discrepancy is not due to the CSR mechanism, since it does not play an essential role in the high-energy regime as pointed out above.

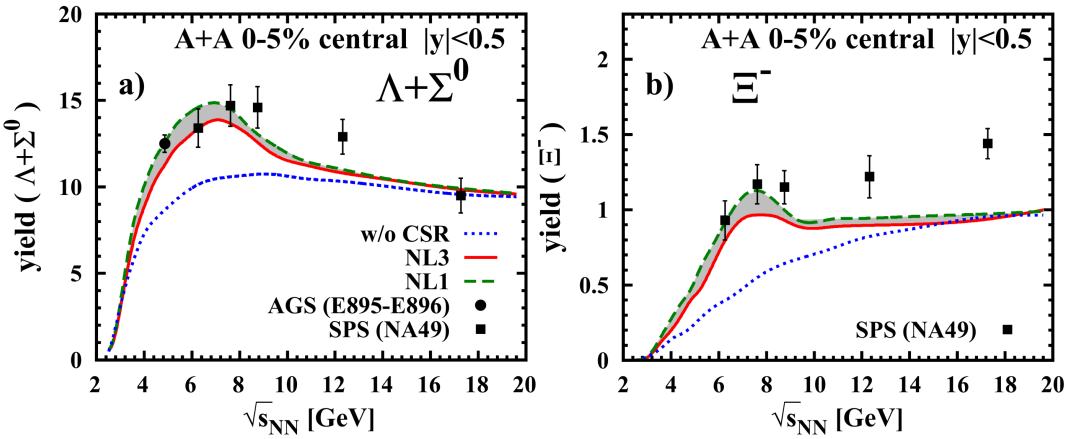

Figure 6.7 – The yields of $(\Lambda + \Sigma^0)$ (left) and Ξ^- (right) at midrapidity from 5% central Au+Au collisions as a function of the invariant energy $\sqrt{s_{NN}}$ up to the top SPS energy in comparison to the experimental data from Refs. [212, 217].

6.3 System size and centrality dependence

In this section we explore other aspects of CSR in heavy-ion collisions. First, we analyze the dependence of the strange to non-strange particle ratios on the size of the colliding system (cf. also Ref. [374]). Second, we investigate the effects of CSR on the strange particle yields for different centralities of Au+Au collision. In Fig. 6.8 we present the particle ratios K^+/π^+, K^-/π^- and $(\Lambda+\Sigma^0)/\pi$ from PHSD for three types of collision systems. The aim here is to explore how the variation of the system size modifies the excitation functions shown in the previous section. In Fig. 6.8 we display the calculations for ^{197}Au + ^{197}Au in blue, for ^{40}Ca + ^{40}Ca in green and for ^{12}C + ^{12}C in red.

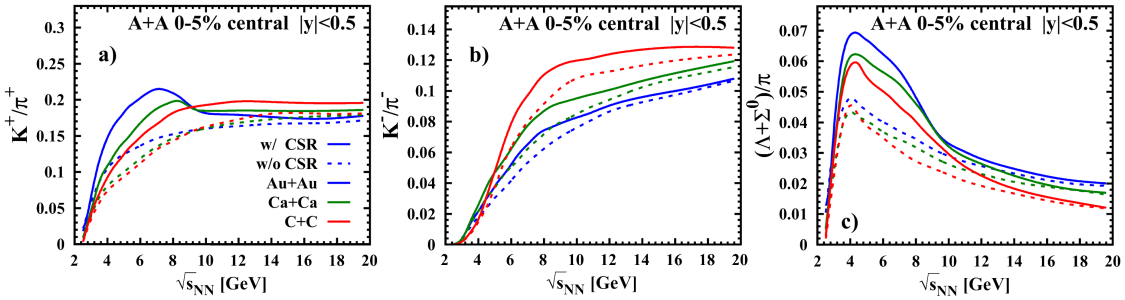

Figure 6.8 – The ratios K^+/π^+, K^-/π^- and $(\Lambda+\Sigma^0)/\pi$ at midrapidity from 5% central symmetric A+A collisions as a function of the invariant energy $\sqrt{s_{NN}}$. The solid lines show the results from PHSD including CSR with NL1 parameters, the dashed lines show the result from PHSD without CSR. The blue lines refer to Au+Au collisions, the green lines to Ca+Ca collisions and the red lines to C+C collisions.

The considered scenarios are the default PHSD without CSR (dashed lines) and PHSD including CSR with NL1 as parameter set for the nuclear equation of state from the non-linear $\sigma-\omega$ model (solid lines). The inclusion of CSR gives a strangeness enhancement also in case of smaller system size with respect to Au+Au collisions and this holds for all three particle ratios. In fact, when considering central collisions, a sizeable volume of the system is affected by the partial restoration of chiral symmetry even in case of light ions. We notice that the spread between the scenarios with and without CSR is larger when the size of the system is smaller. This can be explained by the fact that in Ca+Ca and C+C collisions the fraction of the system, which performs the phase transition to the QGP, is smaller with respect to Au+Au collisions, and the string excitations and decays still have a large

strangeness production rate even at larger energies.

These characteristics are evident also in the observation that at large energies the ratio K^+/π^+ is smaller for the Au+Au collisions and larger in C+C collisions. In fact, we recall that the drop of the K^+/π^+ ratio in Fig. 6.7 is due to the appearance of the QGP, since the strangeness production in the QGP phase is suppressed with respect to the hadronic production at fixed energy density. Concerning the "horn" structure in the K^+/π^+ ratio, we notice that the peak of the excitation function becomes less pronounced in case of Ca+Ca and it disappears completely in case of C+C collisions. With decreasing system size the low energy rise of the excitation functions becomes less pronounced. We can also see that the peak for Ca+Ca is shifted to larger energies with respect to the Au+Au case. Differently from the K^+/π^+, the $(\Lambda+\Sigma^0)/\pi$ ratio preserves the same structure for all three colliding systems. In order to produce Λ's the threshold energy of $\sqrt{s_{th}} = 2.55\,\text{GeV}$ (for Σ^0 $\sqrt{s_{th}} = 2.62\,\text{GeV}$) must be reached, so the $(\Lambda+\Sigma^0)/\pi$ ratio increases when the system easily exceeds this value. The peak of the Λ production is not exactly in correspondence of the threshold energy, since we are considering A+A collisions where the available collision energy is distributed among participants and where secondary and even higher order interactions take place. However, it is interesting to notice that the peak position in this excitation function does not move for different systems, different from the K^+/π^+ ratios. At large energies the $(\Lambda+\Sigma^0)/\pi$ ratio decreases as a function of the energy, since the pion production is enhanced in the hadronic re-scattering. However, the pion production is more suppressed for C+C and Ca+Ca collisions since in the small systems the hadronic re-scattering cannot develop as in Au+Au collisions. Finally, we observe no peak structure in the energy dependence of the K^-/π^- ratio in any of the scenarios studied.

Furthermore, in Fig. 6.9 the abundances of pions, kaons and the most abundant hyperons are plotted as a function of the number of participants $\langle N_{part}\rangle$ at midrapidity from Au+Au collisions at 30 A GeV and the ratios K^+/π^+, K^-/π^-, $(\Lambda+\Sigma^0)/\pi^-$ and Ξ^-/π^- are shown for the same collision configuration. In both cases we show the calculations from PHSD including CSR with NL3 as parameter set by solid red lines and the calculations from PHSD without CSR by dotted blue lines.

All particle yields decrease with decreasing number of participants. On the other hand, the ratios appear to be almost constant as a function of the centrality for $\langle N_{part}\rangle > 50$. Only the Ξ^-/π^- ratio smoothly decreases with decreasing $\langle N_{part}\rangle$. The inclusion of CSR produces a strangeness enhancement in the whole range of centralities investigated. Note, however, that very peripheral reactions are not

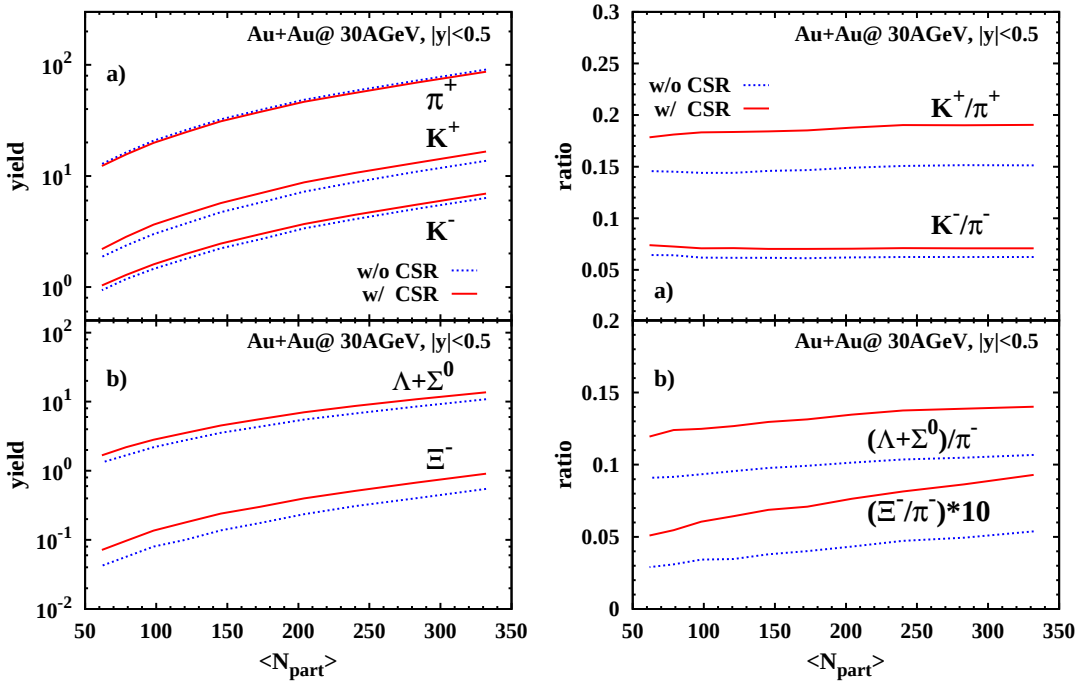

Figure 6.9 – Left: The particle yields of π^+, K^+, K^-, $\Lambda+\Sigma^0$ and Ξ^- at midrapidity from Au+Au collisions at 30 A GeV as a function of the number of participants. The solid (red) lines show the results from PHSD including CSR with NL3 parameters, the dotted (blue) lines result from PHSD without CSR. Right: The particle ratios of K^+/π^+, K^-/π^-, $(\Lambda+\Sigma^0)/\pi^-$ and Ξ^-/π^- at midrapidity from 5% central Au+Au collisions at 30 A GeV as a function of the number of participants.

considered for $\langle N_{part}\rangle < 50$. At $E_{\rm Lab} = 30\,$A GeV the interaction volume of the two colliding nuclei reaches high energy densities such that practically all central cells are influenced by the CSR mechanism independently of the centrality of the collision. Future heavy-ion collision experiments are expected to shed further light on the dynamics of the chiral symmetry restoration by exploring these kind of additional observables.

6.4 Summary

In this chapter we have analyzed the effects of chiral symmetry restoration (CSR) on observables from heavy-ion collisions in the energy range $\sqrt{s_{NN}} = 2 - 200\,$GeV. Essential aspects of CSR have been incorporated in the Schwinger

mechanism for the string decay in the PHSD transport approach, which affects only the hadronic particle production and does not imply modifications in the Quark-Gluon Plasma (QGP) phase. We find that the CSR induces an enhancement of the strange quark fraction γ_s produced via the string decay, while there are no sensible changes in the diquark production and accordingly in baryon-antibaryon production. The s/u ratio, as defined by the Schwinger formula (3.19), increases as a function of the energy density due to CSR and this is reflected in an enhancement of the strange particle abundances with respect to the non-strange ones.

We have performed calculations for different nuclear equations of state (NL1, NL2 and NL3) and thus could quantify the uncertainties in the particle yields and ratios. Since the sets NL1 and NL2 give a larger scalar nucleon density ρ_s at the same energy density as the set NL3, the "horn" in the K^+/π^+ is more pronounced and closer to the experimental data. We mention that the CSR mechanism acts predominantly on the chemistry and not on the kinematics of the string decays. In particular, we found in Ref. [7] that the transverse mass spectra are only slightly modified by the inclusion of the CSR.

We stress that our PHSD calculations provide a microscopic interpretation of the "horn" structure in the excitation function of the K^+/π^+ ratio in central Au+Au (or Pb+Pb) collisions. The steep rise of this ratio at AGS energies is associated to CSR, while the drop at higher SPS energies is due to the appearance of the QGP phase in an increasing volume of the interaction region. We have found an analogous energy dependence for the $(\Lambda+\Sigma^0)/\pi$ ratio, while the excitation function of the K^-/π^- ratio does not show any explicit peak. In general, the PHSD results obtained with the inclusion of CSR are in a good agreement with the available data for all observables analyzed, while calculations without CSR fail substantially.

We have investigated also different sizes of the colliding ions (^{197}Au, ^{40}Ca and ^{12}C) and computed the strange to non-strange particle ratios for these configurations with and without CSR. It is found that the "horn" feature in the K^+/π^+ ratio appears only for larger system sizes, i.e. Au+Au and Ca+Ca, while the "horn" disappears in case of C+C collisions. The $(\Lambda+\Sigma^0)/\pi$ excitation function maintains the peak-structure as we have observed in case of Au+Au collisions also for smaller sizes of the system. Furthermore, we have analyzed the strange particle abundances in Au+Au collisions at 30 A GeV as a function of the number of participants in the collision. As mentioned above, when including CSR in the PHSD calculations we obtain an increase of the strange particle yields with respect to the results from PHSD without CSR and this feature is valid in case of central collisions as well as moderate peripheral collisions.

In conclusion, our microscopic studies support the idea that CSR occurs in hadronic systems with high temperatures and densities before the deconfinement phase transition takes over. We suggest that the strange particle spectra and yields are suitable signatures to study the properties of CSR in HICs in future also as a function of system size and centrality.

Chapter 7

Dynamics at finite baryon chemical potential

* * *

The goal of this chapter is to explore the nonequilibrium Quark-Gluon Plasma - as created in heavy-ion collisions (HICs) - at finite temperature T and baryonic chemical potential μ_B, and find traces of the medium properties (including the μ_B dependence) in experimental observables. As explained in chapter 1, the exploration of the QCD phase diagram as a function of temperature T and baryon chemical potential μ_B can reliably be performed using lattice calculations which show that the transition from hadronic to partonic degrees of freedom is a crossover at low chemical potentials ($\mu_B/T < 2$) [101, 375]. With increasing baryon chemical potential μ_B in the phase diagram, this transition is expected to turn into a first order transition at a critical point [97, 376, 377], which however cannot be addressed by lattice QCD calculations due to the "sign problem" at non-vanishing quark (or baryon) densities. Effective approaches are therefore necessary to model the dominant properties of QCD in equilibrium, i.e. the thermodynamic quantities as well as transport coefficients, as a function of T and μ_B. To this aim the Dynamical QuasiParticle Model (DQPM) has been introduced [120] and will be

This work has been done in collaboration with Olga Soloveva (Frankfurt U.) who evaluated the calculations of the DQPM interaction rates and viscosities as well as the rapidity and p_T distributions in symmetric heavy-ion collisions, and Lucia Oliva (Frankfurt U.) who evaluated the calculations of the rapidity and p_T distributions in asymmetric heavy-ion collisions. All program files and all other plots have been realized by myself.

studied in detail in this chapter in connection with chapter 2. It describes the properties of the Quark-Gluon Plasma (QGP) in terms of massive and interacting quasiparticles and is based on partonic propagators which include real and imaginary self-energies. Even if the extension of the DQPM to finite baryon chemical potentials has been realized previously [230, 378] and the (T, μ_B)-dependence of the transport coefficients (such as shear and bulk viscosities or electric conductivity) for the equilibrated QGP matter have been calculated [230, 378], the QGP properties produced in heavy-ion collisions were not addressed by microscopic calculations within the PHSD so far in a consistent manner.

First, we will provide a brief reminder of the latest version of the DQPM and calculate the QGP thermodynamics in equilibrium in comparison to the available lattice QCD (lQCD) data. In a second step, we explain the calculation of the partonic differential cross sections as a function of T and μ_B employing the effective propagators and couplings from the DQPM. In the following sections we will use these cross sections to evaluate partonic scattering rates for fixed T and μ_B as well as compute transport coefficients like the shear and bulk viscosities η, ζ, in comparison to calculations from lQCD at $\mu_B = 0$. Section 7.5 is devoted to the extraction of the local T and μ_B in the PHSD transport approach and therefore we will investigate which regions of the phase diagram are probed in central collisions of Pb+Pb at $\sqrt{s_{NN}} = 17.3$ and Au+Au at 200 GeV. The calculated total and differential cross sections as well as parton masses - depending on (T, μ_B) - have been implemented in the novel version of PHSD denoted as PHSD5.0. In Section 7.6 we will compare the results of PHSD5.0 to those of PHSD4.0 and experimental data for central heavy-ion collisions from AGS to RHIC energies. Here we concentrate on the evaluation of "bulk" observables such as rapidity distributions and p_T spectra in order to find traces of the μ_B dependence in the QGP dynamics. Furthermore, we explore the sensitivity of rapidity distributions and transverse momentum spectra to the partonic scattering in asymmetric C+Au collisions at the top SPS and RHIC energies. We mention that the topic of this chapter has been partly addressed in various hydrodynamical models [344, 345, 379, 380], hydrodynamical + hadron transport models [197, 343, 381] or more parametric approaches [382]. However, as proposed in Ref. [197], the inclusion of baryon diffusion might lead only to a small effect on the "bulk" observables at BES RHIC energies.

7.1 Reminder of the DQPM and its ingredients

As extracted from experimental observations at RHIC from the strong radial expansion and the scaling of the elliptic flow $v_2(p_T)$ of mesons and baryons with the number of constituent quarks and antiquarks [383], the medium produced in heavy-ion collisions appears to be a strongly interacting system of partons. This characteristic therefore forbids the use of approaches based on perturbative QCD (pQCD) in order to describe the dynamics of the QGP. We present in this section the Dynamical QuasiParticle Model (DQPM) [1] which employs resummed propagators in order to include the non-perturbative features of the QGP which are important for the range of temperatures and chemical potentials studied here.

7.1.1 Quasiparticle properties

As explained in chapter 2, the field quanta in the Kadanoff-Baym theory are described in terms of dressed propagators with complex self-energies. Whereas the real part of the self-energies can be related to a dynamically generated mass or mean-field potentials (of Lorentz scalar, vector or tensor type), the imaginary parts provide information about the lifetime and/or reaction rates in the system [154–160, 386]. The determination/extraction of complex self-energies for the partonic degrees-of-freedom can be performed within the DQPM by fitting lattice QCD calculations in thermal equilibrium. Furthermore, the imaginary parts of the propagators define the spectral functions of the degrees of freedom which might show narrow (or broad) quasiparticle peaks [387]. A further advantage of a propagator based approach is that one can formulate a consistent thermodynamics [388] as well as a causal theory for nonequilibrium configurations on the basis of the Kadanoff-Baym equations.

The basic ideas of the DQPM are as follows:

1. introduce an ansatz (with a few parameters) for the (T and μ_B)-dependence of masses and widths of the dynamical quasiparticles (quarks, antiquarks and gluons) to define the self-energies;

2. define the form of propagators for strongly interacting massive partons;

[1] We refer the reader to Refs. [384, 385] for the initial papers of the DQPM.

3. evaluate the QGP thermodynamics in equilibrium using the Kadanoff-Baym theory and calculate the entropy density s and other thermodynamic quantities such as the pressure P and energy density ϵ

4. compare the DQPM results with the lQCD ones at zero and finite μ_B and T and fix the initial parameters to obtain the best reproduction of the lQCD thermodynamics.

This defines the properties of the quasiparticles, their propagators and couplings. We recall the main ingredients of the DQPM:

1) The DQPM postulates retarded propagators of the quark and gluon degrees-of-freedom (for the QGP in equilibrium) in the form (see Eq. (2.87))

$$G^R(\omega, \mathbf{p}) = \frac{1}{\omega^2 - \mathbf{p}^2 - M^2 + 2i\gamma\omega} \tag{7.1}$$

using $\omega = p_0$ for the energy of the considered particle.

2) The coupling (squared) g^2, which is the essential quantity in the DQPM defining the strength of the interaction and which (as we will see) enters in the definition of the DQPM thermal masses and widths, is extracted from lQCD. In the previous DQPM studies [389–391], an ansatz was used for the (T, μ_B)-dependence of the coupling $g^2 = \alpha_s/(4\pi)$ which needed the extraction of 2 parameters - entering the parametrization of g^2 - from a global fit to the lQCD thermodynamics. Here we follow alternatively a similar procedure as in Refs. [230, 378] to determine the effective coupling (squared) g^2 as a function of temperature T, i.e. the coupling is defined at $\mu_B = 0$ directly by a parametrization of the entropy density from lattice QCD in the following way:

$$g^2(s/s_{SB}) = d\,((s/s_{SB})^e - 1)^f \tag{7.2}$$

with the Stefan-Boltzmann entropy density $s_{SB}^{QCD} = 19/9\ \pi^2 T^3$ and the parameters d = 169.934, e = -0.178434 and f = 1.14631. In the following, we use a parametrization of the entropy density at $\mu_B = 0$ calculated by lQCD from Refs. [95, 392] to determine the DQPM coupling constant as a function of temperature.

The extension to finite μ_B can be worked out in different scenarios. First of all, an expansion of the grand-canonical potential, i.e. the negative pressure P, in terms of μ_B/T can be performed and the expansion coefficients can be calculated by lQCD [101, 393]. This provides a solid framework for small and moderate

μ_B/T. Alternatively, Maxwell relations can be employed to extract the thermodynamic potential at finite μ_B starting from the information given by lQCD at $\mu_B = 0$ [394]. Both methods give almost the same results up to $\mu_B \approx 450$ MeV [395]. For practical purposes the explicit results can be fitted by a scaling ansatz [230] which works up to $\mu_B \approx 450$ MeV and suggests that the phase transition to the QGP is a crossover up to such baryon chemical potentials. We mention that the experimental studies of the STAR Collaboration within the BES program down to bombarding energies of $\sqrt{s_{NN}} = 7.7$ GeV - corresponding to $\mu_B \approx 450$ MeV - did not indicate any critical point in the QCD phase diagram [117] so far.

To obtain the coupling constant at finite baryon chemical potential μ_B, the scaling hypothesis assumes that g^2 is a function of the ratio of the effective temperature $T^* = \sqrt{T^2 + \mu_q^2/\pi^2}$ and the μ_B-dependent critical temperature $T_c(\mu_B)$ as [191]:

$$g^2(T/T_c, \mu_B) = g^2\left(\frac{T^*}{T_c(\mu_B)}, \mu_B = 0\right) \tag{7.3}$$

with $\mu_B = 3\mu_q$, $T_c(\mu_B) = T_c\sqrt{1 - \alpha\mu_B^2}$, where T_c is the critical temperature at vanishing chemical potential (≈ 0.158 GeV) and $\alpha = 0.974$ GeV^{-2}.

In Fig. 7.1 the DQPM running coupling $\alpha_s = g^2(T, \mu_B)/(4\pi)$ is displayed as a function of the scaled temperature $T/T_c(\mu_B)$ for different values of the baryon chemical potential μ_B. We find that with increasing μ_B the effective coupling drops in the vicinity of the critical temperature $T_c(\mu_B)$. This drop is rather moderate up to $\mu_B = 0.4$ GeV (adequate for central Au+Au collisions at 30 A GeV) but becomes significant for $\mu_B = 0.6$ GeV (roughly adequate for central Au+Au collisions at 10 A GeV). A comparison to the lattice results for quenched QCD from Ref. [396] - scaled by $T_c \approx 270$ MeV - shows that the DQPM coupling qualitatively matches the lattice results but is slightly larger for lower μ_B. We note, however, that this comparison should be taken only for orientation since the DQPM coupling corresponds to unquenched QCD with three light flavors ($N_f = 2{+}1$) whereas the lattice results are for quenched QCD ($N_f = 0$). Note that - since the running coupling (squared) $g^2 \sim (11N_c - 2N_f)^{-1}$ ($N_c = 3$) - the coupling is larger for a finite number of flavors N_f compared to $N_f = 0$.

With the coupling g^2 fixed from lQCD one can now specify the dynamical quasiparticle mass (for gluons and quarks) which are assumed to be given by the HTL thermal mass in the asymptotic high-momentum regime, i.e. for gluons by [136, 397]

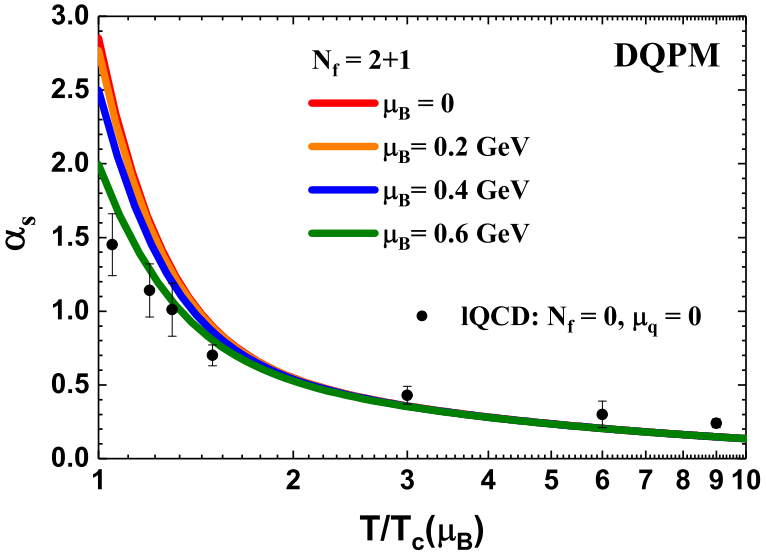

Figure 7.1 – The DQPM running coupling $\alpha_s = g^2(T,\mu_B)/(4\pi)$ (for $N_f = 2{+}1$) as a function of the scaled temperature $T/T_c(\mu_B)$ for different values of the baryon chemical potential μ_B. The lattice results for quenched QCD (for $N_f = 0$) are taken from Ref. [396] and scaled by the critical temperature $T_c \approx 270$ MeV.

$$M_g^2(T,\mu_B) = \frac{g^2(T,\mu_B)}{6}\left(\left(N_c + \frac{1}{2}N_f\right)T^2 + \frac{N_c}{2}\sum_q \frac{\mu_q^2}{\pi^2}\right) , \tag{7.4}$$

and for quarks (antiquarks) by

$$M_{q(\bar{q})}^2(T,\mu_B) = \frac{N_c^2-1}{8N_c} g^2(T,\mu_B)\left(T^2 + \frac{\mu_q^2}{\pi^2}\right) \tag{7.5}$$

where $N_c = 3$ stands for the number of colors while N_f $(= 3)$ denotes the number of flavors. The dynamical masses (7.5) in the QGP appear to be large compared to the bare masses of the light (u,d) quarks and therefore the latter are neglected in Eq. (7.5). However, the strange quark has a larger bare mass which needs to be added to the dynamical mass $M_s(T)$. This essentially suppresses the channel $g \to s + \bar{s}$ relative to the channel $g \to u + \bar{u}$ or $d + \bar{d}$ and controls the strangeness ratio in the QGP. Empirically $M_s(T,\mu_B) = M_u(T,\mu_B) + \Delta M = M_d(T,\mu_B) + \Delta M$ where $\Delta M = 30$ MeV has been used, which has been fixed once in comparison to experimental data for the K^+/π^+ ratio in central Au+Au collisions at $\sqrt{s_{NN}} =$ 200 GeV (see Fig. 6.6). Furthermore, the effective quarks, antiquarks and gluons in the DQPM have finite widths, which are adopted in the form [136]

$$\gamma_g(T,\mu_B) = \frac{1}{3} N_c \frac{g^2(T,\mu_B) T}{8\pi} \ln\left(\frac{2c}{g^2(T,\mu_B)} + 1\right), \tag{7.6}$$

$$\gamma_{q(\bar{q})}(T,\mu_B) = \frac{1}{3} \frac{N_c^2 - 1}{2N_c} \frac{g^2(T,\mu_B) T}{8\pi} \ln\left(\frac{2c}{g^2(T,\mu_B)} + 1\right), \tag{7.7}$$

where $c = 14.4$ is related to a magnetic cut-off, which is an additional parameter of the DQPM. Furthermore, we assume that the width of the strange quark is the same as that for the light (u,d) quarks. The DQPM masses M_i and widths γ_i are displayed in Fig. 7.2 as a function of the temperature T for different values of the chemical potential μ_B. One can see that the masses and widths increase linearly at large temperatures whereas at temperatures close to $T_c(\mu_B)$ the DQPM masses are enhanced. Furthermore, the behavior at finite baryon chemical potential follows the one of the coupling $g^2(T,\mu_B)$, and thus a decrease is observed with increasing μ_B.

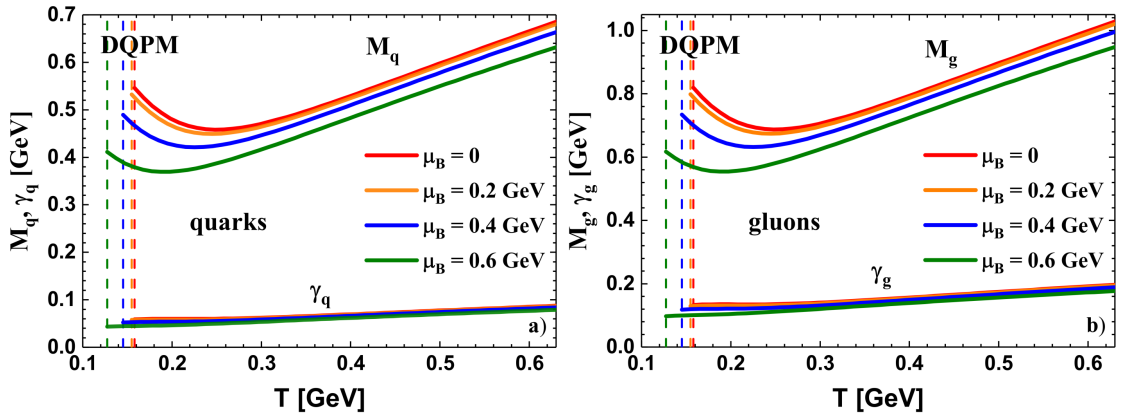

Figure 7.2 – The effective quark (a) and gluon (b) masses M and widths γ (from the parametrizations (7.4), (7.5), (7.6) and (7.7)) as a function of the temperature T for different μ_B. The vertical dashed lines correspond to the μ_B dependent critical temperature $T_c(\mu_B)$ of the DQPM.

The physical processes contributing to the width γ_g are both $gg \leftrightarrow gg$, $gq \leftrightarrow gq$ scattering as well as splitting and fusion reactions $gg \leftrightarrow g$, $gg \leftrightarrow ggg$, $ggg \leftrightarrow gggg$ or $g \leftrightarrow q\bar{q}$ etc. On the fermion side elastic fermion-fermion scattering $pp \leftrightarrow pp$, where p stands for a quark q or antiquark $\bar{q}$, fermion-gluon scattering $pg \leftrightarrow pg$, gluon bremsstrahlung $pp \leftrightarrow pp + g$ or quark-antiquark fusion $q\bar{q} \leftrightarrow g$ etc. contribute to γ_p. Note, however, that the explicit form of (7.6) is derived for hard two-body scatterings only [158]. Furthermore, the widths $\gamma_{q(\bar{q})}(T)$ and $\gamma_g(T)$ provide only

information on the total interaction rates and not on the individual differential cross sections. The computation of these cross sections will be carried out here in leading order on the basis of the propagators (7.1) and coupling (7.2)-(7.3) in Section 7.2 which in turn will allow to recalculate the widths (7.6) and (7.7) and explore the validity of the quasiparticle limit in the time-like sector.

7.1.2 Spectral functions

In line with the propagator (7.1) the parton spectral functions (or imaginary parts of the propagator $\rho = -2\,\mathrm{Im}\,G^R$) are no longer δ-functions in the invariant mass squared but given by

$$\begin{aligned}\rho_j(\omega,\mathbf{p}) &= \frac{\gamma_j}{\tilde{E}_j}\left(\frac{1}{(\omega-\tilde{E}_j)^2+\gamma_j^2}-\frac{1}{(\omega+\tilde{E}_j)^2+\gamma_j^2}\right)\\ &\equiv \frac{4\omega\gamma_j}{\left(\omega^2-\mathbf{p}^2-M_j^2\right)^2+4\gamma_j^2\omega^2}\end{aligned} \tag{7.8}$$

separately for quarks, antiquarks and gluons ($j = q, \bar{q}, g$). Here $\tilde{E}_j^2(\mathbf{p}) = \mathbf{p}^2 + M_j^2 - \gamma_j^2$, where the widths γ_j and masses M_j from the DQPM have been described above. The spectral function (7.8) is antisymmetric in ω and normalized as [398]

$$\int_{-\infty}^{\infty}\frac{d\omega}{2\pi}\;\omega\;\rho_j(\omega,\mathbf{p}) = \int_{0}^{\infty}\frac{d\omega}{2\pi}\;2\omega\;\rho_j(\omega,\mathbf{p}) = 1 \tag{7.9}$$

as mandatory for quantum field theory. We illustrate in Fig. 7.3 the behavior of the spectral function ρ as a function of the energy ω and momentum $\mathbf{p}$ for a fixed value of the pole mass $M = 0.5$ GeV and width $\gamma = 0.1$ GeV. One can see that the peak of the spectral function is situated at the "pole energy" $E = \sqrt{\mathbf{p}^2 + M^2}$ (see the vertical dashed lines on the left-hand side of Fig. 7.3) and that its value decreases with increasing momentum. Also at larger momenta, the space-like sector $\omega < p$ (indicated by the thick dashed lines on the left-hand side of Fig. 7.3) has a bigger contribution to the integral of the spectral function (7.9) and asymptotically is found to contribute equally as the time-like part.

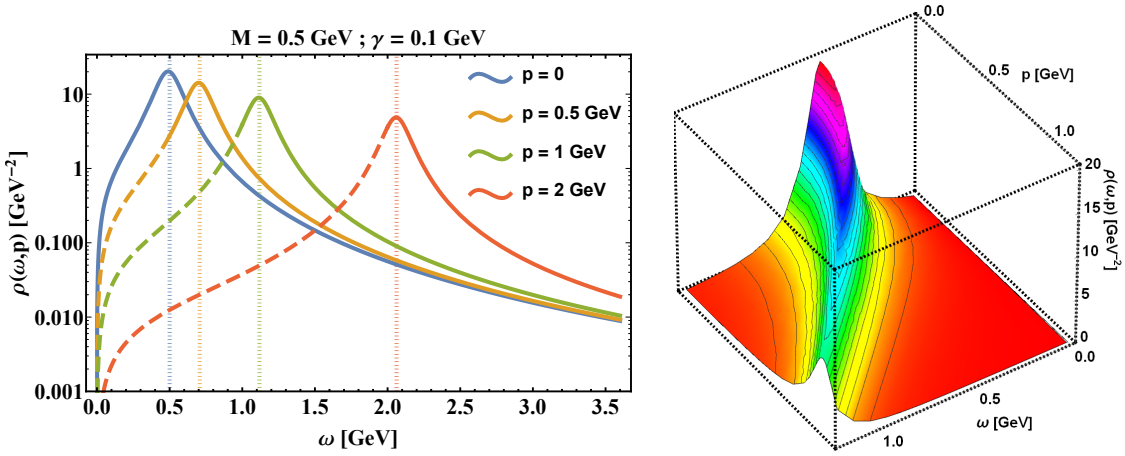

Figure 7.3 – Lorentzian spectral function from Eq. (7.8) as a function of the energy ω and momentum $\mathbf{p}$. The pole mass is taken to be $M = 0.5$ GeV and the width $\gamma = 0.1$ GeV for illustration.

7.1.3 Thermodynamics within the DQPM

With the quasiparticle properties (or propagators) chosen as described above, one can evaluate the entropy density $s(T,\mu_B)$, the pressure $P(T,\mu_B)$ and energy density $\epsilon(T,\mu_B)$ in a straight forward manner by starting with the entropy density and number density in the propagator representation from Baym [388, 399],

$$s^{dqp} = -\int \frac{d\omega}{2\pi}\frac{d^3p}{(2\pi)^3}\Big[d_g\,\frac{\partial n_B}{\partial T}\Big(\mathrm{Im}(\ln -\Delta^{-1}) + \mathrm{Im}\,\Pi\,\mathrm{Re}\,\Delta\Big) \tag{7.10}$$

$$+\sum_{q=u,d,s} d_q\,\frac{\partial n_F(\omega-\mu_q)}{\partial T}\Big(\mathrm{Im}(\ln -S_q^{-1}) + \mathrm{Im}\,\Sigma_q\,\mathrm{Re}\,S_q\Big)$$

$$+\sum_{\bar{q}=\bar{u},\bar{d},\bar{s}} d_{\bar{q}}\,\frac{\partial n_F(\omega+\mu_q)}{\partial T}\Big(\mathrm{Im}(\ln -S_{\bar{q}}^{-1}) + \mathrm{Im}\,\Sigma_{\bar{q}}\,\mathrm{Re}\,S_{\bar{q}}\Big)\Big]$$

$$n^{dqp} = -\int \frac{d\omega}{2\pi}\frac{d^3p}{(2\pi)^3}\Big[\sum_{q=u,d,s} d_q\,\frac{\partial n_F(\omega-\mu_q)}{\partial \mu_q}\Big(\mathrm{Im}(\ln -S_q^{-1}) + \mathrm{Im}\,\Sigma_q\,\mathrm{Re}\,S_q\Big) \tag{7.11}$$

$$+\sum_{\bar{q}=\bar{u},\bar{d},\bar{s}} d_{\bar{q}}\,\frac{\partial n_F(\omega+\mu_q)}{\partial \mu_q}\Big(\mathrm{Im}(\ln -S_{\bar{q}}^{-1}) + \mathrm{Im}\,\Sigma_{\bar{q}}\,\mathrm{Re}\,S_{\bar{q}}\Big)\Big]$$

where $n_B(\omega) = (\exp(\omega/T) - 1)^{-1}$ and $n_F(\omega - \mu_q) = (\exp((\omega - \mu_q)/T) + 1)^{-1}$ denote the Bose-Einstein and Fermi-Dirac distribution functions, respectively, while $\Delta = (p^2 - \Pi)^{-1}$, $S_q = (p^2 - \Sigma_q)^{-1}$ and $S_{\bar{q}} = (p^2 - \Sigma_{\bar{q}})^{-1}$ stand for the full (scalar) quasiparticle propagators of gluons g, quarks q and antiquarks $\bar{q}$. In Eq. (7.10)-(7.11) Π and $\Sigma = \Sigma_q \approx \Sigma_{\bar{q}}$ denote the (retarded) quasiparticle self-energies. Furthermore, the number of transverse gluonic degrees-of-freedom is $d_g = 2 \times (N_c^2 - 1)$ while for the fermion degrees-of-freedom we use $d_q = 2 \times N_c$ and $d_{\bar{q}} = 2 \times N_c$.

In principle, Π as well as Δ are Lorentz tensors and should be evaluated in a nonperturbative framework. The DQPM treats these degrees-of-freedom as independent scalar fields (for each color and spin projection) with scalar self-energies which are assumed to be identical for quarks and antiquarks. This is expected to hold well for the entropy and number density. Note that one has to treat quarks and antiquarks separately in Eqs. (7.10)-(7.11) as their abundance differs at finite quark chemical potential $\mu_q = \mu_B/3$.

With the choice (7.1) the complex self-energies $\Pi = M_g^2 - 2i\omega\gamma_g$ and $\Sigma_q = M_q^2 - 2i\omega\gamma_q$ are fully defined via (7.4), (7.5), (7.6), (7.7). Note that the retarded propagator (7.1) resembles the propagator of a damped harmonic oscillator (with an additional $\mathbf{p}^2$) and preserves microcausality also for $\gamma > M$ [164], i.e. in case of overdamped motion. Although the 'Ansatz' for the parton propagators is not QCD it has been shown that a variety of QCD observables on the lattice are compatible with this choice [136].

In case the real and imaginary parts of the propagators Δ and S are fixed, the entropy density (7.10) and number density (7.11) can be evaluated numerically. As we deal with a grand-canonical ensemble the Maxwell relations give,

$$s = \frac{\partial P}{\partial T} \quad ; \quad n_B = \frac{\partial P}{\partial \mu_B} \ , \tag{7.12}$$

such that the pressure can be obtained by integration of the entropy density s over T and of the baryon density n_B over μ_B as:

$$P(T, \mu_B) = P(T_0, 0) + \int_{T_0}^{T} s(T', 0)\ dT' + \int_0^{\mu_B} n_B(T, \mu_B')\ d\mu_B' \tag{7.13}$$

where one identifies the 'full' entropy density s and baryon density n_B with the quasiparticle entropy density s^{dqp} (7.10) and baryon density $n_B = n^{dqp}/3$ (7.11).

The starting point T_0 for the integration in T is chosen between $0.1 < T < 0.15$ GeV where the entropy density is taken in accordance to the lattice QCD results from Ref. [95] in the hadronic sector.

The energy density ϵ then follows from the thermodynamical relation

$$\epsilon = Ts - P + \mu_B n_B \tag{7.14}$$

and thus is also fixed by the entropy $s(T, \mu_B)$ and baryon density $n_B(T, \mu_B)$ as well as the interaction measure

$$I := \epsilon - 3P = Ts - 4P + \mu_B n_B \tag{7.15}$$

that vanishes for massless and noninteracting degrees-of-freedom at $\mu_B = 0$.

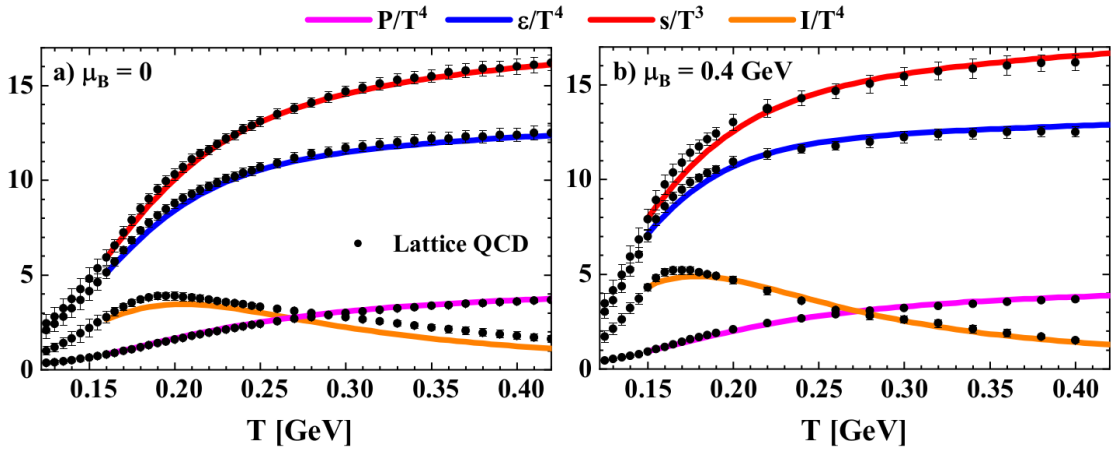

Figure 7.4 – The scaled pressure $P(T)/T^4$ (pink line), entropy density $s(T)/T^3$ (red line), scaled energy density $\epsilon(T)/T^4$ (blue line), and interaction measure (7.15) (orange line), from the DQPM in comparison to the lQCD results from Refs. [95, 392] (full dots) for $\mu_B = 0$ (a) and $\mu_B = 400$ MeV (b).

A direct comparison of the resulting entropy density $s(T)$ (7.10), pressure $P(T)$ (7.13), energy density $\epsilon(T)$ (7.14) and interaction measure (7.15) from the DQPM with lQCD results from the BMW group [95, 392] at $\mu_B = 0$ (a) and $\mu_B = 400$ MeV (b) is presented in Fig. 7.4. The dimensionless results s/T^3, P/T^4 and ϵ/T^4, are shown to demonstrate the scaling with temperature. The agreement is sufficiently good for the entropy and energy density as well as for the pressure. A satisfactory agreement also holds for the dimensionless 'interaction measure', i.e.

$(\epsilon - 3P)/T^4$ (cf. orange line in Fig. 7.4). In Fig. 7.5 we show the resulting baryon density $n_B(T)$ for different values of μ_B for the case of the DQPM (full lines) as well as for the DQPM* [230, 378] (dashed lines). The DQPM* is very similar as the DQPM in its assumptions since it differs only by the fact that the parton masses and widths possess a momentum dependence. Although the latter does not lead to significant changes in case of the thermodynamic quantities shown in Fig. 7.4, one can see that the baryon density is better described in case of the DQPM* compared to the DQPM which underestimates the lQCD data.

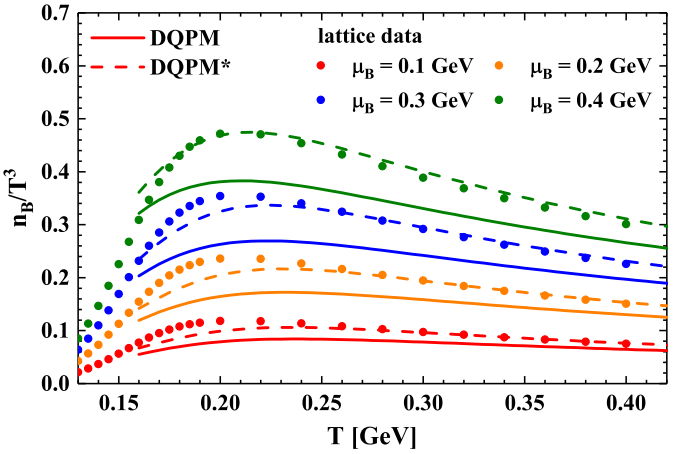

Figure 7.5 – The scaled baryon density $n_B(T)/T^3$ from the DQPM (solid lines) and the DQPM* (dashed lines) in comparison to the lQCD results from Refs. [95, 392] (full dots) for different values of the baryon chemical potential μ_B.

7.2 Differential cross sections for partonic interactions

Although the DQPM inherits the information on the total interaction rates of the degrees of freedom in terms of widths it lacks the individual total as well as differential cross sections for different reaction channels with partons that are needed in the collision terms of a consistent relativistic transport approach. In PHSD these cross sections have been parametrized so far to comply with the individual widths of quarks, antiquarks and gluons as a function of energy density (cf. chapter 3) which can be related to the temperature T by the lQCD equation of state (EoS). In this chapter we will calculate these total and differential cross sections in leading order for the individual partonic channels on the basis of the DQPM propagators

and couplings. This will allow to explore the energy and angular dependence of partonic cross sections additionally on their T and μ_B dependence.

7.2.1 Definitions

On-shell case The differential cross section for a $2 \to 2$ process of on-shell particles $(1+2 \to 3+4)$ is given by:

$$d\sigma^{\text{on}} = \frac{d^3p_3}{(2\pi)^3 2E_3} \frac{d^3p_4}{(2\pi)^3 2E_4} (2\pi)^4 \delta^{(4)}(p_1+p_2-p_3-p_4) \frac{|\bar{\mathcal{M}}|^2}{F}, \tag{7.16}$$

where the flux is defined by $F = v_{\text{rel}}\, 2E_1\, 2E_2$ with $v_{\text{rel}} = |\vec{v}_1 - \vec{v}_2|$, and the on-shell energies for the particle are $E_j = \sqrt{\mathbf{p}_j^2 + M_j^2}$. $|\bar{\mathcal{M}}|^2$ denotes the matrix element squared averaged over the color and spin of the incoming particles, and summed over those of the final particles. We want to evaluate the cross section in the rest frame of the heat bath where the Fermi-Dirac or Bose-Einstein functions describe the particle distributions. The only factor in Eq. (7.16) which is not Lorentz invariant is the flux factor F while the other factors, the Lorentz Invariant Phase Space (LIPS), the matrix element $|\bar{\mathcal{M}}|^2$ and the delta function for energy-momentum conservation, are invariant. This implies that the cross section can be calculated in any frame, but the flux factor has to be correctly taken into account according to the actual frame of interest (see also Appendix C).

The cross section is usually evaluated in the center of mass (CM) frame of the collision for simplicity. In this case the momenta of the colliding particles obey $\mathbf{p}_1 + \mathbf{p}_2 = \mathbf{p}_3 + \mathbf{p}_4 = \mathbf{p} = \vec{0}$, and the notation $|\mathbf{p_1}| = |\mathbf{p_2}| = p_i$ and $|\mathbf{p_3}| = |\mathbf{p_4}| = p_f$ is used. The flux factor becomes $F^{\text{CM}} = 4p_i\sqrt{s}$ and, after simplification, Eq. (7.16) reads:

$$d\sigma_{\text{on}}^{\text{CM}} = \frac{p_f\, d\Omega}{16\pi^2\sqrt{s}} \frac{|\bar{\mathcal{M}}|^2}{F^{\text{CM}}} = \frac{d\Omega}{64\pi^2 s} \frac{p_f}{p_i} |\bar{\mathcal{M}}|^2, \tag{7.17}$$

where s is the Mandelstam variable and $d\Omega$ is the differential solid angle corresponding to one of the final particles. The momenta of the initial (i) and final particles (f) in the CM frame is found to be:

$$p_{i,f} = \frac{\sqrt{\left(s - (M_{i,f} + M'_{i,f})^2\right)\left(s - (M_{i,f} - M'_{i,f})^2\right)}}{2\sqrt{s}}, \tag{7.18}$$

with $M_{i,f}$ and $M'_{i,f}$ being the masses of the colliding partons. The total cross section is obtained by performing the integral in Eq. (7.17) over $d\Omega$ as:

$$\sigma_{\rm on}^{\rm CM} = \frac{1}{32\pi s}\frac{p_f}{p_i}\int_{-1}^{1} d\cos(\theta)|\bar{\mathcal{M}}|^2, \tag{7.19}$$

where θ is the final polar angle of one of the final particle in the CM frame. In the CM frame, the collision is independent from the azimuthal angle ϕ and the corresponding integration gives a factor 2π.

Off-shell case In the off-shell case, the energy of the partons, as well their momenta, are independent degrees of freedom and a general definition of an 'off-shell cross section' is not possible due to the lack of asymptotically stable states. However, transition matrix elements for different incoming and outgoing 4-momenta can be well defined also off-shell. By transforming the Lorentz invariant phase space in Eq. (7.16), one can include the off-shell effects for the scattering of time-like particles - in case of a well defined incoming flux $F = v_{\rm rel}\ 2\omega_1\ 2\omega_2$ - by integrating over the energy of the final time-like particles as:

$$\begin{aligned} F d\sigma^{\rm off} = &\frac{d^4p_3}{(2\pi)^4}\ \frac{d^4p_4}{(2\pi)^4}\ \tilde{\rho}_3(\omega_3,\mathbf{p}_3)\ \theta(\omega_3)\ \tilde{\rho}_4(\omega_4,\mathbf{p}_4)\ \theta(\omega_4) \\ &\times (2\pi)^4\delta^{(4)}\left(p_1+p_2-p_3-p_4\right)|\bar{\mathcal{M}}|^2 \end{aligned} \tag{7.20}$$

with the renormalized time-like spectral functions

$$\tilde{\rho}_j(\omega_j,\mathbf{p}_j) = \frac{\rho(\omega_j,\mathbf{p}_j)\ \theta(p_j^2)}{\int_0^\infty \frac{d\omega_j}{(2\pi)}\ 2\omega_j\ \rho(\omega_j,\mathbf{p}_j)\ \theta(p_j^2)}, \tag{7.21}$$

where the spectral function ρ_i in (7.21) - corresponding to the parton type i - is taken from Eq. (7.8). The final parton masses are defined as $m_i^2 = p_i^2 = \omega_i^2 - \mathbf{p}_i^2$ where p_i is the 4-momentum of particle i. One can verify that by replacing the spectral functions by their on-shell value:

$$\begin{aligned} \lim_{\gamma_j\to 0}\ \rho_j(\omega,\mathbf{p}) &= 2\pi\ \delta(\omega^2-\mathbf{p}^2-M_j^2) \\ &= \frac{\pi}{\omega}\ \left[\delta(\omega-\sqrt{\mathbf{p}^2+M_j^2})+\delta(\omega+\sqrt{\mathbf{p}^2+M_j^2})\right], \end{aligned} \tag{7.22}$$

the off-shell cross section leads to the on-shell one as defined previously in Eq. (7.16).

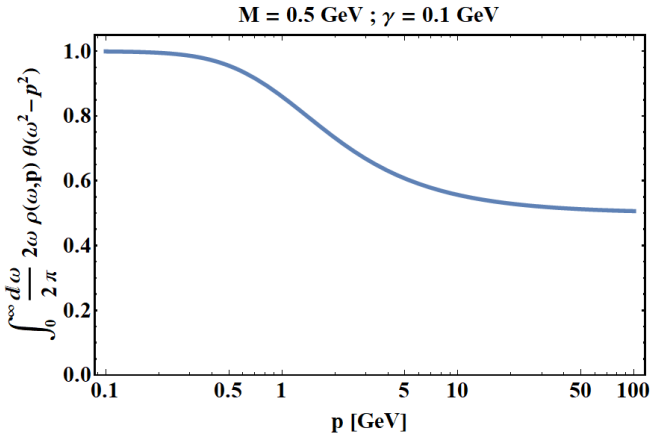

Figure 7.6 – Denominator of the renormalized spectral function $\tilde{\rho}$ in Eq. (7.21) as a function of the momentum in the heat bath.

We follow the same strategy as in the previous subsection and evaluate the differential "off-shell cross section" for time-like quanta in the center of mass system of the collision for convenience. By making use of the delta function in Eq. (7.20), one can integrate over d^4p_4 to obtain the total cross section in the CM frame by performing the integrations with the appropriate boundaries (see Appendix B) as:

$$F^{\mathrm{CM}}\sigma_{\mathrm{off}}^{\mathrm{CM}} = \frac{1}{(2\pi)^3}\int_0^{\sqrt{s}/2} p_f^2\; dp_f\; d\cos(\theta) \int_{p_f}^{\sqrt{s}-p_f} d\omega_3^{\mathrm{CM}} \tilde{\rho}_3(\omega_3,\mathbf{p}_3)\; \tilde{\rho}_4(\omega_4,\mathbf{p}_4)\; |\bar{\mathcal{M}}|^2 \tag{7.23}$$

for $F^{CM} = 4p_i^{\mathrm{CM}}\sqrt{s}$. Bear in mind that even if the calculation of the cross section is performed in the center of mass system, the energies and momenta entering the spectral functions (7.8) should be expressed in the heat bath frame by applying the appropriate Lorentz transformations.

We mention that one can simplify the off-shell energy integration by an integration over the final masses of the partons in the non-relativistic limit. The off-shell cross section from Eq. (7.20) then becomes [389]:

$$\sigma_{\mathrm{off}}^{\mathrm{BW}} = \int_0^{\sqrt{s}} dm_3 \int_0^{\sqrt{s}-m_3} dm_4\; \rho^{\mathrm{BW}}(m_3)\; \rho^{\mathrm{BW}}(m_4) \int d\sigma_{\mathrm{on}}^{\mathrm{CM}}, \tag{7.24}$$

where the Breit-Wigner spectral function $\rho^{\rm BW}$ in Ref. [389] is obtained from Eq. (7.8) in the limit $\omega \to m$:

$$\rho_i^{\rm BW}(m) = \frac{2}{\pi} \frac{2m^2\gamma_i}{(m^2 - M_i^2)^2 + (2m\gamma_i)^2}. \tag{7.25}$$

This distribution fulfills the normalization $\int_0^\infty dm\ \rho^{\rm BW}(m) = 1$. We refer the reader to the Appendix B for a comparison between the Lorentzian and Breit-Wigner spectral functions.

7.2.2 Partonic scattering

In the framework of the DQPM, quarks and gluons are massive with a finite lifetime associated to their interaction width. In order to calculate the matrix elements corresponding to a scattering of DQPM partons, the scalar propagator (7.1) has to be replaced by the following propagators - with full Lorentz structure - to describe a massive vector gluon and massive (spin 1/2) fermion with a finite width [389]:

$$= -i\delta_{ab} \frac{g^{\mu\nu} - q^\mu q^\nu / M_g^2}{q^2 - M_g^2 + 2i\gamma_g q_0}, \tag{7.26}$$

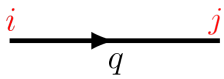

$$= i\delta_{ij} \frac{\not{q} + M_q}{q^2 - M_q^2 + 2i\gamma_q q_0}, \tag{7.27}$$

where q is the 4-momentum of the exchanged particle. The delta functions ensure that the exchanged quark or gluon is connected with other parts of the diagram with the same color (a, b for the gluon and i, j for the quark). The invariant matrix element (squared) $|\bar{\mathcal{M}}|^2$, entering the differential cross section in Eqs. (7.16)-(7.20), is calculated in leading order, and is averaged over initial - and summed over final - spin and colors. In the following, we employ a degeneracy factor for spin and color of $d_q = 2 \times N_c = 6$ for quarks, and $d_g = 2 \times (N_c^2 - 1) = 16$ for gluons in consistency with Eqs. (7.10)-(7.11). Each matrix element can be decomposed into several channels known as $t-$,$u-$,$s-$channels for quark-quark (qq') and quark-gluon (qg) scatterings, as well as a 4-point interaction for the case of gluon-gluon (gg) scattering. For details we refer the reader to the Appendices B and continue with the actual results.

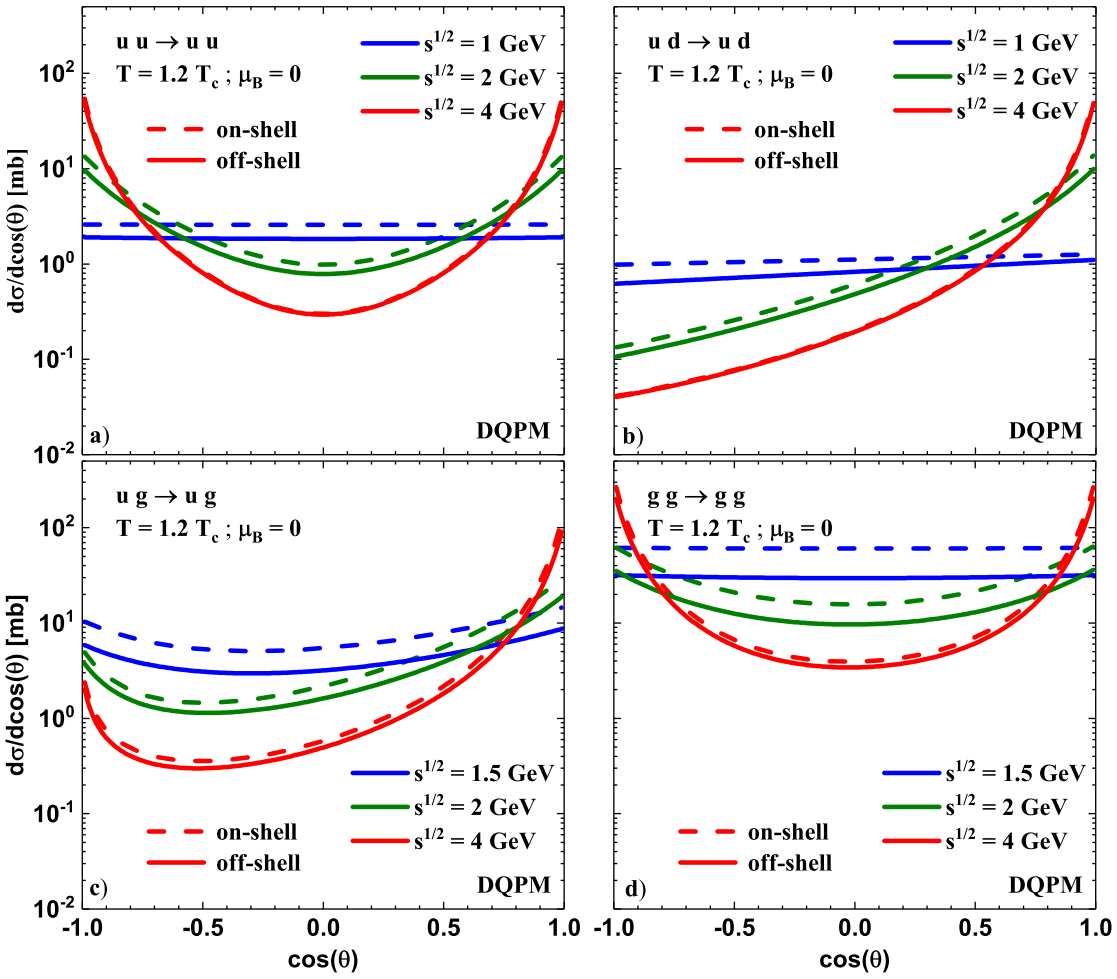

Figure 7.7 – Elastic differential cross sections between different partons for the on-shell case (dashed lines) from Eq. (7.17) and the "off-shell case" (solid lines) evaluated in the center of mass of the collision system as a function of the angle $\cos(\theta)$ between the initial and final momentum of one of the partons for $T = 1.2T_c$ and $\mu_B = 0$. The initial masses of the colliding partons are taken as the pole masses from Eqs. (7.4)-(7.5). The different lines correspond to different collision energies $\sqrt{s}$ from 1 to 4 GeV (see legend).

In Fig. 7.7 we show the differential cross sections between different partons for the on-shell case (dashed lines) from Eq. (7.17) and the "off-shell case" (solid lines) evaluated in the center of mass of the collision system as a function of the collision energy $\sqrt{s}$. In these examples the initial masses of the colliding partons are taken as the pole masses from Eqs. (7.4)-(7.5) to allow for a comparison between on-shell and off-shell scattering, i.e. for the same initial states. In all cases

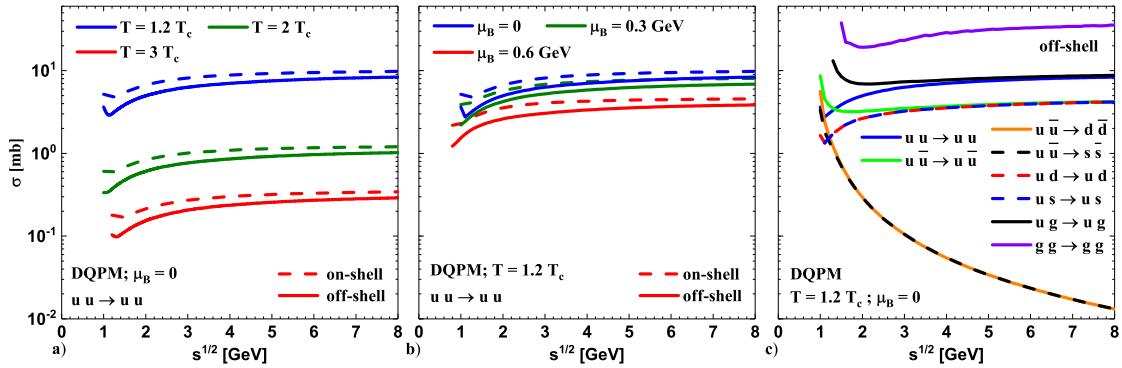

Figure 7.8 – Cross sections between different partons for the on-shell case (dashed lines) from Eq. (7.19) and the "off-shell case" (solid lines) from Eq. (7.23) evaluated in the center of mass of the collision system as a function of the collision energy $\sqrt{s}$ (see text for a detailed description). The initial masses of the colliding partons are taken as the pole masses from Eqs. (7.4)-(7.5).

($uu \to uu$ (a), $ud \to ud$ (b), $ug \to ug$ (c), $gg \to gg$ (d)) the cross sections are almost isotropic at $\sqrt{s} \approx 1$ GeV (close to threshold) and increase in anisotropy with increasing $\sqrt{s}$. Furthermore, the on-shell case (dashed lines) gives slightly larger cross sections than the off-shell case (solid lines) especially for low collisional energies, since for a larger $\sqrt{s}$ the energy integration over the final states in Eq. (7.23) covers more of the spectral functions.

Fig. 7.8 (a) displays the angle integrated cross section for $uu \to uu$ scattering as a function of $\sqrt{s}$ for temperatures of $T = 1.2T_c$ (blue), $T = 2T_c$ (green), and $T = 3T_c$ (red) for the on-shell (dashed lines) and off-shell (solid lines) cases at $\mu_B = 0$. Again the initial masses of the colliding partons are taken as the pole masses from Eqs. (7.4)-(7.5) to obtain the same initial flux F. At all temperatures T the cross section does not change very much with collision energy $\sqrt{s}$ and the difference between the on-shell and off-shell case again decreases with increasing $\sqrt{s}$. The explicit dependence of the $uu \to uu$ cross section on the chemical potential is shown in Fig. 7.8 (b) for $\mu_B = 0$ (blue), $\mu_B = 0.3$ GeV (green) and $\mu_B = 0.6$ GeV (red) at $T = 1.2T_c$ for the on-shell (dashed lines) and off-shell (solid lines) cases. While the dependencies on $\sqrt{s}$ are similar we find a small decrease of the cross section with increasing chemical potential μ_B which can be traced back to a decreasing coupling with μ_B at fixed temperature T (see Fig. 7.1). Fig. 7.8 (c), furthermore, shows the dependence of all cross sections calculated on the collision energy $\sqrt{s}$ in the off-shell case for $T = 1.2T_c$ and $\mu_B = 0$. While most of the channels do not change drastically with $\sqrt{s}$ - except for thresholds - the flavor changing processes $u\bar{u} \to d\bar{d}$ and $u\bar{u} \to s\bar{s}$ drop fast with increasing energy since they contain only a

$s-$channel contribution.

With all differential partonic cross sections fixed as a function of T and μ_B (above the phase boundary) we can now continue with transport properties of the hot QGP as a function of T and μ_B employing the partonic energy-momentum distributions from the DQPM.

7.3 Collisional widths of the hot and dense QGP

On-shell case In the on-shell case all energies of the particles are taken to be $E^2 = \mathbf{p}^2 + M^2$ where M is the pole mass. The on-shell interaction rate for the corresponding parton is given by [386, 400, 401]:

$$\begin{aligned}\Gamma_i^{\rm on}(\mathbf{p}_i, T, \mu_q) = \frac{1}{2E_i} \sum_{j=q,\bar{q},g} \int \frac{d^3p_j}{(2\pi)^3 2E_j}\ d_j\ f_j(E_j, T, \mu_q) \\ \times \int \frac{d^3p_3}{(2\pi)^3 2E_3} \int \frac{d^3p_4}{(2\pi)^3 2E_4} (1 \pm f_3)(1 \pm f_4) \\ \times |\bar{\mathcal{M}}|^2(p_i, p_j, p_3, p_4)\ (2\pi)^4 \delta^{(4)}\left(p_i + p_j - p_3 - p_4\right) \\ = \sum_{j=q,\bar{q},g} \int \frac{d^3p_j}{(2\pi)^3}\ d_j\ f_j\ v_{\rm rel} \int d\sigma^{\rm on}_{ij\to 34}\ (1 \pm f_3)(1 \pm f_4), \end{aligned} \tag{7.28}$$

where d_j is the degeneracy factor for spin and color (for quarks $d_q = 2 \times N_c$ and for gluons $d_g = 2 \times (N_c^2 - 1)$), and with the shorthand notation $f_j = f_j(E_j, T, \mu_q)$ for the distribution functions. In Eq. (7.28) and in all this section, the notation $\sum_{j=q,\bar{q},g}$ includes the contribution from all possible partons which in our case are the gluons and the (anti-)quarks of three different flavors (u, d, s). The Pauli-blocking (-) and Bose-enhancement (+) factors account for the available density of final states. Note that here all quantities have to be expressed in the rest frame of the heat bath, implying that the on-shell cross section $d\sigma^{\rm on}$ from Eq. (7.17) has to be modified according to the different fluxes:

$$F^{\rm HB} \sigma^{\rm HB} = \sigma^{\rm CM} F^{\rm CM}, \tag{7.29}$$

where the quantities denoted by HB are expressed in the rest frame of the heat bath and CM in the center of mass frame of the collision. To evaluate the average

width of the partons i, we finally have to average its interaction rate (7.28) over its momentum distribution,

$$\Gamma_i^{\rm on}(T,\mu_q) = \frac{d_i}{n_i^{\rm on}(T,\mu_q)} \int \frac{d^3p_i}{(2\pi)^3}\; f_i(E_i,T,\mu_q)\; \Gamma_i^{\rm on}(\mathbf{p}_i,T,\mu_q) \tag{7.30}$$

with the on-shell density of partons i at T and μ_q given by

$$n_i^{\rm on}(T,\mu_q) = d_i \int \frac{d^3p_i}{(2\pi)^3}\; f_i(E_i,T,\mu_q). \tag{7.31}$$

The distribution $dn_u^{\rm on}/dp$ is illustrated in the left-hand side of Fig. 7.9 as a function of the $u-$quark momentum for different temperatures. First one can see that the number of particles increases with temperature ($n \propto T^3$) and also that the distribution is shifted to higher momenta. As a result, the mean momentum of the particles increases with the temperature $\langle p \rangle \approx 3T$. On the right-hand side of Fig. 7.9 is shown the distribution of $u-$quark scatterings as a function of the collisional energy $\sqrt{s}$. One can see that accordingly to the momentum distribution dn_u^{on}/dp, larger values of $\sqrt{s}$ can be probed with increasing temperatures. Since the masses of the colliding particles are fixed to the pole mass, a sharp threshold is observed for the energy $\sqrt{s_{threshold}} = 2M_u(T)$.

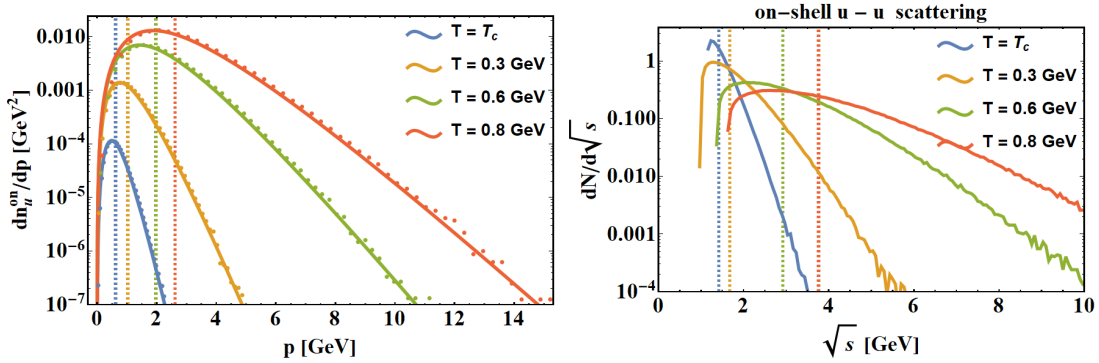

Figure 7.9 – Left: Distribution of on-shell $u-$quarks as a function of the momentum for different temperatures at $\mu_B = 0$. The dots represent the distribution evaluated by Monte-Carlo and the vertical dashed lines to the mean momentum of the particles for each temperature. Right: Distribution of on-shell $u-$quark scatterings as a function of the invariant energy $\sqrt{s}$ for different temperatures at $\mu_B = 0$. The vertical dashed lines correspond to the mean $\sqrt{s}$ for each temperature.

Off-shell case In order to obtain the width for the off-shell DQPM time-like partons, we have to calculate the interaction rate for the corresponding parton i with momentum $\mathbf{p}_i$ due to collisions with time-like particles j leading to final time-like particles 3 and 4 by integrating additionally over all energies ω_j in the time-like sector:

$$\Gamma_i^{\rm off}(\mathbf{p}_i,T,\mu_q) = \int_0^\infty \frac{d\omega_i}{(2\pi)}\ \tilde{\rho}_i \sum_{j=q,\bar{q},g} \int \frac{d^4p_j}{(2\pi)^4}\ \theta(\omega_j)\ d_j\ \tilde{\rho}_j\ f_j$$
$$\times \int \frac{d^4p_3}{(2\pi)^4}\ \theta(\omega_3)\ \tilde{\rho}_3 \int \frac{d^4p_4}{(2\pi)^4}\ \theta(\omega_4)\ \tilde{\rho}_4(1\pm f_3)(1\pm f_4)$$
$$\times |\bar{\mathcal{M}}|^2(p_i,p_j,p_3,p_4)\ (2\pi)^4\delta^{(4)}\left(p_i+p_j-p_3-p_4\right), \tag{7.32}$$

where the shorthand notation $\tilde{\rho}$ (7.21) for the renormalized time-like spectral functions $\tilde{\rho}_j(\omega_j,\mathbf{p}_j)$ has been used and $f_j = f_j(\omega_j,T,\mu_q)$ for the distribution functions. We mention that the limit (7.32) discards damping processes between the time-like and space-like sector which are assumed to be subleading. To evaluate the average time-like width of the partons i, we finally have to average its interaction rate as:

$$\Gamma_i^{\rm off}(T,\mu_q) = \frac{d_i}{n_i^{\rm off}(T,\mu_q)} \int \frac{d^4p_i}{(2\pi)^4}\ \theta(\omega_i)\ \tilde{\rho}_i\ f_i(\omega_i,T,\mu_q) \times \sum_{j=q,\bar{q},g} \int \frac{d^4p_j}{(2\pi)^4}\ \theta(\omega_j)\ d_j\ \tilde{\rho}_j\ f_j \tag{7.33}$$
$$\times \int \frac{d^4p_3}{(2\pi)^4}\ \theta(\omega_3)\ \tilde{\rho}_3 \int \frac{d^4p_4}{(2\pi)^4}\ \theta(\omega_4)\ \tilde{\rho}_4(1\pm f_3)(1\pm f_4)$$
$$\times |\bar{\mathcal{M}}|^2(p_i,p_j,p_3,p_4)\ (2\pi)^4\delta^{(4)}\left(p_i+p_j-p_3-p_4\right),$$

with the off-shell density of time-like partons i given by

$$n_i^{\rm off}(T,\mu_q) = d_i \int \frac{d^4p_i}{(2\pi)^4}\ \theta(\omega_i)\ 2\omega_i\ \tilde{\rho}_i\ f_i(T,\mu_q). \tag{7.34}$$

The distribution $dn_u^{\rm off}/dp/d\omega$ is illustrated in Fig. 7.10 as a function of the $u-$quark energy ω for different momenta at a temperature of 0.158 GeV (left) and 0.8 GeV (right). A similar behavior is observed as in Fig. 7.3 for the spectral function since this distribution is also peaked at the "pole" energy $E_u = \sqrt{\mathbf{p}^2+M_u^2}$. However,

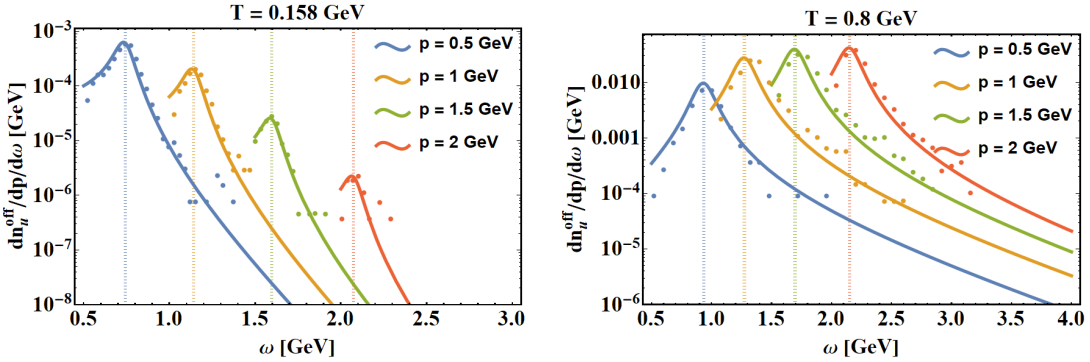

Figure 7.10 – Distribution of off-shell $u-$quarks as a function of the energy ω for different momenta for a temperature of 0.158 GeV (left) and 0.8 GeV (right) for $\mu_B = 0$. The dots represent the distribution evaluated by Monte-Carlo, and the vertical dashed lines correspond to "pole energy" E_u.

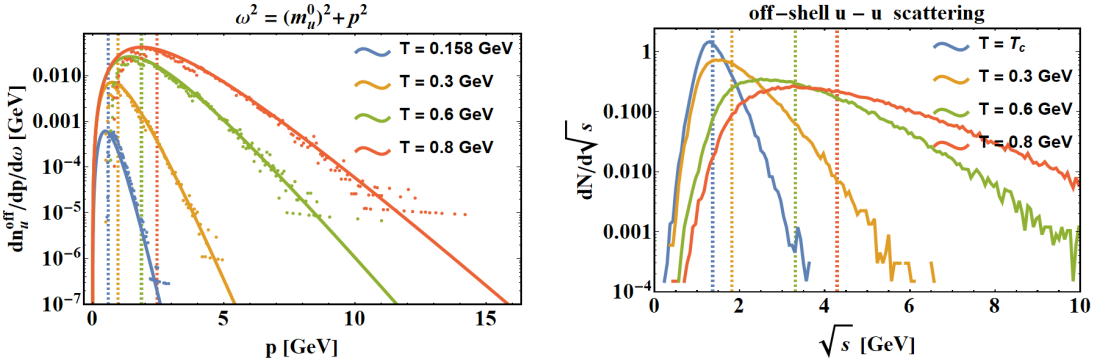

Figure 7.11 – Left: Distribution of off-shell $u-$quarks as a function of the momentum for the fixed energy E_u and for different temperatures at $\mu_B = 0$. The dots represent the distribution evaluated by Monte-Carlo and the vertical dashed lines to the mean momentum of the particles for each temperature. Right: Distribution of off-shell $u-$quark scatterings as a function of the invariant energy $\sqrt{s}$ for different temperatures at $\mu_B = 0$. The vertical dashed lines correspond to the mean $\sqrt{s}$ for each temperature.

in the left-hand side of Fig. 7.10, an enhancement is seen at lower values of the energy ω due to the Fermi-Dirac distribution, whereas the latter favors larger energies at higher temperatures (right-hand side of Fig. 7.10). In Fig. 7.11, the same comments as for Fig. 7.9 apply, expect for the energy distribution of $u-$quarks collisions where no sharp threshold is observed due to the off-shellness of the initial particles.

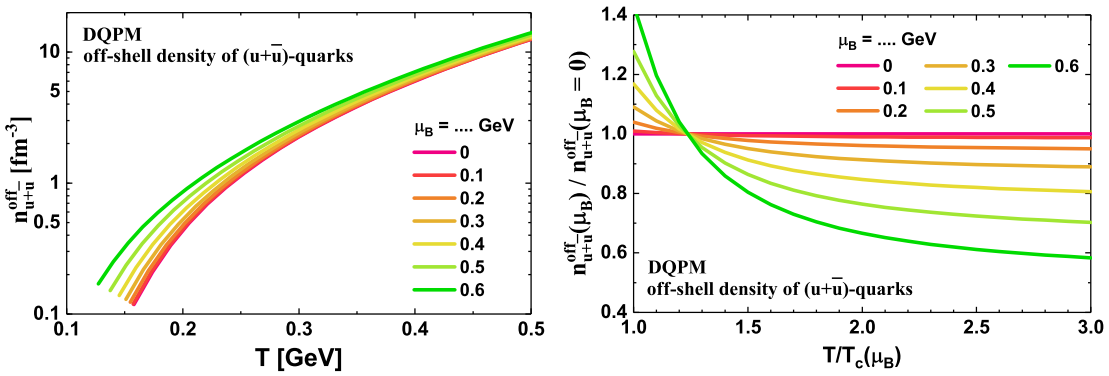

Figure 7.12 – Left: Density of $u+\bar{u}$ quarks as a function of the temperature T for different values of the chemical potential μ_B. Right: Ratio of the density of $u+\bar{u}$ quarks at finite μ_B over the one at $\mu_B = 0$ as a function of the temperature T.

In Fig. 7.12 we investigate the dependence of the $(u+\bar{u})$-quark density on the baryon chemical potential μ_B. One can see on the left-hand side of Fig. 7.12 that the density $n^{\rm off}_{u+\bar{u}}$ increases with μ_B for a fixed temperature. However as a function of the scaled temperature $T/T_c(\mu_B)$, one can see that the density of $u+\bar{u}$ quarks is enhanced close to $T_c(\mu_B)$ with increasing μ_B, and suppressed at higher temperatures (as seen in the right-hand side of Fig. 7.12).

After these preliminaries, we will now study the total interaction of a light quark q and a gluon g and see that it is closely related to the parton densities studied before. In fact, as seen from Eq. (7.28)-(7.32), the interaction rate of particle i is directly proportional to the density of the colliding partner j and its degeneracy factor d_j, and to their interaction cross section σ_{ij} as:

$$\Gamma_i \propto \sum_j d_j \; f_j \; \sigma_{ij}. \tag{7.35}$$

If we consider the $u-$quark scattering, we obtain for all the possible interaction channels:

- (1) : $uu \to uu$; $\Gamma_{uu\to uu} \propto d_u \; f_u \; \sigma_{uu\to uu}$ (t + u channels)
- (2) : $u\bar{u} \to u\bar{u}$; $\Gamma_{u\bar{u}\to u\bar{u}} \propto d_{\bar{u}} \; f_{\bar{u}} \; \sigma_{u\bar{u}\to u\bar{u}}$ (t + s channels)
- (3) : $u\bar{u} \to d\bar{d}$; $\Gamma_{u\bar{u}\to d\bar{d}} \propto d_{\bar{u}} \; f_{\bar{u}} \; \sigma_{u\bar{u}\to d\bar{d}}$ (s channel)
- (4) : $u\bar{u} \to s\bar{s}$; $\Gamma_{u\bar{u}\to s\bar{s}} \propto d_{\bar{u}} \; f_{\bar{u}} \; \sigma_{u\bar{u}\to s\bar{s}}$ (s channel)
- (5) : $ud \to ud$; $\Gamma_{ud\to ud} \propto d_d \; f_d \; \sigma_{ud\to ud}$ (t channel)

- (6) : $u\bar{d} \to u\bar{d}$; $\Gamma_{u\bar{d}\to u\bar{d}} \propto d_{\bar{d}}\ f_{\bar{d}}\ \sigma_{u\bar{d}\to u\bar{d}}$ (t channel)
- (7) : $us \to us$; $\Gamma_{us\to us} \propto d_s\ f_s\ \sigma_{us\to us}$ (t channel)
- (8) : $u\bar{s} \to u\bar{s}$; $\Gamma_{u\bar{s}\to u\bar{s}} \propto d_{\bar{s}}\ f_{\bar{s}}\ \sigma_{u\bar{s}\to u\bar{s}}$ (t channel)
- (9) : $ug \to ug$; $\Gamma_{ug\to ug} \propto d_g\ f_g\ \sigma_{ug\to ug}$ (t channel).

Adding up all the contributions, we get for the light quark total interaction rate:

$$\Gamma_u = \sum_q \Gamma_{uq} + \sum_{\bar{q}} \Gamma_{u\bar{q}} + \Gamma_{ug} \tag{7.36}$$
$$= (1) + (5) + (7) + (2) + (3) + (4) + (6) + (8) + (9).$$

Similarly for a gluon g, the possible interaction channels are:

- (10) : $gu \to gu$; $\Gamma_{gu\to gu} \propto d_u\ f_u\ \sigma_{gu\to gu}$ = $gd \to gd$; $\Gamma_{gd\to gd} \propto d_d\ f_d\ \sigma_{gd\to gd}$ (t + u + s channels)
- (11) : $g\bar{u} \to g\bar{u}$; $\Gamma_{g\bar{u}\to g\bar{u}} \propto d_{\bar{u}}\ f_{\bar{u}}\ \sigma_{g\bar{u}\to g\bar{u}}$ = $g\bar{d} \to g\bar{d}$; $\Gamma_{g\bar{d}\to g\bar{d}} \propto d_{\bar{d}}\ f_{\bar{d}}\ \sigma_{g\bar{d}\to g\bar{d}}$ (t + u + s channels)
- (12) : $gs \to gs$; $\Gamma_{gs\to gs} \propto d_s\ f_s\ \sigma_{gs\to gs}$ (t + u + s channels)
- (13) : $g\bar{s} \to g\bar{s}$; $\Gamma_{g\bar{s}\to g\bar{s}} \propto d_{\bar{s}}\ f_{\bar{s}}\ \sigma_{g\bar{s}\to g\bar{s}}$ (t + u + s channels)
- (14) : $gg \to gg$; $\Gamma_{gg\to gg} \propto d_g\ f_g\ \sigma_{gg\to gg}$ (t + u + s channels + 4 point amplitude).

Adding up all the contributions, we get for the gluon g total interaction rate:

$$\Gamma_g = \sum_q \Gamma_{gq} + \sum_{\bar{q}} \Gamma_{g\bar{q}} + \Gamma_{gg} \tag{7.37}$$
$$= 2 \times (10) + (12) + 2 \times (11) + (13) + (14).$$

Fig. 7.13 (top panel) shows the "off-shell interaction rate" Γ_q^{coll} of a light quark q as a function of the temperature T for $\mu_B = 0$ (a) and $\mu_B = 0.4$ GeV (b). The contributions from the scattering with light quarks (green), antiquarks (blue) and gluons (pink) (see also Eq. (7.36)) are given by the lower hatched bands. At μ_B

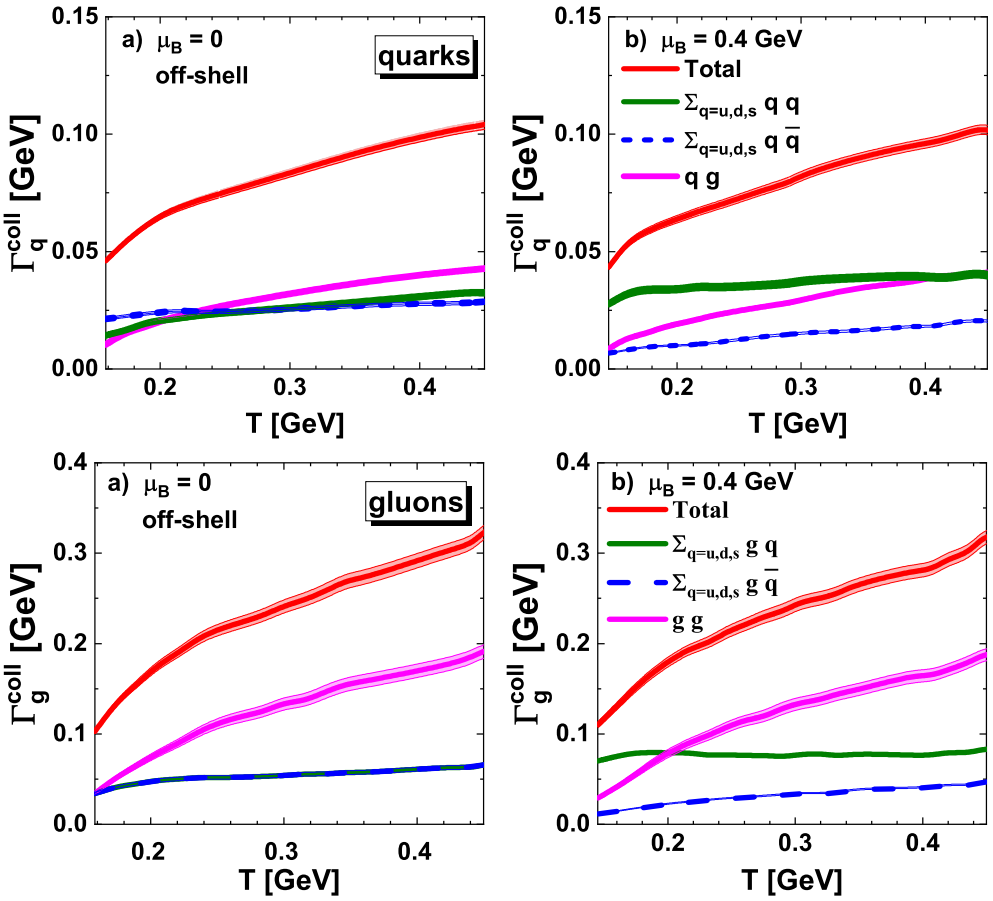

Figure 7.13 – Off-shell collision rate from Eq. (7.33) of a light quark q (top panel) and of a gluon g (lower panel) as a function of the temperature T for $\mu_B = 0$ (a) and $\mu_B = 0.4$ GeV (b) (blue lines). The contributions from the scattering with light quarks (green), antiquarks (blue) and gluons (pink) are given by the lower hatched bands which arise from the finite statistics in the evaluation of the integrals by Monte Carlo.

$= 0$ the total width $\Gamma_q^{\rm coll}$ to a large extend stems from quark-gluon scattering and increases with temperature while the contributions from scatterings with quarks and antiquarks are about equal and subdominant. At $\mu_B = 0.4$ GeV the quarks are more abundant than the antiquarks and the contributions from scatterings with quarks increase while that from collisions with antiquarks decrease relative to $\mu_B = 0$. The contributions from collisions with gluons slightly decreases also with μ_B which can be attributed to a decrease of the cross sections with μ_B as noted before. Fig. 7.13 (lower panel) shows the off-shell interaction rate of a gluon g as a function of the temperature T for $\mu_B = 0$ (a) and $\mu_B = 0.4$ GeV (b). The contributions

from the scattering with light quarks (green), antiquarks (blue) and gluons (pink) (see also Eq. (7.37)) are given by the lower hatched bands. The discussion of the contributions to the total widths is very similar to the case of quark scattering. Fig. 7.14, gives an overview on the width Γ_q (a) and width Γ_g (b) as a function of the scaled temperature $T/T_c(\mu_B)$ and chemical potential μ_B. While the dependencies on temperature are similar for fixed μ_B we see a general slight decrease of the total widths at high T and a slight increase close to $T_c(\mu_B)$ in connection with Fig. 7.12. In summarizing this section we find that the collisional widths for time-like partons are sizable and increase with temperature (as in the DQPM) but still remain substantially smaller than the pole masses in Fig. 7.2. Accordingly, a quasiparticle interpretation for time-like quanta should approximately hold.

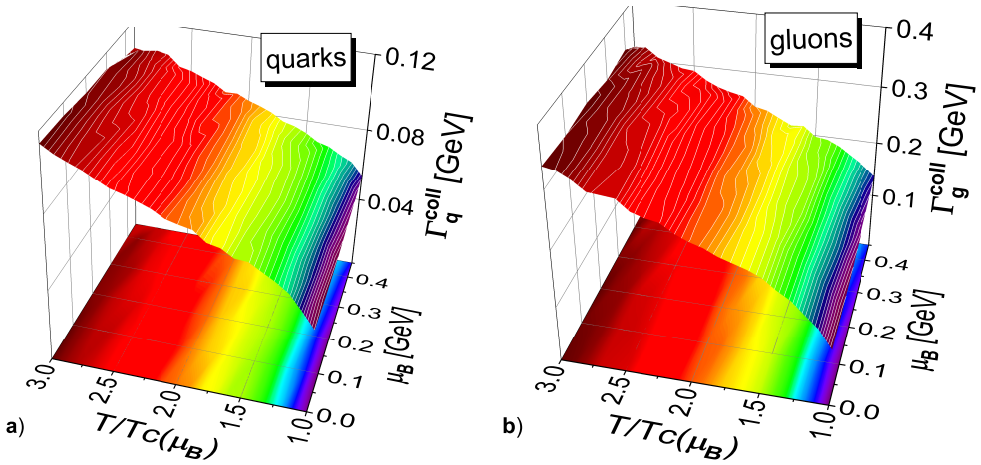

Figure 7.14 – Off-shell collision rate of a quark (a) and gluon (b) as a function of the scaled temperature $T/T_c(\mu_B)$ and the baryon chemical potential μ_B from Eq. (7.33).

7.4 Transport properties of the hot and dense QGP

The starting point to evaluate viscosity coefficients of partonic matter is the Kubo formalism [127, 402–408] which was used to calculate the viscosities for a previous version of the DQPM within the PHSD in a box with periodic boundary conditions (cf. Ref. [262]). We focus here on the calculation of the shear viscosity based on Refs. [403–406] which reads:

$$\eta^{\rm Kubo}(T,\mu_q) = -\int \frac{d^4p}{(2\pi)^4}\; p_x^2 p_y^2 \sum_{i=q,\bar{q},g} d_i\; \frac{\partial f_i(\omega)}{\partial \omega}\; \rho_i(\omega,\mathbf{p})^2 \tag{7.38}$$

$$= \frac{1}{15T}\int \frac{d^4p}{(2\pi)^4}\; \mathbf{p}^4 \sum_{i=q,\bar{q},g} d_i\,((1\pm f_i(\omega))f_i(\omega))\,\rho_i(\omega,\mathbf{p})^2,$$

where the notation $f_i(\omega) = f_i(\omega,T,\mu_q)$ is used for the distribution functions, and ρ_i denotes the spectral functions from Eq. (7.8). We note that the derivative of the distribution function accounts for the Pauli-blocking (-) and Bose-enhancement (+) factors. Following Ref. [405], we can evaluate the integral over $\omega = p_0$ in Eq. (7.38) by using the residue theorem. When keeping only the leading order contribution in the width γ from the residue - evaluated at the poles of the spectral function $\omega_i = \pm\tilde{E}(\mathbf{p}) \pm i\gamma$ - we finally obtain:

$$\eta^{\rm RTA}(T,\mu_q) = \frac{1}{15T}\int \frac{d^3p}{(2\pi)^3} \sum_{i=q,\bar{q},g} \frac{\mathbf{p}^4}{E_i^2\;\Gamma_i(\mathbf{p}_i,T,\mu_q)}\; d_i\,((1\pm f_i(E_i))f_i(E_i)) + \mathcal{O}(\Gamma_i), \tag{7.39}$$

which corresponds to the expression derived in the relaxation-time approximation (RTA) [267, 268, 409–411] by identifying the interaction rate Γ with 2γ as expected from transport theory in the quasiparticle limit [149] (cf. Chapter 2). This interaction rate $\Gamma_i(\mathbf{p}_i,T,\mu_q)$ (inverse relaxation time) is calculated microscopically by Eq. (7.28). We recall that the pole energy is $E_i^2 = p^2 + M_i^2$ where M_i is the pole mass given in the DQPM by Eqs. (7.4)-(7.5). As in the previous section, we use here the notation $\sum_{j=q,\bar{q},g}$ which includes the contribution from all possible partons which in our case are the gluons and the (anti-)quarks of three different flavors (u,d,s).

The actual results are displayed the in left-hand side of Fig. 7.15 for the ratios of shear viscosity to entropy density η/s as a function of the scaled temperature T/T_c for $\mu_B = 0$ in comparison to those from lattice QCD [412]. The solid green line ($\eta^{\rm Kubo}/s$) shows the result from the original DQPM in the Kubo formalism while the dashed green line ($\eta^{\rm RTA}_{2\gamma}/s$) shows the same result in the quasiparticle approximation (7.39) by replacing Γ_i by $2\gamma_i$. The solid red line ($\eta^{\rm RTA}_{\Gamma^{\rm on}}/s$) results from Eq. (7.39) using the interaction rate $\Gamma^{\rm on}$ (7.28) calculated by the microscopic differential cross sections in the on-shell limit in the DQPM. We find that - apart from temperatures close to T_c - the ratios η/s do not differ very much and have a similar behavior as a function of temperature. The approximation (7.39) of the shear viscosity is found to be very close to the one from the Kubo formalism (7.38)

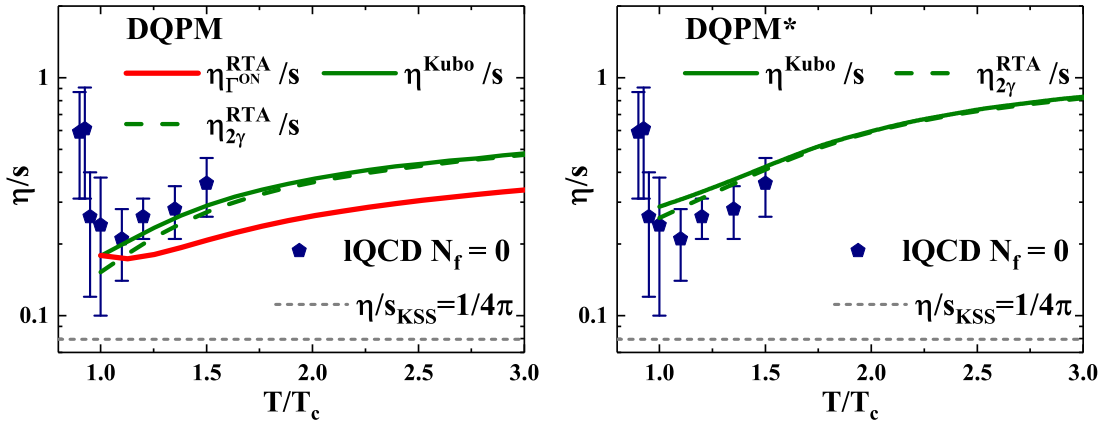

Figure 7.15 – The ratio of shear viscosity to entropy density as a function of the scaled temperature T/T_c for $\mu_B = 0$ from Eq. (7.38-7.39) evaluated with the DQPM (left) and DQPM* (right). The solid green line ($\eta^{\rm Kubo}/s$) shows the results from the original DQPM in the Kubo formalism while the dashed green line ($\eta^{\rm RTA}_{2\gamma}/s$) shows the same result in the quasiparticle approximation (7.39). The solid red line ($\eta^{\rm RTA}_{\Gamma^{\rm on}}/s$) results from Eq. (7.39) using the interaction rate $\Gamma^{\rm on}$ (7.28) calculated by the microscopic differential cross sections in the on-shell limit. The dashed gray line demonstrates the Kovtun-Son-Starinets bound [264, 265] $(\eta/s)_{\rm KSS} = 1/(4\pi)$, and the symbols show lQCD data for pure SU(3) gauge theory taken from Ref. [412] (pentagons).

indicating that the quasiparticle limit ($\gamma \ll M$) holds in the DQPM. We mention that these results for η/s are in accordance with the Bayesian analysis from Ref. [413] at large temperatures whereas near the critical temperature we obtain larger values. We have also checked that the shear viscosity does not differ substantially if one uses the momentum-dependent interaction rate from Eq. (7.28) or the averaged one from Eq. (7.30). In the right-hand side of Fig. 7.15 we show for comparison the results obtained from the DQPM* where the shear viscosity is obtained by taking the momentum dependent width $\gamma(p, T, \mu_B)$ from Refs. [230, 378].

An overview for the ratio of shear viscosity to entropy density η/s as a function of the scaled temperature $T/T_c(\mu_B)$ and μ_B is given in Fig. 7.16 in case of the Kubo formalism (a) (7.38) and the on-shell limit (7.39) (b). There is no strong variation with μ_B for fixed $T/T_c(\mu_B)$, however, the ratio increases slightly with μ_B in the on-shell limit while it slightly drops with μ_B in the Kubo formalism for the DQPM. Accordingly, there is some model uncertainty when extracting the shear viscosity in the different approximations.

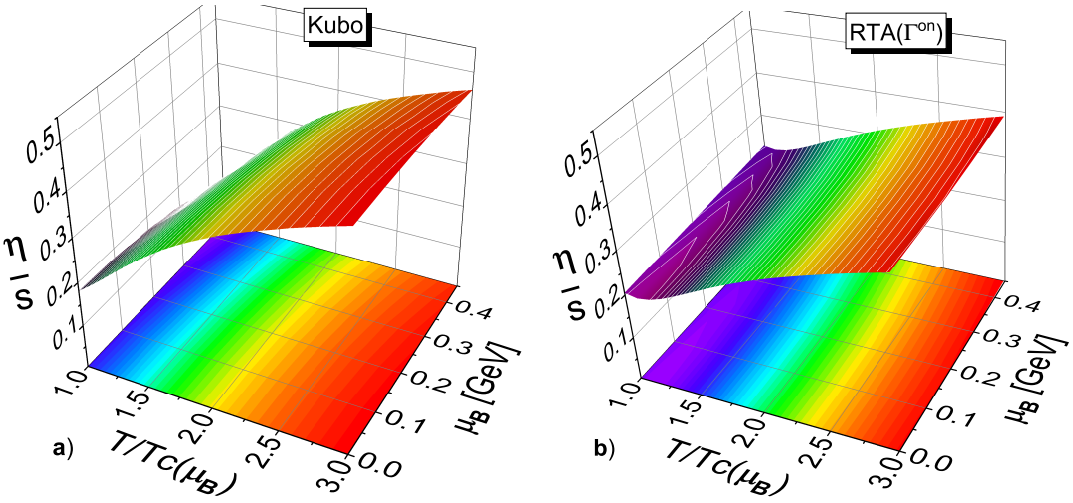

Figure 7.16 – The ratio of shear viscosity to entropy density η/s as a function of the scaled temperature $T/T_c(\mu_B)$ and baryon chemical potential μ_B calculated within the Kubo formalism (a) from Eq. (7.38) and in the Relaxation Time Approximation (RTA) (b) from Eq. (7.39) using the on-shell interaction rate $\Gamma^{\rm on}$ from Eq. (7.28).

We can also evaluate the bulk viscosity associated with the DQPM which, in the relaxation time approximation, reads [411]:

$$\zeta^{\rm RTA}(T,\mu_q) = \frac{1}{9T}\int \frac{d^3p}{(2\pi)^3} \sum_{i=q,\bar{q},g} \frac{1}{E_i^2\ \Gamma_i(\mathbf{p}_i,T,\mu_q)} \left[\mathbf{p}^2 - 3c_s^2\left(E_i^2 - T^2\frac{dM_i^2}{dT^2}\right)\right]^2 d_i\ f_i \tag{7.40}$$

where c_s^2 is the speed of sound squared. The actual results are displayed in Fig. 7.17 for the ratios of bulk viscosity to entropy density ζ/s as a function of the scaled temperature T/T_c for $\mu_B = 0$. The thick red line corresponds to the results using the on-shell interaction rate $\Gamma^{\rm on}$, whereas the dashed green line is obtained by using the parton width 2γ in Eq. (7.40). Again, we obtain here a very similar behavior between these two calculations. For comparison, we also show the bulk viscosity from the DQPM* (dashed blue line) which is also found to be larger compared to the DQPM as for the shear viscosity in Fig. 7.15.

In summarizing this section we find that the results for the ratio of shear and bulk viscosities over entropy density from the original DQPM and those from the microscopic calculations are similar and within error bars compatible with present results from lattice QCD. However, having the differential cross sections for each partonic channel at hand one might find substantial differences for nonequilibrium

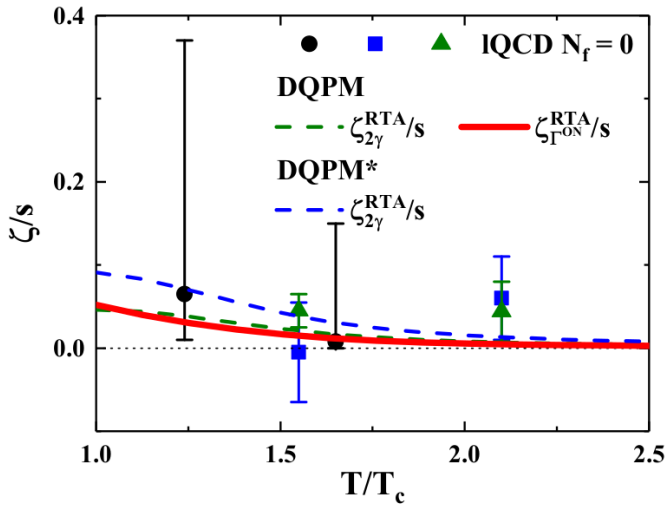

Figure 7.17 – The bulk viscosity ζ/s as a function of the scaled temperature T/T_c for $\mu_B = 0$ from Eq. (7.40). The symbols show lQCD data for pure SU(3) gauge theory taken from Refs. [414] (circles) and [415] (squares and triangles). The dashed green line shows the result from the original DQPM while the solid red line results from the microscopic differential cross sections, and the dashed blue line from the original DQPM*.

configurations as encountered in relativistic heavy-ion collisions where a QGP is formed initially out-of equilibrium.

7.5 Extraction of T and μ_B from PHSD in heavy-ion collisions

Since PHSD is a microscopic off-shell transport approach it does not incorporate thermodynamic Lagrange parameters such as T and μ_B that characterize the system in equilibrium. In order to extract the required information (the temperature T and baryon chemical potential μ_B) - defining the parton properties and differential scattering processes in the PHSD space-time grid - we use a parametrization of the lQCD equation of state from Ref. [416] where the pressure is expanded as:

$$\frac{P}{T^4} = c_0(T) + c_2(T)\left(\frac{\mu_B}{T}\right)^2 + c_4(T)\left(\frac{\mu_B}{T}\right)^4 + c_6(T)\left(\frac{\mu_B}{T}\right)^6 + \mathcal{O}\left(\mu_B^8\right). \qquad (7.41)$$

This equation of state matches the conditions of a heavy-ion collision where strangeness neutrality $\langle n_S \rangle = 0$ is realized on average and where the relation between

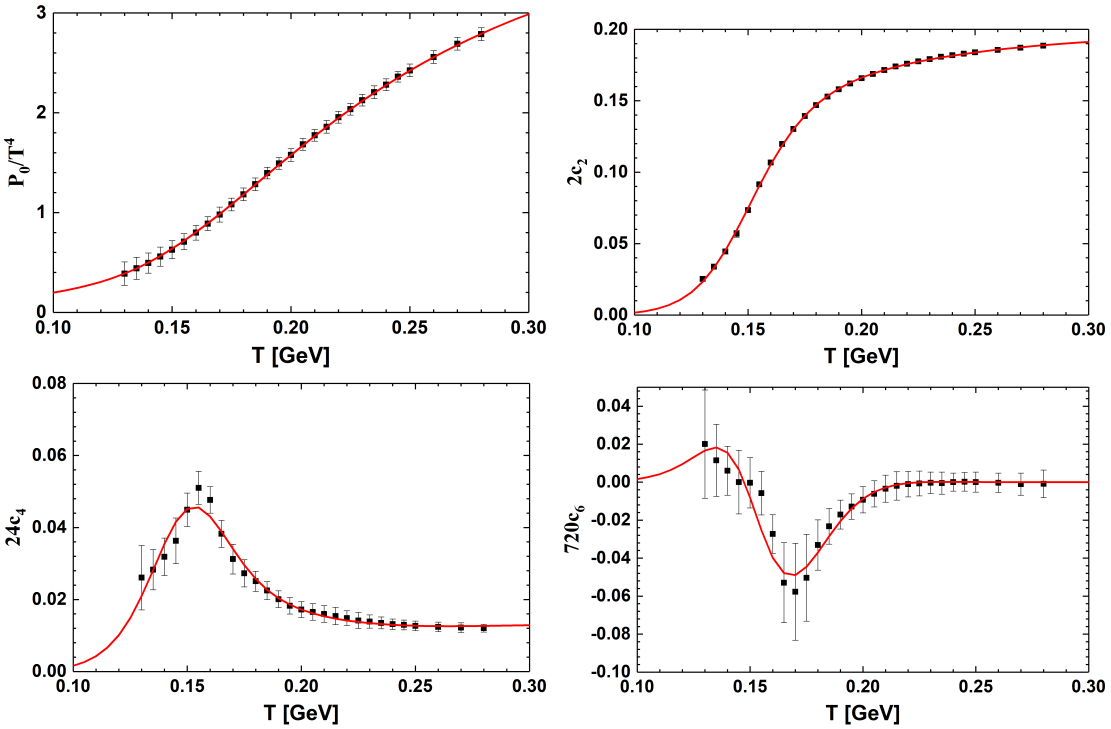

Figure 7.18 – Parametrization of the different coefficients c_i in Eq. (7.41) in comparison with the actual lattice data from Ref. [416].

electric charge and baryon number $\langle n_Q \rangle = 0.4\ \langle n_B \rangle$ is fixed by the content of the initial nuclei. We show the corresponding fit in Fig. 7.18 of the different coefficients $c_i(T)$ and in Fig. 7.19 the result for the pressure P, the baryon density n_B, the energy density ϵ and the entropy density s for different values of μ_B as a function of the temperature T. The inclusion of the 6^{th} order coefficient c_6 induces wiggles in the EoS due to oscillating contributions as seen in Fig. 7.19. We study in the left-hand side of Fig. 7.20 the effect of including the coefficients c_i up to a certain order in Eq. (7.41) by looking at the isentropic trajectories (which are defined by a constant ratio of entropy density over baryon density s/n_B) in the $(T - \mu_B)$ plane. According to Ref. [416], these different values of s/n_B correspond to the trajectories of heavy-ion collisions from the beam-energy-scan program at RHIC ($\sqrt{s_{NN}} = 200$ GeV, 62.4 GeV, 39 GeV, 27 GeV, 19.6 GeV and 14.5 GeV). One can see that, when including only the 2^{nd} order coefficient c_2, this construction is definitely not applicable at large chemical potentials $\mu_B/T > 2$ since the line $s/n_B = 30$ breaks down. But when adding the contribution from the 4^{th} order coefficient c_4, the line $s/n_B = 30$ behaves smoothly and correctly crosses the critical temperature line as expected. As one can see the inclusion of the 6^{th} order coefficient c_6 does not lead to considerable changes for $\mu_B/T < 3$ and will be discarded in the

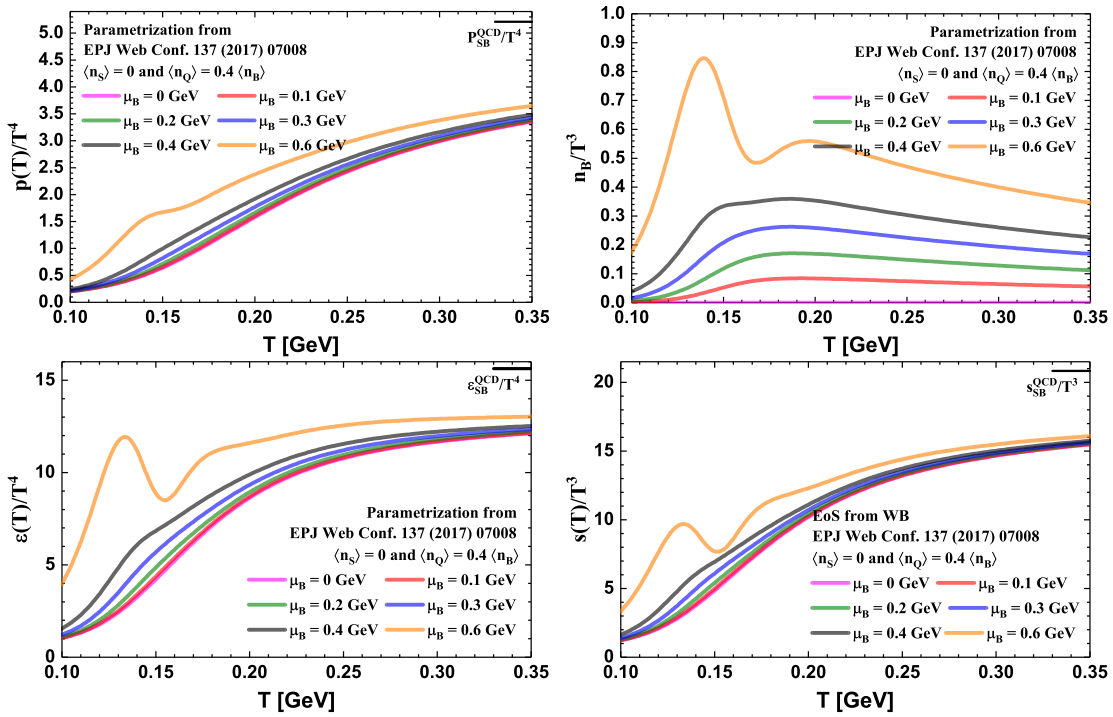

Figure 7.19 – The pressure P, baryon density n_B, energy density ϵ and entropy density s, as a result of the fit of the different coefficients c_i in Eq. (7.41) from the lattice data of Ref. [416]. The horizontal black lines indicate the Stefan-Boltzmann limits ($P_{SB}^{QCD}/T^4 = 19/36\ \pi^2$, $e_{SB}^{QCD}/T^4 = 19/12\ \pi^2$, $s_{SB}^{QCD}/T^3 = 19/9\ \pi^2$) corresponding to a non-interacting gas of massless quarks and gluons at vanishing chemical potential.

following. Note that the parametrization of the coefficients $c_i(T)$ in Eq. (7.41) is also in agreement with lattice QCD data below T_c which allows for an evaluation of T and μ_B also in the hot hadronic phase. Indeed, one can see in Fig. 7.20 that the different lines merge below the critical temperature $T_c(\mu_B)$ with the results from the Hadron Resonance Gas (HRG) model from Ref. [416]. On the right-hand side of Fig. 7.20 one can additionally see that the isentropic trajectories roughly correspond to a fixed ratio of μ_B/T, which is exactly the case when considering an ideal quark-gluon gas [417]. We point out that these results have to be taken as estimates in the regions of large chemical potentials for $\mu_B/T > 3$.

In each space-time cell of the PHSD grid, the thermodynamic quantities are calculated by the method developed in chapter 4, i.e. by diagonalization of the energy momentum tensor $T^{\mu\nu}$. To study the matter at finite baryon density, we calculate additionally the net-baryon current,

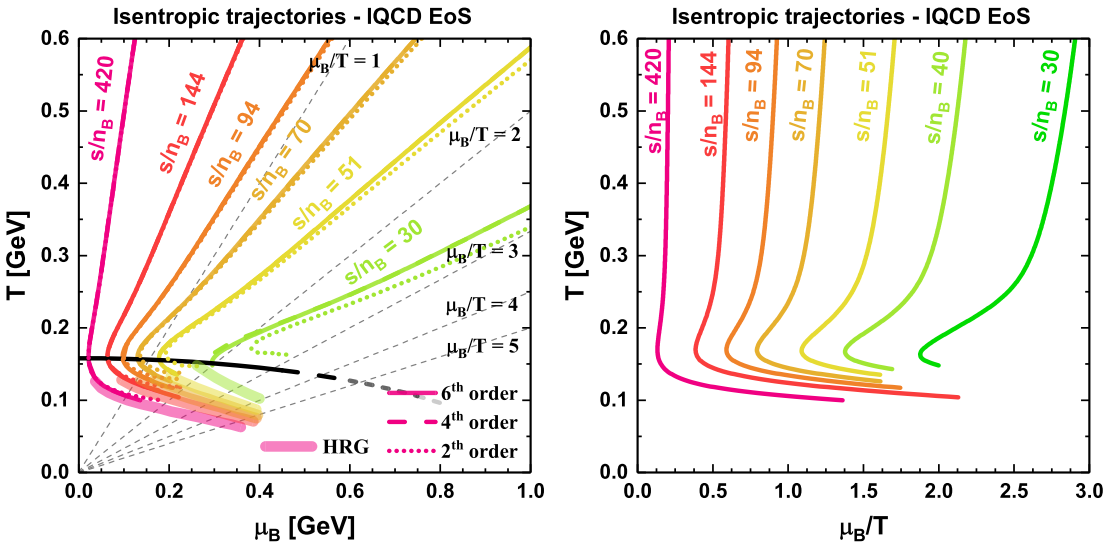

Figure 7.20 – Isentropic trajectories for different ratios of the entropy density over the baryon density s/n_B. On the left-hand side, the black line corresponds to the DQPM critical temperature $T_c(\mu_B)$ and the dashed gray lines correspond to different values of μ_B/T for orientation. The lines indicating the results from the Hadron Resonance Gas (HRG) model are taken from Ref. [416].

$$J_B^\mu = \sum_i \frac{p_i^\mu}{E_i} \frac{(q_i - \bar{q}_i)}{3}, \tag{7.42}$$

with q_i ($\bar{q}_i$) being the number of light quarks (antiquarks) within particle i. To obtain the local net-baryon density we apply the Lorentz transformation defined via

$$n_B = \gamma_E \left(J_B^0 - \vec{\beta_E} \cdot \vec{J_B} \right) = \frac{J_B^0}{\gamma_E}, \tag{7.43}$$

where $\vec{\beta_E} = \vec{J_B}/J_B^0$ is known as the Eckart velocity [418] and γ_E is the associated Lorentz factor. We mention that by using the Eckart velocity $\vec{\beta_E}$ to transform the net-baryon current, the spatial part of the latter automatically vanishes whereas, this is not guaranteed when employing the energy flow u^μ from Eq. (4.6).

We illustrate in Fig. 7.21 our extraction method and show the time and rapidity dependence of the energy density ϵ and baryon density n_B extracted from the PHSD in the central cell ($x = y = 0$) of 5% central Pb+Pb collisions at 158 A GeV. As previously explained, the parallel ensemble method is used in the PHSD

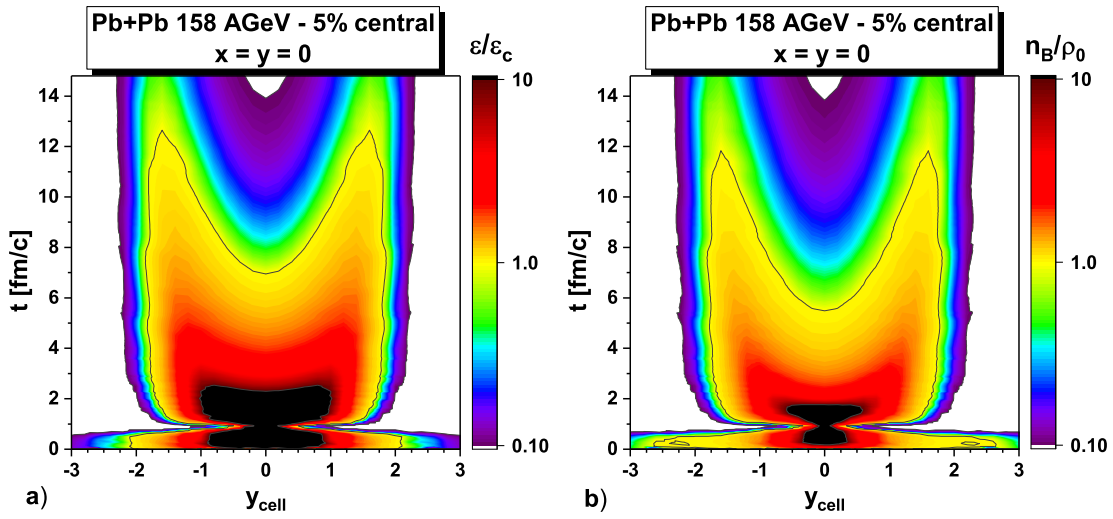

Figure 7.21 – The energy density ϵ (left) and baryon density n_B (right) as a function of the cell rapidity $y_{\rm cell}$ at different times t for 5% central Pb+Pb collisions at 158 A GeV extracted from the central cell $x = y = 0$ of the PHSD. The energy density and baryon density are respectively divided by the critical energy density $\epsilon_c = 0.5$ GeV/fm^3 and the saturation density $\rho_0 = 0.17$ fm^{-3}. The initial time $t = 0$ is systematically taken to be the time of the first nucleon-nucleon collision.

implying that the densities are averaged over a large number of parallel events ($\sim$ 250 for AGS energies, $\sim$ 150 for top SPS and $\sim$ 30 for top RHIC). With this procedure, even if each event contains only a few particles per cell, the overall profile is relatively smooth in space-time. Furthermore, in the evaluation of the energy density ϵ and baryon density n_B leading quarks or diquarks are included since they carry most of the baryon number in the string fragmentation picture (cf. Chapter 3). The cell rapidity $y_{\rm cell}$ is evaluated from the cell 4-velocity $u^\mu = \gamma(1, \vec{\beta})$ in Eq. (4.6) as $y_{\rm cell} = 1/2 \log((1+\beta_z)/(1-\beta_z))$. For illustration, we have scaled the energy and baryon densities by the critical energy density $\epsilon_c = 0.5$ GeV/fm^3 used in the PHSD and the saturation density $\rho_0 = 0.17$ fm^{-3}, respectively. One can see that at the collision time ($t = 0$) a high amount of energy is deposited into the midrapidity region whereas at higher rapidities the initial nuclei are still intact. Indeed, we observe that around the initial rapidity of the nuclei ($y_N \approx 2.9$) the baryon density is still around the saturation density ρ_0. After the passing time $t = R/\gamma_N \approx 0.75$ fm/c, all the initial nucleons in the central cell ($x = y = 0$) have interacted and maximal values for the energy density and baryon density are reached which are of the order of $\epsilon \approx 5$ GeV/fm^3 and $n_B \approx 2$ fm^{-3}, respectively. We can identify approximatively constant values of ϵ and n_B as a function of the cell rapidity $y_{\rm cell}$ along parabolas of proper time $\tau \sim t/\cosh(y_{\rm cell})$. After $\tau \approx 6$ fm/c the energy density reaches the

critical value ϵ_c implying that quarks and gluons hadronize into hadrons, whereas the baryon density appears to be slightly lower than the saturation density ρ_0.

In the beginning of heavy-ion collisions the created medium is highly anisotropic due to the longitudinal expansion. In order to correct for the anisotropy we apply the *shape generalized equation of state* developed in Ref. [419] in order to extract values for the temperature T and baryon chemical potential μ_B. In this framework, the energy density ϵ^{anis} and pressure components of an anisotropic medium are evaluated by the following expressions:

$$\epsilon^{\text{anis}} = \epsilon^{\text{EoS}} \quad r(x) \tag{7.44}$$

$$P_\perp = P^{\text{EoS}} \quad \Big[r(x) + 3xr'(x)\Big] \tag{7.45}$$

$$P_\parallel = P^{\text{EoS}} \quad \Big[r(x) - 6xr'(x)\Big], \tag{7.46}$$

where $P_\perp$ and $P_\parallel$ are, respectively, the transverse and longitudinal pressures, and ϵ^{EoS} and P^{EoS} are the equilibrium energy density and pressure from which a temperature T and chemical potential μ_B can be extracted. The anisotropy parameter x can be approximated as a function of the pressure components as $P_\parallel/P_\perp = x^{-3/4}$, and the function $r(x)$ reads:

$$r(x) = \begin{cases} \dfrac{x^{-1/3}}{2}\left[1 + \dfrac{x\ \text{arctanh}\sqrt{1-x}}{\sqrt{1-x}}\right] \text{for } x \leq 1 \\ \dfrac{x^{-1/3}}{2}\left[1 + \dfrac{x \arctan\sqrt{x-1}}{\sqrt{x-1}}\right] \text{for } x \geq 1\ . \end{cases} \tag{7.47}$$

In a PHSD simulation, we calculate in each of the cells the energy density ϵ^{PHSD}, the baryon density n_B^{PHSD}, as well as the pressure components $P_\perp^{\text{PHSD}}$ and $P_\parallel^{\text{PHSD}}$, from which one can evaluate the function $r(x)$ in Eq. (7.47). In order to find the temperature T and baryon chemical potential μ_B according to the lattice EoS - constructed at the beginning of this section 7.5 - we have to solve the following system of equations:

$$\begin{cases} \epsilon^{\text{EoS}}(T, \mu_B) = \epsilon^{\text{PHSD}}/r(x) \\ n_B^{\text{EoS}}(T, \mu_B) = n_B^{\text{PHSD}} \end{cases} \tag{7.48}$$

where the left-hand sides represent the lattice EoS which depends on the unknowns

T and μ_B, whereas on the right-hand sides of these equations we have the energy density and baryon density evaluated in PHSD. In Eq. (7.48) the energy density from PHSD $\epsilon^{\rm PHSD}$ is divided by the function $r(x)$ from Eq. (7.47) to account for the anisotropy of the considered cell according to the *shape generalized equation of state* in Eq. (7.44). We solve this system by using the Newton-Raphson method [420, 421] (more details can be found in Appendix E).

We now turn to the evaluation of T and μ_B in actual PHSD simulations for Au+Au collisions. As an example for our results we show in Fig. 7.22 the ratio μ_B/T as a function of the cell rapidity $y_{\rm cell}$ at different times (from 1 to 6 fm/c) for 5% central Pb+Pb collisions at 158 A GeV. The largest ratios are seen for all times for rapidities closer to projectile and target rapidities (cf. Ref. [382]) while at midrapidity this ratio is initially high (at $t = 1$ fm/c), but drops to $\mu_B/T \sim 2$ at $t = 2$ fm/c and remains approximately constant afterwards. The constant value of μ_B/T is well in agreement with the expected isentropic trajectory $s/n_B = 40$ at this collisional energy as seen in the right-hand side of Fig. 7.20. We mention that this profile is very close to that calculated in the hydrodynamics + hadronic transport approach by Denicol et al. (Fig. 5 in Ref. [197]) and also shows an increase of μ_B/T with increasing $|y|$.

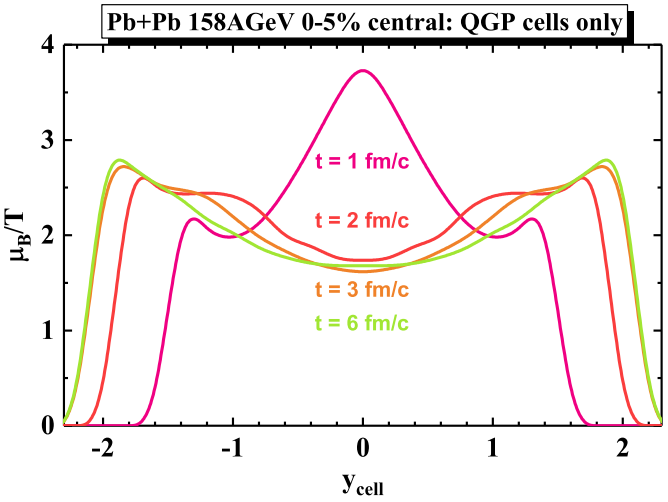

Figure 7.22 – The ratio μ_B/T as a function of the cell rapidity $y_{\rm cell}$ at different times t for 5% central Pb+Pb collisions at 158 A GeV from PHSD.

Fig. 7.23 shows the temperature profile and the ratio of the longitudinal over transverse pressure (for the central cell) as a function of the cell rapidity $y_{\rm cell}$ and different times (from 0.15 to 7 fm/c) for a 5% central Au+Au collision at $\sqrt{s_{NN}} =$

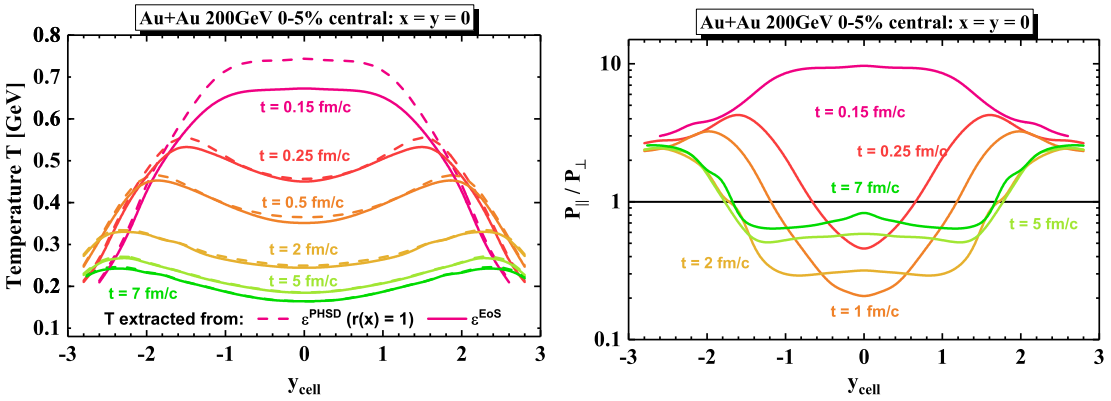

Figure 7.23 – The temperature profile (left) and the ratio of the longitudinal over transverse pressure (right) (for the central cell) as a function of the cell rapidity $y_{\rm cell}$ and at different times (from 0.15 to 7 fm/c) for a 5% central Au+Au collision at $\sqrt{s_{NN}} = 200$ GeV from PHSD. The dashed lines on the right-hand side result when extracting the temperature directly from the energy density of the central cell in PHSD $\epsilon^{\rm PHSD}$ while the solid lines refer to the extraction from the equation of state $\epsilon^{\rm EoS}$.

200 GeV. This temperature profile initially ($t = 0.15$ fm/c) has a broad maximum at midrapidity but for $t > 0.25$ fm/c slight maxima at $|y_{\rm cell}| \approx 1.5$ appear which move to higher cell rapidity with increasing time while the average temperature drops rapidly in time. The lowest temperatures (at midrapidity), however, are still on the level of 250 MeV at $t = 2$ fm/c, i.e. well above the critical temperature T_c. We note in passing that the temperature profiles from two different extraction methods, directly from the energy density of the cell in PHSD $\epsilon^{\rm PHSD}$ (dashed lines) - setting $r(x) = 1$ in Eq. (7.48) - and from the equation of state $\epsilon^{\rm EoS}$ (solid lines) are practically the same for $t \geq 0.25$ fm/c and provide an idea about the accuracy of our extraction method. Indeed, one can see on the right-hand side of Fig. 7.23 that the pressure anisotropy is large at $t = 0.15$ fm/c but then the ratio $P_{||}/P_{\perp}$ progressively converges to one with increasing time.

We now focus on the space-time distribution of the extracted temperatures T (left column) and chemical potentials μ_B (right column) for a 5% central collision of Pb+Pb at 158 A GeV from PHSD as shown in Fig. 7.24. These distributions correspond to the transverse plane (x, y) - orthogonal to the beam direction - at $z = 0$, i.e. in the center of the collision zone. For early times we find the temperatures of the fireball to be well above T_c practically everywhere with a maximum in the center. Then the fireball expands in space with time while the temperature (and thus the QGP region) drops accordingly. Indeed at $t = 4$ fm/c the temperature

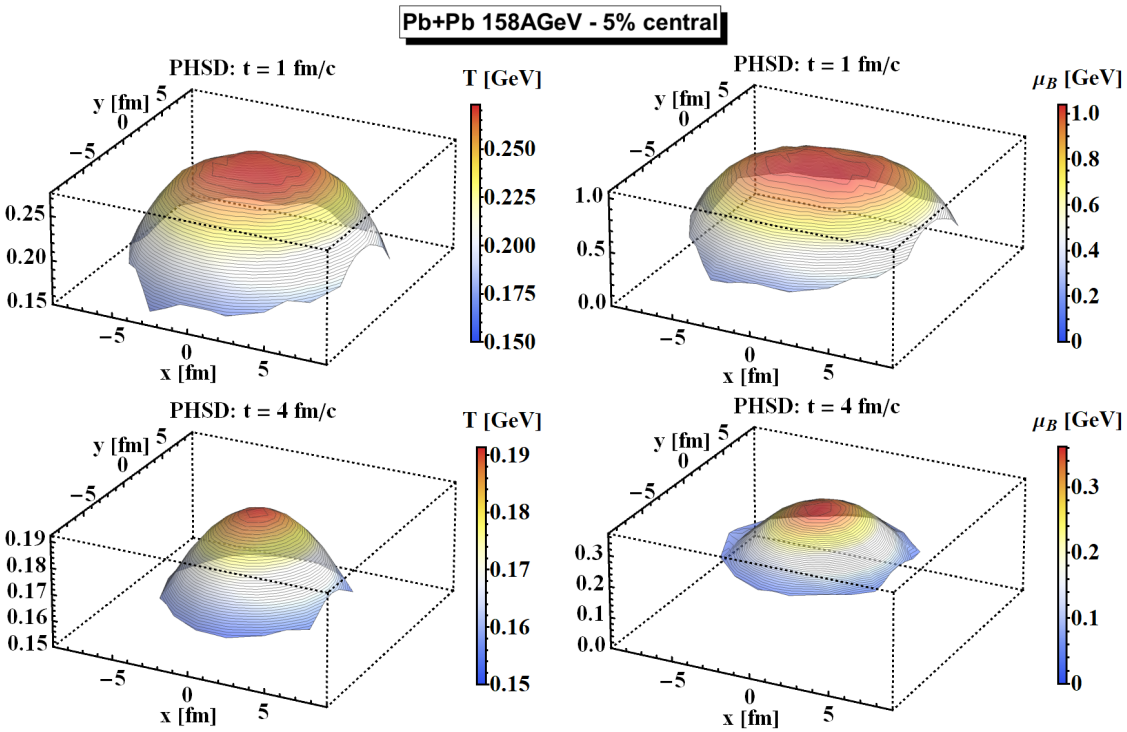

Figure 7.24 – (Left) The temperature profile in (x, y) (at $z = 0$) at 1 and 4 fm/c after the initial collision in case of a 5% central Pb+Pb collision at 158 A GeV from PHSD. (Right) The profile in the chemical potential μ_B in (x, y) (at $z = 0$) for different times from 0.5 to 6 fm/c for the same collision.

is above T_c only in the very central region whereas on the outside hadronization already occurred. This is in line with the common picture of fireball expansion and hadronization. However, the profile in the chemical potential μ_B (right column) shows that the chemical potential μ_B is very large for early times in the whole fireball and drops to values of around $\approx 0.2 - 0.3$ in the hot QGP zone for $t \approx 4$ fm/c.

We investigate now the time evolution of the distribution in T and μ_B for cells having a temperature $T > T_c(\mu_B)$ at midrapidity ($|y_{\rm cell}| < 0.5$) for 5% central heavy-ion collisions. Fig. 7.25 (a) shows this distribution for a Au+Au collision at $\sqrt{s_{NN}} = 200$ GeV from PHSD for times $t < 0.5$ fm/c, 0.5 fm/c $< t <$ 2 fm/c and $t > 2$ fm/c. The scale corresponds to the number of cells in the PHSD event in the considered bin in $T - \mu_B$ divided by the total number of cells in the corresponding time window while the solid black line is the DQPM phase boundary for orientation. At the very early times $t < 0.5$ fm/c the distribution peaks at $T \approx$ 0.3 GeV and is concentrated around $\mu_B \approx 0$. For times 0.5 fm/c $< t <$ 2 fm/c

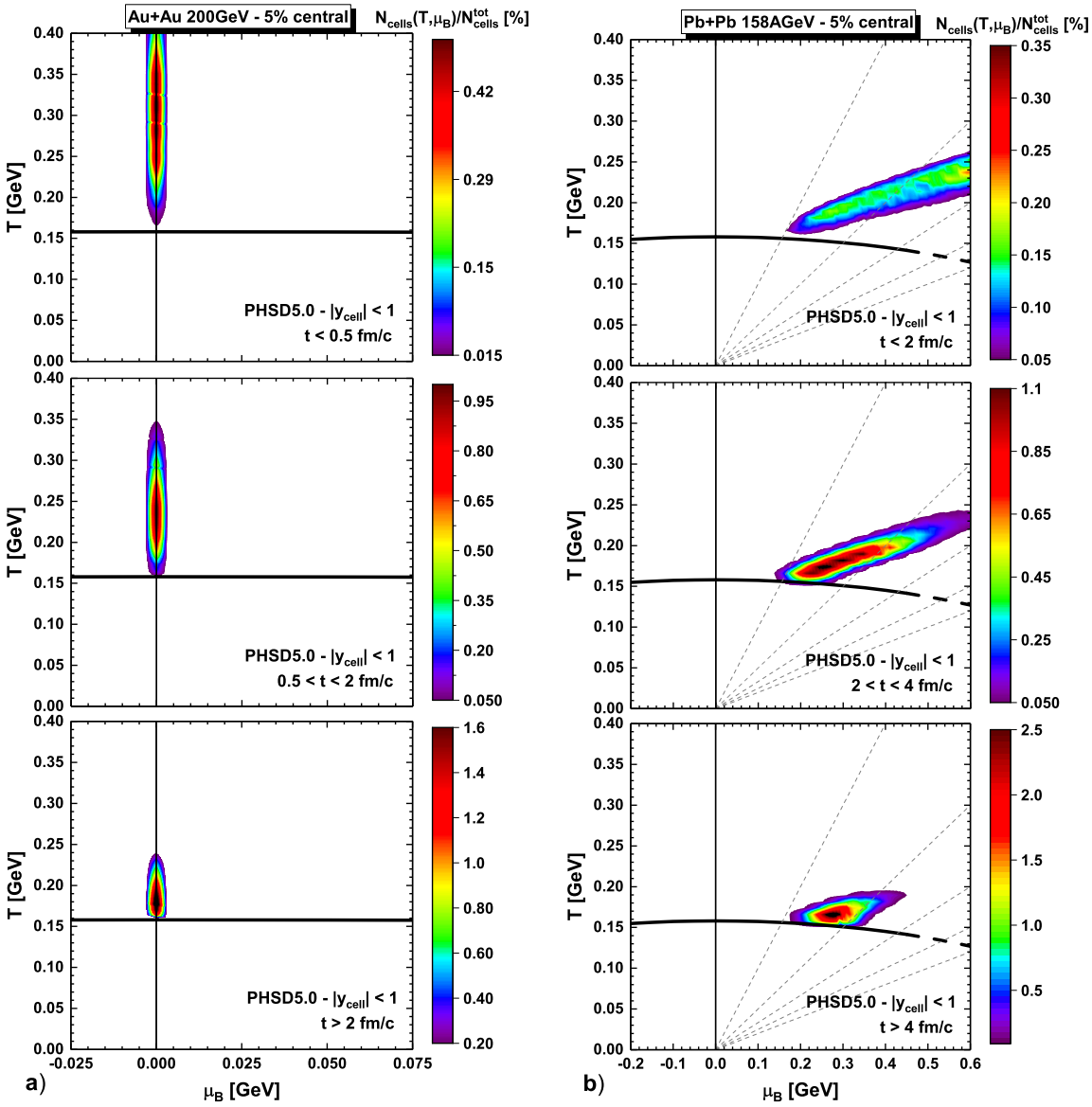

Figure 7.25 – Distributions in T and μ_B as extracted from the DQPM equation of state in a PHSD simulation of a central Au+Au collision at $\sqrt{s_{NN}} = 200$ GeV (a) and of a central Pb+Pb collision at 158 A GeV (b) for cells with a temperature $T > T_c(\mu_B)$. The scale corresponds to the number of cells in the PHSD event in the considered bin in $T - \mu_B$ divided by the total number of cells in the corresponding time window (see legend). The solid black line is the DQPM phase boundary for orientation, the gray dashed lines indicate ratios of μ_B/T ranging from 1 to 5 while the vertical line stands for $\mu_B = 0$.

the average temperature has dropped to about 0.24 GeV and for later times ($t >$ 2 fm/c) the distribution peaks at an average temperature slightly above T_c and more cells occupy larger values of μ_B which, however, are subdominant compared to the vanishing μ_B region. Note that a negative μ_B implies that there are more antiquarks (antibaryons) than quarks (baryons) in the individual cell. This time evolution of the distribution at the top RHIC energy matches well known expectations.

Fig. 7.25 (b) shows the distribution in T and μ_B for cells at midrapidity ($|y_{\text{cell}}| < 0.5$) in case of Pb+Pb collisions at 158 A GeV from PHSD for times $t <$ 2 fm/c, 2 fm/c $< t <$ 4 fm/c and $t >$ 4 fm/c. For early times $t <$ 2 fm/c the distribution peaks at a temperature of about 0.25 GeV and a sizable chemical potential of about 0.6 GeV while for times in the interval 2 fm/c $< t <$ 4 fm/c the maximum has dropped already to an average temperature $\sim$ 0.18 GeV and a chemical potential of about 0.3 GeV. For later times $t >$ 4 fm/c the distribution (above T_c) essentially stays around $\mu_B \approx 0.25$ GeV. We mention that the values of μ_B probed around the transition temperature T_c in the PHSD are in accordance with the expectation from statistical models which for central Pb+Pb collisions at 158 A GeV quote a value of $\mu_B = 0.2489$ GeV [422]. Furthermore, the trajectory of the fireball in the (T, μ_B) plane resembles the isentropic trajectories shown in Fig. 7.20, which for this energy corresponds approximatively to a fixed ratio of entropy over baryon density of $s/n_B \approx 40$ [423] and a fixed ratio of $\mu_B/T \approx 2$ (see Fig. 7.20). To assess the similarities between the isentropic trajectories in the (T, μ_B) plane and the PHSD results, we directly calculate the ratio of entropy density over baryon density as:

$$\frac{\langle s \rangle}{\langle n_B \rangle} = \frac{\int d^3x \; s(T, \mu_B)}{\int d^3x \; n_B(T, \mu_B)}. \tag{7.49}$$

The corresponding results are shown in the left-hand side of Fig. 7.26 for different collisional energies as a function of time in the midrapidity region. We can see that the actual values of the ratio of $\langle s \rangle / \langle n_B \rangle$ increase at early times and approximately stay constant during the duration of the QGP phase, i.e. by example from 1.5 to 6 fm/c for the case of 158 AGeV. Furthermore, these values correspond well to the expectations which are $s/n_B \approx 420$, 40 and 20 for $\sqrt{s_{NN}} = 200$, 17.3 and 7.6 GeV, respectively. This is in accordance with the fact that entropy is dominantly created at the beginning of heavy-ion collisions and remains approximatively constant as a function of time during the evolution of the QGP [423]. The latter can approximately be described as an ideal fluid in local equilibrium, which perfectly conserves entropy, since dissipations or frictions are neglected in this limit.

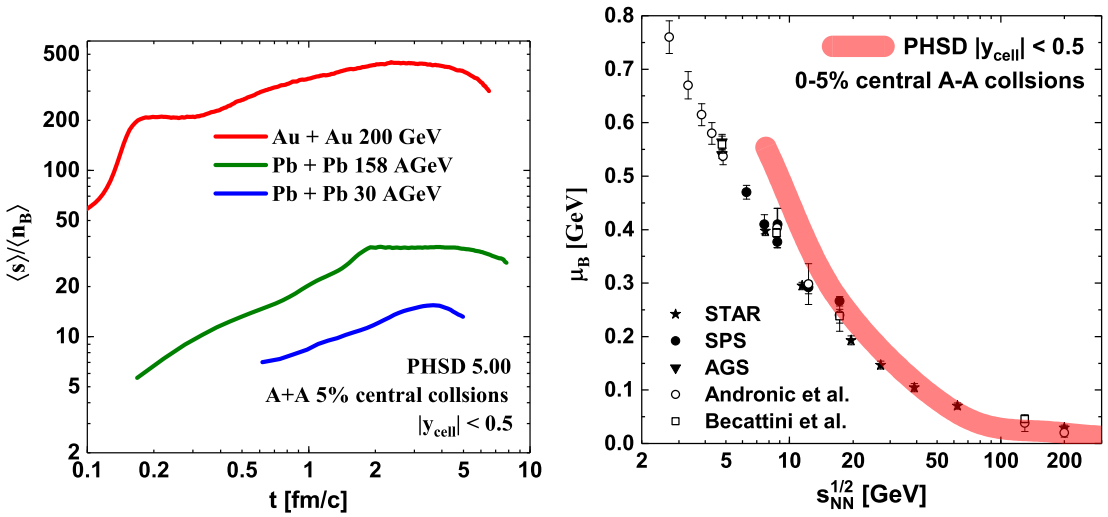

Figure 7.26 – (Left) Ratio of the averaged entropy density over averaged baryon density $\langle s\rangle/\langle n_B\rangle$ in the midrapidity region for different collisional energies of heavy-ions as a function of time. (Right) Averaged baryon chemical potential μ_B extracted from PHSD simulations around the chemical freeze-out temperature T_{ch} in comparison with the values obtained from statistical models [117, 422, 424].

We close this section by summarizing the previous results and show in the right-hand side of Fig. 7.26 the average baryon chemical potential (from PHSD simulations) taken around the chemical freeze-out temperature (given by the statistical analysis from Refs. [117, 422, 424]). We looked only at cells in the midrapidity region to compare with the results from the statistical models. One should again stress that we compare two completely different quantities here: one is μ_B obtained from a statistical analysis of the final particle spectra, and the other is the average μ_B probed in a PHSD simulation around the chemical freeze-out temperature (the latter itself being obtained by a statistical analysis). As one can see in Fig. 7.26, these two quantities are in a fairly good agreement especially at high energies where μ_B is rather small. At low collisional energies the extracted value of μ_B from the transport calculation (from cells at midrapidity) becomes slightly larger; this might partly be related to the fact that our equation of state might not be valid any more for such large values of μ_B/T as probed in this regime.

7.6 Observables from relativistic nucleus-nucleus collisions

As mentioned before the PHSD transport approach [225, 226] is a microscopic covariant dynamical model for strongly interacting systems formulated on the basis of Kadanoff-Baym equations [120] for Green's functions in phase-space representation (in first order gradient expansion beyond the quasiparticle approximation). The approach consistently describes the full evolution of a relativistic heavy-ion collision from the initial hard scatterings and string formation through the dynamical deconfinement phase transition to the strongly-interacting quark-gluon plasma (sQGP) as well as hadronization and the subsequent interactions in the expanding hadronic phase as in the Hadron-String-Dynamics (HSD) transport approach [187] (cf. Chapter 3). Note that at lower bombarding energies - without any partonic phase - the PHSD approach merges to the HSD approach with only hadronic and string degrees of freedom. Since we only look for modifications in the partonic sector - cf. Sections 7.2 and 7.3, we do not further specify the hadronic sector and refer the reader to Refs. [7, 9, 187] for details. We recall that in the PHSD4.0 version the partonic cross sections are parametrized as a function of the energy density to comply with the individual widths of quarks, antiquarks and gluons (cf. Ref. [192]), while the parton masses are parametrized as a function of the scalar density (cf. Ref. [226]).

7.6.1 AGS-SPS energies

We start with lower and intermediated energies covered experimentally by the AGS (BNL) and SPS (CERN) with a focus on central Au+Au or Pb+Pb collisions. We will compare results for the "bulk" observables (rapidity distributions and p_T- or m_T-spectra) from PHSD calculations based on the default DQPM parameters (PHSD4.0) with the new PHSD5.0 including the differential cross sections from section 7.2 for the individual partonic channels at finite T and μ_B as well as the parton masses $M_i(T, \mu_B)$ from Eqs. (7.4)-(7.5). A comparison to the available experimental data is included (for orientation) but not discussed explicitly since this has been done in earlier work in detail [7, 9, 136].

Fig. 7.27 displays the actual results for hadronic rapidity distributions in case of 5% central Au+Au collisions at 10.7 A GeV for PHSD4.0 (green dot-dashed lines), PHSD5.0 with partonic cross sections and parton masses calculated for μ_B

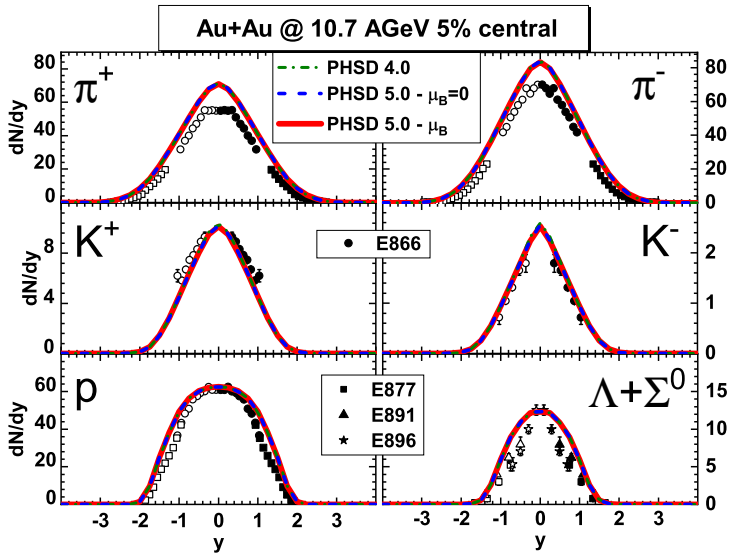

Figure 7.27 – The rapidity distributions for 5% central Au+Au collisions at 10.7 A GeV for PHSD4.0 (green dot-dashed lines), PHSD5.0 with partonic cross sections and parton masses calculated for $\mu_B = 0$ (blue dashed lines) and with cross sections and parton masses evaluated at the actual chemical potential μ_B in each individual space-time cell (red lines) in comparison to the experimental data from the E866 [366], E877 [367], E891 [368], E877 [369] and E896 [212] collaborations. All PHSD results are the same within the linewidth.

= 0 (blue dashed lines), and with cross sections and parton masses evaluated at the actual chemical potential μ_B in each individual space-time cell (red lines) in comparison to the experimental data from the E866 [366], E877 [367], E891 [368], E877 [369] and E896 [212] collaborations. Here we focus on the most abundant hadrons, i.e. pions, kaons, protons and neutral hyperons. We note in passing that the effects of chiral symmetry restoration from chapter 6 are incorporated. As seen from Fig. 7.27 there is no difference in rapidity distributions for all the hadron species from the different versions of PHSD within linewidth which implies that there is no sensitivity to the new partonic differential cross sections and parton masses employed. One could argue that this result might be due to the low amount of QGP produced at this energy but the different PHSD calculations for 5% central Pb+Pb collisions at 30 A GeV in Fig. 7.28 for the hadronic rapidity distributions do not provide a different picture, too. Only when stepping up to the top SPS energy of 158 A GeV one can identify a small difference in the antibaryon sector ($\bar{p}$, $\bar{\Lambda}+\bar{\Sigma}^0$) in case of 5% central Pb+Pb collisions (cf. Fig. 7.29).

According to the studies above there is apparently no sizable sensitivity in

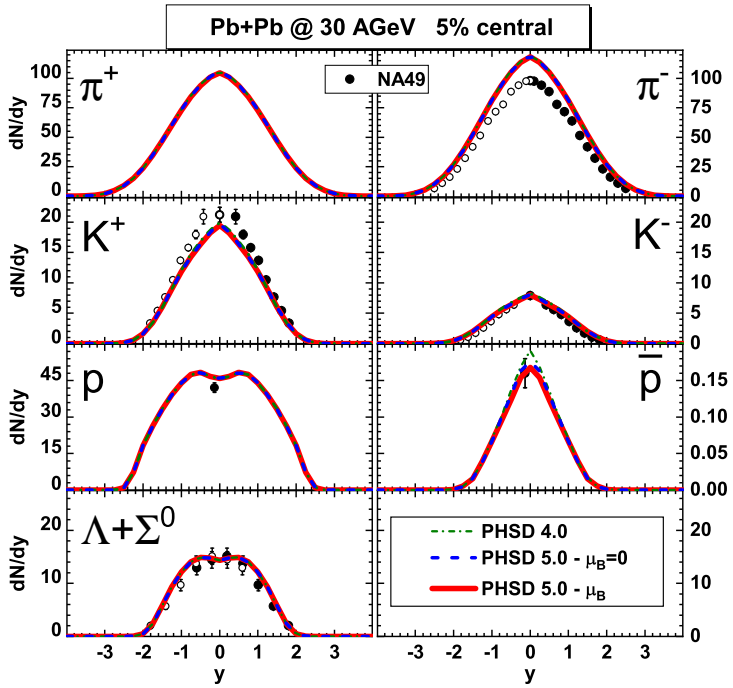

Figure 7.28 – The rapidity distributions for 5% central Pb+Pb collisions at 30 A GeV for PHSD4.0 (green dot-dashed lines), PHSD5.0 with partonic cross sections and parton masses calculated for $\mu_B = 0$ (blue dashed lines) and with cross sections and parton masses evaluated at the actual chemical potential μ_B in each individual space-time cell (red lines) in comparison to the experimental data from the NA49 Collaboration [214, 216, 217]. All PHSD results are practically the same within the linewidth.

the hadronic rapidity distributions to the actual differential partonic cross sections, but one has to explore the transverse dynamics in addition. To this end we show in Figs. 7.30 the transverse momentum distributions for 5% central Au+Au and Pb+Pb collisions at 10.7 A GeV, 30 A GeV, and 158 A GeV, at midrapidity ($|y| < 0.5$) for PHSD4.0 (green lines), PHSD5.0 with partonic cross sections and parton masses calculated for $\mu_B = 0$ (blue lines) and with cross sections and parton masses evaluated at the actual chemical potential μ_B in each individual space-time cell (red lines) in comparison to the experimental data from the E917 and E866 collaborations [209, 210], and the NA49 collaboration [214–217, 370, 371]. Here the solid lines stand for positively charged particles while the dashed lines display the results for negatively charged particles. We find that at 30 A GeV there is practically no change in the p_T spectra for all PHSD versions; only at 158 A GeV tiny changes in the p_T spectra become visible for transverse momenta above about 2.5 GeV/c. Furthermore for 10.7 A GeV Au+Au collisions we do not find any

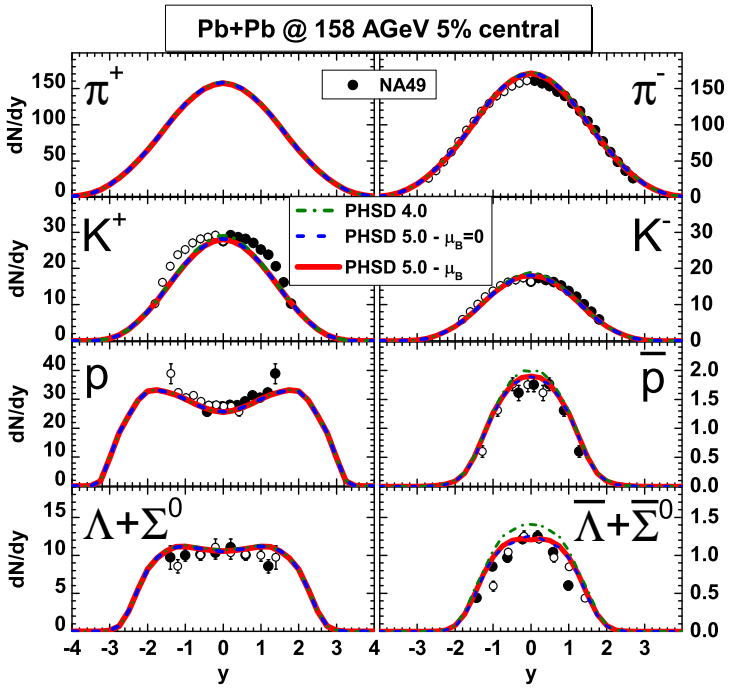

Figure 7.29 – The rapidity distributions for 5% central Pb+Pb collisions at 158 A GeV for PHSD4.0 (green dot-dashed lines), PHSD5.0 with partonic cross sections and parton masses calculated for $\mu_B = 0$ (blue dashed lines) and with cross sections and parton masses evaluated at the actual chemical potential μ_B in each individual space-time cell (red lines) in comparison to the experimental data from the NA49 Collaboration [215, 370–372]. All PHSD results are the same within the linewidth except for the antibaryons.

changes also in the p_T spectra within the linewidth (cf. Fig. 7.30). Apparently, the space-time volume of the partonic phase is too small at AGS and SPS energies even in central Pb+Pb collisions such that one has practically no sensitivity to the microscopic collisional details in the partonic phase. However, this might change for ultra-relativistic collision systems where the QGP phase becomes dominant.

7.6.2 RHIC energies

As demonstrated in chapter 4 one expects a dominantly partonic phase in central Au+Au collisions at $\sqrt{s_{NN}} = 200$ GeV especially when gating on midrapidity. However, the differences between PHSD4.0 and PHSD5.0 (with and without μ_B-dependence) in the hadronic rapidity distributions for 5% central Au+Au col-

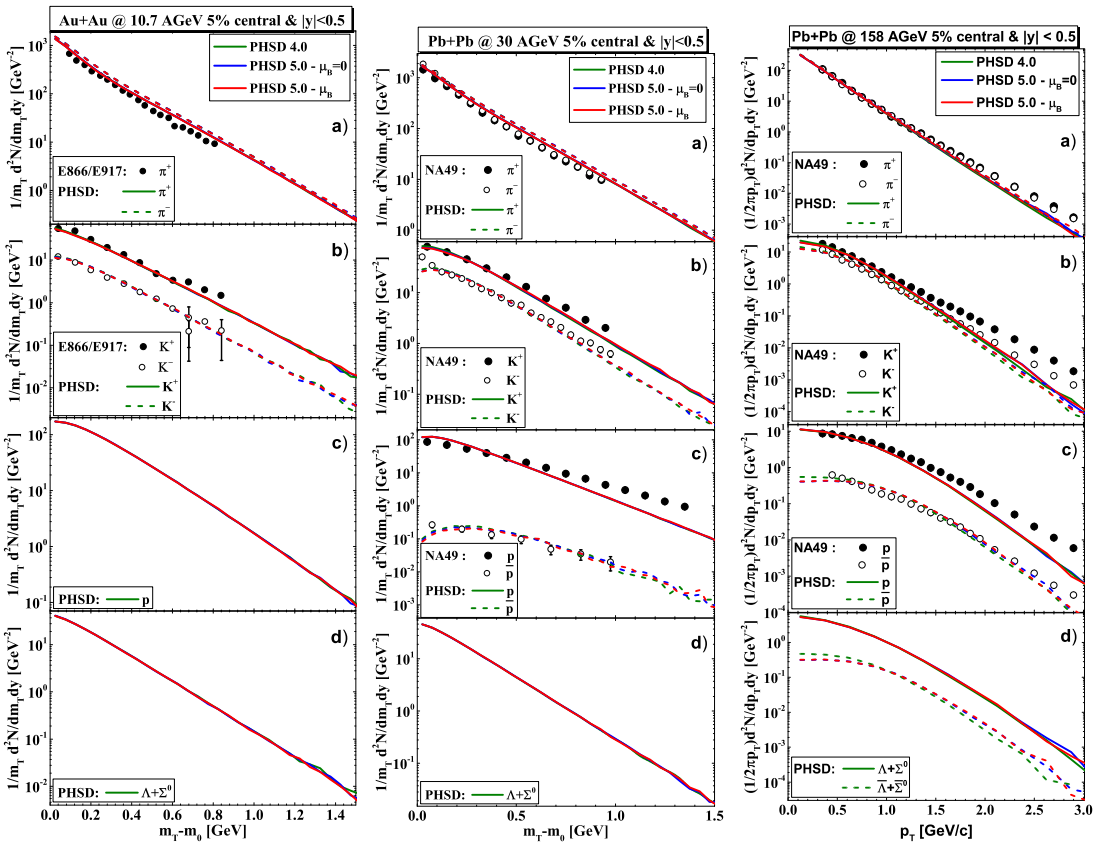

Figure 7.30 – The transverse momentum distributions for 5% central Au+Au collisions at 11 A GeV (left panel) and Pb+Pb collisions at 30 A GeV (middle panel) and 158 A GeV (right panel), in midrapidity ($|y| < 0.5$) for PHSD4.0 (green lines), PHSD5.0 with partonic cross sections and parton masses calculated for $\mu_B = 0$ (blue lines) and with cross sections and parton masses evaluated at the actual chemical potential μ_B in each individual space-time cell (red lines) in comparison to the experimental data from the E917 and E866 collaborations [209, 210] (left), from the NA49 Collaboration [214, 216, 217] (middle) and [215, 370, 371] (right).

lisions turn out to be rather small for mesons ($\pi^{\pm}, K^{\pm}$) and also for baryons and antibaryons ($p, \bar{p}, \Lambda + \Sigma^0, \bar{\Lambda} + \bar{\Sigma}^0$) (cf. Fig. 7.31) such that no robust conclusion on the partonic collisional dynamics can be drawn even in this case.

This also holds true for the transverse momentum distributions at midrapidity ($|y| < 0.5$) for these collisions when comparing the results from the different PHSD versions with each other and the data from the PHENIX [311] and STAR [425] collaborations in Fig. 7.32. Only for high transverse momenta small differences

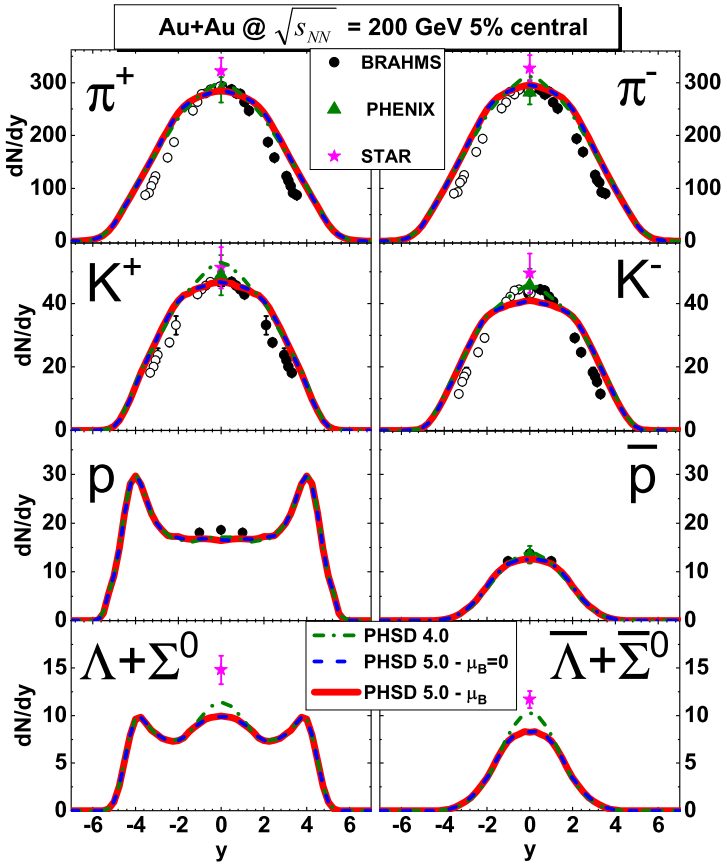

Figure 7.31 – The rapidity distributions for 5% central Au+Au collisions at $\sqrt{s_{NN}}$ = 200 GeV for PHSD4.0 (green dot-dashed lines), PHSD5.0 with partonic cross sections and parton masses calculated for $\mu_B = 0$ (blue dashed lines) and with cross sections and parton masses evaluated at the actual chemical potential μ_B in each individual space-time cell (red lines) in comparison to the experimental data from the BRAHMS [310, 312], PHENIX [311] and STAR [425] collaborations.

can be seen with the tendency to improve the description of the data in the novel versions of PHSD5.0 with the microscopic differential partonic cross sections.

7.6.3 Asymmetric systems

Since the central collisions of the heavy systems (Au+Au or Pb+Pb) only provide information on the total partonic reaction rate and not on details of the partonic collisional dynamics one has to explore asymmetric heavy-ion collisions -

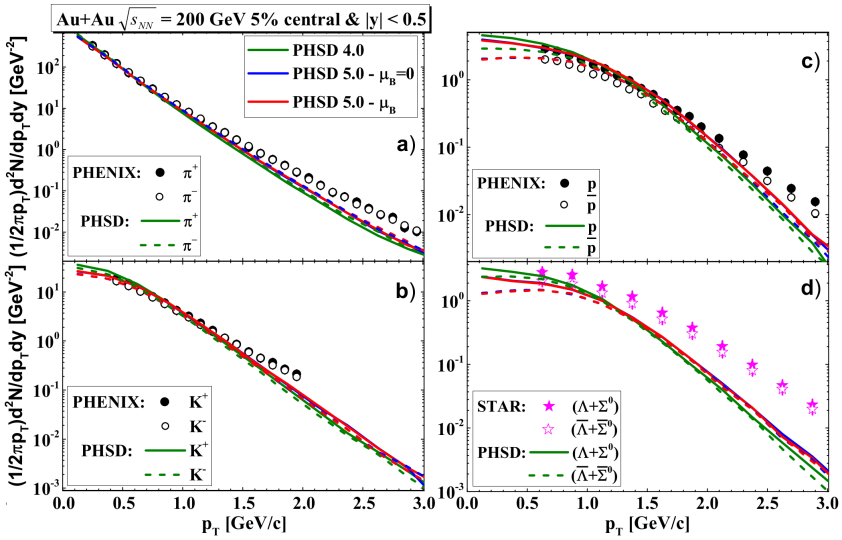

Figure 7.32 – The transverse momentum distributions for 5% central Au+Au collisions at $\sqrt{s_{NN}} = 200$ GeV and midrapidity ($|y| < 0.5$) for PHSD4.0 (green lines), PHSD5.0 with partonic cross sections and parton masses calculated for $\mu_B = 0$ (blue lines) and with cross sections and parton masses evaluated at the actual chemical potential μ_B in each individual space-time cell (red lines) in comparison to the experimental data from the PHENIX [311] and STAR [425] collaborations.

such as C+Au or Cu+Au - in addition in order find out a possible sensitivity to the partonic collisions. To this end we have performed a systematic study of 5% C+Au and Cu+Au collisions at bombarding energies from AGS to top RHIC energies for the "bulk" observables within the different PHSD versions. We note that (without explicit representation) we did not find any difference at 10.7 A GeV and 30 A GeV as in case of the heavy symmetric systems for the hadronic rapidity distributions and transverse momentum spectra at midrapidity. For Cu+Au the actual results - w.r.t. to the differences between PHSD4.0 and PHSD5.0 - at all bombarding energies turned out to be very similar to the central Au+Au or Pb+Pb collisions such that an explicit representation is discarded. Only in case of 5% C+Au reactions at top SPS and top RHIC energies some differences have been found which will be discussed in the following.

The rapidity distributions of hadrons for 5% central C+Au collisions are displayed in Figs. 7.33 for 158 A GeV and $\sqrt{s_{NN}} = 200$ GeV. Note that the rapidity distributions are no longer symmetric in rapidity y but enhanced for $y < 0$ (Au-going side). There is no change of the pion and baryon distributions at both energies for the different PHSD versions as in case of the heavy symmetric systems

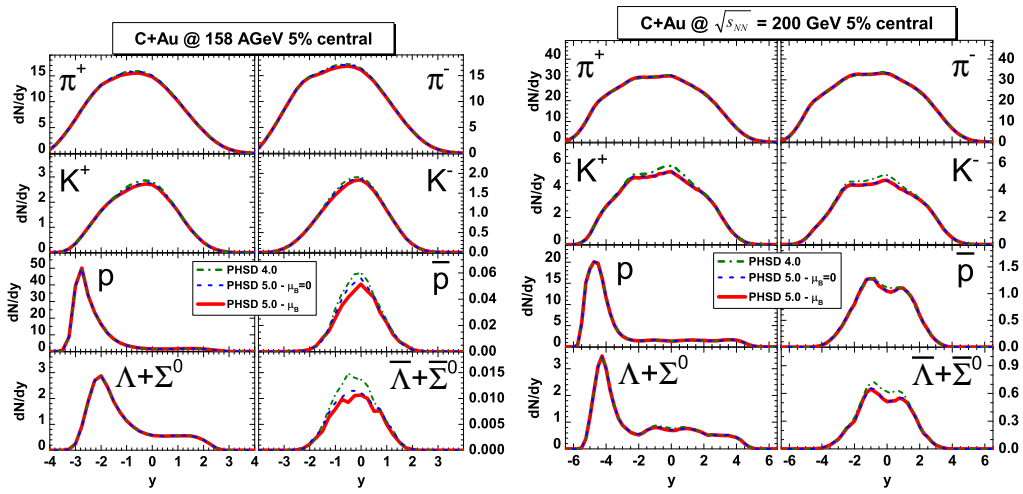

Figure 7.33 – The rapidity distributions for 5% central C+Au collisions at 158 A GeV (left) and at $\sqrt{s_{NN}} = 200$ GeV (right) for PHSD4.0 (green dot-dashed lines), PHSD5.0 with partonic cross sections and parton masses calculated for $\mu_B = 0$ (blue dashed lines) and with cross sections and parton masses evaluated at the actual chemical potential μ_B in each individual space-time cell (red lines).

while tiny differences can again be seen in the antibaryon spectra. However, in case of C+Au now there is also a small signal in the kaon rapidity distributions which is more pronounced at $\sqrt{s_{NN}} = 200$ GeV. This suggests that the strangeness degree of freedom might be explored in very asymmetric systems to obtain additional information on the partonic scattering dynamics.

The transverse momentum spectra of hadrons at midrapidity (for C+Au) are shown in Figs. 7.34 for 158 A GeV and $\sqrt{s_{NN}} = 200$ GeV. There is practically no difference in the PHSD4.0 and PHSD5.0 results for pions, kaons, protons and antiprotons and only a very small signal in the antihyperons can be identified. Nevertheless, our results for this very asymmetric system can be considered as predictions for the production of the most abundant hadron species at top SPS and RHIC energies.

7.7 Summary

In this chapter we have extended the PHSD transport approach (PHSD4.0 [7, 136]) to incorporate differential "off-shell cross sections" for all binary partonic channels that are based on the same effective propagators and couplings as em-

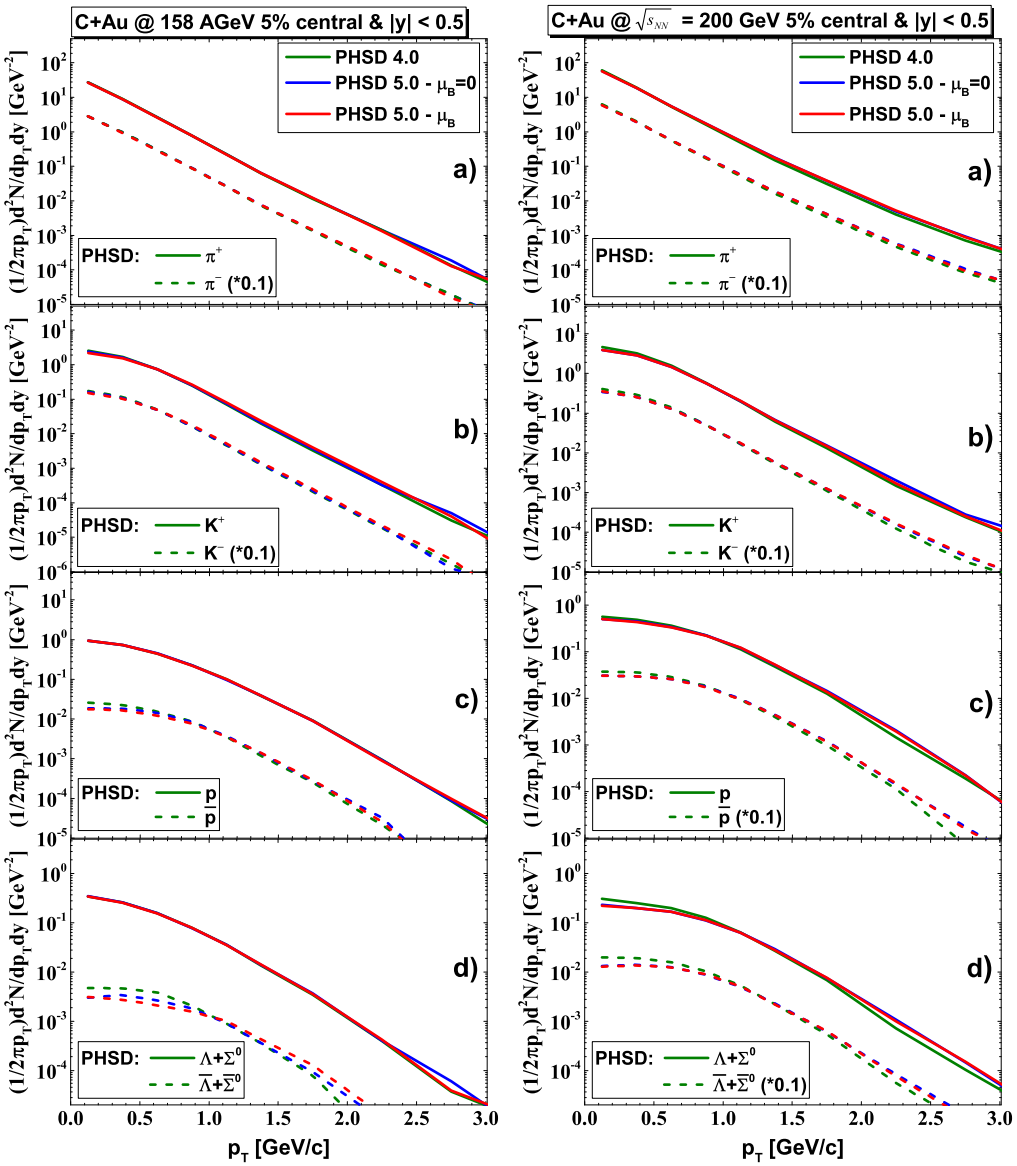

Figure 7.34 – The transverse momentum distributions for 5% central C+Au collisions at 158 A GeV (left) and at $\sqrt{s_{NN}} = 200$ GeV (right), at midrapidity ($|y| < 0.5$) for PHSD4.0 (green lines), PHSD5.0 with partonic cross sections and parton masses calculated for $\mu_B = 0$ (blue lines) and with cross sections and parton masses evaluated at the actual chemical potential μ_B in each individual space-time cell (red lines).

ployed in the QGP equation of state and the parton propagation. To this end we have recalled the extraction of the partonic masses and the coupling g^2 from lattice QCD data (within the DQPM) and calculated the partonic differential cross sections as a function of T and μ_B for the leading tree-level diagrams (cf. Appendices B). Furthermore, in Section 7.3 we have used these differential cross sections to evaluate partonic scattering rates for fixed T and μ_B as well as to compute the ratio of the shear viscosity η and bulk viscosity ζ to entropy density s within the Kubo formalism in comparison to calculations from lQCD. It turns out that the ratios η/s and ζ/s calculated with the partonic scattering rates in the relaxation-time approximation are very similar to the original result from the DQPM and to lQCD results such that the present extension of the approach does not lead to different partonic transport properties except for temperatures close to T_c. We recall that the novel PHSD version (PHSD5.0) is practically parameter free in the partonic sector since the effective coupling (squared) is determined by a fit to the scaled entropy density from lQCD. The dynamical masses for quarks and gluons then are fixed by the HTL expressions. The interaction rate in the time-like sector is, furthermore, calculated in leading order employing the DQPM propagators and coupling.

When implementing the differential cross sections and parton masses into the PHSD5.0 approach one has to specify the "Lagrange parameters" T and μ_B in each computational cell in space-time. This has been done by employing a state-of-the-art equation of state from lattice QCD [416] and a diagonalization of the energy-momentum tensor from PHSD as described in chapter 4. Detailed results for T and μ_B have been presented for central collisions of Pb+Pb at $\sqrt{s_{NN}} = 17.3$ and Au+Au 200 GeV in the (T, μ_B) plane as a function of reaction time. It turns out that the evolution of the QGP from the PHSD at $\sqrt{s_{NN}} = 17.3$ with T above T_c follows closely the expectation from the isentropic trajectories while at the top RHIC energy the distribution in T and μ_B spreads around zero for all reaction times considered.

In Section 7.5 we then have calculated 5% central Au+Au (or Pb+Pb) collisions and compared the results for hadronic rapidity distributions and transverse momentum spectra (at midrapidity) from the previous PHSD4.0 with the novel version PHSD5.0 (with and without the explicit dependence of the partonic differential cross sections and parton masses on μ_B). No differences for all the hadron "bulk" observables from the various PHSD versions have been found at AGS and FAIR/NICA energies within linewidth which implies that there is no sensitivity to the new partonic differential cross sections employed. Only in case of the kaons and the antibaryons $\bar{p}$ and $\bar{\Lambda} + \bar{\Sigma}^0$, a small difference between PHSD4.0 and PHSD5.0

could be seen at top SPS and top RHIC energies, however, no clear difference between the PHSD5.0 calculations with partonic cross sections for $\mu_B = 0$ and actual μ_B in the local cells. When considering very asymmetric collisions of C+Au, a small sensitivity to the partonic scatterings was found in the kaon and antibaryon rapidity distributions, too. However, it will be very hard to extract a robust signal experimentally.

Our findings can be understood as follows: The fact that we find only small traces of the μ_B-dependence of partonic scattering dynamics in heavy-ion "bulk" observables - although the differential cross sections and parton masses clearly depend on μ_B - implies that one needs a sizable partonic density and large space-time QGP volume to explore the dynamics in the QGP phase. These conditions are only fulfilled at high bombarding energies (top SPS, RHIC energies) where, however, μ_B is rather low. On the other hand, decreasing the bombarding energy to FAIR/NICA energies and, thus increasing μ_B, leads to collisions that are dominated by the hadronic phase where the extraction of information about the parton dynamics will be rather complicated based on "bulk" observables. Further investigations of other observables (such as flow coefficients v_n of particles and antiparticles, fluctuations and correlations) might contain more visible "μ_B-traces" from the QGP phase.

Summary and Discussion

* * *

In this dissertation we investigated the nonequilibrium properties of the Quark-Gluon Plasma (QGP) as produced in relativistic heavy-ion collisions. To this end we employed the Parton-Hadron-String Dynamics (PHSD) transport approach which describes the whole evolution of heavy-ion collisions from the first collisions of the initial nucleons, to the formation of the Quark-Gluon Plasma, its hadronization at later times, and to the final hadronic interactions. Indeed, only fully microscopic nonequilibrium transport approaches can shed light about the evolution and equilibration in time of the matter produced in heavy-ion collisions. The PHSD applies generalized transport equations, which result from the evolution equation for the Green's functions, i.e. the Kadanoff-Baym equations, to the description of relativistic heavy-ion collisions. Concerning the degrees-of-freedom of the Quark-Gluon Plasma, we employed the Dynamical QuasiParticle Model (DQPM) where partons are described as interacting quasiparticles with sizable and imaginary self-energies. The latter are fitted in order to reproduce the lattice QCD equation of state in equilibrium at finite temperatures T and small chemical potentials μ_B, and thus directly incorporates the non-perturbative nature of QCD.

The Quark-Gluon Plasma is predominantly produced in the case of very high energy heavy-ion collisions with a lifetime of several fm/c where most of the total energy is converted into deconfined matter. In that energy regime, we first compared the dynamics of the Quark-Gluon Plasma from the PHSD to a 2D+1 viscous hydrodynamical model in order to investigate the major differences between these two descriptions in the evolution of the QGP. Contrary to microscopic transport approaches, hydrodynamical models can only describe the Quark-Gluon Plasma after a time of about ≈ 1 fm/c where the medium shows some degree of thermalization since they work under the assumption of local equilibrium. We initialized the hydrodynamical simulations with nonequilibrium initial conditions from the PHSD when the medium was found to be sufficiently in equilibrium in the midrapidity region (after ≈ 0.6 fm/c). Before, the pressure anisotropy is well too large to be handled by the viscous hydrodynamical model since at the very beginning of the collision the transverse pressure largely dominates while the transverse pressure develops progressively in time. After adjusting the parameters of the hydrodynamical model such that it reproduces the one intrinsically present in the PHSD

(such as the equation of state or the shear and bulk viscosities), we compare the evolution of the Quark-Gluon Plasma in the two models. To extract the relevant quantities for our comparison such as energy density, flow velocities and pressure, we performed a diagonalization of the energy-momentum tensor as obtained in the space-time grid of the PHSD. The hydrodynamical evolution is smooth in time while the PHSD evolution contains fluctuating small structures which are seen by example in the energy density, velocity or temperature profiles in the transverse plane of a central Au+Au collision at $\sqrt{s_{NN}} = 200$ GeV. To quantify these differences we looked at the Fourier modes of the energy density profile and we indeed fond short-wavelength spatial components in the PHSD at all times while in the hydrodynamical model only the global long-wavelength modes survive. Furthermore, we looked at the spatial and momentum eccentricities of the fireball as a function of time and we found that the eccentricities in each single PHSD event possess strong fluctuations while in the hydrodynamical simulations they remain smooth. However, by averaging over a large number of PHSD profiles, we find a very good agreement between the QGP evolution of PHSD and the hydrodynamical model. To conclude we observed that the PHSD transport approach and the hydrodynamical model are very similar to each other when averaging over a large number of PHSD events. While in the hydrodynamical simulations one assumes that the QGP is a continuous fluid, the PHSD contains much more structures due to the finite number of particles in each simulation. It would be interesting to extend this comparison in the full rapidity range by using a 3D+1 hydrodynamical model. However, this requires a conversion of the energy momentum tensor from the PHSD in Milne coordinates which has already been developed (see appendix D) and used in the context of Ref. [3] where the effects of different QGP evolutions were studied with respect to the charm quark evolution. In order to compare the PHSD evolution of the Quark-Gluon Plasma in an even earlier stage of heavy-ion collisions, one would additionally need to employ an anisotropic fluid dynamical description [426] which directly incorporates the nonequilibrium nature of the medium.

An other advantage of using a microscopic transport equation is that we are able to track the chemical composition and equilibration of the QGP as a function of time, while the only relevant information in hydrodynamical models is the equation of state. Especially, we studied the effect of having different compositions of the Quark-Gluon Plasma at its appearance in relativistic heavy-ion collisions. By keeping the same energy-momentum tensor, we considered a purely gluonic (Scenario I) or a purely quarkonic (Scenario II) initial condition of the QGP. We found that within the PHSD, the equilibration of strange quarks is too slow such that in Scenario I the rapidity spectra of K^+ is greatly underestimated in comparison

to experimental data, while the purely quarkonic scenario is in accordance with the latter. The differential elliptic flow was not found to be sensitive to the different degrees-of-freedom, but electromagnetic observables which are dominantly produced by quark-antiquark annihilation $q + \bar{q} \to g + \gamma$, or gluon-Compton-scattering $q(\bar{q}) + g \to q(\bar{q}) + \gamma$, are found to be much more reduced in Scenario I since gluons do not carry electric charge. However, the final dilepton spectra does not allow us to discriminate between the two scenarios due to experimental uncertainties and to the large contribution from charmed mesons in the intermediate mass range. However, we found in Ref. [5] that a clear signal from the QGP can be obtained by studying low collisional energies where the charm quark production becomes subdominant. Future experimental data from the Beam Energy Scan program could be used in order to study in more detail the content of the Quark-Gluon Plasma at low collisional energies.

We kept studying the initial stage of heavy-ion collisions and especially the Schwinger mechanism for the string decay in the PHSD transport approach where essential aspects of chiral symmetry restoration (CSR) have been implemented. The scalar quark condensate $\langle \bar{q}q \rangle$, being the order parameter for the restoration of chiral symmetry, directly influences the constituent quark masses which are used to calculate the relative probabilities to produce a certain quark flavor in the string fragmentation process. In particular, we found that a partial restoration of chiral symmetry implies an enhancement of the strange quark fraction $\gamma_s \sim s/u$ via the string decay. However, this mechanism only influences the hadronic particle production whereas at high energy collisions most of the produced matter is converted in the deconfined state of the Quark-Gluon Plasma where the parton masses are defined by the DQPM. We indeed found that CSR occurs at low collisional energies due to the high baryon density and we consequently observed a steep rise of the K^+/π^+ ratio in central A+A collisions with increasing energy. With the appearance of the QGP at high energies, we observe a drop in the same K^+/π^+ ratio since the enhancement of the strange quark production by CSR only occurs in a hadronic medium. As a result, the "horn" seen in experimental data for the K^+/π^+ ratio as a function of the collisional energy is well described by the PHSD including aspects of CSR while calculations without CSR fail substantially. Furthermore, we tested the dependence of our results on the nuclear equation of state by employing different parametrizations (NL1, NL2 and NL3) and in all cases we recovered the same "horn" feature. This supports the reliability of the CSR mechanism as implemented in the PHSD model. The effect of CSR has also been studied in the strange baryon sector where a "horn" structure is seen as well when including the CSR. However, more precise experimental data would be needed in the case of multistrange baryons in order to precisely confront the CSR as currently

implemented in the PHSD. We stress that our PHSD calculations provide a microscopic interpretation of the "horn" structure in the excitation function of the K^+/π^+ ratio in central heavy-ion collisions. The effect of CSR can be additionally tested by considering different sizes of the colliding ions (^{197}Au, ^{40}Ca and ^{12}C) where we found a decrease of the "horn" structure when decreasing the system size and even a disappearance in case of C+C collisions. This suggests that the strange particle spectra and yields are suitable signatures to study the properties of CSR in heavy-ion collisions in future also as a function of the system size or centrality.

In the last chapter of this dissertation we focused on the dynamics of the Quark-Gluon Plasma at finite baryon chemical potential μ_B which becomes relevant in the description of low energy heavy-ion collisions. Indeed, we found that at the top SPS energy ($\sqrt{s_{NN}} = 17.3$ GeV) the chemical potential which is probed in central Pb+Pb collisions is well in accordance with the expectation from a statistical analysis ($\mu_B \approx 0.25$ GeV). Moreover, the trajectory of the fireball in the $(T-\mu_B)$-plane was found to be similar to the isentropic trajectories corresponding to a fixed ratio of the entropy density over baryon density s/n_B. The DQPM was employed in order to describe the QGP phase at finite temperature T and chemical potential μ_B and to construct partonic differential cross sections which are needed in a microscopic transport approach such as PHSD. However, we only observe a modest change of the partonic cross sections and the shear viscosity calculated within the DQPM with respect to the chemical potential μ_B. This also holds for a variety of hadronic observables from central A+A collisions in the energy range 5 GeV $\leq \sqrt{s_{NN}} \leq$ 200 GeV with practically no sensitivity of rapidity and p_T distributions to the μ_B dependence of the parton masses and partonic cross sections. We observe small variations in the strangeness sector in all studied collisional systems (A+A and C+Au), however, it will be very hard to extract a robust signal experimentally. Furthermore, a large space-time QGP volume, which would be needed to explore the dynamics of the partonic phase, is only produced at very high collisional energies where the baryon chemical potential is almost vanishing. When decreasing the bombarding energy, the hadronic phase becomes dominant and accordingly, it would be difficult to extract signals from the partonic dynamics based only on "bulk" observables. Further investigation on more precise observables, such as flow coefficients of particles and antiparticles, might contain more visible "μ_B-traces" from the QGP phase at low collisional energies.

Appendix A

Classical Kinetic Theory

* * *

In the context of Hamiltonian mechanics, a classical physical system is described at any time t by a set of canonical coordinates $(\boldsymbol{q_i}(t),\ \boldsymbol{p_i}(t))$ associated for each particle (with $i = 1, ..., N$). The evolution of the system is determined by **Hamilton's equations**:

$$\dot{\boldsymbol{p}}_i = \frac{\partial \boldsymbol{p}_i}{\partial t} = -\frac{\partial \mathcal{H}(t, \boldsymbol{q}_i(t), \boldsymbol{p}_i(t))}{\partial \boldsymbol{q}_i} \quad ; \quad \dot{\boldsymbol{q}}_i = \frac{\partial \boldsymbol{q}_i}{\partial t} = \frac{\partial \mathcal{H}(t, \boldsymbol{q}_i(t), \boldsymbol{p}_i(t))}{\partial \boldsymbol{p}_i}, \tag{A.1}$$

where $\mathcal{H}$ denotes the Hamiltonian which often corresponds to the total energy of the system.

The complete description of a gas composed of N classical particles is possible knowing the position $\boldsymbol{q}_i(t)$ and the momentum $\boldsymbol{p}_i(t)$ at a fixed time t for each of these particles with $1 \leq i \leq N$. In statistical mechanics, this specific configuration of particles is called a microstate and is described by a single point in the set of $6N$ coordinates called a phase-space, defined by the coordinates and momenta of each of the particles. Since the microstate can fluctuate according to the defined macrostate of the system, it is useful to introduce the phase-space density $\rho(t, \boldsymbol{q}_i, \boldsymbol{p}_i)$ corresponding to the probability of observing a certain microstate in an infinitesimal volume $\prod_{i=1}^{N} d^3q_i d^3p_i$ around the coordinates $(\boldsymbol{q}_i, \boldsymbol{p}_i)$. From the canonical equations (A.1), one can deduce the evolution of the phase-space distribution $\rho(t, \boldsymbol{q}_i, \boldsymbol{p}_i)$ from the continuity equation:

$$0 = \frac{\partial \rho(t, \boldsymbol{q}_i, \boldsymbol{p}_i)}{\partial t} + \boldsymbol{\nabla} \cdot (\rho(t, \boldsymbol{q}_i, \boldsymbol{p}_i)\ \boldsymbol{u}(t, \boldsymbol{q}_i, \boldsymbol{p}_i)) \,. \tag{A.2}$$

One can prove using Hamilton's equations (A.1) that the divergence of the phase-space velocity $\boldsymbol{u}(t, \boldsymbol{q}_i, \boldsymbol{p}_i)$ is:

$$\boldsymbol{\nabla} \cdot \boldsymbol{u}(t, \boldsymbol{q}_i, \boldsymbol{p}_i) = \frac{\partial \dot{\boldsymbol{q}}_i}{\partial \boldsymbol{q}_i} + \frac{\partial \dot{\boldsymbol{p}}_i}{\partial \boldsymbol{p}_i} = 0. \tag{A.3}$$

This latter condition corresponds in fact to an incompressible flow. From Eq.(A.2) we obtain the **Liouville equation**, which states that the evolution of the phase-space density is constant along a phase-space trajectory:

$$0 = \frac{\partial \rho(t, \boldsymbol{q}_i, \boldsymbol{p}_i)}{\partial t} + \frac{\partial \rho(t, \boldsymbol{q}_i, \boldsymbol{p}_i)}{\partial \boldsymbol{q}_i} \cdot \frac{\partial \boldsymbol{q}_i}{\partial t} + \frac{\partial \rho(t, \boldsymbol{q}_i, \boldsymbol{p}_i)}{\partial \boldsymbol{p}_i} \cdot \frac{\partial \boldsymbol{p}_i}{\partial t} = \frac{d\rho(t, \boldsymbol{q}_i, \boldsymbol{p}_i)}{dt} \tag{A.4}$$

$$0 = \frac{\partial \rho(t, \boldsymbol{q}_i, \boldsymbol{p}_i)}{\partial t} + \frac{\partial \rho(t, \boldsymbol{q}_i, \boldsymbol{p}_i)}{\partial \boldsymbol{q}_i} \cdot \frac{\partial \mathcal{H}}{\partial \boldsymbol{p}_i} - \frac{\partial \rho(t, \boldsymbol{q}_i, \boldsymbol{p}_i)}{\partial \boldsymbol{p}_i} \cdot \frac{\partial \mathcal{H}}{\partial \boldsymbol{q}_i} \tag{A.5}$$

$$0 = \frac{\partial \rho(t, \boldsymbol{q}_i, \boldsymbol{p}_i)}{\partial t} + \{\rho(t, \boldsymbol{q}_i, \boldsymbol{p}_i), \mathcal{H}\} \tag{A.6}$$

where $\{...\}$ denotes the non-relativistic Poisson bracket.

In kinetic theory, the goal is usually to describe gases containing a very large number of identical particles in terms of macroscopic quantities, starting from their equation of motion. To compute macroscopic quantities, any observable O can be averaged over the ensemble as:

$$\langle O(t) \rangle = \frac{\int \prod_{i=1}^{N} d^3 q_i \; d^3 p_i \; O(\boldsymbol{q}_i, \boldsymbol{p}_i) \rho(t, \boldsymbol{q}_i, \boldsymbol{p}_i)}{\int \prod_{i=1}^{N} d^3 q_i \; d^3 p_i \; \rho(t, \boldsymbol{q}_i, \boldsymbol{p}_i)}. \tag{A.7}$$

A.1 Distribution function

The use of the phase-space distribution $\rho(t, \boldsymbol{q}_i, \boldsymbol{p}_i)$, describing the system in terms of the coordinates of each individual particles, becomes prohibitive for a very large number of particles and actually contains too much information to compute macroscopic quantities like the pressure or energy of the system. To reduce the complexity of the problem, one introduces $n-$particle distribution functions which represent the probability distribution of a set of $n-$particles with $n < N$. These reduced distribution functions are obtained by integrating the other phase-space

coordinates and taking into account a combinatorial factor:

$$f_n(t,\boldsymbol{q}_1,\boldsymbol{p}_1,...\boldsymbol{q}_n,\boldsymbol{p}_n) = \frac{N!}{(N-n)!}\int \prod_{i=n+1}^{N} d^3q_i\ d^3p_i\ \rho(t,\boldsymbol{q}_i,\boldsymbol{p}_i) \tag{A.8}$$

$$= \frac{N!}{(N-n)!}\ \rho_n(t,\boldsymbol{q}_1,\boldsymbol{p}_1,...\boldsymbol{q}_n,\boldsymbol{p}_n). \tag{A.9}$$

To proceed further one can assume an Hamiltonian containing two-body interactions between the particles as:

$$\mathcal{H}(\boldsymbol{q}_i,\boldsymbol{p}_i) = \sum_{i=1}^{N}\left(\frac{\boldsymbol{p}_i^2}{2m} + U(\boldsymbol{q}_i) + \frac{1}{2}\sum_{j=1}^{N} V_{ij}(\boldsymbol{q}_i-\boldsymbol{q}_j)\right), \tag{A.10}$$

where U is some external potential and V_{ij} refers to a two-body interaction between the particles i and j with $V_{ii}=0$. Inserting this Hamiltonian into the Liouville equation (A.6), we obtain the following equation:

$$\frac{\partial\rho}{\partial t} + \sum_{i=1}^{N}\left[\frac{\boldsymbol{p_i}}{m}\cdot\frac{\partial\rho}{\partial\boldsymbol{q}_i} - \left(\frac{\partial U}{\partial\boldsymbol{q}_i} + \sum_{j=1}^{N}\frac{\partial V_{ij}}{\partial\boldsymbol{q}_i}\right)\cdot\frac{\partial\rho}{\partial\boldsymbol{p}_i}\right] = 0. \tag{A.11}$$

The integration of this equation over the phase-space $\prod_{i=n+1}^{N} d^3\boldsymbol{q}_i d^3\boldsymbol{p}_i$ leads to the evolution of the $n-$particle distribution function:

$$\frac{\partial f_n}{\partial t} + \sum_{i=1}^{n}\left[\frac{\boldsymbol{p_i}}{m}\cdot\frac{\partial f_n}{\partial\boldsymbol{q}_i} - \left(\frac{\partial U}{\partial\boldsymbol{q}_i} + \sum_{j=1}^{n}\frac{\partial V_{ij}}{\partial\boldsymbol{q}_i}\right)\cdot\frac{\partial f_n}{\partial\boldsymbol{p}_i}\right]$$

$$= \frac{N!}{(N-n)!}\int \prod_{k=n+1}^{N} d^3q_k\ d^3p_k\ \sum_{i=1}^{n}\sum_{j=n+1}^{N}\frac{\partial V_{ij}}{\partial\boldsymbol{q}_i}\cdot\frac{\partial\rho}{\partial\boldsymbol{p}_i}. \tag{A.12}$$

The left side of this equation is obtained from the part in Eq. (A.11) when the sum over i and j runs only until n. In that case, ρ can be directly integrated to obtain f_n since all the prefactors depend only on the variables $(\boldsymbol{q}_1,\boldsymbol{p}_1,...\boldsymbol{q}_n,\boldsymbol{p}_n)$. When the sum over i and j runs between $n+1$ and N, an integration by part shows that this contribution is zero taking into account that the phase-space distribution vanishes at the limits of integration [427]. The right side, also being obtained using integration by parts, corresponds to the contribution from the particle interactions and can be further simplified by noticing that the sum over $j=n+1$ to N gives $(N-n)$ equal contributions:

$$\frac{\partial f_n}{\partial t}+\sum_{i=1}^{n}\left[\frac{\boldsymbol{p_i}}{m}\cdot\frac{\partial f_n}{\partial \boldsymbol{q}_i}-\left(\frac{\partial U}{\partial \boldsymbol{q}_i}+\sum_{j=1}^{n}\frac{\partial V_{ij}}{\partial \boldsymbol{q}_i}\right)\cdot\frac{\partial f_n}{\partial \boldsymbol{p}_i}\right] = \int d^3q_{n+1}\; d^3p_{n+1}\;\sum_{i=1}^{n}\frac{\partial V_{i,(n+1)}}{\partial \boldsymbol{q}_i}\cdot\frac{\partial f_{n+1}}{\partial \boldsymbol{p}_i}. \tag{A.13}$$

The set of coupled integro-differential equations is called the **BBGKY (Bogoliubov-Born-Green-Kyrkwood-Yvon) hierarchy** [428–432] and relates the $n-$particle distribution function to the $(n+1)$-particle distribution function through the 2-particle interaction introduced in the Hamiltonian (A.10). This system of equations indicates that the flow of the $n-$particle distribution function (left side of Eq. (A.13)) can be modified due to the interactions with the $(n+1)$-distribution (right side of Eq. (A.13)), which depends itself on the higher order distribution functions. In the case of a non-interacting system, we recover the same evolution for f_n as in the Liouville equation (A.6).

A.2 Boltzmann and Vlasov equation

In the context of kinetic theory, the $1-$particle distribution is of particular interest and is defined as:

$$f(t,\boldsymbol{x},\boldsymbol{p}) = \langle\sum_{i=1}^{N}\delta\left(\boldsymbol{x}-\boldsymbol{q}_i\right)\delta\left(\boldsymbol{p}-\boldsymbol{p}_i\right)\rangle \tag{A.14}$$

$$= N\int\prod_{i=2}^{N} d^3q_i\; d^3p_i\; \rho(t,\boldsymbol{x},\boldsymbol{p},\boldsymbol{q}_2,\boldsymbol{p}_2,...\boldsymbol{q}_N,\boldsymbol{p}_N). \tag{A.15}$$

The latter corresponds to the density of particles per phase-space volume around a particular point of the phase-space $(\boldsymbol{x},\boldsymbol{p})$. Its evolution can be obtained by taking the $n=1$ case in the BBGKY hierarchy (A.13):

$$\frac{\partial f}{\partial t}+\left[\frac{\boldsymbol{p}}{m}\cdot\frac{\partial f}{\partial \boldsymbol{q}}-\boldsymbol{F}\cdot\frac{\partial f}{\partial \boldsymbol{p}}\right]=\left(\frac{\partial f}{\partial t}\right)_{\text{coll}}=\int d^3q_2\; d^3p_2\; \boldsymbol{F}_{1,2}\cdot\frac{\partial f_2}{\partial \boldsymbol{p}}, \tag{A.16}$$

where we introduced for simplicity the notation $\boldsymbol{F}$ for the external force, and $\boldsymbol{F}_{1,2}$ for the pair force exerted by other particles on the particle 1. The right term of

Eq.(A.16) has been generalized in the so-called **collision term**, that represents the change in the distribution function due to collisions. The term inside the brackets on the left is known as the **drift term**; it simply describes the change in the particle distribution according to the motion of each particle.

To derive the Boltzmann equation, it is assumed that we are dealing with a dilute medium, or more specifically that the mean-free time of the particles is much larger than the collision duration. One can start from the evolution of f_2 dictated by the BBGKY hierarchy and simplify the expression to obtain the evolution equation for f, but we will explain it here without any tedious mathematical derivations.

The collision term can in general be decomposed in two contributions: a loss and a gain term. Indeed, collisions can either kick-in or kick-out particles from the considered phase-space volume. These two terms can be expressed as [433]:

$$C_{\text{gain}} = \frac{1}{2}\int d^3p_2 \; d^3p_1' \; d^3p_2' \; w(1'2' \to 12) \; f_2(\boldsymbol{x}, \boldsymbol{p}_1', \boldsymbol{p}_2', t) \tag{A.17}$$

$$C_{\text{loss}} = \frac{1}{2}\int d^3p_2 \; d^3p_1' \; d^3p_2' \; w(12 \to 1'2') \; f_2(\boldsymbol{x}, \boldsymbol{p}_1, \boldsymbol{p}_2, t), \tag{A.18}$$

where $d^3p_1' \; d^3p_2' \; w(12 \to 1'2')$ is the rate for the particle 1 and 2 to be scattered in the momentum range $(\boldsymbol{p}_1', \boldsymbol{p}_2')$ to $(\boldsymbol{p}_1' + d\boldsymbol{p}_1', \boldsymbol{p}_2' + d\boldsymbol{p}_2')$. In the case of elastic processes, the **detailed balance** condition states that these processes are time-reversible and thus that a particular process and its reverse have the same probability to happen:

$$w(12 \to 1'2') = w(1'2' \to 12). \tag{A.19}$$

The next step to simplify the collision term and the 2-particle distribution function, which is widely used in kinetic theory, is to simply ignore the correlation between the particles before their collision. This simplification is known as the *Stosszahlansatz*, or the "**molecular chaos hypothesis**":

$$f_2(\boldsymbol{x}, \boldsymbol{p}_1, \boldsymbol{p}_2, t) = f(\boldsymbol{x}, \boldsymbol{p}_1, t) \; f(\boldsymbol{x}, \boldsymbol{p}_2, t). \tag{A.20}$$

One can relate the transition rate to the differential cross-section by:

$$v_{12} \; d\sigma = d^3p_1' \; d^3p_2' \; w(12 \to 1'2'), \tag{A.21}$$

where $v_{12} = |\boldsymbol{v}_1 - \boldsymbol{v}_2|$ is the relative velocity between the colliding particles, and finally obtain the **Boltzmann** collision term:

$$\left(\frac{\partial f}{\partial t}\right)_{\text{coll}} = \frac{1}{2}\int d^3p_2 \int d\Omega\; v_{12}\left(\frac{d\sigma}{d\Omega}\right)\Big(f(\boldsymbol{x},\boldsymbol{p}_1',t)f(\boldsymbol{x},\boldsymbol{p}_2',t) - f(\boldsymbol{x},\boldsymbol{p}_1,t)f(\boldsymbol{x},\boldsymbol{p}_2,t)\Big)\,, \tag{A.22}$$

where Ω is the solid angle between the initial and final relative momenta. The integrals over the momenta in Eq. (A.18) can be carried out due to energy and momentum conservation in the collisional process.

In the case of long-range conservative forces between the particles like in plasma physics dealing with the Coulomb potential, the Boltzmann equation cannot be used since it only considers $2 \to 2$ (instantaneous) collisions. By using again the "molecular chaos hypothesis", the 2-particle distribution function in Eq. (A.16) reduces to a product of 1-particle distribution functions and leads to the (collisionless) **Vlasov equation** [434]:

$$\boxed{\frac{\partial f}{\partial t} + \left[\frac{\boldsymbol{p}}{m}\cdot\frac{\partial f}{\partial \boldsymbol{q}} - \left(\boldsymbol{F} + \bar{\boldsymbol{F}}_{1,2}\right)\cdot\frac{\partial f}{\partial \boldsymbol{p}}\right] = 0}\,, \tag{A.23}$$

where $\bar{\boldsymbol{F}}_{1,2} = \int d^3q_2 d^3p_2\; \boldsymbol{F}_{1,2} f(\boldsymbol{q}_2,\boldsymbol{p}_2)$ is the averaged force exerted on particle 1: this is known as **mean-field approximation** since the particle interactions with the surrounding medium are only taken into account through an averaged force.

Appendix B

Leading-order cross section from the DQPM

* * *

B.1 SU(3) algebra

The **Gell-Mann matrices** [77] provide a representation of the infinitesimal generators of the special unitary group called SU(3) corresponding to QCD with 3 color degrees of freedom. The Lie algebra of this group has dimension $N^2-1=8$ and therefore it has a set of eight linearly independent generators, which can be written as λ_i, with i taking values from 1 to 8:

$$\lambda_1=\begin{pmatrix}0&1&0\\1&0&0\\0&0&0\end{pmatrix},\ \lambda_2=\begin{pmatrix}0&-i&0\\i&0&0\\0&0&0\end{pmatrix},\ \lambda_3=\begin{pmatrix}1&0&0\\0&-1&0\\0&0&0\end{pmatrix}$$

$$\lambda_4=\begin{pmatrix}0&0&1\\0&0&0\\1&0&0\end{pmatrix},\ \lambda_5=\begin{pmatrix}0&0&-i\\0&0&0\\i&0&0\end{pmatrix},\ \lambda_6=\begin{pmatrix}0&0&0\\0&0&1\\0&1&0\end{pmatrix} \tag{B.1}$$

$$\lambda_7=\begin{pmatrix}0&0&0\\0&0&-1\\0&i&0\end{pmatrix},\ \lambda_8=\frac{1}{\sqrt{3}}\begin{pmatrix}1&0&0\\0&1&0\\0&0&-2\end{pmatrix}.$$

Usually the generators of SU(3) are written as $T^a = \lambda^a/2$ with the following properties:

- The representations of a SU(N) group are $N \times N$ hermitian and traceless matrices with determinant 1: $(T^a_{ij})^\dagger = (T^a_{ji})^\star = T^a_{ij}$
- Normalization: $T^a_{ji} T^b_{ij} = \mathrm{Tr}\left[T^a T^b\right] = T_F \delta_{ab}$ with $T_F = 1/2$
- Fierz identify: $\sum_a T^a_{ij} T^a_{kl} = \frac{1}{2}\left(\delta_{il}\delta_{kj} - \frac{1}{N}\delta_{ij}\delta_{kl}\right)$
- Commutation relation:
  - $\left[T^a, T^b\right] = i f^{abc} T^c$ where f^{abc} are the structure constants ($= 0$ in case of an Abelian Lie group), which are antisymmetric with the interchange of two indices and respect the condition $f^{acd} f^{bcd} = N\delta^{ab}$. We can define the matrices corresponding to the structure constants as $(F_a)_{bc} = -i f_{abc}$ and show that $\mathrm{Tr}\left[F_a F_b\right] = N\delta_{ab}$ and $\mathrm{Tr}\left[F_a F_b F_a F_c\right] = \frac{N^2}{2}\delta_{bc}$.
  - $\left\{T^a, T^b\right\} = 4/N\ \ \delta^{ab} I_N + 4 d^{abc} T^c$ where d^{abc} are constants and respect the following conditions: $d^{acd} d^{bcd} = \frac{N^2-4}{N}\delta^{ab}$ and $f^{acd} d^{bcd} = 0$
- $\mathrm{Tr}\left[T^a T^b T^a T^c\right] = -\frac{1}{4N}\delta_{bc}$ and $\mathrm{Tr}\left[T^a T^b T^c\right] = \frac{1}{4}(d^{abc} + i f_{abc})$.

The gluons are consequently described by the generators T^a where a corresponds to the gluon color. The eight possible color states of the gluon are called the "color octet" and are obtained by:

$$g^a_{ij} \propto \ \lambda^a_{ij} = \langle c|\lambda^a|c\rangle = \sum_{i,j=1}^{3} c^\dagger_j \ \lambda^a \ c_i = \left(\bar{r},\ \bar{b},\ \bar{g}\right) \lambda^a \begin{pmatrix} r \\ b \\ g \end{pmatrix}$$

with c being the color vector. We obtain for each gluon the following color composition:

$$g^1 = (r\bar{b} + b\bar{r})/\sqrt{2} \qquad g^2 = -i(r\bar{b} - b\bar{r})/\sqrt{2} \qquad g^3 = (r\bar{r} - b\bar{b})/\sqrt{2}$$

$$g^4 = (r\bar{g} + g\bar{r})/\sqrt{2} \qquad g^5 = -i(r\bar{g} - g\bar{r})/\sqrt{2} \qquad g^6 = (b\bar{g} + g\bar{b})/\sqrt{2}$$

$$g^7 = -i(b\bar{g} - g\bar{b})/\sqrt{2} \qquad g^8 = (r\bar{r} + b\bar{b} - 2g\bar{g})/\sqrt{6}.$$

We could imagine a 9^{th} gluon carrying no colors that would be considered as a "color singlet" state $(r\bar{r}+b\bar{b}+g\bar{g})\sqrt{3}$ but such a state is forbidden by the confinement hypothesis and simply doesn't exist in nature. However, color singlet states can be observed in nature in terms of $q\bar{q}$ bound states (mesons). In that case, we can show by calculating the color factor of a singlet state that the potential between this colorless $q\bar{q}$ pair is actually attractive. In the case of a color octet $q\bar{q}$ pair the potential is found to be repulsive. These two properties are consistent with the fact that we only observe colorless objects in nature.

Note

In the case of massless photons/gluons, only transverse modes can be physical; this implies that their spins can only get values of ± 1 (right- or left-handed polarizations). In this case, the degeneracy factor for the gluons is $d_g = 2(N_c^2-1) = 16$. But in the case of a finite mass vector boson, both longitudinal and transverse modes are possible and the spin can then get the values $-1, 0, +1$. In this case, the degeneracy factor would become $d_g = 3(N_c^2-1) = 24$.

In a finite temperature medium, massless gauge bosons such as photons and gluons can acquire an effective mass through the interaction with the medium (see [397] for details on the Hard Thermal Loop derivation). The dispersion relation of these quasiparticles can be obtained from the self-energy which is different in the longitudinal and transverse direction of motion. At low momentum, the effective mass acquired by the particle is the same in the longitudinal and transverse direction, but at higher momenta, the longitudinal modes are suppressed and only the two transverse modes can propagate.

So which gluonic degrees of freedom should be taken into account in a quasiparticle approach? First, the Stefan-Boltzmann limit has to be reached at very high temperature [435], and in order to fulfil this condition the number of gluonic degrees of freedom has to be $d_g = 2(N_c^2-1) = 16$, or tend to this value when $T \to \infty$ [436]. Secondly, in the calculation of thermodynamics quantities it appears that the modes with high momenta $q > T$ contribute most. The spectral strength of longitudinal modes is found to be suppressed at high momenta [399, 437] so it is ignored for simplicity and one considers only the contribution from the two transverse modes. This is why the factor $d_g = 2(N_c^2-1) = 16$ is used for the gluon degeneracy in the following calculation.

B.2 Calculation of leading-order Feynman diagrams

In this Section we give the details on the calculation of the matrix elements used to evaluate the DQPM partonic cross sections which are based on Refs. [389, 438, 439]. The gamma matrices are denoted by γ^μ and the Dirac spinors are u for particles and v for antiparticles. The final analytical expressions for the matrix elements used in the PHSD code were evaluated using FeynCalc [440, 441].

Note

In the DQPM, only transverse gluons are included in the calculation of thermodynamic quantities since the contribution of hard longitudinal gluons (plasmons) is found to be negligible [399, 437]. In the context of calculating thermodynamic quantities, the DQPM gluons can equivalently be seen as massive 'scalar' gluons with only 2 polarization states. This allows to use a simple form for the spectral function which is taken of Lorentzian shape as an *Ansatz* [384]. In this description, the gluon self-energy is not a tensor which can be separated in longitudinal and transverse components like in the Hard Thermal Loops approximation scheme [397], but is simply taken as a scalar. Accordingly, the DQPM gluon propagator used in the calculation of the DQPM cross section is the one of a massive scalar boson and is justified at low momenta where longitudinal and transverse gluons are equivalent. The same Lorentzian spectral function is used to describe the DQPM quarks [385] implying that their self-energy contains only scalar contributions which are assumed to be the same for quarks and antiquarks [120]. Similarly as for the longitudinal gluons, plasminos or antiquark holes (fermions with a negative helicity over chirality ratio [397]) are not counted in thermodynamic quantities since their contribution is negligible [399, 437]. In the calculation of cross sections, no distinction is made between particle and hole excitations since their self-energy is taken to be identical, which is justified similarly as for the gluons at low momentum. These simplifications allow a description of thermodynamic and transport coefficients from lattice QCD calculation from the DQPM partons only by adjusting a few parameters defining the DQPM parton self-energies.

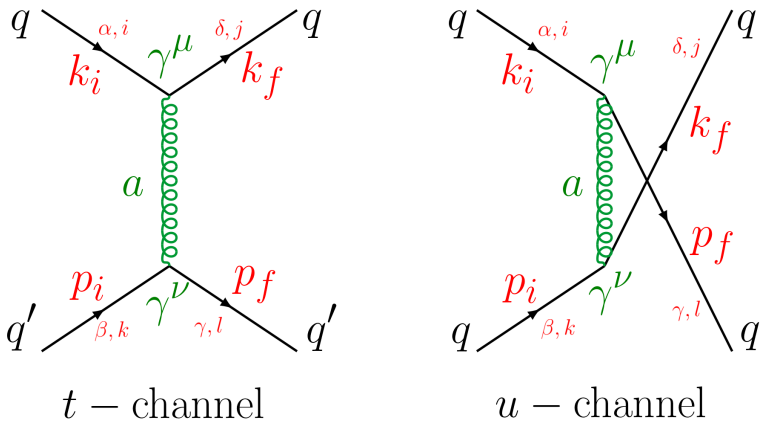

Figure B.1 – Leading order Feynman diagrams for the $qq \to qq$ process. The indices $i,j,k,l = 1-3$ denote the quark colors, $a,b = 1-8$ the gluon colors, the quark flavor is indicated by the indices $\alpha,\beta = u,d,...$ and the Mandelstam variables are given by the momenta as $s = (k_i + p_i)^2 = (k_f + p_f)^2$, $t = (k_i - k_f)^2 = (p_i - p_f)^2$, $u = (k_i - p_f)^2 = (p_i - k_f)^2$.

B.2.1 Quark-quark scattering $qq \to qq$

The invariant amplitudes corresponding to the Feynman diagrams in Fig. B.1 are:

$$i\mathcal{M}_t(q^i_\alpha q^k_\beta \to q^j_\alpha q^l_\beta) = \tag{B.2}$$

$$\bar{u}^j_\alpha(k_f)(-ig\gamma^\mu T^a_{ij})u^i_\alpha(k_i)\left[-i\delta_{ab}\frac{g_{\mu\nu} - (q^t_\mu q^t_\nu)/M_g^2}{(k_f - k_i)^2 - M_g^2 + 2i\gamma_g\omega_t}\right]\bar{u}^l_\beta(p_f)(-ig\gamma^\nu T^b_{kl})u^k_\beta(p_i),$$

$$i\mathcal{M}_u(q^i_\alpha q^k_\beta \to q^j_\alpha q^l_\beta) = \tag{B.3}$$

$$-\delta_{\alpha\beta}\ \bar{u}^j_\alpha(k_f)(-ig\gamma^\nu T^a_{kj})u^k_\beta(p_i)\left[-i\delta_{ab}\frac{g_{\mu\nu} - (q^u_\mu q^u_\nu)/M_g^2}{(p_f - k_i)^2 - M_g^2 + 2i\gamma_g\omega_u}\right]\bar{u}^l_\beta(p_f)(-ig\gamma^\mu T^b_{il})u^i_\alpha(k_i),$$

where the energy of the exchanged gluon is $\omega_t = |E_{k_f} - E_{k_i}|$ and $\omega_u = |E_{p_f} - E_{k_i}|$, and its momentum denoted by $q^\mu_t = (k_f - k_i)^\mu$ and $q^\mu_u = (p_i - k_f)^\mu$. Note that a minus sign appears between the t- and u-channel matrix elements since they differ only by the interchange of the external fermions. With some simplifications we get:

$$\mathcal{M}_t(q_\alpha^i q_\beta^k \to q_\alpha^j q_\beta^l) = \tag{B.4}$$

$$(T_{ij}^a T_{kl}^a)\ \frac{g^2}{t - M_g^2 + 2i\gamma_g\omega_t}\ \bar{u}_\alpha^j(k_f)\gamma^\mu u_\alpha^i(k_i)\left[g_{\mu\nu} - (q_\mu^t q_\nu^t)/M_g^2\right]\bar{u}_\beta^l(p_f)\gamma^\nu u_\beta^k(p_i),$$

$$\mathcal{M}_u(q_\alpha^i q_\beta^k \to q_\alpha^j q_\beta^l) = \tag{B.5}$$

$$-\delta_{\alpha\beta}(T_{kj}^a T_{il}^a)\ \frac{g^2}{u - M_g^2 + 2i\gamma_g\omega_u}\ \bar{u}_\alpha^j(k_f)\gamma^\nu u_\beta^k(p_i)\left[g_{\mu\nu} - (q_\mu^u q_\nu^u)/M_g^2\right]\bar{u}_\beta^l(p_f)\gamma^\mu u_\alpha^i(k_i).$$

We are interested in the invariant amplitude squared averaged over initial states of spin and color and summed over final states :

$$|\bar{\mathcal{M}}(q_\alpha q_\beta \to q_\alpha q_\beta)|^2 = \frac{1}{N_c^2}\sum_{\text{color}}\frac{1}{(2s_{q_1}+1)(2s_{q_2}+1)}\sum_{\text{spin}}|\mathcal{M}_t + \mathcal{M}_u|^2 \tag{B.6}$$

$$= \frac{1}{9}\sum_{\text{color}}\frac{1}{4}\sum_{\text{spin}}\left(|\mathcal{M}_t|^2 + |\mathcal{M}_u|^2 + \mathcal{M}_t\mathcal{M}_u^\star + \mathcal{M}_t^\star\mathcal{M}_u\right).$$

Let's start first to average over quark colors for the $t-$channel diagram. We get:

$$\frac{1}{9}\sum_{\text{color}}(T_{ij}^a T_{kl}^a)(T_{ij}^b T_{kl}^b)^\star = \frac{1}{9}\sum_{\text{color}}(T_{ij}^a T_{kl}^a)(T_{ij}^{b\star} T_{kl}^{b\star}) = \frac{1}{9}\sum_{\text{color}}(T_{ij}^a T_{kl}^a)(T_{ji}^b T_{lk}^b) \tag{B.7}$$

$$= \frac{1}{9}\sum_{\text{color}}\text{Tr}\left[T^a T^b\right]\text{Tr}\left[T^a T^b\right] = \frac{1}{9}\sum_{a=1}^{8}\frac{1}{2}\delta_{ab}\frac{1}{2}\delta_{ab} = \frac{2}{9}.$$

We can find in the same way the factor 2/9 for the $u-$channel as well. For the interference term $\mathcal{M}_t\mathcal{M}_u^\star$ (or $\mathcal{M}_t^\star\mathcal{M}_u$), we have:

$$\frac{1}{9}\sum_{\text{color}}(T_{ij}^a T_{kl}^a)(T_{kj}^b T_{il}^b)^\star = \frac{1}{9}\sum_{\text{color}}(T_{ij}^a T_{kl}^a)(T_{kj}^{b\star} T_{il}^{b\star}) = \frac{1}{9}\sum_{\text{color}}(T_{ij}^a T_{kl}^a)(T_{jk}^b T_{li}^b)$$

$$= \frac{1}{9}\sum_{a=1}^{8}\text{Tr}\left[T^a T^b T^a T^b\right] = \frac{1}{9}\sum_{a=1}^{8}\left(\frac{-1}{12}\right) = \frac{1}{9}\left(-\frac{2}{3}\right). \tag{B.8}$$

Now let's calculate the sum over spins for the $t-$channel diagram squared:

$$
\begin{aligned}
|\mathcal{M}_t|^2 &= \mathcal{M}_t\mathcal{M}_t^\star \qquad\qquad (B.9)\\
&\propto \frac{g^4}{(t-M_g^2)^2+(2\gamma_g\omega_t)^2}\left[\bar{u}_\alpha(k_f)\gamma^\mu u_\alpha(k_i)\left[g_{\mu\nu}-(q_\mu^t q_\nu^t)/M_g^2\right]\bar{u}_\beta(p_f)\gamma^\nu u_\beta(p_i)\right]\\
&\quad\times\left[\bar{u}_\alpha(k_f)\gamma^\eta u_\alpha(k_i)\left[g_{\eta\tau}-(q_\eta^t q_\tau^t)/M_g^2\right]\bar{u}_\beta(p_f)\gamma^\tau u_\beta(p_i)\right]^\star\\
&\propto \frac{g^4}{(t-M_g^2)^2+(2\gamma_g\omega_t)^2}\left[\bar{u}_\alpha(k_f)\gamma^\mu u_\alpha(k_i)\left[g_{\mu\nu}-(q_\mu^t q_\nu^t)/M_g^2\right]\bar{u}_\beta(p_f)\gamma^\nu u_\beta(p_i)\right]\\
&\quad\times\left[\bar{u}_\beta(p_i)\gamma^\tau u_\beta(p_f)\left[g_{\eta\tau}-(q_\eta^t q_\tau^t)/M_g^2\right]\bar{u}_\alpha(k_i)\gamma^\eta u_\alpha(k_f)\right],\\
|\overline{\mathcal{M}}_t|^2 &= \frac{g^4/(9\times 2)}{(t-M_g^2)^2+(2\gamma_g\omega_t)^2}\mathrm{Tr}\left[(\not{k}_f+m_f)\gamma^\mu(\not{k}_i+m_i)\gamma^\eta\right]\mathrm{Tr}\left[(\not{p}_f+m'_f)\gamma^\nu(\not{p}_i+m'_i)\gamma^\tau\right]\\
&\quad\times\left[g_{\mu\nu}-(q_\mu^t q_\nu^t)/M_g^2\right]\left[g_{\eta\tau}-(q_\eta^t q_\tau^t)/M_g^2\right] \qquad (B.10)\\
&= \frac{g^4/(9\times 2)}{(t-M_g^2)^2+(2\gamma_g\omega_t)^2}\;4\left(k_f^\mu k_i^\eta+k_f^\eta k_i^\mu+g^{\mu\eta}(m_f m_i-k_f.k_i)\right)\\
&\quad\times 4\left(p_f^\nu p_i^\tau+p_f^\tau p_i^\nu+g^{\nu\tau}(m'_f m'_i-p_f.p_i)\right)\left[g_{\mu\nu}-(q_\mu^t q_\nu^t)/M_g^2\right]\left[g_{\eta\tau}-(q_\eta^t q_\tau^t)/M_g^2\right].
\end{aligned}
$$

In the same way we can evaluate the $u-$ channel squared as:

$$
\begin{aligned}
|\mathcal{M}_u|^2 &\propto \delta_{\alpha\beta}\frac{g^4}{(u-M_g^2)^2+(2\gamma_g\omega_u)^2}\left[\bar{u}_\alpha(k_f)\gamma^\nu u_\beta(p_i)\left[g_{\mu\nu}-(q_\mu^u q_\nu^u)/M_g^2\right]\bar{u}_\beta(p_f)\gamma^\mu u_\alpha(k_i)\right]\\
&\quad\times\left[\bar{u}_\alpha(k_i)\gamma^\eta u_\beta(p_f)\left[g_{\eta\tau}-(q_\eta^u q_\tau^u)/M_g^2\right]\bar{u}_\beta(p_i)\gamma^\tau u_\alpha(k_f)\right], \qquad (B.11)\\
|\overline{\mathcal{M}}_u|^2 &= \delta_{\alpha\beta}\frac{g^4/(9\times 2)}{(u-M_g^2)^2+(2\gamma_g\omega_u)^2}\mathrm{Tr}\left[(\not{k}_f+m_f)\gamma^\nu(\not{p}_i+m'_i)\gamma^\tau\right]\mathrm{Tr}\left[(\not{p}_f+m'_f)\gamma^\mu(\not{k}_i+m_i)\gamma^\eta\right]\\
&\quad\times\left[g_{\mu\nu}-(q_\mu^u q_\nu^u)/M_g^2\right]\left[g_{\eta\tau}-(q_\eta^u q_\tau^u)/M_g^2\right] \qquad (B.12)\\
&= \delta_{\alpha\beta}\frac{g^4/(9\times 2)}{(u-M_g^2)^2+(2\gamma_g\omega_u)^2}\;4\left(k_f^\nu p_i^\tau+k_f^\tau p_i^\nu+g^{\nu\tau}(m_f m'_i-k_f.p_i)\right)\\
&\quad\times 4\left(p_f^\mu k_i^\eta+p_f^\eta k_i^\mu+g^{\mu\eta}(m'_f m_i-p_f.k_i)\right)\left[g_{\mu\nu}-(q_\mu^u q_\nu^u)/M_g^2\right]\left[g_{\eta\tau}-(q_\eta^u q_\tau^u)/M_g^2\right].
\end{aligned}
$$

The interference term $t-u$ as:

$$\begin{aligned}\sum_{\text{spin}} \mathcal{M}_t \mathcal{M}_u^\star \propto & -\delta_{\alpha\beta} \frac{g^2}{t - M_g^2 + 2i\gamma_g\omega_t} \frac{g^2}{u - M_g^2 - 2i\gamma_g\omega_u} \\ & \times \sum_{\text{spin}} \left[\bar{u}_\alpha(k_f)\gamma^\mu u_\alpha(k_i)\left[g_{\mu\nu} - (q_\mu^t q_\nu^t)/M_g^2\right]\bar{u}_\beta(p_f)\gamma^\nu u_\beta(p_i)\right] \\ & \times \left[\bar{u}_\alpha(k_i)\gamma^\eta u_\beta(p_f)\left[g_{\eta\tau} - (q_\eta^u q_\tau^u)/M_g^2\right]\bar{u}_\beta(p_i)\gamma^\tau u_\alpha(k_f)\right] \\ \propto & -\delta_{\alpha\beta}\ g^4 \frac{(t-M_g^2)(u-M_g^2) + 4\gamma_g^2\omega_t\omega_u + 2i\gamma_g(\omega_u(t-M_g^2) - \omega_t(u-M_g^2))}{\left((t-M_g^2)^2 + (2\gamma_g\omega_t)^2\right)\left((u-M_g^2)^2 + (2\gamma_g\omega_u)^2\right)} \\ & \times \mathrm{Tr}\left[(\not{k}_f + m_f)\gamma^\mu(\not{k}_i + m_i)\gamma^\eta(\not{p}_f + m_f')\gamma^\nu(\not{p}_i + m_i')\gamma^\tau\right] \\ & \times \left[g_{\mu\nu} - (q_\mu^t q_\nu^t)/M_g^2\right]\left[g_{\eta\tau} - (q_\eta^u q_\tau^u)/M_g^2\right],\end{aligned} \tag{B.13}$$

$$\begin{aligned}\sum_{\text{spin}} \mathcal{M}_t^\star \mathcal{M}_u \propto & -\delta_{\alpha\beta} \frac{g^2}{t - M_g^2 - 2i\gamma_g\omega_t} \frac{g^2}{u - M_g^2 + 2i\gamma_g\omega_u} \\ & \times \sum_{\text{spin}} \left[\bar{u}_\beta(p_i)\gamma^\tau u_\beta(p_f)\left[g_{\eta\tau} - (q_\eta^t q_\tau^t)/M_g^2\right]\bar{u}_\alpha(k_i)\gamma^\eta u_\alpha(k_f)\right] \\ & \times \left[\bar{u}_\alpha(k_f)\gamma^\nu u_\beta(p_i)\left[g_{\mu\nu} - (q_\mu^u q_\nu^u)/M_g^2\right]\bar{u}_\beta(p_f)\gamma^\mu u_\alpha(k_i)\right] \\ \propto & -\delta_{\alpha\beta}\ g^4 \frac{(t-M_g^2)(u-M_g^2) + 4\gamma_g^2\omega_t\omega_u - 2i\gamma_g(\omega_u(t-M_g^2) - \omega_t(u-M_g^2))}{\left((t-M_g^2)^2 + (2\gamma_g\omega_t)^2\right)\left((u-M_g^2)^2 + (2\gamma_g\omega_u)^2\right)} \\ & \times \mathrm{Tr}\left[(\not{p}_i + m_i')\gamma^\tau(\not{p}_f + m_f')\gamma^\mu(\not{k}_i + m_i)\gamma^\eta(\not{k}_f + m_f)\gamma^\nu\right] \\ & \times \left[g_{\mu\nu} - (q_\mu^u q_\nu^u)/M_g^2\right]\left[g_{\eta\tau} - (q_\eta^t q_\tau^t)/M_g^2\right].\end{aligned} \tag{B.14}$$

We know that $\sum_{\text{spin}} (\mathcal{M}_t\mathcal{M}_u^\star + \mathcal{M}_t^\star\mathcal{M}_u) = \sum_{\text{spin}} 2\mathcal{R}(\mathcal{M}_t\mathcal{M}_u^\star) = \sum_{\text{spin}} 2\mathcal{R}(\mathcal{M}_t^\star\mathcal{M}_u)$ is real. In order to fulfil this, we can figure out that the traces in the two interference terms are in fact equal and then the imaginary parts cancel out.

Finally we can write:

$$\overline{\mathcal{M}_t\mathcal{M}_u^\star}+\overline{\mathcal{M}_t^\star\mathcal{M}_u}=\frac{2}{3}\delta_{\alpha\beta}\frac{g^4/(9\times2)\left((t-M_g^2)(u-M_g^2)+4\gamma_g^2\omega_t\omega_u\right)}{\left((t-M_g^2)^2+(2\gamma_g\omega_t)^2\right)\left((u-M_g^2)^2+(2\gamma_g\omega_u)^2\right)}$$
$$\times\,\mathrm{Tr}\left[(\not p_i+m_i')\gamma^\tau(\not p_f+m_f')\gamma^\mu(\not k_i+m_i)\gamma^\eta(\not k_f+m_f)\gamma^\nu\right]$$
$$\times\left[g_{\mu\nu}-(q_\mu^u q_\nu^u)/M_g^2\right]\left[g_{\eta\tau}-(q_\eta^t q_\tau^t)/M_g^2\right]. \tag{B.15}$$

Note

The $t-$channel matrix element has the same expression for qq, $q\bar{q}$ or $\bar{q}\bar{q}$ scattering. Factors of $(\not p_i-m_i')$ and $(\not p_f-m_f')$ will appear in the trace for a $q\bar{q}$ scattering and the minus signs in front of the masses actually cancel to give the same results as for qq scattering. Other terms corresponding to an odd number of γ-matrices give no contribution to the trace.

Note

Why are $\sum_{\text{spin}}\mathcal{R}(\mathcal{M}_t\mathcal{M}_u^\star)$ and $\sum_{\text{spin}}\mathcal{R}(\mathcal{M}_t^\star\mathcal{M}_u)$ equal?

We can see that both quantities have a similar expression, just the trace is different where actually the order of the terms is just inverted. Let's hint that these traces are the same with an example considering the trace of four γ-matrices ($(\gamma^\mu)^\dagger=\gamma^0\gamma^\mu\gamma^0$ and $(\gamma^0)^2=I_4$) :

$$\mathrm{Tr}\left[\not A\not B\not C\not D\right]=\mathrm{Tr}\left[(\not A\not B\not C\not D)^T\right]=\mathrm{Tr}\left[\not D^T\not C^T\not B^T\not A^T\right]=\mathrm{Tr}\left[\not D^\star\not C^\star\not B^\star\not A^\star\right]$$
$$=\mathrm{Tr}\left[(\not D\not C\not B\not A)^\star\right]=\mathrm{Tr}\left[\not D\not C\not B\not A\right]^\star=\mathrm{Tr}\left[\not D\not C\not B\not A\right].$$

B.2.2 Quark-antiquark scattering $q\bar{q} \to q\bar{q}$

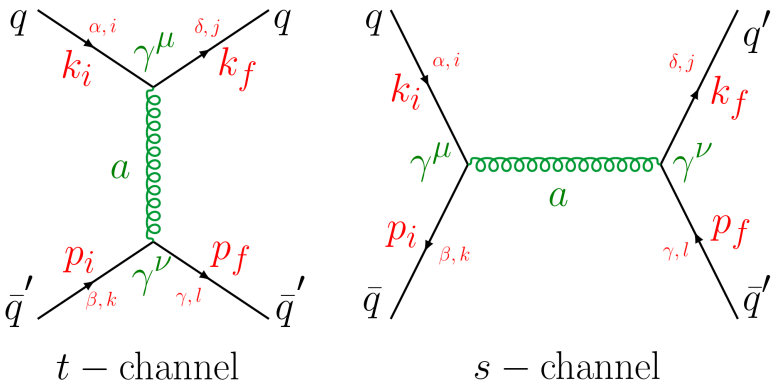

Figure B.2 – Leading order Feynman diagrams for the $q\bar{q} \to q\bar{q}$ process. The indices $i,j,k,l = 1-3$ denote the quark colors, $a,b = 1-8$ the gluon colors, the quark flavor is indicated by the indices $\alpha,\beta = u,d,...$ and the Mandelstam variables are given by the momenta as $s = (k_i+p_i)^2 = (k_f+p_f)^2$, $t = (k_i-k_f)^2 = (p_i-p_f)^2$, $u = (k_i-p_f)^2 = (p_i-k_f)^2$

The invariant amplitude corresponding to the $s-$channel Feynman diagrams is:

$$i\mathcal{M}_s(q^i_\alpha q^k_\beta \to q^j_\alpha q^l_\beta) = \tag{B.16}$$

$$-\delta_{\alpha\bar{\beta}}\delta_{\delta\bar{\gamma}}\ \bar{u}^j_\delta(k_f)(-ig\gamma^\nu T^b_{lj})v^l_\gamma(p_f)\left[-i\delta_{ab}\frac{g_{\mu\nu}-(q^s_\mu q^s_\nu)/M_g^2}{(k_i+p_i)^2-M_g^2+2i\gamma_g\omega_s}\right]\bar{v}^k_\beta(p_i)(-ig\gamma^\mu T^a_{ik})u^i_\alpha(k_i),$$

where the energy of the exchanged gluon is $\omega_s = |E_{k_i}+E_{p_i}|$, and its momentum denoted by $q^\mu_s = (k_i+p_i)^\mu$. Note that this matrix element should get a minus sign with respect to the t-channel matrix element since they are equivalent under the change of an initial quark with a final antiquark or an initial antiquark with a final quark. With some simplifications we get:

$$\mathcal{M}_s(q^i_\alpha q^k_\beta \to q^j_\alpha q^l_\beta) = \tag{B.17}$$

$$-\delta_{\alpha\bar{\beta}}\delta_{\delta\bar{\gamma}}\ (T^a_{ik}T^a_{lj})\ \frac{g^2}{s-M_g^2+2i\gamma_g\omega_s}\ \bar{u}^j_\delta(k_f)\gamma^\nu v^l_\gamma(p_f)\left[g_{\mu\nu}-(q^s_\mu q^s_\nu)/M_g^2\right]\bar{v}^k_\beta(p_i)\gamma^\mu u^i_\alpha(k_i).$$

By applying a crossing relation to the $t-$channel diagram we can directly obtain:

$$|\overline{\mathcal{M}}_s|^2 = \delta_{\alpha\bar{\beta}}\delta_{\delta\bar{\gamma}}\ \frac{g^4/(9\times 2)}{(s-M_g^2)^2+(2\gamma_g\omega_s)^2}\mathrm{Tr}\left[(\not{p}_i - m_i')\gamma^\eta(\not{k}_i+m_i)\gamma^\mu\right] \tag{B.18}$$
$$\times\,\mathrm{Tr}\left[(\not{p}_f - m_f')\gamma^\nu(\not{k}_f+m_f)\gamma^\tau\right]\left[g_{\mu\nu}-(q_\mu^s q_\nu^s)/M_g^2\right]\left[g_{\eta\tau}-(q_\eta^s q_\tau^s)/M_g^2\right].$$

For the interference term between the $t-$ and $s-$channel we get:

$$\overline{\mathcal{M}_t\mathcal{M}_s^\star}+\overline{\mathcal{M}_t^\star\mathcal{M}_s} = \frac{2}{3}\ \delta_{\alpha\bar{\beta}}\delta_{\delta\bar{\gamma}}\delta_{\alpha\delta}\delta_{\beta\gamma}\frac{g^4/(9\times 2)\left((t-M_g^2)(s-M_g^2)+4\gamma_g^2\omega_t\omega_s\right)}{\left((t-M_g^2)^2+(2\gamma_g\omega_t)^2\right)\left((s-M_g^2)^2+(2\gamma_g\omega_s)^2\right)}$$
$$\times\,\mathrm{Tr}\left[(\not{k}_f+m_f)\gamma^\eta(\not{k}_i+m_i)\gamma^\mu(\not{p}_i-m_i')\gamma^\tau(\not{p}_f-m_f')\gamma^\nu\right]$$
$$\times\left[g_{\mu\nu}-(q_\mu^s q_\nu^s)/M_g^2\right]\left[g_{\eta\tau}-(q_\eta^t q_\tau^t)/M_g^2\right]. \tag{B.19}$$

The final amplitude squared for the $q\bar{q}$ process can finally be written as follows:

$$|\bar{\mathcal{M}}(q_\alpha q_\beta\to q_\alpha q_\beta)|^2 = |\overline{\mathcal{M}}_t|^2+|\overline{\mathcal{M}}_s|^2+\overline{\mathcal{M}_t\mathcal{M}_s^\star}+\overline{\mathcal{M}_t^\star\mathcal{M}_s}. \tag{B.20}$$

B.2.3 Quark-gluon scattering $gq \to gq$

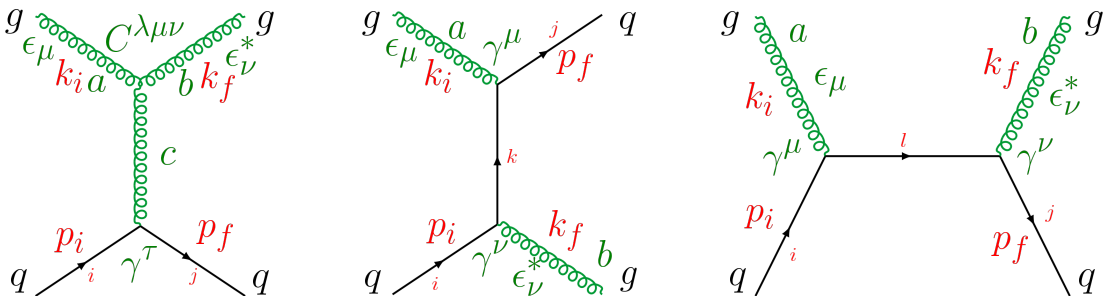

Figure B.3 – Leading order Feynman diagrams for the $gq \to gq$ process. The indices $i,j,k,l = 1-3$ denote the quark colors, $a,b = 1-8$ the gluon colors, the quark flavor is indicated by the indices $\alpha,\beta = u,d,...$ and the Mandelstam variables are given by the momenta as $s = (k_i+p_i)^2 = (k_f+p_f)^2$, $t = (k_i-k_f)^2 = (p_i-p_f)^2$, $u = (k_i-p_f)^2 = (p_i-k_f)^2$

The invariant amplitudes corresponding to the Feynman diagrams in Fig. B.3 are:

$$i\mathcal{M}_t(g^a q^i \to g^b q^j) = \tag{B.21}$$

$$(\epsilon^\star_{b,f})_\nu \left(-g f^{cab} C^{\lambda\mu\nu}(k_i-k_f,-k_i,k_f)\right)(\epsilon_{a,i})_\mu \left[-i\frac{g_{\lambda\tau}-(q^t_\lambda q^t_\tau)/M_g^2}{(k_f-k_i)^2-M_g^2+2i\gamma_g\omega_t}\right]$$

$$\times \bar{u}^j(p_f)(-ig\gamma^\tau T^c_{ij})u^i(p_i),$$

$$\mathcal{M}_t(g^a q^i \to g^b q^j) = \tag{B.22}$$

$$\frac{-ig^2}{t-M_g^2+2i\gamma_g\omega_t} f^{cab}T^c_{ij}\ (\epsilon^\star_{b,f})_\nu C^{\lambda\mu\nu}(k_i-k_f,-k_i,k_f)(\epsilon_{a,i})_\mu \left[g_{\lambda\tau}-(q^t_\lambda q^t_\tau)/M_g^2\right]\bar{u}^j(p_f)\gamma^\tau u^i(p_i),$$

with the 3-gluon vertex $C^{\lambda\mu\nu}(q_1,q_2,q_3) = \left[(q_1-q_2)^\nu g^{\lambda\mu}+(q_2-q_3)^\lambda g^{\mu\nu}+(q_3-q_1)^\mu g^{\lambda\nu}\right]$ and the momentum of the exchanged gluon $q^\mu_t = (k_f-k_i)^\mu$.

$$i\mathcal{M}_u(g^a q^i \to g^b q^j) = \bar{u}^j(p_f)(-ig\gamma^\mu T^a_{kj})(\epsilon_{a,i})_\mu \left[i\frac{\not{q}^u + M_q}{u - M_q^2 + 2i\gamma_q\omega_u} \right] (\epsilon^\star_{b,f})_\nu (-ig\gamma^\nu T^b_{ik}) u^i(p_i),$$

$$\mathcal{M}_u(g^a q^i \to g^b q^j) = (T^b_{ik}T^a_{kj}) \frac{-g^2}{u - M_q^2 + 2i\gamma_q\omega_u} \bar{u}^j(p_f)\gamma^\mu(\epsilon_{a,i})_\mu(\not{p}_i - \not{k}_f + M_q)(\epsilon^\star_{b,f})_\nu\gamma^\nu u^i(p_i), \tag{B.23}$$

$$i\mathcal{M}_s(g^a q^i \to g^b q^j) = \bar{u}^j(p_f)(-ig\gamma^\nu T^b_{lj})(\epsilon^\star_{b,f})_\nu \left[i\frac{\not{q}^s + M_q}{s - M_q^2 + 2i\gamma_q\omega_s} \right] (\epsilon_{a,i})_\mu (-ig\gamma^\mu T^a_{il}) u^i(p_i),$$

$$\mathcal{M}_s(g^a q^i \to g^b q^j) = (T^a_{il}T^b_{lj}) \frac{-g^2}{s - M_q^2 + 2i\gamma_q\omega_s} \bar{u}^j(p_f)\gamma^\nu(\epsilon^\star_{b,f})_\nu(\not{k}_i + \not{p}_i + M_q)(\epsilon_{a,i})_\mu\gamma^\mu u^i(p_i). \tag{B.24}$$

The final invariant amplitude squared will be (see the note in the previous section for the gluon degeneracy d_g):

$$\begin{aligned} |\overline{\mathcal{M}}(gq \to gq)|^2 =& \frac{1}{3\times 8} \sum_{\text{color}} \frac{1}{2d_g} \sum_{\text{spin}} |\mathcal{M}(g^a q^i \to g^b q^j)|^2 \qquad \text{(B.25)} \\ =& |\overline{\mathcal{M}}_t|^2 + |\overline{\mathcal{M}}_u|^2 + |\overline{\mathcal{M}}_s|^2 + 2\mathcal{R}[\overline{\mathcal{M}_t\mathcal{M}_u^\star}] + 2\mathcal{R}[\overline{\mathcal{M}_t\mathcal{M}_s^\star}] + 2\mathcal{R}[\overline{\mathcal{M}_u\mathcal{M}_s^\star}]. \end{aligned}$$

We derive the color factors, averaged over initial states and summed over final states:

$$\begin{aligned} t-\text{channel}: \ \frac{1}{3\times 8}\sum f^{cab}f^{dab}\ T^c_{ij}T^d_{ji} &= \frac{1}{3\times 8}\sum \left(N\delta^{cd}\right) \text{Tr}\left[T^cT^d\right] \\ &= \frac{1}{3\times 8}\sum \left(N\delta^{cd}\right)\left(\frac{1}{2}\delta^{cd}\right) = \frac{1}{2}, \end{aligned} \tag{B.26}$$

$$u-\text{channel}: \ \frac{1}{3\times 8}\sum T^b_{ik}T^a_{kj}\ T^b_{jk}T^a_{ki} = \frac{1}{3\times 8}\sum \text{Tr}\left[T^bT^a\right]\text{Tr}\left[T^bT^a\right] = \frac{2}{9}, \tag{B.27}$$

$$s-\text{channel}: \ \frac{1}{3\times 8}\sum T^a_{il}T^b_{lj}\ T^b_{jl}T^a_{li} = \frac{1}{3\times 8}\sum \text{Tr}\left[T^aT^b\right]\text{Tr}\left[T^aT^b\right] = \frac{2}{9}, \tag{B.28}$$

$$(t-u)-\text{cross-term}: \frac{1}{3\times 8}\sum f^{cab}T^c_{ij}\ T^a_{jk}T^b_{ki} = \frac{1}{3\times 8}\sum f^{cab}\mathrm{Tr}\left[T^cT^aT^b\right]$$
$$= \frac{1}{3\times 8}\sum f^{cab}\frac{1}{4}\left[d^{cab}+if^{cab}\right] = \frac{1}{3\times 8}\sum \frac{iN}{4} = \frac{i}{4}, \quad \text{(B.29)}$$

$$(u-t)-\text{cross-term}: \frac{1}{3\times 8}\sum f^{cab}T^c_{ji}\ T^b_{ik}T^a_{kj} = \frac{1}{3\times 8}\sum f^{cab}\mathrm{Tr}\left[T^cT^bT^a\right]$$
$$= \frac{-1}{3\times 8}\sum f^{cba}\frac{1}{4}\left[d^{cba}+if^{cba}\right] = \frac{-1}{3\times 8}\sum \frac{iN}{4} = \frac{-i}{4}, \quad \text{(B.30)}$$

$$(t-s)-\text{cross-term}: \frac{1}{3\times 8}\sum f^{cab}T^c_{ij}\ T^b_{jk}T^a_{ki} = \frac{1}{3\times 8}\sum f^{cab}\mathrm{Tr}\left[T^cT^bT^a\right]$$
$$= \frac{-1}{3\times 8}\sum f^{cba}\frac{1}{4}\left[d^{cba}+if^{cba}\right] = \frac{-1}{3\times 8}\sum \frac{iN}{4} = \frac{-i}{4}, \quad \text{(B.31)}$$

$$(s-t)-\text{cross-term}: \frac{1}{3\times 8}\sum f^{cab}T^c_{ji}\ T^a_{ik}T^b_{kj} = \frac{1}{3\times 8}\sum f^{cab}\mathrm{Tr}\left[T^cT^aT^b\right]$$
$$= \frac{1}{3\times 8}\sum f^{cab}\frac{1}{4}\left[d^{cab}+if^{cab}\right] = \frac{1}{3\times 8}\sum \frac{iN}{4} = \frac{i}{4}, \quad \text{(B.32)}$$

$$(u-s)/(s-u)-\text{cross-term}: \frac{1}{3\times 8}\sum T^b_{ik}T^a_{kj}\ T^b_{jl}T^a_{li} = \frac{1}{3\times 8}\sum \mathrm{Tr}\left[T^bT^aT^bT^a\right]$$
$$= \frac{1}{3\times 8}\sum \frac{-1}{4N} = \frac{-1}{36}. \quad \text{(B.33)}$$

Now let's calculate the invariant amplitudes summed and averaged over colors and spins:

$$|\overline{\mathcal{M}}_t|^2 = \frac{g^4/(4d_g)}{(t-M_g^2)^2+(2\gamma_g\omega_t)^2}\ \mathrm{Tr}\left[(\not{p}_f+m'_f)\gamma^{\tau'}(\not{p}_i+m'_i)\gamma^{\tau}C^{\lambda\mu\nu}(k_i-k_f,-k_i,k_f)\right.$$
$$\left.\times\left[g_{\lambda\tau}-(q^t_\lambda q^t_\tau)/M_g^2\right]C^{\lambda'\mu'\nu'}(k_i-k_f,-k_i,k_f)\left[g_{\lambda'\tau'}-(q^t_{\lambda'}q^t_{\tau'})/M_g^2\right]\right]$$
$$\times\sum_{\text{pol.}}(\epsilon_i)_\mu(\epsilon_i^\star)_{\mu'}\sum_{\text{pol.}}(\epsilon_f)_{\nu'}(\epsilon_f^\star)_\nu \quad \text{(B.34)}$$

with the 3-gluon vertex

$$C^{\lambda\mu\nu}(k_i-k_f,-k_i,k_f) = \left[(2k_i-k_f)^\nu g^{\lambda\mu}-(k_i+k_f)^\lambda g^{\mu\nu}+(2k_f-k_i)^\mu g^{\lambda\nu}\right]. \quad \text{(B.35)}$$

In the case of a massive gluon, the sum over polarizations is given by:

$$\sum_{\text{pol.}}(\epsilon_i)_\mu(\epsilon_i^\star)_{\mu'} = -g_{\mu\mu'} + \frac{(k_i)_\mu(k_i)_{\mu'}}{(M_i)_g^2}, \tag{B.36}$$

$$|\overline{\mathcal{M}_u}|^2 = \frac{g^4/(9d_g)}{(u-M_q^2)^2+(2\gamma_q\omega_u)^2}\ \text{Tr}\left[(\not p_f + m'_f)\gamma^{\mu'}(\not p_i - \not k_f + M_q)\gamma^{\nu'}(\not p_i + m'_i)\gamma^{\nu}(\not p_i - \not k_f + M_q)\gamma^{\mu}\right]$$
$$\times \sum_{\text{pol.}}(\epsilon_i)_\mu(\epsilon_i^\star)_{\mu'}\sum_{\text{pol.}}(\epsilon_f)_{\nu'}(\epsilon_f^\star)_\nu, \tag{B.37}$$

$$|\overline{\mathcal{M}_s}|^2 = \frac{g^4/(9d_g)}{(s-M_q^2)^2+(2\gamma_q\omega_s)^2}\ \text{Tr}\left[(\not p_f + m'_f)\gamma^{\nu'}(\not k_i + \not p_i + M_q)\gamma^{\mu'}(\not p_i + m'_i)\gamma^{\mu}(\not k_i + \not p_i + M_q)\gamma^{\nu}\right]$$
$$\times \sum_{\text{pol.}}(\epsilon_i)_\mu(\epsilon_i^\star)_{\mu'}\sum_{\text{pol.}}(\epsilon_f)_{\nu'}(\epsilon_f^\star)_\nu, \tag{B.38}$$

$$2\mathcal{R}\overline{[\mathcal{M}_t\mathcal{M}_u^\star]} = \frac{-2g^4/(8d_g)\left((t-M_g^2)(u-M_q^2)+4\gamma_g\gamma_q\omega_t\omega_u\right)}{\left((t-M_g^2)^2+(2\gamma_g\omega_t)^2\right)\left((u-M_q^2)^2+(2\gamma_q\omega_u)^2\right)}$$
$$\times \text{Tr}\left[(\not p_f + m'_f)\gamma^{\mu'}(\not p_i - \not k_f + M_q)\gamma^{\nu'}(\not p_i + m'_i)\gamma^{\tau}C^{\lambda\mu\nu}(k_i-k_f,-k_i,k_f)\left[g_{\lambda\tau}-(q_\lambda^t q_\tau^t)/M_g^2\right]\right]$$
$$ztimes\sum_{\text{pol.}}(\epsilon_i)_\mu(\epsilon_i^\star)_{\mu'}\sum_{\text{pol.}}(\epsilon_f)_{\nu'}(\epsilon_f^\star)_\nu, \tag{B.39}$$

$$2\mathcal{R}\overline{[\mathcal{M}_t\mathcal{M}_s^\star]} = \frac{2g^4/(8d_g)\left((t-M_g^2)(s-M_q^2)+4\gamma_g\gamma_q\omega_t\omega_s\right)}{\left((t-M_g^2)^2+(2\gamma_g\omega_t)^2\right)\left((s-M_q^2)^2+(2\gamma_q\omega_s)^2\right)}$$
$$\times \text{Tr}\left[(\not p_f + m'_f)\gamma^{\nu'}(\not k_i + \not p_i + M_q)\gamma^{\mu'}(\not p_i + m'_i)\gamma^{\tau}C^{\lambda\mu\nu}(k_i-k_f,-k_i,k_f)\left[g_{\lambda\tau}-(q_\lambda^t q_\tau^t)/M_g^2\right]\right]$$
$$\times \sum_{\text{pol.}}(\epsilon_i)_\mu(\epsilon_i^\star)_{\mu'}\sum_{\text{pol.}}(\epsilon_f)_{\nu'}(\epsilon_f^\star)_\nu, \tag{B.40}$$

$$2\mathcal{R}\overline{[\mathcal{M}_u\mathcal{M}_s^\star]} = \frac{-2g^4/(72d_g)\left((u-M_q^2)(s-M_q^2)+4\gamma_q^2\omega_u\omega_s\right)}{\left((u-M_q^2)^2+(2\gamma_q\omega_u)^2\right)\left((s-M_q^2)^2+(2\gamma_q\omega_s)^2\right)}$$
$$\times \text{Tr}\left[(\not p_f + m'_f)\gamma^{\nu'}(\not k_i + \not p_i + M_q)\gamma^{\mu'}(\not p_i + m'_i)\gamma^{\nu}(\not p_i - \not k_f + M_q)\gamma^{\mu}\right]$$
$$\times \sum_{\text{pol.}}(\epsilon_i)_\mu(\epsilon_i^\star)_{\mu'}\sum_{\text{pol.}}(\epsilon_f)_{\nu'}(\epsilon_f^\star)_\nu. \tag{B.41}$$

B.2.4 Gluon-gluon scattering $gg \to gg$

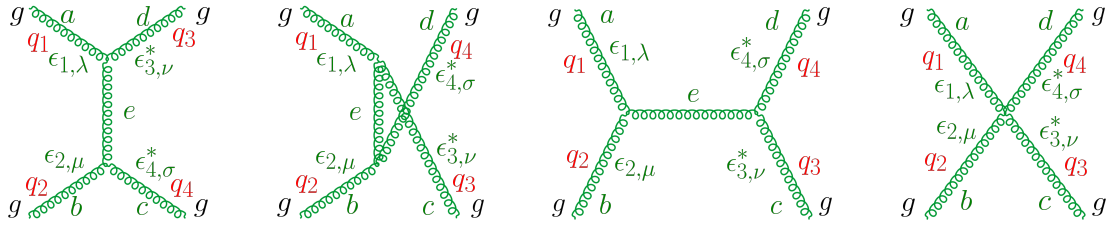

Figure B.4 – Leading order Feynman diagrams for the $gg \to gg$ process. The indices $a, b = 1-8$ denote the gluon colors and the Mandelstam variables are given by the momenta as $s = (q_1+q_2)^2 = (q_3+q_4)^2$, $t = (q_1-q_4)^2 = (q_2-q_3)^2$, $u = (q_1-q_3)^2 = (q_2-q_4)^2$

The invariant amplitudes corresponding to the above Feynman diagrams are:

$$i\mathcal{M}_t(g^a g^b \to g^c g^d) = (\epsilon^\star_{d,4})_\sigma \left(-g f^{ead} C^{\tau\lambda\sigma}(q_1-q_4,-q_1,q_4)\right)(\epsilon_{a,1})_\lambda \tag{B.42}$$
$$\times \left[-i\frac{g_{\tau\tau'} - (q^t_\tau q^t_{\tau'})/M_g^2}{(q_4-q_1)^2 - M_g^2 + 2i\gamma_g\omega_t}\right](\epsilon^\star_{c,3})_\nu \left(-g f^{ecb} C^{\tau'\nu\mu}(-q_3+q_2,q_3,-q_2)\right)(\epsilon_{b,2})_\mu,$$

$$\mathcal{M}_t(g^a g^b \to g^c g^d) = \frac{-g^2}{t - M_g^2 + 2i\gamma_g\omega_t} f^{ead} f^{ecb} C^{\tau\lambda\sigma}(q_1-q_4,-q_1,q_4) C^{\tau'\nu\mu}(-q_3+q_2,q_3,-q_2)$$
$$\times \left[g_{\tau\tau'} - (q^t_\tau q^t_{\tau'})/M_g^2\right](\epsilon^\star_{d,4})_\sigma (\epsilon_{a,1})_\lambda (\epsilon^\star_{c,3})_\nu (\epsilon_{b,2})_\mu, \tag{B.43}$$

$$i\mathcal{M}_s(g^a g^b \to g^c g^d) = (\epsilon^\star_{d,4})_\sigma \left(-g f^{edc} C^{\tau'\sigma\nu}(-q_4-q_3,q_4,q_3)\right)(\epsilon^\star_{c,3})_\nu \tag{B.44}$$
$$\times \left[-i\frac{g_{\tau\tau'} - (q^s_\tau q^s_{\tau'})/M_g^2}{(q_1+q_2)^2 - M_g^2 + 2i\gamma_g\omega_s}\right](\epsilon_{b,2})_\mu \left(-g f^{eba} C^{\tau\mu\lambda}(q_2+q_1,-q_2,-q_1)\right)(\epsilon_{a,1})_\lambda$$

$$\mathcal{M}_s(g^a g^b \to g^c g^d) = \frac{-g^2}{s - M_g^2 + 2i\gamma_g\omega_s} f^{edc} f^{eba} C^{\tau'\sigma\nu}(-q_4-q_3,q_4,q_3) C^{\tau\mu\lambda}(q_2+q_1,-q_2,-q_1)$$
$$\times \left[g_{\tau\tau'} - (q^s_\tau q^s_{\tau'})/M_g^2\right](\epsilon^\star_{d,4})_\sigma (\epsilon^\star_{c,3})_\nu (\epsilon_{b,2})_\mu (\epsilon_{a,1})_\lambda, \tag{B.45}$$

$$i\mathcal{M}_u(g^a g^b \to g^c g^d) = (\epsilon^\star_{d,4})_\sigma \left(-g f^{edb} C^{\tau'\sigma\mu}(-q_4+q_2, q_4, -q_2)\right)(\epsilon_{b,2})_\mu \tag{B.46}$$
$$\times \left[-i\frac{g_{\tau\tau'} - (q^u_\tau q^u_{\tau'})/M_g^2}{(q_2-q_4)^2 - M_g^2 + 2i\gamma_g\omega_u}\right](\epsilon^\star_{c,3})_\nu \left(-g f^{eac} C^{\tau\lambda\nu}(q_1-q_3, -q_1, q_3)\right)(\epsilon_{a,1})_\lambda,$$

$$\mathcal{M}_u(g^a g^b \to g^c g^d) = \frac{-g^2}{u - M_g^2 + 2i\gamma_g\omega_u} f^{edb} f^{eac} C^{\tau'\sigma\mu}(-q_4+q_2, q_4, -q_2) \tag{B.47}$$
$$\times C^{\tau\lambda\nu}(q_1-q_3, -q_1, q_3)\left[g_{\tau\tau'} - (q^u_\tau q^u_{\tau'})/M_g^2\right](\epsilon^\star_{d,4})_\sigma(\epsilon_{b,2})_\mu(\epsilon^\star_{c,3})_\nu(\epsilon_{a,1})_\lambda,$$

with the 3-gluon vertex $C^{\lambda\mu\nu}(q_1,q_2,q_3) = \left[(q_1-q_2)^\nu g^{\lambda\mu} + (q_2-q_3)^\lambda g^{\mu\nu} + (q_3-q_1)^\mu g^{\lambda\nu}\right]$ and the momentum of the exchanged gluon $q_t^\mu = (q_4-q_1)^\mu$, $q_s^\mu = (q_1+q_2)^\mu$ and $q_u^\mu = (q_2-q_4)^\mu$.

The 4-point invariant amplitude is given by (according to Refs. [438, 439]):

$$i\mathcal{M}_4(g^a g^b \to g^c g^d) = -ig^2\left[f^{abe}f^{cde}(g^{\lambda\nu}g^{\mu\sigma} - g^{\lambda\sigma}g^{\mu\nu}) + f^{ace}f^{bde}(g^{\lambda\mu}g^{\nu\sigma} - g^{\lambda\sigma}g^{\nu\mu})\right.$$
$$\left. + f^{ade}f^{cbe}(g^{\lambda\mu}g^{\sigma\nu} - g^{\lambda\nu}g^{\sigma\mu})\right](\epsilon^\star_{d,4})_\sigma(\epsilon^\star_{c,3})_\nu(\epsilon_{b,2})_\mu(\epsilon_{a,1})_\lambda, \tag{B.48}$$
$$\mathcal{M}_4(g^a g^b \to g^c g^d) = -f^{abe}f^{cde}\mathcal{M}_4^s - f^{ace}f^{bde}\mathcal{M}_4^u - f^{ade}f^{cbe}\mathcal{M}_4^t. \tag{B.49}$$

Note that the structure constants in front of $\mathcal{M}_4^u$ are opposite to the one found in $\mathcal{M}^u$, whereas the other structure constants are the same for the $t-$ and $s-$channels. The final invariant amplitude squared will be:

$$|\overline{\mathcal{M}}(gg\to gg)|^2 = \frac{1}{8\times 8}\sum_{\text{color}}\frac{1}{d_g^2}\sum_{\text{spin}}|\mathcal{M}(g^a g^b \to g^c g^d)|^2 \tag{B.50}$$
$$= |\overline{\mathcal{M}}_t|^2 + |\overline{\mathcal{M}}_s|^2 + |\overline{\mathcal{M}}_u|^2 + |\overline{\mathcal{M}}_4|^2 + 2\mathcal{R}\overline{[\mathcal{M}_t\mathcal{M}_s^\star]} + 2\mathcal{R}\overline{[\mathcal{M}_t\mathcal{M}_u^\star]}$$
$$+ 2\mathcal{R}\overline{[\mathcal{M}_u\mathcal{M}_s^\star]} + 2\mathcal{R}\overline{[\mathcal{M}_t\mathcal{M}_4^\star]} + +2\mathcal{R}\overline{[\mathcal{M}_s\mathcal{M}_4^\star]} + +2\mathcal{R}\overline{[\mathcal{M}_u\mathcal{M}_4^\star]}.$$

We derive the color factors, averaged over initial states and summed over final states:

$$t-\text{channel}: \frac{1}{8\times 8}\sum f^{ead}f^{ecb}f^{e'da}f^{e'bc} = \frac{1}{8\times 8}\sum \mathrm{Tr}\left[F_eF_{e'}\right]\mathrm{Tr}\left[F_eF_{e'}\right]$$
$$= \frac{1}{8\times 8}\sum \left(N\delta^{ee'}\right)\left(N\delta^{ee'}\right) = \frac{9}{8}, \tag{B.51}$$

$$s-\text{channel}: \frac{1}{8\times 8}\sum f^{edc}f^{eba}f^{e'cd}f^{e'ab} = \frac{1}{8\times 8}\sum \mathrm{Tr}\left[F_eF_{e'}\right]\mathrm{Tr}\left[F_eF_{e'}\right]$$
$$= \frac{1}{8\times 8}\sum \left(N\delta^{ee'}\right)\left(N\delta^{ee'}\right) = \frac{9}{8}, \tag{B.52}$$

$$u-\text{channel}: \frac{1}{8\times 8}\sum f^{edb}f^{eac}f^{e'bd}f^{e'ca} = \frac{1}{8\times 8}\sum \mathrm{Tr}\left[F_eF_{e'}\right]\mathrm{Tr}\left[F_eF_{e'}\right]$$
$$= \frac{1}{8\times 8}\sum \left(N\delta^{ee'}\right)\left(N\delta^{ee'}\right) = \frac{9}{8}, \tag{B.53}$$

$$(t-u)-\text{cross-term}: \frac{1}{8\times 8}\sum f^{ead}f^{ecb}f^{e'bd}f^{e'ca} = \frac{1}{8\times 8}\sum \mathrm{Tr}\left[F_eF_{e'}F_eF_{e'}\right]$$
$$= \frac{1}{8\times 8}\sum \left(\frac{N^2}{2}\delta^{ee'}\right) = \frac{9}{16}, \tag{B.54}$$

$$(t-s)-\text{cross-term}: \frac{1}{8\times 8}\sum f^{ead}f^{ecb}f^{e'cd}f^{e'ab} = \frac{1}{8\times 8}\sum \mathrm{Tr}\left[F_eF_{e'}F_eF_{e'}\right]$$
$$= \frac{1}{8\times 8}\sum \left(\frac{N^2}{2}\delta^{ee'}\right) = \frac{9}{16}, \tag{B.55}$$

$$(u-s)-\text{cross-term}: \frac{1}{8\times 8}\sum f^{edb}f^{eac}f^{e'cd}f^{e'ab} = \frac{-1}{8\times 8}\sum \mathrm{Tr}\left[F_eF_{e'}F_eF_{e'}\right]$$
$$= \frac{-1}{8\times 8}\sum \left(\frac{N^2}{2}\delta^{ee'}\right) = \frac{-9}{16}. \tag{B.56}$$

The color factors for conjugate channels are the same. Now let's calculate the invariant amplitudes summed and averaged over colors and spins:

	$\mathcal{M}_t$	$\mathcal{M}_u$	$\mathcal{M}_s$	$\mathcal{M}_4^t$	$\mathcal{M}_4^u$	$\mathcal{M}_4^s$
$\mathcal{M}_4^s$	9/16	-9/16	9/8	9/16	9/16	9/8
$\mathcal{M}_4^u$	-9/16	-9/8	9/16	-9/16	9/8	9/16
$\mathcal{M}_4^t$	9/8	9/16	9/16	9/8	-9/16	9/16

Table B.1 – Color factors $\frac{1}{8\times 8}\sum ....$ associated to 4-point amplitudes and cross-terms with other channels.

$$|\overline{\mathcal{M}}_t|^2 = \frac{9g^4/(8d_g^2)}{(t-M_g^2)^2+(2\gamma_g\omega_t)^2}\; C^{\tau\lambda\sigma}(q_1-q_4,-q_1,q_4)C^{\tau'\nu\mu}(-q_3+q_2,q_3,-q_2)$$
$$\times C^{\rho\sigma'\lambda'}(q_4-q_1,-q_4,q_1)C^{\rho'\mu'\nu'}(-q_2+q_3,q_2,-q_3)\left[g_{\tau\tau'}-(q_\tau^t q_{\tau'}^t)/M_g^2\right]$$
$$\times\left[g_{\rho\rho'}-(q_\rho^t q_{\rho'}^t)/M_g^2\right]\sum_{\text{pol.}}(\epsilon_1)_\lambda(\epsilon_1^\star)_{\lambda'}\sum_{\text{pol.}}(\epsilon_2)_\mu(\epsilon_2^\star)_{\mu'}\sum_{\text{pol.}}(\epsilon_3)_{\nu'}(\epsilon_3^\star)_\nu\sum_{\text{pol.}}(\epsilon_4)_{\sigma'}(\epsilon_4^\star)_\sigma, \tag{B.57}$$

with the sum over polarizations of a massive gluon given by:

$$\sum_{\text{pol.}}(\epsilon_i)_\mu(\epsilon_i^\star)_{\mu'} = -g_{\mu\mu'}+\frac{(k_i)_\mu(k_i)_{\mu'}}{M_{g,i}^2}, \tag{B.58}$$

$$|\overline{\mathcal{M}}_s|^2 = \frac{9g^4/(8d_g^2)}{(s-M_g^2)^2+(2\gamma_g\omega_s)^2}\; C^{\tau'\sigma\nu}(-q_4-q_3,q_4,q_3)C^{\tau\mu\lambda}(q_2+q_1,-q_2,-q_1)$$
$$\times C^{\rho'\nu'\sigma'}(q_3+q_4,-q_3,-q_4)C^{\rho\lambda'\mu'}(-q_1-q_2,q_1,q_2)\left[g_{\tau\tau'}-(q_\tau^s q_{\tau'}^s)/M_g^2\right]$$
$$\times\left[g_{\rho\rho'}-(q_\rho^s q_{\rho'}^s)/M_g^2\right]\sum_{\text{pol.}}(\epsilon_1)_\lambda(\epsilon_1^\star)_{\lambda'}\sum_{\text{pol.}}(\epsilon_2)_\mu(\epsilon_2^\star)_{\mu'}\sum_{\text{pol.}}(\epsilon_3)_{\nu'}(\epsilon_3^\star)_\nu\sum_{\text{pol.}}(\epsilon_4)_{\sigma'}(\epsilon_4^\star)_\sigma, \tag{B.59}$$

$$|\overline{\mathcal{M}}_u|^2 = \frac{9g^4/(8d_g^2)}{(u-M_g^2)^2+(2\gamma_g\omega_u)^2}\; C^{\tau'\sigma\mu}(-q_4+q_2,q_4,-q_2)C^{\tau\lambda\nu}(q_1-q_3,-q_1,q_3)$$
$$\times C^{\rho'\mu'\sigma'}(-q_2+q_4,q_2,-q_4)C^{\rho\nu'\lambda'}(q_3-q_1,-q_3,q_1)\left[g_{\tau\tau'}-(q_\tau^u q_{\tau'}^u)/M_g^2\right]$$
$$\times\left[g_{\rho\rho'}-(q_\rho^u q_{\rho'}^u)/M_g^2\right]\sum_{\text{pol.}}(\epsilon_1)_\lambda(\epsilon_1^\star)_{\lambda'}\sum_{\text{pol.}}(\epsilon_2)_\mu(\epsilon_2^\star)_{\mu'}\sum_{\text{pol.}}(\epsilon_3)_{\nu'}(\epsilon_3^\star)_\nu\sum_{\text{pol.}}(\epsilon_4)_{\sigma'}(\epsilon_4^\star)_\sigma, \tag{B.60}$$

$$2\mathcal{R}\overline{[\mathcal{M}_t\mathcal{M}_u^\star]} = \frac{9g^4/(8d_g^2)\left((t-M_g^2)(u-M_g^2)+4\gamma_g^2\omega_t\omega_u\right)}{\left((t-M_g^2)^2+(2\gamma_g\omega_t)^2\right)\left((u-M_g^2)^2+(2\gamma_g\omega_u)^2\right)}\, C^{\tau\lambda\sigma}(q_1-q_4,-q_1,q_4)$$
$$\times C^{\tau'\nu\mu}(-q_3+q_2,q_3,-q_2)C^{\rho'\mu'\sigma'}(-q_2+q_4,q_2,-q_4)C^{\rho\nu'\lambda'}(q_3-q_1,-q_3,q_1)\left[g_{\tau\tau'}-(q_\tau^t q_{\tau'}^t)/M_g^2\right]$$
$$\times\left[g_{\rho\rho'}-(q_\rho^u q_{\rho'}^u)/M_g^2\right]\sum_{\text{pol.}}(\epsilon_1)_\lambda(\epsilon_1^\star)_{\lambda'}\sum_{\text{pol.}}(\epsilon_2)_\mu(\epsilon_2^\star)_{\mu'}\sum_{\text{pol.}}(\epsilon_3)_{\nu'}(\epsilon_3^\star)_\nu\sum_{\text{pol.}}(\epsilon_4)_{\sigma'}(\epsilon_4^\star)_\sigma, \tag{B.61}$$

$$2\mathcal{R}\overline{[\mathcal{M}_t\mathcal{M}_s^\star]} = \frac{9g^4/(8d_g^2)\left((t-M_g^2)(s-M_g^2)+4\gamma_g^2\omega_t\omega_s\right)}{\left((t-M_g^2)^2+(2\gamma_g\omega_t)^2\right)\left((s-M_g^2)^2+(2\gamma_g\omega_s)^2\right)}C^{\tau\lambda\sigma}(q_1-q_4,-q_1,q_4)$$
$$\times C^{\tau'\nu\mu}(-q_3+q_2,q_3,-q_2)C^{\rho'\nu'\sigma'}(q_3+q_4,-q_3,-q_4)C^{\rho\lambda'\mu'}(-q_1-q_2,q_1,q_2)\left[g_{\tau\tau'}-(q_\tau^t q_{\tau'}^t)/M_g^2\right]$$
$$\times\left[g_{\rho\rho'}-(q_\rho^s q_{\rho'}^s)/M_g^2\right]\sum_{\text{pol.}}(\epsilon_1)_\lambda(\epsilon_1^\star)_{\lambda'}\sum_{\text{pol.}}(\epsilon_2)_\mu(\epsilon_2^\star)_{\mu'}\sum_{\text{pol.}}(\epsilon_3)_{\nu'}(\epsilon_3^\star)_\nu\sum_{\text{pol.}}(\epsilon_4)_{\sigma'}(\epsilon_4^\star)_\sigma, \tag{B.62}$$

$$2\mathcal{R}\overline{[\mathcal{M}_u\mathcal{M}_s^\star]} = \frac{-9g^4/(8d_g^2)\left((u-M_g^2)(s-M_g^2)+4\gamma_g^2\omega_u\omega_s\right)}{\left((u-M_g^2)^2+(2\gamma_g\omega_u)^2\right)\left((s-M_g^2)^2+(2\gamma_g\omega_s)^2\right)}C^{\tau'\sigma\mu}(-q_4+q_2,q_4,-q_2)$$
$$\times C^{\tau\lambda\nu}(q_1-q_3,-q_1,q_3)C^{\rho'\nu'\sigma'}(q_3+q_4,-q_3,-q_4)C^{\rho\lambda'\mu'}(-q_1-q_2,q_1,q_2)\left[g_{\tau\tau'}-(q_\tau^u q_{\tau'}^u)/M_g^2\right]$$
$$\times\left[g_{\rho\rho'}-(q_\rho^s q_{\rho'}^s)/M_g^2\right]\sum_{\text{pol.}}(\epsilon_1)_\lambda(\epsilon_1^\star)_{\lambda'}\sum_{\text{pol.}}(\epsilon_2)_\mu(\epsilon_2^\star)_{\mu'}\sum_{\text{pol.}}(\epsilon_3)_{\nu'}(\epsilon_3^\star)_\nu\sum_{\text{pol.}}(\epsilon_4)_{\sigma'}(\epsilon_4^\star)_\sigma, \tag{B.63}$$

$$|\overline{\mathcal{M}}_4|^2 = \frac{g^4}{d_g^2}\left[\frac{9}{8}\left(|\mathcal{M}_4^s|^2+|\mathcal{M}_4^u|^2+|\mathcal{M}_4^t|^2\right)+2\times\frac{9}{16}\left(\mathcal{R}[\mathcal{M}_4^s\mathcal{M}_4^u]+\mathcal{R}[\mathcal{M}_4^s\mathcal{M}_4^t]-\mathcal{R}[\mathcal{M}_4^t\mathcal{M}_4^u]\right)\right]$$
$$\times\sum_{\text{pol.}}(\epsilon_1)_\lambda(\epsilon_1^\star)_{\lambda'}\sum_{\text{pol.}}(\epsilon_2)_\mu(\epsilon_2^\star)_{\mu'}\sum_{\text{pol.}}(\epsilon_3)_{\nu'}(\epsilon_3^\star)_\nu\sum_{\text{pol.}}(\epsilon_4)_{\sigma'}(\epsilon_4^\star)_\sigma, \tag{B.64}$$

$$2\mathcal{R}\overline{[\mathcal{M}_t\mathcal{M}_4^\star]} = \frac{g^4/d_g^2(t-M_g^2)}{(t-M_g^2)+(2\gamma_g\omega_t)^2}\; C^{\tau\lambda\sigma}(q_1-q_4,-q_1,q_4)C^{\tau'\nu\mu}(-q_3+q_2,q_3,-q_2)$$
$$\times\left[\frac{9}{16}(g^{\sigma'\mu'}g^{\nu'\lambda'}-g^{\sigma'\lambda'}g^{\nu'\mu'})-\frac{9}{16}(g^{\sigma'\nu'}g^{\mu'\lambda'}-g^{\sigma'\lambda'}g^{\mu'\nu'})+\frac{9}{8}(g^{\sigma'\nu'}g^{\lambda'\mu'}-g^{\sigma'\mu'}g^{\lambda'\nu'})\right]$$
$$\times\left[g_{\tau\tau'}-(q_\tau^t q_{\tau'}^t)/M_g^2\right]\sum_{\text{pol.}}(\epsilon_1)_\lambda(\epsilon_1^\star)_{\lambda'}\sum_{\text{pol.}}(\epsilon_2)_\mu(\epsilon_2^\star)_{\mu'}\sum_{\text{pol.}}(\epsilon_3)_{\nu'}(\epsilon_3^\star)_\nu\sum_{\text{pol.}}(\epsilon_4)_{\sigma'}(\epsilon_4^\star)_\sigma, \tag{B.65}$$

$$2\mathcal{R}\overline{[\mathcal{M}_s\mathcal{M}_4^\star]} = \frac{g^4/d_g^2(s-M_g^2)}{(s-M_g^2)^2+(2\gamma_g\omega_s)^2}\; C^{\tau'\sigma\nu}(-q_4-q_3,q_4,q_3)C^{\tau\mu\lambda}(q_2+q_1,-q_2,-q_1)$$
$$\times\left[\frac{9}{8}(g^{\sigma'\mu'}g^{\nu'\lambda'}-g^{\sigma'\lambda'}g^{\nu'\mu'})+\frac{9}{16}(g^{\sigma'\nu'}g^{\mu'\lambda'}-g^{\sigma'\lambda'}g^{\mu'\nu'})+\frac{9}{16}(g^{\sigma'\nu'}g^{\lambda'\mu'}-g^{\sigma'\mu'}g^{\lambda'\nu'})\right]$$
$$\times\left[g_{\tau\tau'}-(q_\tau^s q_{\tau'}^s)/M_g^2\right]\sum_{\text{pol.}}(\epsilon_1)_\lambda(\epsilon_1^\star)_{\lambda'}\sum_{\text{pol.}}(\epsilon_2)_\mu(\epsilon_2^\star)_{\mu'}\sum_{\text{pol.}}(\epsilon_3)_{\nu'}(\epsilon_3^\star)_\nu\sum_{\text{pol.}}(\epsilon_4)_{\sigma'}(\epsilon_4^\star)_\sigma, \tag{B.66}$$

$$2\mathcal{R}\overline{[\mathcal{M}_u\mathcal{M}_4^\star]} = \frac{g^4/d_g^2(u-M_g^2)}{(u-M_g^2)^2+(2\gamma_g\omega_u)^2}\; C^{\tau'\sigma\mu}(-q_4+q_2,q_4,-q_2)C^{\tau\lambda\nu}(q_1-q_3,-q_1,q_3)$$
$$\times\left[\frac{-9}{16}(g^{\sigma'\mu'}g^{\nu'\lambda'}-g^{\sigma'\lambda'}g^{\nu'\mu'})-\frac{9}{8}(g^{\sigma'\nu'}g^{\mu'\lambda'}-g^{\sigma'\lambda'}g^{\mu'\nu'})+\frac{9}{16}(g^{\sigma'\nu'}g^{\lambda'\mu'}-g^{\sigma'\mu'}g^{\lambda'\nu'})\right]$$
$$\times\left[g_{\tau\tau'}-(q_\tau^u q_{\tau'}^u)/M_g^2\right]\sum_{\text{pol.}}(\epsilon_1)_\lambda(\epsilon_1^\star)_{\lambda'}\sum_{\text{pol.}}(\epsilon_2)_\mu(\epsilon_2^\star)_{\mu'}\sum_{\text{pol.}}(\epsilon_3)_{\nu'}(\epsilon_3^\star)_\nu\sum_{\text{pol.}}(\epsilon_4)_{\sigma'}(\epsilon_4^\star)_\sigma. \tag{B.67}$$

B.3 Cross section

On-shell case

The cross section for a $2 \to 2$ process is given by:

$$d\sigma^{\rm on} = \frac{|\mathcal{M}|^2}{F} \frac{d^3p_3}{(2\pi)^3 2E_3} \frac{d^3p_4}{(2\pi)^3 2E_4} (2\pi)^4 \delta^{(4)}\left(p_1 + p_2 - p_3 - p_4\right), \tag{B.68}$$

where the flux is defined by $F = v_{\rm rel}\ 2E_1\ 2E_2$ with the definition $v_{\rm rel} = |\mathbf{v}_1 - \mathbf{v}_2|$.

To simplify the Lorentz invariant phase space (LIPS), we need to transform the delta function representing the energy conservation into a constrain on $|\mathbf{p_3}|$. We put $E = E_1 + E_2$ and $\mathbf{p} = \mathbf{p}_1 + \mathbf{p}_2$ to obtain:

$$E = \sqrt{p_3^2 + m_3^2} + \sqrt{(\mathbf{p} - \mathbf{p}_3)^2 + m_4^2}. \tag{B.69}$$

By manipulating this expression and solving it for p_3, we obtain:

$$p_3 = \frac{\mathbf{p}.\mathbf{u}_{\mathbf{p}_3}(s + m_3^2 - m_4^2) + E\sqrt{(s - (m_3+m_4)^2)\,(s - (m_3-m_4)^2) + 4m_3^2\,((\mathbf{p}.\mathbf{u}_{\mathbf{p}_3})^2 - p^2)}}{2(E^2 - (\mathbf{p}.\mathbf{u}_{\mathbf{p}_3})^2)} \tag{B.70}$$

where $\mathbf{u}_{\mathbf{p}_3} = \mathbf{p}_3/|\mathbf{p}_3|$ is the unitary vector of $\mathbf{p}_3$. By using the following derivative:

$$\left|\frac{\partial}{\partial|\mathbf{p_3}|}\left(E - E_3 - E_4\right)\right| = \left|\frac{p_3}{E_3} + \frac{p_3 - \mathbf{p}.\mathbf{u}_{\mathbf{p}_3}}{E_4}\right|, \tag{B.71}$$

we can simplify the Lorentz invariant phase space by integrating over p_3 as:

$$\frac{d^3p_3}{(2\pi)^3 2E_3} \frac{d^3p_4}{(2\pi)^3 2E_4} (2\pi)^4 \delta^{(4)}\left(p_1 + p_2 - p_3 - p_4\right) = \tag{B.72}$$

$$\frac{1}{4\pi^2} \frac{p_3^2\ d\Omega\ dp_3}{4E_3E_4}\ \delta\left(E - E_3 - E_4\right) = \frac{p_3^2\ d\Omega}{(16\pi^2)|E_4 p_3 + E_3(p_3 - \mathbf{p}.\mathbf{u}_{\mathbf{p}_3})|}, \tag{B.73}$$

and obtain the on-shell cross section as:

$$d\sigma^{\rm on} = \frac{p_3^2\ d\Omega}{(16\pi^2)|E_4 p_3 + E_3(p_3 - \mathbf{p}.\mathbf{u}_{\mathbf{p}_3})|}\frac{|\mathcal{M}|^2}{F}. \tag{B.74}$$

In the center of mass (CM) system, we have $\mathbf{p}_1 + \mathbf{p}_2 = \mathbf{p}_3 + \mathbf{p}_4 = \mathbf{p} = \vec{0}$, $\sqrt{s} = (E_1 + E_2) = (E_3 + E_4) = E$, and we use the notation $|\mathbf{p_1}| = |\mathbf{p_2}| = |\mathbf{p_i}|$ and $|\mathbf{p_3}| = |\mathbf{p_4}| = |\mathbf{p_f}|$. The flux F becomes:

$$F^{CM} = 4|\mathbf{p_i}|\sqrt{s}. \tag{B.75}$$

The momentum in the CM frame p_f (and similarly for $|\mathbf{p_i}|$) is obtained from Eq. (B.70) by using $\mathbf{p} = \vec{0}$:

$$\mathbf{p}_{i,f}^{\rm CM} = \frac{\sqrt{\left(s - (m_{i,f} + m'_{i,f})^2\right)\left(s - (m_{i,f} - m'_{i,f})^2\right)}}{2\sqrt{s}}. \tag{B.76}$$

By using the same strategy, we obtain the on-shell cross section evaluated in the center of mass frame as:

$$d\sigma^{\rm on} = \frac{d\Omega}{64\pi^2 s}\frac{|\mathbf{p_f}|}{|\mathbf{p_i}|}|\mathcal{M}|^2. \tag{B.77}$$

Off-shell case

In the off-shell case, the energy of the partons is an independent degree-of-freedom. By transforming the Lorentz invariant phase space as:

$$\frac{d^3p}{2E} = \int d^4p\ \frac{1}{2E}\ \delta(\omega - E) = \int d^4p\ \delta(p^2 - m^2)\ \theta(\omega), \tag{B.78}$$

we can obtain the cross-section averaged over the energy of the final partons by weighting the energy and momentum integration with the spectral function ρ as:

$$d\sigma^{\rm off} = \frac{d^4p_3}{(2\pi)^4}\theta(\omega_3)\frac{d^4p_4}{(2\pi)^4}\theta(\omega_4)\ \tilde{\rho_3}(\omega_3, \mathbf{p}_3)\ \tilde{\rho_4}(\omega_4, \mathbf{p}_4)(2\pi)^4\delta^{(4)}\left(p - p_3 - p_4\right)\frac{|\bar{\mathcal{M}}|^2}{F} \tag{B.79}$$

with $p = p_1 + p_2$, and $\tilde{\rho}$ being the normalized Lorentzian spectral function defined in Chapter 7. One can simplify the off-shell energy integration by an integration

over the final masses of the partons by invoking a non-relativistic approximation, leading to the following cross-section:

$$\sigma^{\rm off} = \int_0^{\sqrt{s}} dm_3 \int_0^{\sqrt{s}-m_3} dm_4 \; \rho^{\rm BW}(m_3) \; \rho^{\rm BW}(m_4) \int d\sigma^{\rm on}, \tag{B.80}$$

where the Breit-Wigner spectral function $\rho^{\rm BW}$ is obtained from the Lorentzian spectral function by taking the limit $\omega \to m$:

$$\rho_i^{\rm BW}(m) = \frac{2}{\pi} \frac{2 \; M_i^2 \; \gamma_i}{(m^2 - M_i^2)^2 + (2 \; M_i \; \gamma_i)^2}. \tag{B.81}$$

This distribution should fulfill the normalization $\int_0^\infty dm \; \rho^{\rm BW}(m) = 1$.

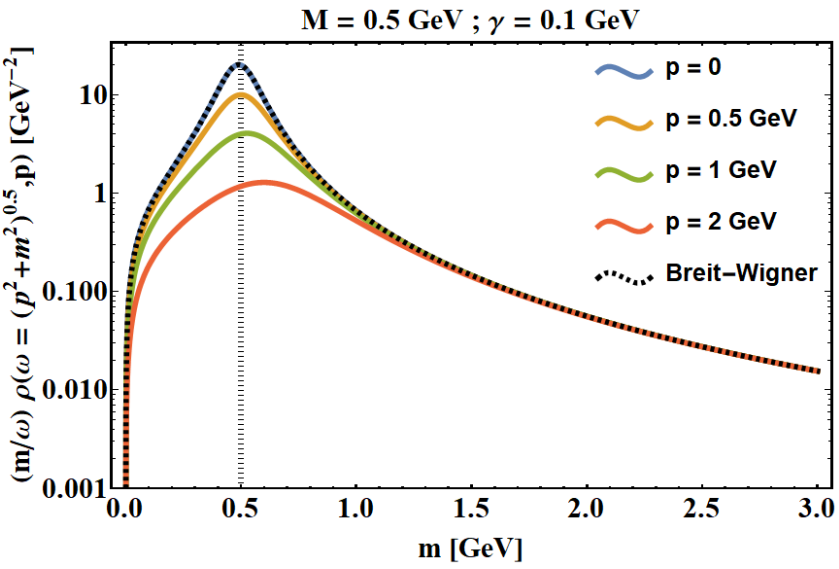

Figure B.5 – Lorentzian spectral function multiplied by the invariant mass m over the energy ω as a function of m for different values of the momentum $\mathbf{p}$. The black dashed curve is the Breit-Wigner distribution from Eq. (B.81) multiplied by π.

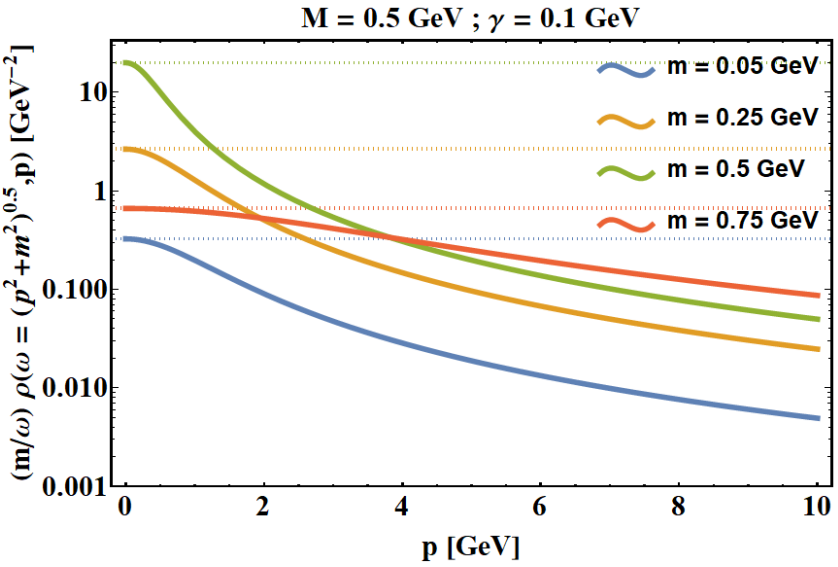

Figure B.6 – Lorentzian spectral function multiplied by the invariant mass m over the energy ω as a function of the momentum $\mathbf{p}$ for different values of the invariant mass m.

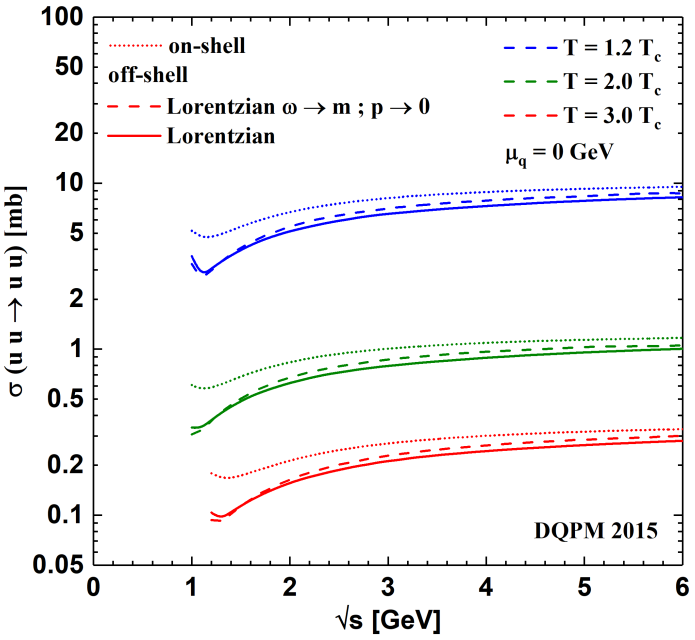

Figure B.7 – On- and off-shell cross section of $u-$quarks with fixed initial masses as a function of the invariant energy $\sqrt{s}$. The limit $\omega \to m$ in the Lorentzian spectral gives the Breit-Wigner shape.

Note

The cross section can be equivalently calculated in the heat bath rest frame or in the center of mass frame since one event can be fully translated from one frame to an other. But the evaluation of the cross section is frame dependant since the flux factor F is not invariant. From Eq. (B.68-B.79), we deduce the following equality between the cross section calculated in the center of mass system (CM) and in the heat bath frame (HB):

$$F^{\mathrm{CM}}\sigma^{\mathrm{CM}} = F^{\mathrm{HB}}\sigma^{\mathrm{HB}}. \tag{B.82}$$

The calculation of the cross section in the heat bath frame is more demanding numerically since the collision system is not symmetric under a rotation over the azimuthal angle ϕ. In the center of mass system, this integration is not needed and the solid angle differential element $d\Omega$ is replaced by $d\Omega = 2\pi d\cos(\theta)$.

Limit of integration for the off-shell cross section

To determine the upper limit of integration for $|\mathbf{p}_3| = p_3$ in the calculation of the off-shell cross section, we use the equation for energy conservation $E_1 + E_2 = E_3 + E_4$ by imposing $m_3 = m_4 = 0$:

$$E_1 + E_2 = p_3 + |\mathbf{p}_1 + \mathbf{p}_2 - \mathbf{p}_3| \tag{B.83}$$

$$(E_1 + E_2 - p_3)^2 = (\mathbf{p}_1 + \mathbf{p}_2)^2 - 2(\mathbf{p}_1 + \mathbf{p}_2).\mathbf{p}_3 + p_3^2$$

$$(E_1 + E_2)^2 - 2(E_1 + E_2)p_3 = (\mathbf{p}_1 + \mathbf{p}_2)^2 - 2(\mathbf{p}_1 + \mathbf{p}_2).\mathbf{p}_3$$

$$s/2 = (E_1 + E_2)p_3 - (\mathbf{p}_1 + \mathbf{p}_2).\mathbf{p}_3$$

$$p_3 = \frac{s/2}{(E_1 + E_2) - (\mathbf{p}_1 + \mathbf{p}_2).\mathbf{u}_{\mathbf{p}_3}} \tag{B.84}$$

When p_3 is fixed, we can obtain the maximum energy ω_3 by using again $m_4 = 0$:

$$\omega_3 = E_1 + E_2 - |\mathbf{p}_1 + \mathbf{p}_2 - \mathbf{p}_3| = E_1 + E_2 - \left((\mathbf{p}_1 + \mathbf{p}_2)^2 - 2(\mathbf{p}_1 + \mathbf{p}_2).\mathbf{p}_3 + p_3^2\right)^{1/2} \tag{B.85}$$

In the center of mass frame, these limits of integration reduce to:

$$p_3 = p_f = \frac{\sqrt{s}}{2} \qquad \omega_3 = \sqrt{s} - p_f \tag{B.86}$$

Appendix C

Realization of a differential cross section

* * *

C.1 Calculation of the cross section

As explained in chapter 4, thermodynamic quantities like energy density or pressure components are more conveniently studied in the local rest frame (LRF) of a fluid cell. In PHSD, one can transform the momenta $p = (E, \vec{p})$ of the particles contained in a cell into its LRF by applying the appropriate Lorentz transformation:

$$E^{\mathrm{LRF}} = \gamma \left[E - (\mathbf{p} \cdot \boldsymbol{\beta}^{\mathrm{cell}}) \right], \qquad \mathbf{p}^{\mathrm{LRF}} = \vec{p} + \gamma \boldsymbol{\beta}^{\mathrm{cell}} \left[\frac{\gamma \ (\mathbf{p} \cdot \boldsymbol{\beta}^{\mathrm{cell}})}{\gamma + 1} - E \right]. \tag{C.1}$$

with $\boldsymbol{\beta}^{\mathrm{cell}}$ being the cell velocity.

A scattering cross-section is conveniently evaluated in the center of mass system (CMS) of the considered collision (see chapter 7). The velocity of the CMS of the collision between a particle 1 and 2 is:

$$\boldsymbol{\beta}^{\mathrm{CM}} = \frac{\mathbf{p_1} + \mathbf{p_2}}{E_1 + E_2}. \tag{C.2}$$

One can prove that using the previous velocity $\boldsymbol{\beta}^{\mathrm{CM}}$, performing the Lorentz transformation of two vectors $\vec{p}_1$ and $\vec{p}_2$ corresponding to two incoming particles about

to interact, systematically we arrive to the following relation in the center of mass system:

$$\mathbf{p}_1^{CM} + \mathbf{p}_2^{CM} = \vec{0}. \tag{C.3}$$

One can either evaluates the DQPM cross sections from chapter 7 in the general case (PHSD frame or LRF of the cell), or in the simplified case of the CMS. This is possible since the integrals appearing in the cross section are invariant, meaning that the result will not depend on the frame of evaluation. In the general case, the off-shell cross section can be evaluated by integrating the energy and momentum of the final particles 3 and 4 as:

$$\begin{aligned}
\sigma^{\text{off}}(p_1,p_2) = & \int \frac{d^4p_3}{(2\pi)^4} \int \frac{d^4p_4}{(2\pi)^4}\ \tilde{\rho}_3(\omega_3,\mathbf{p}_3)\ \theta(\omega_3)\ \tilde{\rho}_4(\omega_4,\mathbf{p}_4)\ \theta(\omega_4) \\
& (2\pi)^4\delta^{(4)}\left(p_1+p_2-p_3-p_4\right)\frac{|\bar{\mathcal{M}}|^2}{F} \qquad \text{(C.4)} \\
= & \int \frac{d^4p_3}{(2\pi)^4}\ \tilde{\rho}_3(\omega_3,\mathbf{p}_3)\ \theta(\omega_3)\ \tilde{\rho}_4(\omega_4,\mathbf{p}_4)\ \theta(\omega_4)\frac{|\bar{\mathcal{M}}|^2}{F} \\
= & \int \frac{d\omega_3}{(2\pi)}\ \frac{p_3^2\ d\phi_3\ d\cos(\theta_3)}{(2\pi)^3}\ \tilde{\rho}_3(\omega_3,\mathbf{p}_3)\ \theta(\omega_3)\ \tilde{\rho}_4(\omega_4,\mathbf{p}_4)\ \theta(\omega_4)\frac{|\bar{\mathcal{M}}|^2}{F}
\end{aligned}$$

The only part of this expression which is not invariant is the initial flux factor F and will therefore have to be evaluated in the frame of interest, which depends on the collision criteria (see next subsection).

For illustration, we now study a collision for a fixed invariant energy $\sqrt{s}$ and a fixed angle $\cos(\theta_{12})$ between the initial momenta of the particles. The magnitude of the initial momenta are taken to be equal such that $\mathbf{p}_1 \cdot \mathbf{p}_2 = |\mathbf{p}_1||\mathbf{p}_2|\cos(\theta_{12}) = |\mathbf{p}_1|^2\cos(\theta_{12})$. Using this configuration, we illustrate in Fig. C.1 the magnitude of the initial momenta $|\mathbf{p}_1| = |\mathbf{p}_2|$ and the corresponding flux factor F as a function of $\sqrt{s}$ and the angle $\cos(\theta_{12})$.

C.2 Collision criteria

In order to decide if two particles will collide or not in a transport approach, one should impose a collision criteria which will depend on the total interaction

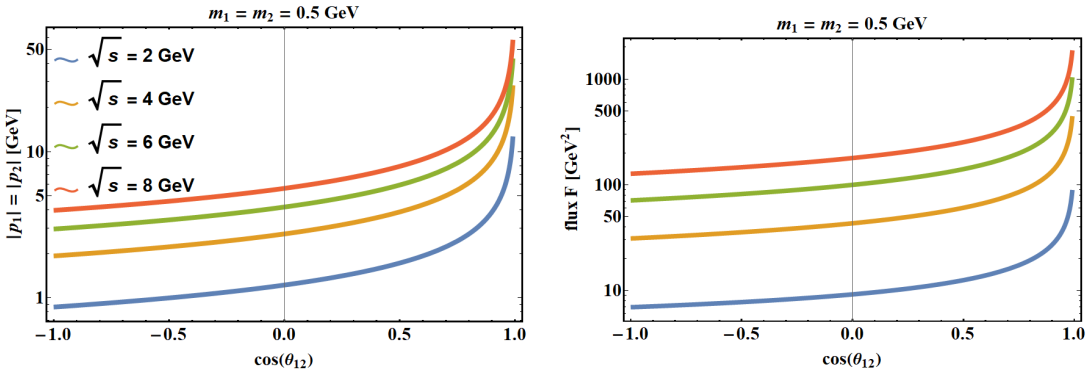

Figure C.1 – Magnitude of the initial momenta (left) and initial flux (right) for a collision varying the collision angle $\cos(\theta_{12})$ between particles 1 and 2 for different values of the invariant energy $\sqrt{s}$.

cross section σ_{tot}, the latter being therefore interpreted as an area. This collision criteria is:

$$b < b_{max} = \sqrt{\sigma_{tot}/\pi}, \tag{C.5}$$

with b being the impact parameter between the two particles, and b_{max} the maximum impact parameter until which a collision can happen. At relativistic energies, one should evaluate the impact parameter b in a covariant way (see Ref. [173]). The reasoning for the evaluation of the impact parameter of a binary collision [442, 443] is detailed here. We study the collision in its center of mass system where the particles are initially at a position $(t_i^{CM}, \vec{x}_i^{CM})$ with $i = 1, 2$. The position of the particle i at time t^{CM} is given by:

$$\vec{x}_i^{CM}(t^{CM}) = \vec{x}_i^{CM}(t_i^{CM}) + \vec{v}_i^{CM}(t^{CM} - t_i^{CM}) \tag{C.6}$$

with $\vec{v}_i^{CM} = \vec{p}_i^{CM}/E_i^{CM}$ being the velocity of particle i in the CM frame. The distance d between the two particles at the time t^{CM} is then given by:

$$d^2(t^{CM}) = \left((\vec{x}_1^{CM}(t^{CM}) - \vec{x}_2^{CM}(t^{CM})\right)^2 = \left(\vec{x}_{12}^{CM} + \vec{v}_{12}^{CM} t^{CM}\right)^2, \tag{C.7}$$

with

$$\vec{x}_{12}^{CM} = \vec{x}_1^{CM} - \vec{v}_1^{CM} - (\vec{x}_2^{CM} - \vec{v}_2^{CM}), \qquad \vec{v}_{12}^{CM} = \vec{v}_1^{CM} - \vec{v}_2^{CM}. \tag{C.8}$$

The impact parameter b is defined as the minimum distance between the two particles. One first has to evaluate the time t_{min}^{CM} at which the distance d between the two particles is minimum:

$$t_{min}^{CM} = -\frac{\vec{x}_{12}^{CM} \cdot \vec{v}_{12}^{CM}}{(\vec{v}_{12}^{CM})^2}, \tag{C.9}$$

which gives, by replacing $t^{CM} \to t_{min}^{CM}$ in Eq. (C.7), the impact parameter:

$$b^2 = (\vec{x}_{12}^{CM})^2 - \frac{(\vec{x}_{12}^{CM} \cdot \vec{v}_{12}^{CM})^2}{(\vec{v}_{12}^{CM})^2}. \tag{C.10}$$

By transforming the quantities into the calculation frame, usually taken as the CM frame of the heavy-ion collision, we obtain:

$$b^2 = R_{12}^2 - \frac{h_{12}^2}{v_{12}^2} \tag{C.11}$$

with

$$\begin{aligned} R_{12}^2 &= (\vec{x}_1 - \vec{x}_2)^2 + (\vec{p}_1 \cdot (\vec{x}_2 - \vec{x}_1)/m_1)^2 \\ h_{12} &= \vec{p}_1 \cdot (\vec{x}_2 - \vec{x}_1)/m_1 - (\vec{p}_2 \cdot (\vec{x}_2 - \vec{x}_1) m_1/(p_1 \cdot p_2)) \\ v_{12}^2 &= 1 - \left(\frac{m_1\ m_2}{p_1 . p_2}\right)^2 . \end{aligned} \tag{C.12}$$

With this procedure, collisions can be decided in a transport approach by using the total interaction cross-section between two particles, which has to be systematically evaluated in the center of mass system of the collision.

C.3 Direction of the final momenta

In order to choose the angle between the particles after their scattering, one uses Monte-Carlo techniques to decide which final angle is favored according to the differential cross section expressed in the CM frame. This angle usually refers to the angle between one of the initial and final particles, which means that in order to attribute the correct angle to a final particle, the momentum of the initial particles also needs to be known in the CM system. Once the final angle is decided, one

has to perform a rotation of an arbitrary vector (in this case the initial momentum of a particle) according to the two spherical angles (θ, ϕ). In the CM frame, the system is symmetric under the angle ϕ and is therefore chosen randomly, while θ is the angle chosen according to the differential cross section. For this purpose, we can use the following transformation from an initial vector $\vec{p}^{\,in}$ into the final vector $\vec{p}^{\,fin}$:

$$\vec{p}^{\,fin} = \begin{pmatrix} p_x^{fin} \\ p_y^{fin} \\ p_z^{fin} \end{pmatrix} = \mathcal{R}_{\vec{u},\theta} \begin{pmatrix} p_x^{in} \\ p_y^{in} \\ p_z^{in} \end{pmatrix}$$

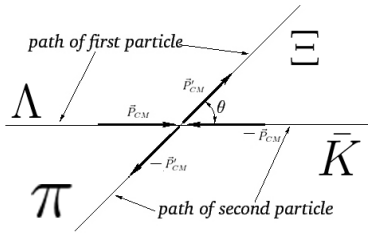

with the rotation matrix $\mathcal{R}_{\vec{u},\theta}$ given by

$$\mathcal{R}_{\vec{u},\theta} = \begin{pmatrix} l\,l\,(1-\cos\theta)+\cos\theta & m\,l\,(1-\cos\theta)-n\,\sin\theta & n\,l\,(1-\cos\theta)+m\,\sin\theta \\ l\,m\,(1-\cos\theta)+n\,\sin\theta & m\,m\,(1-\cos\theta)+\cos\theta & n\,m\,(1-\cos\theta)-l\,\sin\theta \\ l\,n\,(1-\cos\theta)-m\,\sin\theta & m\,n\,(1-\cos\theta)+l\,\sin\theta & n\,n\,(1-\cos\theta)+\cos\theta \end{pmatrix} \tag{C.13}$$

with θ denoting the rotation angle with respect to the unitary vector $\vec{u} = (l, m, n)$. In order to perform a rotation according to the $\theta \in [0, \pi]$ angle, one needs to take $\vec{u}$ perpendicular to the initial vector. For the $\phi \in [0, 2\pi]$ angle, one needs simply to take $\vec{u}$ as the normalized initial vector. The transformation under the angles θ and ϕ of an initial momentum vector is :

$$\vec{p}^{\,fin} = \mathcal{R}_{\vec{u},\phi}\left(\mathcal{R}_{\vec{v},\theta}\ \vec{p^{in}}\right), \tag{C.14}$$

with the two unitary vector $\vec{u} = \vec{p^{in}}/\left|\vec{p^{in}}\right|$ and $\vec{v}$ defined as $\vec{u}.\vec{v} = 0$ and $|\vec{v}| = 1$.

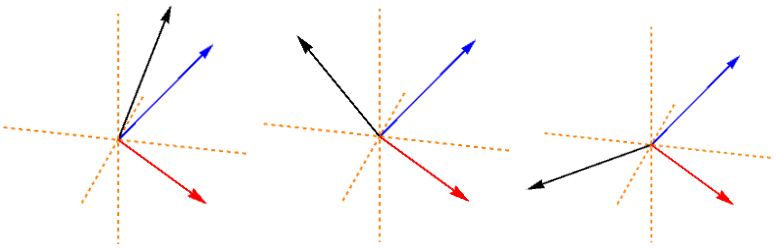

Figure C.2 – Rotation of an initial vector (blue) with respect to one of its transverse unitary vector (red) with an angle of $\theta = \pi/6,\ \pi/2,\ 5\pi/6$.

Appendix D

Energy-momentum tensor in Milne coordinates

* * *

D.1 Definitions

In order to perform hydrodynamic simulations in relativistic heavy-ion collisions, Milne coordinates are chosen and written as a function of the Minkowski coordinates as :

$$\begin{cases} \tau = \sqrt{t^2 - z^2} \\ x \\ y \\ \eta = (1/2)\ \mathrm{Ln}\left((t+z)/(t-z)\right). \end{cases} \tag{D.1}$$

One can also use the following relations to pass from the Milne coordinates to the Minkowski ones:

$$t = \tau\ \cosh\ \eta, \qquad z = \tau\ \sinh\ \eta. \tag{D.2}$$

In the Milne coordinate system, the metric tensor is given by:

$$g^{\mu\nu} = \mathrm{diag}(1, -1, -1, -1/\tau^2) \qquad g_{\mu\nu} = \mathrm{diag}(1, -1, -1, -\tau^2), \tag{D.3}$$

and the 4-momentum p^μ by the components:

$$p^\mu = (p^\tau, p^x, p^y, p^\eta)\,, \tag{D.4}$$

which can be calculated by the help of a Jacobian matrix as:

$$p^\tau = \frac{\partial \tau}{\partial t}\, p^t + \frac{\partial \tau}{\partial z}\, p^z = \cosh\,\eta\; p^t - \sinh\,\eta\; p^z = m_T\,\cosh(y-\eta), \tag{D.5}$$

$$p^\eta = \frac{\partial \eta}{\partial t}\, p^t + \frac{\partial \eta}{\partial z}\, p^z = \frac{-z}{t^2-z^2}\, p^t + \frac{t}{t^2-z^2}\, p^z = -\frac{\sinh\eta}{\tau} p^t + \frac{\cosh\eta}{\tau} p^z = \frac{m_T}{\tau}\,\sinh(y-\eta). \tag{D.6}$$

The velocity vector in Milne coordinates is:

$$u^\mu = \{u^\tau,\; u^x,\; u^y,\; u^\eta\} = \gamma\,\{1,\; \beta^x,\; \beta^y,\; \beta^\eta\}\,, \tag{D.7}$$

where the $\gamma-$factor associated to the cell velocity is:

$$\gamma = \left(1 - \beta_x^2 - \beta_y^2 - \tau^2\beta_\eta^2\right)^{-1/2} = u^\tau. \tag{D.8}$$

The coordinate transformation of the four-velocity between Milne coordinates and Cartesian coordinates is given by [444] (similarly as Eq. (D.5-D.6)):

$$u^\tau = \cosh\,\eta\; u^t - \sinh\,\eta\; u^z, \qquad u^t = \cosh\,\eta\; u^\tau + \tau\,\sinh\,\eta\; u^\eta, \tag{D.9}$$

$$u^\eta = -\frac{\sinh\,\eta}{\tau}\; u^t + \frac{\cosh\,\eta}{\tau}\; u^z, \qquad u^z = \sinh\,\eta\; u^\tau + \tau\,\cosh\,\eta\; u^\eta, \tag{D.10}$$

where the transverse components u^x and u^y are the same in both coordinates. The transformation of the three-dimensional velocity vector $\vec{\beta}$ between Milne and Cartesian coordinates is given by [444]:

$$\text{Milne: } \beta^i = \{\beta^x,\; \beta^y,\; \beta^\eta\} \quad ; \quad \text{Cartesian: } v^i = \{v^x,\; v^y,\; v^z\} \tag{D.11}$$

$$\beta^i = \frac{v^i}{\cosh\,\eta - v^z \sinh\,\eta} \quad (i = x, y) \tag{D.12}$$

$$\beta^\eta = \frac{1}{\tau}\frac{v^z \cosh\,\eta - \sinh\,\eta}{\cosh\,\eta - v^z \sinh\,\eta} \tag{D.13}$$

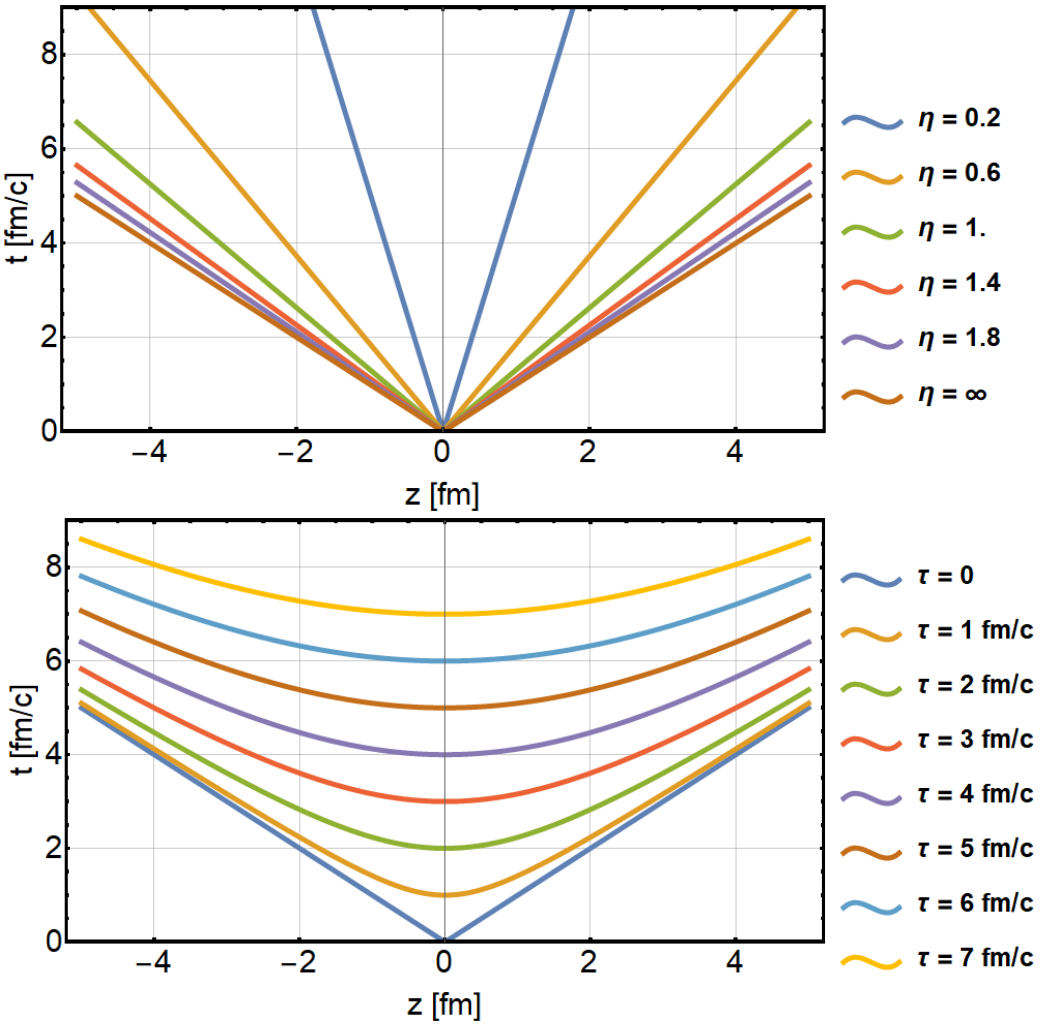

Figure D.1 – Trajectories in the $t-z$ plane for constant values of τ and η.

and accordingly from Milne to Cartesian coordinates by:

$$v^z = \frac{\tau\beta^\eta \cosh\,\eta + \sinh\,\eta}{\tau\beta^\eta \sinh\,\eta + \cosh\,\eta} \tag{D.14}$$

$$v^i = \beta^i\,(\cosh\,\eta - v^z \sinh\,\eta) \quad (i = x, y). \tag{D.15}$$

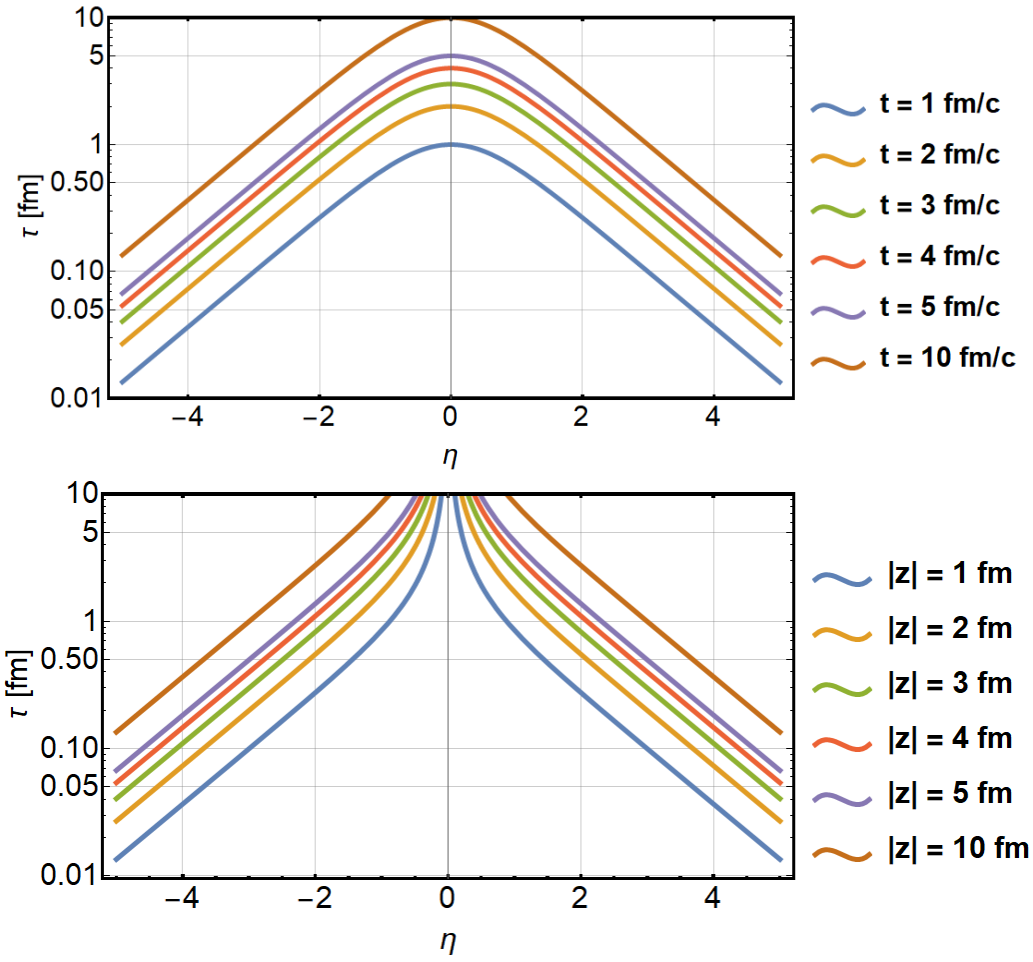

Figure D.2 – Trajectories in the $\tau - \eta$ plane for constant values of t and z.

D.2 Energy-momentum tensor

The energy-momentum tensor from relativistic kinetic theory reads [445]:

$$T^{\mu\nu}(x) = \int \frac{d^3p}{p^0} f(x,p)\; p^\mu p^\nu, \tag{D.16}$$

where p^0 is defined as $p^0 = E = \sqrt{m^2 + \vec{p}^2}$. The distribution function in Cartesian coordinates $(\boldsymbol{x}, \boldsymbol{p}, t)$ can be written in the Klimontovich-Dupree representation as

[446, 447]:

$$f(\boldsymbol{x},\boldsymbol{p},t) = \frac{1}{N}\sum_i^N f_i(\boldsymbol{x},t)\ f_i(\boldsymbol{p},t) \tag{D.17}$$

$$= \frac{1}{N}\sum_i^N \int \delta^{(3)}(\boldsymbol{x}-\boldsymbol{x_i}(t))\ \delta^{(3)}(\boldsymbol{p}-\boldsymbol{p_i}(t))\ \delta(t-t_i)\ dt_i.$$

We can define a coarse-grained distribution function in space by the following formula:

$$f(\boldsymbol{x},\boldsymbol{p},t) = \frac{1}{N}\frac{1}{\Delta^3 x}\sum_i^N \int_{\Delta^3 x} d^3x\ \delta^{(3)}(\boldsymbol{x}-\boldsymbol{x_i}(t))\ \delta^{(3)}(\boldsymbol{p}-\boldsymbol{p_i}(t))\ \delta(t-t_i)\ dt_i, \tag{D.18}$$

where $\Delta^3 x = V = \Delta x \Delta y \Delta z$ is the volume of the cell. The four-dimensional delta function is invariant, i.e. the same in both coordinate systems:

$$\delta(t-t_i)\ \delta^{(3)}(\boldsymbol{x}-\boldsymbol{x_i}(t)) = \delta(\tau-\tau_i)\ 1/\tau\ \delta^{(3)}(\boldsymbol{x'}-\boldsymbol{x'_i}(\tau)) \tag{D.19}$$

with τ_i being the proper time of the particle i. The differential element is also invariant which means $d^4x = dt\ d^3x = \tau\ d^4x' = d\tau\ \tau d\eta\ dxdy$. Then one has to transform the delta function in momentum space with $p' = (p^\tau, p^x, p^y, p^\eta)$:

$$\delta(p^z - p_i^z(\tau)) = \delta(\sinh\eta\ p^\tau + \tau\cosh\eta\ p^\eta - \sinh\eta_i p_i^\tau - \tau\cosh\eta_i p_i^\eta) \tag{D.20}$$

$$= \delta(p^\eta - p_i^\eta) \Big/ \left|\frac{\partial p^z}{\partial p^\eta}\Big|_{p^\eta = p_i^\eta}\right| \tag{D.21}$$

$$= \frac{\delta(p^\eta - p_i^\eta)}{\sinh\eta_i\ \frac{\partial p^\tau}{\partial p^\eta}\Big|_{p^\eta=p_i^\eta} + \tau\cosh\eta_i} \tag{D.22}$$

$$= \frac{\delta(p^\eta - p_i^\eta)}{\sinh\eta_i\ \frac{\tau^2 p_i^\eta}{E_i'} + \tau\cosh\eta_i} = \frac{\delta(p^\eta - p_i^\eta)\ E_i'}{\tau\ E_i}, \tag{D.23}$$

where we used the on-shell condition $E' = p^\tau = \sqrt{m^2 + p_x^2 + p_y^2 + \tau^2 p_\eta^2}$. More generally, we can actually write that [446–448]:

$$f_i(\boldsymbol{p}) = J_i^{-1} f_i(\boldsymbol{p'}), \tag{D.24}$$

where J_i is the Jacobian of the $i-$th particle, which is in our case given by $J_i = \tau E_i / E' i$.

By using the previous formulae, the distribution function in Milne coordinates is (see also [446, 447]):

$$f'(\boldsymbol{x}', \boldsymbol{p}', \tau) = \frac{1}{N} \frac{1}{\Delta^3 x'} \sum_i^N \int d^3x' \; \delta^{(3)}(\boldsymbol{x}' - \boldsymbol{x}'_{\boldsymbol{i}}(\tau)) \; \delta^{(3)}(\boldsymbol{p}' - \boldsymbol{p}'_{\boldsymbol{i}}(\tau)) \; \delta(\tau - \tau_i) \; d\tau_i$$

$$= \frac{1}{N} \frac{1}{\Delta^3 x'} \sum_i^N \int d^3x' \; \delta^{(3)}(\boldsymbol{x}' - \boldsymbol{x}'_{\boldsymbol{i}}(\tau)) \; \delta^{(3)}(\boldsymbol{p}' - \boldsymbol{p}'_{\boldsymbol{i}}(\tau)). \tag{D.25}$$

with the volume in Milne coordinates $\Delta^3 x' = \Delta x \Delta y \, \tau \Delta \eta$ and $d^3 x' = dx \; dy \; d\eta$. If we express $T^{\mu\nu}$ in Eq. (D.16) using the Lorentz-invariance of $dN = f(\boldsymbol{x}, \boldsymbol{p}, t) \; d^3x \; d^3p = f'(\boldsymbol{x}', \boldsymbol{p}', \tau) \; d^3x' \; d^3p'$ [447] we obtain:

$$T^{\mu\nu}(x) = \int \frac{d^3p}{E_i} f(\boldsymbol{x}, \boldsymbol{p}, t) \; p^\mu p^\nu = \frac{1}{\Delta^3 x} \sum_i \frac{p^\mu p^\nu}{E_i} \tag{D.26}$$

$$T^{\mu\nu}(x') = \int \frac{d^3p'}{E'_i} f'(\boldsymbol{x}', \boldsymbol{p}', \tau) \; p^\mu p^\nu = \int \frac{d^3p}{E'_i} f'(\boldsymbol{x}', \boldsymbol{p}, \tau) \; p^\mu p^\nu = \frac{1}{\Delta^3 x'} \sum_i \frac{p^\mu p^\nu}{E'_i} \tag{D.27}$$

with p^μ being the momentum expressed in Milne or Cartesian coordinates.

In order to find the eigenvalues of $T^{\mu\nu}$ using the Milne coordinates in momentum space ($\mu = \tau, x, y, \eta$), we have to calculate the determinant of the corresponding matrix which is the 4^{th} order characteristic polynomial associated to the eigenvalues λ:

$$P(\lambda) = \begin{vmatrix} T^{00} - \lambda & T^{01} & T^{02} & T^{03} \\ T^{10} & T^{11} + \lambda & T^{12} & T^{13} \\ T^{20} & T^{21} & T^{22} + \lambda & T^{23} \\ T^{30} & T^{31} & T^{32} & T^{33} + \lambda/\tau^2 \end{vmatrix}. \tag{D.28}$$

Having the four solutions for this polynomial, we can identify the energy density by the larger and positive solution, and the 3 other solutions are $(-P_i)$, i.e. the pressure components expressed in the LRF.

To obtain the 4-velocity of the cell, the Landau matching condition which gives us this set of equations:

$$\begin{cases} (T^{00}-e)u_\tau + T^{01}u_x + T^{02}u_y + T^{03}u_\eta = 0 \\ T^{10}u_\tau + (T^{11}+e)u_x + T^{12}u_y + T^{13}u_\eta = 0 \\ T^{20}u_\tau + T^{21}u_x + (T^{22}+e)u_y + T^{23}u_\eta = 0 \\ T^{30}u_\tau + T^{31}u_x + T^{32}u_y + (T^{33}+e/\tau^2)u_\eta = 0. \end{cases} \tag{D.29}$$

Rearranging these equations, we can obtain the solutions which are actually for the vector u_ν. To obtain the physical 4-velocity u^μ, we have to multiply by $g^{\mu\nu}u_\nu = u^\mu$.

To illustrate the calculation of the energy momentum tensor in Milne coordinates, we show in Fig. D.3 the temperature profile for a central Au+Au collision at $\sqrt{s_{NN}} = 200$ GeV expressed as a function of the Milne coordinates (τ, η) for the central cell $(x = y = 0)$. We constructed a grid in Milne coordinates with a cell size $\Delta\tau = 0.2$ fm/c, $\Delta x = \Delta y = 1$ fm and $\Delta\eta = 0.1$. Each particle contributes to the energy-momentum tensor with a Gaussian weight where the widths are taken to be $(\Delta x)^2 = (\Delta y)^2$ in the transverse direction and $(\Delta\eta)^2$ in the longitudinal direction. To avoid any over-counting, each particle is restricted to only contribute once in a given bin in proper time τ. In addition, particles with non-real proper

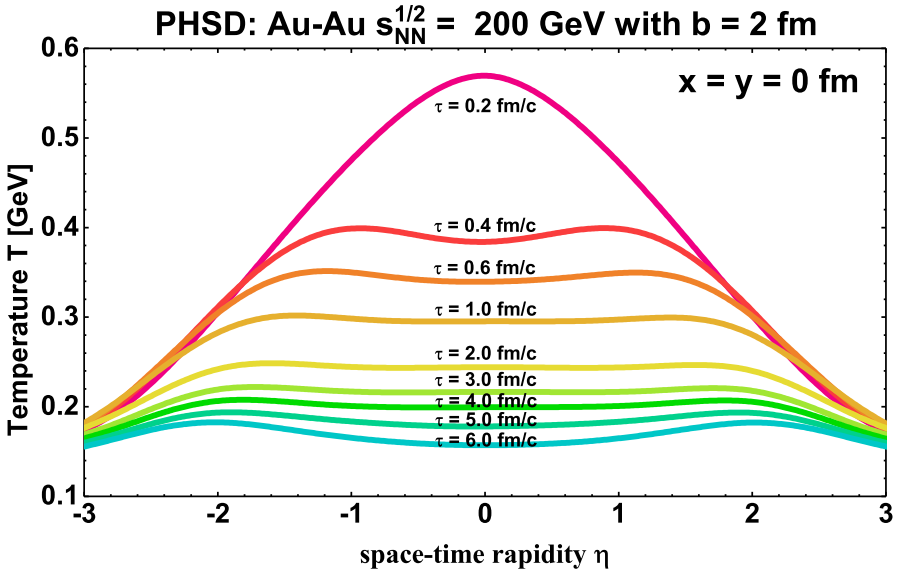

Figure D.3 – Temperature profile as a function of the space-time rapidity η for different proper times τ for a central Au+Au collision at $\sqrt{s_{NN}} = 200$ GeV.

times and space-time rapidities are simply discarded. Using this method, the local energy density e, the pressure components and the cell flow velocity $\vec{\beta}$ are extracted for each space-time cell of the Milne grid. One can see in Fig. D.3 that the temperature profile from PHSD expressed in the Milne coordinates (τ, η) is almost boost-invariant (as expected in a hydrodynamic picture), and that the temperature decreases with τ approximately uniformly as a function of η.

D.3 Numerical procedure

The evaluation of the determinant in Eq. (D.28) gives a 4^{th} order polynomial equation in λ to solve. The four roots x_1, x_2, x_3, x_4 for a general quartic equation $ax^4 + bx^3 + cx^2 + dx + e = 0$ (with $a \neq 0$) are :

$$x_{1,2} = -\frac{b}{4a} - S \pm \frac{1}{2}\sqrt{-4S^2 - 2p + \frac{q}{S}}, \tag{D.30}$$

$$x_{3,4} = -\frac{b}{4a} + S \pm \frac{1}{2}\sqrt{-4S^2 - 2p - \frac{q}{S}} \tag{D.31}$$

with

$$p = \frac{8ac - 3b^2}{8a^2}, \tag{D.32}$$

$$q = \frac{b^3 - 4abc + 8a^2 d}{8a^3}, \tag{D.33}$$

and

$$S = \frac{1}{2}\sqrt{-\frac{2}{3}p + \frac{1}{3a}\left(Q + \frac{\Delta_0}{Q}\right)}, \tag{D.34}$$

$$Q = \sqrt[3]{\frac{\Delta_1 + \sqrt{\Delta_1^2 - 4\Delta_0^3}}{2}} \tag{D.35}$$

with

$$\Delta_0 = c^2 - 3bd + 12ae, \tag{D.36}$$

$$\Delta_1 = 2c^3 - 9bcd + 27b^2 e + 27ad^2 - 72ace. \tag{D.37}$$

Newton–Raphson method

* * *

We want to solve a system of two equations containing two unknowns (x, y):

$$\begin{cases} F = f(x,y) \\ G = g(x,y) \end{cases} \tag{E.1}$$

for given functions f and g.

As a first step, we initialize our calculation by some estimate (x_0, y_0) and we develop at 1st order:

$$\begin{cases} F = f(x_0+\alpha, y_0+\beta) = f(x_0,y_0) + \alpha\dfrac{\partial f(x_0,y_0)}{\partial x} + \beta\dfrac{\partial f(x_0,y_0)}{\partial y} \\ \\ G = g(x_0+\alpha, y_0+\beta) = g(x_0,y_0) + \alpha\dfrac{\partial g(x_0,y_0)}{\partial x} + \beta\dfrac{\partial g(x_0,y_0)}{\partial y}, \end{cases} \tag{E.2}$$

where $\alpha = x_{k+1} - x_k$ and $\beta = y_{k+1} - y_k$. We transform now the system in order to find α and β as:

$$\begin{pmatrix} F - f(x_0,y_0) \\ G - g(x_0,y_0) \end{pmatrix} = \mathbf{J}\begin{pmatrix} \alpha \\ \beta \end{pmatrix} \quad \text{with } \mathbf{J} = \begin{pmatrix} \dfrac{\partial f(x_0,y_0)}{\partial x} & \dfrac{\partial f(x_0,y_0)}{\partial y} \\ \\ \dfrac{\partial g(x_0,y_0)}{\partial x} & \dfrac{\partial g(x_0,y_0)}{\partial y} \end{pmatrix}. \tag{E.3}$$

We can solve this system by inverting the Jacobian matrix J and obtain the fol-

lowing system:

$$\begin{pmatrix}\alpha\\ \beta\end{pmatrix} = \begin{pmatrix}x_{k+1}-x_k\\ \\ y_{k+1}-y_k\end{pmatrix} = \mathbf{J}^{-1}\begin{pmatrix}F-f(x_k,y_k)\\ \\ G-g(x_k,y_k)\end{pmatrix} \quad \text{with } \mathbf{J}^{-1} = \frac{1}{\Delta}\begin{pmatrix}\dfrac{\partial g(x_k,y_k)}{\partial y} & -\dfrac{\partial f(x_k,y_k)}{\partial y}\\ \\ \dfrac{-\partial g(x_k,y_k)}{\partial x} & \dfrac{\partial f(x_k,y_k)}{\partial x}\end{pmatrix} \tag{E.4}$$

with

$$\Delta = \frac{\partial f(x_k,y_k)}{\partial x}\frac{\partial g(x_k,y_k)}{\partial y} - \frac{\partial f(x_k,y_k)}{\partial y}\frac{\partial g(x_k,y_k)}{\partial x} \tag{E.5}$$

being the determinant of the Jacobian matrix $\mathbf{J}$. By developing the matrix product we get the following system:

$$\begin{cases} x_{k+1} = x_k + \dfrac{1}{\Delta}\left(\dfrac{\partial g(x_k,y_k)}{\partial y}(F-f(x_k,y_k)) - \dfrac{\partial f(x_k,y_k)}{\partial y}(G-g(x_k,y_k))\right) \\ \\ y_{k+1} = y_k + \dfrac{1}{\Delta}\left(\dfrac{\partial f(x_k,y_k)}{\partial x}(G-g(x_k,y_k)) - \dfrac{\partial g(x_k,y_k)}{\partial x}(F-f(x_k,y_k))\right). \end{cases} \tag{E.6}$$

This procedure can be applied for the evaluation of the temperature T and baryon chemical potential μ_B in PHSD given some local energy density ϵ^{PHSD} and baryon density n_B^{PHSD} in a specific cell of the space-time grid. The system to solve is then:

$$\begin{cases} \epsilon^{\mathrm{PHSD}} = \epsilon^{\mathrm{EoS}}(T,\mu_B) \\ \\ n_B^{\mathrm{PHSD}} = n_B^{\mathrm{EoS}}(T,\mu_B). \end{cases} \tag{E.7}$$

Acknowledgements

* * *

I would like to thank here all the people that supported me during these four years and half of Ph.D. studies. First of all, I thank my supervisor Prof. Elena Bratkovskaya for the constant support, enthusiasm and guidance which allowed me to achieve this long project. Also thank you for encouraging me to present my work in conferences, I definitely learned a lot thanks to all these new experiences. Next, I want to thank Prof. Wolfgang Cassing for all the discussions and explanations, as well as for the proofreading of this dissertation and the great help in correcting the German summary (Zusammenfassung). I want also to thank my external supervisor, Prof. Joerg Aichelin, who encouraged me to work in the group of Prof. Bratkovskaya in the first place. Special thanks go to Dr. Hamza Berrehrah who helped me a lot to settle here in Frankfurt and also for sharing his experience with me regarding Physics and especially to understand all the subtleties of the DQPM. I thank also Dr. Taesoo Song from whom I learned a lot and who has always been present to help and advice me when needed. In addition, I thank all the people I enjoyed to work with in the PHSD group: Olga Soloveva, Dr. Lucia Oliva, Dr. Eduard Seifert, Dr. Alessia Palmese, PD Dr. Olena Linnyk, Dr. Andrej Ilner, Dr. Daniel Cabrera and Dr. Vadim Voronyuk. I do not forget my classmates during my Master's studies: Benjamin, Alexandre, Fanny, Kévin and especially Grégoire with whom I studied since the first year of Bachelor.

This work has been supported by the HIC for FAIR Frankfurt and the Deutsche Forschungsgemeinschaft (DFG, German Research Foundation) through the grant CRC-TR 211 'Strong-interaction matter under extreme conditions' - Project number 315477589 - TRR 211. The computational resources have been provided by the Center for Scientific Computing (CSC) of the Goethe University Frankfurt and by the Green IT Cube at GSI. I thank also the support from the HGS-HIRe for FAIR which provided travel money as well as interesting lectures.

Je remercie mes parents pour leur soutien tout au long de mes études et pour toujours avoir été à mes côtés, sans eux cette aventure n'aurait pas été possible.

Por último, quiero agradecerte Nicolle por estar siempre a mi lado en todos los desafíos, por apoyarme en todo lo que hago y especialmente por apoyarme durante esta tesis. Espero con ansias lo que el futuro nos depara.

Bibliography

* * *

[1] **P. Moreau**, O. Soloveva, L. Oliva, T. Song, W. Cassing, and E. Bratkovskaya, "Exploring the partonic phase at finite chemical potential within an extended off-shell transport approach", Phys. Rev. **C100**, 014911 (2019), arXiv:1903.10257 [nucl-th] (page XI).

[2] T. Song and **P. Moreau**, "Low-energy Bremsstrahlung photon in relativistic nucleon+nucleon collisions", Phys. Rev. **D98**, 116007 (2018), arXiv:1810.08013 [nucl-th] (page XI).

[3] Y. Xu, S. A. Bass, **P. Moreau**, T. Song, M. Nahrgang, E. Bratkovskaya, P. Gossiaux, J. Aichelin, S. Cao, V. Greco, G. Coci, and K. Werner, "Resolving discrepancies in the estimation of heavy quark transport coefficients in relativistic heavy-ion collisions", Phys. Rev. **C99**, 014902 (2019), arXiv:1809.10734 [nucl-th] (pages XI, 182).

[4] T. Song, W. Cassing, **P. Moreau**, and E. Bratkovskaya, "Discrepancy in low transverse momentum dileptons from relativistic heavy-ion collisions", Phys. Rev. **C98**, 041901 (2018), arXiv:1806.09377 [nucl-th] (page XI).

[5] T. Song, W. Cassing, **P. Moreau**, and E. Bratkovskaya, "Open charm and dileptons from relativistic heavy-ion collisions", Phys. Rev. **C97**, 064907 (2018), arXiv:1803.02698 [nucl-th] (pages XI, 183).

[6] Y. Xu, **P. Moreau**, T. Song, M. Nahrgang, S. A. Bass, and E. Bratkovskaya, "Traces of nonequilibrium dynamics in relativistic heavy-ion collisions", Phys. Rev. **C96**, 024902 (2017), arXiv:1703.09178 [nucl-th] (page XI).

[7] A. Palmese, W. Cassing, E. Seifert, T. Steinert, **P. Moreau**, and E. L. Bratkovskaya, " Chiral symmetry restoration in heavy-ion collisions at intermediate energies", Phys. Rev. **C94**, 044912 (2016), arXiv:1607.04073 [nucl-th] (pages XII, 127, 170, 177).

[8] **P. Moreau**, O. Linnyk, W. Cassing, and E. Bratkovskaya, "Examinations of the early degrees of freedom in ultrarelativistic nucleus-nucleus collisions", Phys. Rev. **C93**, 044916 (2016), arXiv:1512.02875 [nucl-th] (page XII).

[9] W. Cassing, A. Palmese, **P. Moreau**, and E. L. Bratkovskaya, "Chiral symmetry restoration versus deconfinement in heavy-ion collisions at high baryon density", Phys. Rev. **C93**, 014902 (2016), arXiv:1510.04120 [nucl-th] (pages XII, 98, 170).

[10] T. Song, E. Bratkovskaya, W. Cassing, and **P. Moreau**, "Electromagnetic probes of the quark-gluon plasma", Astronomische Nachrichten **340**, 157–162 (2019), eprint: https://onlinelibrary.wiley.com/doi/pdf/10.1002/asna.201913580 (page XII).

[11] T. Song, E. L. Bratkovskaya, W. Cassing, and **P. Moreau**, "Electromagnetic emissivity of hot and dense matter", J. Phys. Conf. Ser. **1070**, 012006 (2018) (page XII).

[12] E. L. Bratkovskaya, W. Cassing, **P. Moreau**., and A. Palmese, "Chiral Symmetry Restoration and Deconfinement in Heavy-Ion Collisions", in *Chapter of the book "Walter Greiner Memorial Volume", edited by Peter O Hess and Horst Stöcker, World Scientific, Singapore, 2018, p. 71-89 (ISBN: 978-981-3234-27-7)* (2018), pp. 71–89 (page XII).

[13] E. L. Bratkovskaya, W. Cassing, A. Palmese, and **P. Moreau**, "Chiral Symmetry Restoration in Heavy-ion Collisions at High Baryon Density", Acta Phys. Polon. Supp. **10**, 507 (2017) (page XII).

[14] **P. Moreau**, Y. Xu, T. Song, M. Nahrgang, S. Bass, and E. Bratkovskaya, "Traces of non-equilibrium dynamics in relativistic heavy-ion collisions", PoS **CPOD2017**, 042 (2018), arXiv:1711.10223 [nucl-th] (page XII).

[15] E. L. Bratkovskaya, W. Cassing, **P. Moreau**, and T. Song, "Review of the theoretical heavy-ion physics", in Proceedings, 3rd International Conference on Particle Physics and Astrophysics (ICPPA 2017): Moscow, Russia, October 2-5, 2017 (2017), arXiv:1711.01976 [nucl-th] (page XII).

[16] E. L. Bratkovskaya, A. Palmese, W. Cassing, E. Seifert, T. Steinert, and **P. Moreau**, "Chiral symmetry restoration versus deconfinement in heavy-ion collisions at high baryon density", J. Phys. Conf. Ser. **878**, 012018 (2017) (page XII).

[17] **P. Moreau**, A. Palmese, W. Cassing, E. Seifert, T. Steinert, and E. L. Bratkovskaya, "Evidence for chiral symmetry restoration in heavy-ion collisions", Nucl. Phys. **A967**, 836–839 (2017), arXiv:1704.05946 [nucl-th] (page XIII).

[18] **P. Moreau**, W. Cassing, A. Palmese, and E. L. Bratkovskaya, "(Anti-) strangeness in heavy-ion collisions", J. Phys. Conf. Ser. **742**, 012016 (2016) (page XIII).

[19] E. L. Bratkovskaya, W. Cassing, **P. Moreau**, and A. Palmese, "Observables and open problems for NICA", Eur. Phys. J. **A52**, 219 (2016) (page XIII).

[20] **P. Moreau**, W. Cassing, A. Palmese, and E. Bratkovskaya, "Hadron Production within PHSD", Acta Phys. Polon. Supp. **9**, 279 (2016), arXiv:1603.02832 [nucl-th] (page XIII).

[21] **P. Moreau**, F. Li, C.-M. Ko, W. Cassing, and E. Bratkovskaya, "Anti- strangeness production in heavy-ion collisions", J. Phys. Conf. Ser. **668**, 012072 (2016), arXiv:1509.04455 [nucl-th] (pages XIII, 68).

[22] D. I. Mendeleev, "Sootnoshenie svoistv s atomnym vesom elementov (the correlation of properties with the atomic weights of the elements", Zh. Russ. Fiz.-Khim. O-va. **1**, 60–77 (1869); D. Mendelejeff, "Ueber die Beziehungen der Eigeschaften zu den Atomgewichten der Elemente (On the relationship of the properties of the elements to their atomic weights", Z. Chem. **12**, 405–406 (1869), (page 6).

[25] J. C. Maxwell M.A., "V. Illustrations of the dynamical theory of gases.—Part I. On the motions and collisions of perfectly elastic spheres", Philosophical Magazine Series 4 **19**, 19–32 (1860), eprint: http://www.tandfonline.com/doi/pdf/10.1080/14786446008642818; "II. Illustrations of the dynamical theory of gases", ibid. **20**, 21–37 (1860), eprint: http://www.tandfonline.com/doi/pdf/10.1080/14786446008642902, (page 6).

[28] L. Boltzmann, "Weitere Studien über das Wärmegleichgewicht unter Gasmolekülen (Further studies of the warm equilibrium of gas molecules)", in *Sitzungberichte der Kaiserlichen Akademie der Wissenschaften in Wien. Mathematisch-Naturwissen Classe*, 66 (1872), pp. 275–370 (page 6).

[29] J. J. Thomson M.A. F.R.S., "XL. Cathode Rays", Philosophical Magazine Series 5 **44**, 293–316 (1897), eprint: http://dx.doi.org/10.1080/14786449708621070 (page 6).

[30] A. Einstein, "Über die von der molekularkinetischen Theorie der Wärme geforderte Bewegung von in ruhenden Flüssigkeiten suspendierten Teilchen (On the movement of small particles suspended in a stationary liquid demanded by the molecular-kinetic theory of heat)", Annalen der Physik **322**, 549–560 (1905) (page 6).

[31] J. C. Maxwell, "A dynamical theory of the electromagnetic field", Philosophical Transactions of the Royal Society of London **155**, 459–512 (1865), eprint: http://rstl.royalsocietypublishing.org/content/155/459.full.pdf+html (page 7).

[32] M. Planck, "Ueber eine Verbesserung der Wien'schen Spektralgleichung (On an improvement of wien's equation for the spectrum)", Verhandlungen der Deutschen physikalischen Gesellschaft **2**, 202 (1900); "Ueber das Gesetz der Energieverteilung im Normalspectrum (On the theory of the energy distribution law of the normal spectrum)", ibid. **2**, 237 (1900), (page 7).

[35] A. Einstein, "Über einen die Erzeugung und Verwandlung des Lichtes betreffenden heuristischen Gesichtspunkt (On a heuristic point of view about the creation and conversion of light)", Annalen der Physik **322**, 132–148 (1905) (page 7).

[36] E. Rutherford, "The scattering of alpha and beta particles by matter and the structure of the atom", Philosophical Magazine **21**, 669–688 (1911) (page 7).

[37] E. Rutheford F.R.S., "LI. Collision of α particles with light atoms I. Hydrogen", Philosophical Magazine Series 6 **37**, 537–561 (1919), eprint: http://dx.doi.org/10.1080/14786440608635916 (page 7).

[38] N. Bohr, "I. On the constitution of atoms and molecules", Philosophical Magazine Series 6 **26**, 1–25 (1913), eprint: http://dx.doi.org/10.1080/14786441308634955; "XXXVII. On the constitution of atoms and molecules", ibid. **26**, 476–502 (1913), eprint: http://dx.doi.org/10.1080/14786441308634993, (page 7).

[41] W. Heisenberg, "Über quantentheoretische Umdeutung kinematischer und mechanischer Beziehungen (Quantum theoretical re-interpretation of kinematic and mechanical relations)", Zeitschrift für Physik **33**, 879–893 (1925) (page 7).

[42] L. De Broglie, "Recherches sur la théorie des Quanta", Theses (Nov. 1924), eprint: https://tel.archives-ouvertes.fr/tel-00006807/file/tel-00006807.pdf (page 7).

[43] E. Schrödinger, "Quantisierung als Eigenwertproblem (Quantization as an eigenvalue problem)", Annalen der Physik **384**, 361–376 (1926) (page 7).

[44] C. P. Enz and K. v. Meyenn, "Über den zusammenhang des abschlusses der elektronengruppen im atom mit der komplexstruktur der spektren (On the connexion between the completion of electron groups in an atom with the complex structure of spectra)", in *Wolfgang pauli: das gewissen der physik*, edited by C. P. Enz and K. v. Meyenn (Vieweg+Teubner Verlag, Wiesbaden, 1988), pp. 181–200 (page 7).

[45] P. A. M. Dirac, "The quantum theory of the electron", Proceedings of the Royal Society of London A: Mathematical, Physical and Engineering Sciences **117**, 610–624 (1928), eprint: http://rspa.royalsocietypublishing.org/content/117/778/610.full.pdf (page 8).

[46] A. Einstein, "Ist die trägheit eines körpers von seinem energieinhalt abhängig? (Does the inertia of a body depend upon its energy-content?)", Annalen der Physik **323**, 639–641 (1905) (page 8).

[47] M. Gell-Mann, "A schematic model of baryons and mesons", Physics Letters **8**, 214 –215 (1964) (page 8).

[48] G Zweig, "An SU_3 model for strong interaction symmetry and its breaking; Version 2", Version 1 is CERN preprint 8182/TH.401, Jan. 17, 1964, 80 p (1964) (page 8).

[49] D. Galbraith, *Standard Model of the Standard Model*, https://webfest.web.cern.ch/content/standard-model-standard-infographic, 2012 (page 9).

[50] E. D. Bloom, D. H. Coward, H. DeStaebler, J. Drees, G. Miller, L. W. Mo, R. E. Taylor, M. Breidenbach, J. I. Friedman, G. C. Hartmann, and H. W. Kendall, "High-energy inelastic $e-p$ scattering at 6° and 10°", Phys. Rev. Lett. **23**, 930–934 (1969); M. Breidenbach, J. I. Friedman, H. W. Kendall, E. D. Bloom, D. H. Coward, H. DeStaebler, J. Drees, L. W. Mo, and R. E. Taylor, "Observed behavior of highly inelastic electron-proton scattering", ibid. **23**, 935–939 (1969), (page 8).

[53] J. E. A. et al., "Discovery of a narrow resonance in e^+e^- annihilation", Phys. Rev. Lett. **33**, 1406–1408 (1974) (page 8).

[54] J. J. Aubert, U. Becker, P. J. Biggs, J. Burger, M. Chen, G. Everhart, P. Goldhagen, J. Leong, T. McCorriston, T. G. Rhoades, M. Rohde, S. C. C. Ting, S. L. Wu, and Y. Y.

Lee, "Experimental observation of a heavy particle j", Phys. Rev. Lett. **33**, 1404–1406 (1974) (page 8).

[55] S. W. Herb, D. C. Hom, L. M. Lederman, J. C. Sens, H. D. Snyder, J. K. Yoh, J. A. Appel, B. C. Brown, C. N. Brown, W. R. Innes, K. Ueno, T. Yamanouchi, A. S. Ito, H. Jöstlein, D. M. Kaplan, and R. D. Kephart, "Observation of a dimuon resonance at 9.5 gev in 400-gev proton-nucleus collisions", Phys. Rev. Lett. **39**, 252–255 (1977) (page 8).

[56] F. A. et al., "Observation of top quark production in $\overline{p}p$ collisions with the collider detector at fermilab", Phys. Rev. Lett. **74**, 2626–2631 (1995); S. A. et al., "Search for high mass top quark production in $p\overline{p}$ collisions at $\sqrt{s} = 1.8$ tev", ibid. **74**, 2422–2426 (1995), (page 8).

[59] C. B. et al., "Experimental search for Upsilon decay into 3 gluons", (1979) (page 8).

[60] R. B. et al., "Evidence for planar events in e+e- annihilation at high energies", Physics Letters B **86**, 243 –249 (1979) (page 8).

[61] G. A. et al. (ATLAS Collaboration), "Observation of a new particle in the search for the standard model higgs boson with the {atlas} detector at the {lhc}", Physics Letters B **716**, 1 –29 (2012); S. C. et al. (CMS collaboration), "Observation of a new boson at a mass of 125 gev with the {cms} experiment at the {lhc}", ibid. **716**, 30 –61 (2012), (page 9).

[64] B. Struminsky, "Magnetic moments of baryons in the quark model", JINR publication P-1939, Dubna (1965) (page 9).

[65] O. W. Greenberg, "Spin and Unitary Spin Independence in a Paraquark Model of Baryons and Mesons", Phys. Rev. Lett. **13**, 598–602 (1964) (page 9).

[66] M. Y. Han and Y. Nambu, "Three Triplet Model with Double SU(3) Symmetry", Phys. Rev. **139**, [,187(1965)], B1006–B1010 (1965) (page 9).

[67] M. Tanabashi et al., "Review of Particle Physics", Phys. Rev. **D98**, 030001 (2018) (pages 10, 17, 57, 58).

[68] C.-N. Yang and R. L. Mills, "Conservation of Isotopic Spin and Isotopic Gauge Invariance", Phys. Rev. **96**, [,150(1954)], 191–195 (1954) (page 10).

[69] D. J. Gross and F. Wilczek, "Ultraviolet Behavior of Nonabelian Gauge Theories", Phys. Rev. Lett. **30**, [,271(1973)], 1343–1346 (1973) (page 11).

[70] H. D. Politzer, "Reliable Perturbative Results for Strong Interactions?", Phys. Rev. Lett. **30**, [,274(1973)], 1346–1349 (1973) (page 11).

[71] K. Yagi, T. Hatsuda, and Y. Miake, "Quark-gluon plasma: From big bang to little bang", Camb. Monogr. Part. Phys. Nucl. Phys. Cosmol. **23**, 1–446 (2005) (pages 11, 23, 67).

[72] E. Noether, "Invariante variationsprobleme", ger, Nachrichten von der Gesellschaft der Wissenschaften zu Göttingen, Mathematisch-Physikalische Klasse **1918**, 235–257 (1918) (page 11).

[73] M. D. Schwartz, *Quantum Field Theory and the Standard Model* (Cambridge University Press, 2014) (pages 11, 30).

[74] K. Huang, *QUARKS, LEPTONS AND GAUGE FIELDS* (1982) (pages 12, 13, 15, 110).

[75] S. P. Klevansky, "The Nambu-Jona-Lasinio model of quantum chromodynamics", Rev. Mod. Phys. **64**, 649–708 (1992) (pages 12, 13).

[76] M. Gell-Mann, "The eightfold way: a theory of strong interaction symmetry", 10.2172/4008239 (page 13).

[77] M. Gell-Mann, "Symmetries of baryons and mesons", Phys. Rev. **125**, 1067–1084 (1962) (pages 13, 191).

[78] F. Tanedo, *Helicity, chirality, mass, and the higgs*, (2011) https://www.quantumdiaries.org/2011/06/19/helicity-chirality-mass-and-the-higgs/ (page 14).

[79] J. Goldstone, "Field theories with « superconductor » solutions", Il Nuovo Cimento (1955-1965) **19**, 154–164 (1961) (page 15).

[80] V. Koch, "Aspects of chiral symmetry", Int. J. Mod. Phys. **E6**, 203–250 (1997), arXiv:nucl-th/9706075 [nucl-th] (page 15).

[81] S. L. Adler, "Axial vector vertex in spinor electrodynamics", Phys. Rev. **177**, [,241(1969)], 2426–2438 (1969) (page 15).

[82] J. S. Bell and R. Jackiw, "A PCAC puzzle: $\pi^0 \to \gamma\gamma$ in the σ-model", Il Nuovo Cimento A (1965-1970) **60**, 47–61 (1969) (page 15).

[83] G. 't Hooft, "Symmetry Breaking Through Bell-Jackiw Anomalies", Phys. Rev. Lett. **37**, [,226(1976)], 8–11 (1976) (page 15).

[84] B. R. Holstein, "Anomalies for pedestrians", American Journal of Physics **61**, 142–147 (1993), eprint: https://doi.org/10.1119/1.17328 (page 15).

[85] E. Witten, "Current Algebra Theorems for the U(1) Goldstone Boson", Nucl. Phys. **B156**, 269–283 (1979) (page 15).

[86] G. Veneziano, "U(1) Without Instantons", Nucl. Phys. **B159**, 213–224 (1979) (page 15).

[87] K. G. Wilson, "Confinement of Quarks", Phys. Rev. **D10**, [,319(1974)], 2445–2459 (1974) (page 16).

[88] C. Ratti, "Lattice QCD and heavy ion collisions: a review of recent progress", Rept. Prog. Phys. **81**, 084301 (2018), arXiv:1804.07810 [hep-lat] (pages 16, 18).

[89] G. C. Wick, "Properties of Bethe-Salpeter Wave Functions", Phys. Rev. **96**, 1124–1134 (1954) (page 16).

[90] M. Bach, V. Lindenstruth, O. Philipsen, and C. Pinke, "Lattice QCD based on OpenCL", Comput. Phys. Commun. **184**, 2042–2052 (2013), arXiv:1209.5942 [hep-lat] (page 16).

[91] M. Wagner, S. Diehl, T. Kuske, and J. Weber, "An introduction to lattice hadron spectroscopy for students without quantum field theoretical background", in (2013), arXiv:1310.1760 [hep-lat] (page 18).

[92] A. Bazavov et al., "Chiral crossover in QCD at zero and non-zero chemical potentials", (2018), arXiv:1812.08235 [hep-lat] (page 18).

[93] F. R. Brown, F. P. Butler, H. Chen, N. H. Christ, Z.-h. Dong, W. Schaffer, L. I. Unger, and A. Vaccarino, "On the existence of a phase transition for QCD with three light quarks", Phys. Rev. Lett. **65**, 2491–2494 (1990) (page 18).

[94] A. Bazavov et al., "Equation of state in (2+1)-flavor QCD", Phys. Rev. **D90**, 094503 (2014), arXiv:1407.6387 [hep-lat] (pages 18, 73).

[95] S. Borsanyi, Z. Fodor, C. Hoelbling, S. D. Katz, S. Krieg, and K. K. Szabo, "Full result for the QCD equation of state with 2+1 flavors", Phys. Lett. **B730**, 99–104 (2014), arXiv:1309.5258 [hep-lat] (pages 18, 132, 139, 140).

[96] S. Borsanyi, Z. Fodor, C. Hoelbling, S. D. Katz, S. Krieg, C. Ratti, and K. K. Szabo, "Is there still any T_c mystery in lattice QCD? Results with physical masses in the continuum limit III", JHEP **09**, 073 (2010), arXiv:1005.3508 [hep-lat] (page 18).

[97] C. S. Fischer, "QCD at finite temperature and chemical potential from Dyson–Schwinger equations", Prog. Part. Nucl. Phys. **105**, 1–60 (2019), arXiv:1810.12938 [hep-ph] (pages 19, 129).

[98] "The Frontiers of Nuclear Science, A Long Range Plan", (2008), arXiv:0809.3137 [nucl-ex] (page 20).

[99] H.-T. Ding, F. Karsch, and S. Mukherjee, "Thermodynamics of strong-interaction matter from Lattice QCD", Int. J. Mod. Phys. **E24**, 1530007 (2015), arXiv:1504.05274 [hep-lat] (page 20).

[100] C. Schmidt, *Fluctuations of conserved charges in the quark gluon plasma*, (2014) http://www.gauss-centre.eu/gauss-centre/EN/Projects/ElementaryParticlePhysics/2014/schmidt_QGP.html?nn=1361054 (page 20).

[101] A. Bazavov et al., "The QCD Equation of State to $\mathcal{O}(\mu_B^6)$ from Lattice QCD", Phys. Rev. **D95**, 054504 (2017), arXiv:1701.04325 [hep-lat] (pages 20, 129, 132).

[102] F. Tanedo, *Evolution of the early universe*, (2018) https://phys.libretexts.org/Bookshelves/University_Physics/Book%3A_University_Physics_(OpenStax)/Map%3A_University_Physics_III_-_Optics_and_Modern_Physics_(OpenStax)/11%3A_Particle_Physics_and_Cosmology/11.7%3A_Evolution_of_the_Early_Universe (page 21).

[103] L. Van Hove, "Multiplicity Dependence of p(T) Spectrum as a Possible Signal for a Phase Transition in Hadronic Collisions", Phys. Lett. **B118**, [,334(1982)], 138 (1982) (page 22).

[104] D. Teaney, J. Lauret, and E. V. Shuryak, "Flow at the SPS and RHIC as a quark gluon plasma signature", Phys. Rev. Lett. **86**, 4783–4786 (2001), arXiv:nucl-th/0011058 [nucl-th] (pages 22, 95).

[105] J. Rafelski and B. Muller, "Strangeness Production in the Quark - Gluon Plasma", Phys. Rev. Lett. **48**, [Erratum: Phys. Rev. Lett.56,2334(1986)], 1066 (1982) (pages 22, 107).

[106] C. Blume and C. Markert, "Strange hadron production in heavy ion collisions from SPS to RHIC", Prog. Part. Nucl. Phys. **66**, 834–879 (2011), arXiv:1105.2798 [nucl-ex] (pages 22, 107).

[107] T. Matsui and H. Satz, "J/ψ Suppression by Quark-Gluon Plasma Formation", Phys. Lett. **B178**, 416–422 (1986) (page 22).

[108] U. W. Heinz, "The Strongly coupled quark-gluon plasma created at RHIC", J. Phys. **A42**, 214003 (2009), arXiv:0810.5529 [nucl-th] (page 23).

[109] A. Adare et al., "Energy Loss and Flow of Heavy Quarks in Au+Au Collisions at s(NN)**(1/2) = 200-GeV", Phys. Rev. Lett. **98**, 172301 (2007), arXiv:nucl-ex/0611018 [nucl-ex] (page 23).

[110] M. M. Aggarwal et al., "An Experimental Exploration of the QCD Phase Diagram: The Search for the Critical Point and the Onset of De-confinement", (2010), arXiv:1007.2613 [nucl-ex] (page 24).

[111] M. Gazdzicki, Z Fodor, and G Vesztergombi, *Study of Hadron Production in Hadron-Nucleus and Nucleus-Nucleus Collisions at the CERN SPS*, tech. rep. CERN-SPSC-2006-034. SPSC-P-330, revised version submitted on 2006-11-06 12:38:20 (CERN, Geneva, 2006) (page 24).

[112] A. N. Sissakian, V. D. Kekelidze, and A. S. Sorin, "The nuclotron-based ion collider fAcility at the Joint Institute for Nuclear Research", Nucl. Phys. **A827**, [,1083(2009)], 630C–637C (2009) (page 24).

[113] P. Spiller and G. Franchetti, "The FAIR accelerator project at GSI", Nucl. Instrum. Meth. **A561**, 305–309 (2006) (page 24).

[114] M. Kotulla et al., "Strong interaction studies with antiprotons. Letter of intent for PANDA (Antiproton Annihilations at Darmstadt)", (2004) (page 24).

[115] B. Friman, C. Hohne, J. Knoll, S. Leupold, J. Randrup, R. Rapp, and P. Senger, "The CBM physics book: Compressed baryonic matter in laboratory experiments", Lect. Notes Phys. **814**, pp.1–980 (2011) (page 24).

[116] P. Braun-Munzinger, K. Redlich, and J. Stachel, "Particle production in heavy ion collisions", 491–599 (2003), arXiv:nucl-th/0304013 [nucl-th] (page 24).

[117] L. Adamczyk et al., "Bulk Properties of the Medium Produced in Relativistic Heavy-Ion Collisions from the Beam Energy Scan Program", Phys. Rev. **C96**, 044904 (2017), arXiv:1701.07065 [nucl-ex] (pages 25, 67, 133, 169).

[118] L. P. Kadanoff and G. Baym, *Quantum Statistical mechanics* (W. A. Benjamin, Inc., New York, 1962) (pages 29, 33, 42–44, 68).

[119] S. Juchem, "Nonequilibrium Quantum-Field Dynamics and Off-Shell Transport", PhD thesis (Giessen U., 2003) (page 29).

[120] W. Cassing, "From Kadanoff-Baym dynamics to off-shell parton transport", Eur. Phys. J. ST **168**, 3–87 (2009), arXiv:0808.0715 [nucl-th] (pages 29, 33, 42, 44, 45, 52, 68, 69, 96, 129, 170, 194).

[121] T. Kita, "Introduction to Nonequilibrium Statistical Mechanics with Quantum Field", Prog. Theor. Phys. **123**, 581–658 (2010), arXiv:1005.0393 [cond-mat.stat-mech] (page 30).

[122] F. J. Dyson, "The S matrix in quantum electrodynamics", Phys. Rev. **75**, 1736–1755 (1949) (page 31).

[123] G. C. Wick, "The Evaluation of the Collision Matrix", Phys. Rev. **80**, [,592(1950)], 268–272 (1950) (page 33).

[124] S. Mrowczynski and P. Danielewicz, "Green Function Approach to Transport Theory of Scalar Fields", Nucl. Phys. **B342**, 345–380 (1990) (pages 33, 36, 37).

[125] Yu. B. Ivanov, J. Knoll, and D. N. Voskresensky, "Selfconsistent approximations to nonequilibrium many body theory", Nucl. Phys. **A657**, 413–445 (1999), arXiv:hep-ph/9807351 [hep-ph] (pages 33, 36, 37).

[126] W. Cassing and S. Juchem, "Semiclassical transport of particles with dynamical spectral functions", Nucl. Phys. **A665**, 377–400 (2000), arXiv:nucl-th/9903070 [nucl-th] (pages 33, 43, 44, 51).

[127] R. Kubo, "Statistical mechanical theory of irreversible processes. 1. General theory and simple applications in magnetic and conduction problems", J. Phys. Soc. Jap. **12**, 570–586 (1957) (pages 35, 154).

[128] P. C. Martin and J. S. Schwinger, "Theory of many particle systems. 1.", Phys. Rev. **115**, [,427(1959)], 1342–1373 (1959) (page 35).

[129] O. Klein, "Quantentheorie und fünfdimensionale relativitätstheorie", Zeitschrift für Physik **37**, 895–906 (1926) (page 36).

[130] W. Gordon, "Der comptoneffekt nach der schrödingerschen theorie", Zeitschrift für Physik **40**, 117–133 (1926) (page 36).

[131] J. D. Bjorken and S. D. Drell, "Relativistic quantum fields", (1965) (page 36).

[132] C. Itzykson and J. B. Zuber, *Quantum Field Theory*, International Series In Pure and Applied Physics (McGraw-Hill, New York, 1980) (page 36).

[133] M. E. Peskin and D. V. Schroeder, *An Introduction to quantum field theory* (Addison-Wesley, Reading, USA, 1995) (pages 36, 110).

[134] J. M. Luttinger and J. C. Ward, "Ground state energy of a many fermion system. 2.", Phys. Rev. **118**, 1417–1427 (1960) (page 37).

[135] G. Baym, "Selfconsistent approximation in many body systems", Phys. Rev. **127**, 1391–1401 (1962) (page 37).

[136] O. Linnyk, E. L. Bratkovskaya, and W. Cassing, "Effective QCD and transport description of dilepton and photon production in heavy-ion collisions and elementary processes", Prog. Part. Nucl. Phys. **87**, 50–115 (2016), arXiv:1512.08126 [nucl-th] (pages 38, 98, 102, 133, 134, 138, 170, 177).

[137] R. D. Mattuck, *A Guide to Feynman Diagrams in the Many Body Problem (Second Edition)* (1976) (page 38).

[138] D. C. Langreth, "Linear and nonlinear response theory with applications", in *Linear and nonlinear electron transport in solids*, edited by J. T. Devreese and V. E. van Doren (Springer US, Boston, MA, 1976), pp. 3–32 (page 38).

[139] "Contour-ordered green functions", in *Quantum kinetics in transport and optics of semiconductors* (Springer Berlin Heidelberg, Berlin, Heidelberg, 2008), pp. 63–73 (page 38).

[140] K. Balzer and M. Bonitz, *Nonequilibrium green's functions approach to inhomogeneous systems*, Vol. 867 (Jan. 2013) (page 38).

[141] E. P. Wigner, "On the quantum correction for thermodynamic equilibrium", Phys. Rev. **40**, 749–760 (1932) (page 40).

[142] J.-P. Blaizot and E. Iancu, "The Quark gluon plasma: Collective dynamics and hard thermal loops", Phys. Rept. **359**, 355–528 (2002), arXiv:hep-ph/0101103 [hep-ph] (pages 42, 47, 48).

[143] C. Greiner and S. Leupold, "Stochastic interpretation of Kadanoff-Baym equations and their relation to Langevin processes", Annals Phys. **270**, 328–390 (1998), arXiv:hep-ph/9802312 [hep-ph] (page 43).

[144] W. Botermans and R. Malfliet, "Quantum transport theory of nuclear matter", Phys. Rept. **198**, 115–194 (1990) (pages 43–45, 52).

[145] W. Cassing and S. Juchem, "Semiclassical transport of hadrons with dynamical spectral functions in A + A collisions at SIS / AGS energies", Nucl. Phys. **A672**, 417–445 (2000), arXiv:nucl-th/9910052 [nucl-th] (pages 43, 44, 48, 51, 52).

[146] S. Leupold, "Towards a test particle description of transport processes for states with continuous mass spectra", Nucl. Phys. **A672**, 475–500 (2000), arXiv:nucl-th/9909080 [nucl-th] (pages 43, 44, 53).

[147] Yu. B. Ivanov, J. Knoll, and D. N. Voskresensky, "Resonance transport and kinetic entropy", Nucl. Phys. **A672**, 313–356 (2000), arXiv:nucl-th/9905028 [nucl-th] (pages 43, 44).

[148] Yu. B. Ivanov, J. Knoll, and D. N. Voskresensky, "Selfconsistent approach to off-shell transport", Phys. Atom. Nucl. **66**, 1902–1920 (2003), arXiv:nucl-th/0303006 [nucl-th] (pages 43, 44).

[149] J.-P. Blaizot and E. Iancu, "A Boltzmann equation for the QCD plasma", Nucl. Phys. **B557**, 183–236 (1999), arXiv:hep-ph/9903389 [hep-ph] (pages 46, 48, 155).

[150] P. Danielewicz, "Quantum Theory of Nonequilibrium Processes. 1.", Annals Phys. **152**, 239–304 (1984) (page 47).

[151] P. Danielewicz and M. Gyulassy, "Dissipative Phenomena in Quark Gluon Plasmas", Phys. Rev. **D31**, 53–62 (1985) (page 47).

[152] A. Hosoya and K. Kajantie, "Transport Coefficients of QCD Matter", Nucl. Phys. **B250**, 666–688 (1985) (page 47).

[153] H. Heiselberg, G. Baym, C. J. Pethick, and J. Popp, "Transport coefficients of relativistic plasmas", Nucl. Phys. **A544**, 569C–572C (1992) (page 47).

[154] H. A. Weldon, "Simple Rules for Discontinuities in Finite Temperature Field Theory", Phys. Rev. **D28**, 2007 (1983) (pages 48, 131).

[155] V. V. Lebedev and A. V. Smilga, "Spectrum of Quark - Gluon Plasma", Annals Phys. **202**, 229–270 (1990) (pages 48, 131).

[156] E. Braaten and R. D. Pisarski, "Calculation of the gluon damping rate in hot QCD", Phys. Rev. **D42**, 2156–2160 (1990) (pages 48, 131).

[157] E. Braaten and R. D. Pisarski, "Calculation of the quark damping rate in hot QCD", Phys. Rev. **D46**, 1829–1834 (1992) (pages 48, 131).

[158] R. D. Pisarski, "Damping rates for moving particles in hot QCD", Phys. Rev. **D47**, 5589–5600 (1993) (pages 48, 131, 135).

[159] S. Jeon, "Hydrodynamic transport coefficients in relativistic scalar field theory", Phys. Rev. **D52**, 3591–3642 (1995), arXiv:hep-ph/9409250 [hep-ph] (pages 48, 131).

[160] E.-k. Wang and U. W. Heinz, "The plasmon in hot phi**4 theory", Phys. Rev. **D53**, 899–910 (1996), arXiv:hep-ph/9509333 [hep-ph] (pages 48, 49, 131).

[161] U. W. Heinz, K. Kajantie, and T. Toimela, "Gauge Covariant Linear Response Analysis of QCD Plasma Oscillations", Annals Phys. **176**, 218 (1987) (page 48).

[162] M. H. Thoma and M. Gyulassy, "Quark Damping and Energy Loss in the High Temperature QCD", Nucl. Phys. **B351**, 491–506 (1991) (page 48).

[163] J.-P. Blaizot and E. Iancu, "Lifetimes of quasiparticles and collective excitations in hot QED plasmas", Phys. Rev. **D55**, 973–996 (1997), arXiv:hep-ph/9607303 [hep-ph] (page 48).

[164] L. Rauber and W. Cassing, "Microcausality in strongly interacting fields", Phys. Rev. **D89**, 065008 (2014), arXiv:1401.5381 [nucl-th] (pages 49, 138).

[165] S. Jeon, "Computing spectral densities in finite temperature field theory", Phys. Rev. **D47**, 4586–4607 (1993), arXiv:hep-ph/9210227 [hep-ph] (page 49).

[166] C.-Y. Wong, "Dynamics of nuclear fluid. VIII. Time-dependent Hartree-Fock approximation from a classical point of view", Phys. Rev. **C25**, 1460–1475 (1982) (page 51).

[167] S. Juchem, "Nonequilibrium Quantum-Field Dynamics and Off-Shell Transport", PhD thesis (Giessen U., 2003) (pages 51, 52).

[168] W. Cassing and S. Juchem, "Semiclassical transport of particles with dynamical spectral functions", Nuclear Physics A **665**, 377 –400 (2000) (page 52).

[169] O. Buss, T. Gaitanos, K. Gallmeister, H. van Hees, M. Kaskulov, O. Lalakulich, A. B. Larionov, T. Leitner, J. Weil, and U. Mosel, "Transport-theoretical Description of Nuclear Reactions", Phys. Rept. **512**, 1–124 (2012), arXiv:1106.1344 [hep-ph] (page 53).

[170] R. D. Woods and D. S. Saxon, "Diffuse Surface Optical Model for Nucleon-Nuclei Scattering", Phys. Rev. **95**, 577–578 (1954) (page 56).

[171] L. H. Thomas, "The calculation of atomic fields", Mathematical Proceedings of the Cambridge Philosophical Society **23**, 542–548 (1927) (page 56).

[172] E. Fermi, "Un metodo statistico per la determinazione di alcune priorieta dell'atome", Rend. Accad. Naz. Lincei **6**, 32 (1927) (page 56).

[173] T. Kodama, S. B. Duarte, K. C. Chung, R. Donangelo, and R. A.M. S. Nazareth, "Causality and relativistic effects in intranuclear cascade calculations", Phys. Rev. **C29**, 2146–2152 (1984) (pages 59, 219).

[174] B. Nilsson-Almqvist and E. Stenlund, "Interactions Between Hadrons and Nuclei: The Lund Monte Carlo, Fritiof Version 1.6", Comput. Phys. Commun. **43**, 387 (1987) (page 59).

[175] B. Andersson, G. Gustafson, and H. Pi, "The FRITIOF model for very high-energy hadronic collisions", Z. Phys. **C57**, 485–494 (1993) (page 59).

[176] T. Sjostrand, S. Mrenna, and P. Z. Skands, "PYTHIA 6.4 Physics and Manual", JHEP **05**, 026 (2006), arXiv:hep-ph/0603175 [hep-ph] (page 59).

[177] T. Sjostrand and M. Bengtsson, "The Lund Monte Carlo for Jet Fragmentation and e+ e- Physics. Jetset Version 6.3: An Update", Comput. Phys. Commun. **43**, 367 (1987) (page 59).

[178] M. Cardoso, N. Cardoso, and P. Bicudo, "Lattice QCD computation of the colour fields for the static hybrid quark-gluon-antiquark system, and microscopic study of the Casimir scaling", Phys. Rev. **D81**, 034504 (2010), arXiv:0912.3181 [hep-lat] (pages 59, 60).

[179] G. S. Bali and K. Schilling, "Static quark - anti-quark potential: Scaling behavior and finite size effects in SU(3) lattice gauge theory", Phys. Rev. **D46**, 2636–2646 (1992) (page 60).

[180] C. E. Detar, O. Kaczmarek, F. Karsch, and E. Laermann, "String breaking in lattice quantum chromodynamics", Phys. Rev. **D59**, 031501 (1999), arXiv:hep-lat/9808028 [hep-lat] (page 60).

[181] T. Sjöstrand, "The Lund Model and some extensions", Workshop on Collective effects in small collisions systems, 2017 (page 61).

[182] J. Geiss, W. Cassing, and C. Greiner, "Strangeness production in the hsd transport approach from sis to SPS energies", Nucl. Phys. **A644**, 107–138 (1998), arXiv:nucl-th/9805012 [nucl-th] (pages 60, 62, 107).

[183] B. Andersson, G. Gustafson, G. Ingelman, and T. Sjostrand, "Parton Fragmentation and String Dynamics", Phys. Rept. **97**, 31–145 (1983) (page 61).

[184] S. Ferreres-Solé and T. Sjöstrand, "The space–time structure of hadronization in the Lund model", Eur. Phys. J. **C78**, 983 (2018), arXiv:1808.04619 [hep-ph] (page 61).

[185] J. S. Schwinger, "On gauge invariance and vacuum polarization", Phys. Rev. **82**, [,116(1951)], 664–679 (1951) (pages 61, 114).

[186] W. Ehehalt and W. Cassing, "Relativistic transport approach for nucleus nucleus collisions from SIS to SPS energies", Nucl. Phys. **A602**, 449–486 (1996) (page 62).

[187] W. Cassing and E. L. Bratkovskaya, "Hadronic and electromagnetic probes of hot and dense nuclear matter", Phys. Rept. **308**, 65–233 (1999) (pages 62, 68, 95, 170).

[188] W. Cassing, "Anti-baryon production in hot and dense nuclear matter", Nucl. Phys. **A700**, 618–646 (2002), arXiv:nucl-th/0105069 [nucl-th] (page 62).

[189] E. Seifert and W. Cassing, "Baryon-antibaryon annihilation and reproduction in relativistic heavy-ion collisions", Phys. Rev. **C97**, 024913 (2018), arXiv:1710.00665 [hep-ph] (page 62).

[190] E. Seifert and W. Cassing, "Baryon-antibaryon dynamics in relativistic heavy-ion collisions", Phys. Rev. **C97**, 044907 (2018), arXiv:1801.07557 [hep-ph] (page 62).

[191] W. Cassing, "Dynamical quasiparticles properties and effective interactions in the sQGP", Nucl. Phys. **A795**, 70–97 (2007), arXiv:0707.3033 [nucl-th] (pages 62, 64, 96, 133).

[192] V. Ozvenchuk, O. Linnyk, M. I. Gorenstein, E. L. Bratkovskaya, and W. Cassing, "Dynamical equilibration of strongly interacting "infinite" parton matter within the parton-hadron-string dynamics transport approach", Phys. Rev. **C87**, 024901 (2013), arXiv:1203.4734 [nucl-th] (pages 63, 100, 105, 108, 170).

[193] P. K. Sahu, A. Hombach, W. Cassing, and U. Mosel, "Baryon flow at SIS energies and beyond", Nucl. Phys. **A640**, 493–504 (1998), arXiv:nucl-th/9801043 [nucl-th] (page 66).

[194] P. K. Sahu, W. Cassing, U. Mosel, and A. Ohnishi, "Baryon flow from SIS to AGS energies", Nucl. Phys. **A672**, 376–386 (2000), arXiv:nucl-th/9907002 [nucl-th] (page 66).

[195] P. Danielewicz, R. Lacey, and W. G. Lynch, "Determination of the equation of state of dense matter", Science **298**, 1592–1596 (2002), arXiv:nucl-th/0208016 [nucl-th] (page 66).

[196] Yu. B. Ivanov and D. Blaschke, "Baryon stopping in heavy-ion collisions at E_{lab} = 2A-200A GeV", Eur. Phys. J. **A52**, 237 (2016) (page 66).

[197] G. S. Denicol, C. Gale, S. Jeon, A. Monnai, B. Schenke, and C. Shen, "Net baryon diffusion in fluid dynamic simulations of relativistic heavy-ion collisions", Phys. Rev. **C98**, 034916 (2018), arXiv:1804.10557 [nucl-th] (pages 66, 130, 164).

[198] I. G. Bearden et al., "Nuclear stopping in Au + Au collisions at s(NN)**(1/2) = 200-GeV", Phys. Rev. Lett. **93**, 102301 (2004), arXiv:nucl-ex/0312023 [nucl-ex] (page 66).

[199] I. C. Arsene et al., "Nuclear stopping and rapidity loss in Au+Au collisions at s(NN)**(1/2) = 62.4-GeV", Phys. Lett. **B677**, 267–271 (2009), arXiv:0901.0872 [nucl-ex] (page 66).

[200] L. D. McLerran and R. Venugopalan, "Gluon distribution functions for very large nuclei at small transverse momentum", Phys. Rev. **D49**, 3352–3355 (1994), arXiv:hep-ph/9311205 [hep-ph] (page 67).

[201] L. D. McLerran and R. Venugopalan, "Computing quark and gluon distribution functions for very large nuclei", Phys. Rev. **D49**, 2233–2241 (1994), arXiv:hep-ph/9309289 [hep-ph] (pages 67, 96).

[202] E. Iancu, A. Leonidov, and L. D. McLerran, "Nonlinear gluon evolution in the color glass condensate. 1.", Nucl. Phys. **A692**, 583–645 (2001), arXiv:hep-ph/0011241 [hep-ph] (page 67).

[203] Y. Mehtar-Tani and G. Wolschin, "Baryon Stopping as a new Probe of Geometric Scaling", Phys. Rev. Lett. **102**, 182301 (2009), arXiv:0811.1721 [hep-ph] (page 67).

[204] Y. Mehtar-Tani and G. Wolschin, "Baryon stopping and saturation physics in relativistic collisions", Phys. Rev. **C80**, 054905 (2009), arXiv:0907.5444 [hep-ph] (page 67).

[205] F. O. Duraes, A. V. Giannini, V. P. Goncalves, and F. S. Navarra, "Baryon stopping in the Color Glass Condensate formalism: A phenomenological study", Phys. Rev. **C89**, 035205 (2014), arXiv:1401.7888 [hep-ph] (page 67).

[206] L. D. McLerran, S. Schlichting, and S. Sen, "Spacetime picture of baryon stopping in the color-glass condensate", Phys. Rev. **D99**, 074009 (2019), arXiv:1811.04089 [hep-ph] (page 67).

[207] J. L. Klay et al., "Charged pion production in 2 to 8 A-GeV central au+au collisions", Phys. Rev. **C68**, 054905 (2003), arXiv:nucl-ex/0306033 [nucl-ex] (pages 67, 122).

[208] J. L. Klay et al., "Longitudinal flow from 2-A-GeV to 8-A-GeV Au+Au collisions at the Brookhaven AGS", Phys. Rev. Lett. **88**, 102301 (2002), arXiv:nucl-ex/0111006 [nucl-ex] (page 67).

[209] L. Ahle et al., "Excitation function of K+ and pi+ production in Au + Au reactions at 2/A-GeV to 10/A-GeV", Phys. Lett. **B476**, 1–8 (2000), arXiv:nucl-ex/9910008 [nucl-ex] (pages 67, 172, 174).

[210] L Ahle et al., "An Excitation function of K- and K+ production in Au + Au reactions at the AGS", Phys. Lett. **B490**, 53–60 (2000), arXiv:nucl-ex/0008010 [nucl-ex] (pages 67, 172, 174).

[211] B. B. Back et al., "Anti-lambda production in Au+Au collisions at 11.7-AGeV/c", Phys. Rev. Lett. **87**, 242301 (2001), arXiv:nucl-ex/0101008 [nucl-ex] (page 67).

[212] S. Albergo et al., "Lambda spectra in 11.6-A-GeV/c Au Au collisions", Phys. Rev. Lett. **88**, 062301 (2002) (pages 67, 120, 123, 171).

[213] C. Pinkenburg et al., "Production and collective behavior of strange particles in Au + Au collisions at 2-AGeV - 8-AGeV", Nucl. Phys. **A698**, 495–498 (2002), arXiv:nucl-ex/0104025 [nucl-ex] (page 67).

[214] C. Alt et al., "Pion and kaon production in central Pb + Pb collisions at 20-A and 30-A-GeV: Evidence for the onset of deconfinement", Phys. Rev. **C77**, 024903 (2008), arXiv:0710.0118 [nucl-ex] (pages 67, 120, 172, 174).

[215] S. V. Afanasiev et al., "Energy dependence of pion and kaon production in central Pb + Pb collisions", Phys. Rev. **C66**, 054902 (2002), arXiv:nucl-ex/0205002 [nucl-ex] (pages 67, 120, 172–174).

[216] C. Alt et al., "Energy and centrality dependence of anti-p and p production and the anti-Lambda/anti-p ratio in Pb+Pb collisions between 20/A-GeV and 158/A-Gev", Phys. Rev. **C73**, 044910 (2006) (pages 67, 120, 172, 174).

[217] C. Alt et al., "Energy dependence of Lambda and Xi production in central Pb+Pb collisions at A-20, A-30, A-40, A-80, and A-158 GeV measured at the CERN Super Proton Synchrotron", Phys. Rev. **C78**, 034918 (2008), arXiv:0804.3770 [nucl-ex] (pages 67, 120, 122, 123, 172, 174).

[218] C. Alt et al., "Omega- and anti-Omega+ production in central Pb + Pb collisions at 40-AGeV and 158-AGeV", Phys. Rev. Lett. **94**, 192301 (2005), arXiv:nucl-ex/0409004 [nucl-ex] (page 67).

[219] F. Antinori et al., "Energy dependence of hyperon production in nucleus nucleus collisions at SPS", Phys. Lett. **B595**, 68–74 (2004), arXiv:nucl-ex/0403022 [nucl-ex] (page 67).

[220] M. U. Ashraf, "Measurements of strange hadrons K^0_S, Λ and Ξ from Au+Au collisions at $\sqrt{s_{NN}} = 14.5$ GeV in STAR", J. Phys. Conf. Ser. **668**, 012095 (2016) (page 67).

[221] K. Adcox et al., "Measurement of the Lambda and anti-Lambda particles in Au+Au collisions at $\sqrt{s_{NN}}$ = 130-GeV", Phys. Rev. Lett. **89**, 092302 (2002), arXiv:nucl-ex/0204007 [nucl-ex] (page 67).

[222] B. I. Abelev et al., "Systematic Measurements of Identified Particle Spectra in pp, d^+ Au and Au+Au Collisions from STAR", Phys. Rev. **C79**, 034909 (2009), arXiv:0808.2041 [nucl-ex] (page 67).

[223] M. M. Aggarwal et al., "Strange and Multi-strange Particle Production in Au+Au Collisions at $\sqrt{s_{NN}} = 62.4$ GeV", Phys. Rev. **C83**, 024901 (2011), arXiv:1010.0142 [nucl-ex] (pages 67, 122).

[224] W. Cassing and E. L. Bratkovskaya, "Parton transport and hadronization from the dynamical quasiparticle point of view", Phys. Rev. **C78**, 034919 (2008), arXiv:0808.0022 [hep-ph] (pages 68, 72, 89).

[225] W. Cassing and E. L. Bratkovskaya, "Parton-Hadron-String Dynamics: an off-shell transport approach for relativistic energies", Nucl. Phys. **A831**, 215–242 (2009), arXiv:0907.5331 [nucl-th] (pages 68, 95, 170).

[226] E. L. Bratkovskaya, W. Cassing, V. P. Konchakovski, and O. Linnyk, "Parton-Hadron-String Dynamics at Relativistic Collider Energies", Nucl. Phys. **A856**, 162–182 (2011), arXiv:1101.5793 [nucl-th] (pages 68, 95, 170).

[227] S. Juchem, W. Cassing, and C. Greiner, "Quantum dynamics and thermalization for out-of-equilibrium phi**4 theory", Phys. Rev. **D69**, 025006 (2004), arXiv:hep-ph/0307353 [hep-ph] (page 68).

[228] S. Juchem, W. Cassing, and C. Greiner, "Nonequilibrium quantum field dynamics and off-shell transport for phi**4 theory in (2+1)-dimensions", Nucl. Phys. **A743**, 92–126 (2004), arXiv:nucl-th/0401046 [nucl-th] (page 68).

[229] W. Cassing, E. L. Bratkovskaya, and S. Juchem, "Excitation functions of hadronic observables from SIS to RHIC energies", Nucl. Phys. **A674**, 249–276 (2000), arXiv:nucl-th/0001024 [nucl-th] (page 68).

[230] H. Berrehrah, E. Bratkovskaya, T. Steinert, and W. Cassing, "A dynamical quasiparticle approach for the QGP bulk and transport properties", Int. J. Mod. Phys. **E25**, 1642003 (2016), arXiv:1605.02371 [hep-ph] (pages 68, 78, 130, 132, 133, 140, 156).

[231] R. C. Hwa and C. B. Yang, "Scaling behavior at high p(T) and the p / pi ratio", Phys. Rev. **C67**, 034902 (2003), arXiv:nucl-th/0211010 [nucl-th] (page 69).

[232] V. Greco, C. M. Ko, and P. Levai, "Parton coalescence and anti-proton / pion anomaly at RHIC", Phys. Rev. Lett. **90**, 202302 (2003), arXiv:nucl-th/0301093 [nucl-th] (page 69).

[233] R. J. Fries, B. Muller, C. Nonaka, and S. A. Bass, "Hadronization in heavy ion collisions: Recombination and fragmentation of partons", Phys. Rev. Lett. **90**, 202303 (2003), arXiv:nucl-th/0301087 [nucl-th] (page 69).

[234] Z.-W. Lin, C. M. Ko, B.-A. Li, B. Zhang, and S. Pal, "A Multi-phase transport model for relativistic heavy ion collisions", Phys. Rev. **C72**, 064901 (2005), arXiv:nucl-th/0411110 [nucl-th] (pages 69, 95).

[235] I. Arsene et al., "Quark gluon plasma and color glass condensate at RHIC? The Perspective from the BRAHMS experiment", Nucl. Phys. **A757**, 1–27 (2005), arXiv:nucl-ex/0410020 [nucl-ex] (page 71).

[236] K. Adcox et al., "Formation of dense partonic matter in relativistic nucleus-nucleus collisions at RHIC: Experimental evaluation by the PHENIX collaboration", Nucl. Phys. **A757**, 184–283 (2005), arXiv:nucl-ex/0410003 [nucl-ex] (page 71).

[237] B. B. Back et al., "The PHOBOS perspective on discoveries at RHIC", Nucl. Phys. **A757**, 28–101 (2005), arXiv:nucl-ex/0410022 [nucl-ex] (page 71).

[238] J. Adams et al., "Experimental and theoretical challenges in the search for the quark gluon plasma: The STAR Collaboration's critical assessment of the evidence from RHIC collisions", Nucl. Phys. **A757**, 102–183 (2005), arXiv:nucl-ex/0501009 [nucl-ex] (page 71).

[239] M. Gyulassy and L. McLerran, "New forms of QCD matter discovered at RHIC", Nucl. Phys. **A750**, 30–63 (2005), arXiv:nucl-th/0405013 [nucl-th] (page 71).

[240] B. Muller and J. L. Nagle, "Results from the relativistic heavy ion collider", Ann. Rev. Nucl. Part. Sci. **56**, 93–135 (2006), arXiv:nucl-th/0602029 [nucl-th] (page 71).

[241] B. Muller, J. Schukraft, and B. Wyslouch, "First Results from Pb+Pb collisions at the LHC", Ann. Rev. Nucl. Part. Sci. **62**, 361–386 (2012), arXiv:1202.3233 [hep-ex] (page 71).

[242] H. Song and U. W. Heinz, "Causal viscous hydrodynamics in 2+1 dimensions for relativistic heavy-ion collisions", Phys. Rev. **C77**, 064901 (2008), arXiv:0712.3715 [nucl-th] (pages 72, 95).

[243] C. Shen, Z. Qiu, H. Song, J. Bernhard, S. Bass, and U. Heinz, "The iEBE-VISHNU code package for relativistic heavy-ion collisions", Comput. Phys. Commun. **199**, 61–85 (2016), arXiv:1409.8164 [nucl-th] (pages 72, 73).

[244] R. Derradi de Souza, T. Koide, and T. Kodama, "Hydrodynamic Approaches in Relativistic Heavy Ion Reactions", Prog. Part. Nucl. Phys. **86**, 35–85 (2016), arXiv:1506.03863 [nucl-th] (pages 72, 79).

[245] R. Derradi de Souza, J. Takahashi, T. Kodama, and P. Sorensen, "Effects of initial state fluctuations in the final state elliptic flow measurements using the NeXSPheRIO model", Phys. Rev. **C85**, 054909 (2012), arXiv:1110.5698 [hep-ph] (page 72).

[246] H. Niemi, G. S. Denicol, H. Holopainen, and P. Huovinen, "Event-by-event distributions of azimuthal asymmetries in ultrarelativistic heavy-ion collisions", Phys. Rev. **C87**, 054901 (2013), arXiv:1212.1008 [nucl-th] (page 72).

[247] S. A. Voloshin, "Energy and system size dependence of charged particle elliptic flow and v(2) / eps scaling", J. Phys. **G34**, S883–886 (2007), arXiv:nucl-ex/0701038 [nucl-ex] (page 72).

[248] V. P. Konchakovski, W. Cassing, and V. D. Toneev, "p-Pb collisions at 5.02 TeV in the Parton-Hadron-String-Dynamics transport approach", J. Phys. **G41**, 105004 (2014), arXiv:1401.4409 [nucl-th] (pages 72, 74).

[249] J. Liu, C. Shen, and U. Heinz, "Pre-equilibrium evolution effects on heavy-ion collision observables", Phys. Rev. **C91**, [Erratum: Phys. Rev.C92,no.4,049904(2015)], 064906 (2015), arXiv:1504.02160 [nucl-th] (pages 73, 91).

[250] W. Israel and J. M. Stewart, "Transient relativistic thermodynamics and kinetic theory", Annals Phys. **118**, 341–372 (1979) (page 73).

[251] W. Israel and J. Stewart, "Thermodynamics of nonstationary and transient effects in a relativistic gas", Physics Letters A **58**, 213 –215 (1976) (page 73).

[252] G. S. Denicol, S. Jeon, and C. Gale, "Transport Coefficients of Bulk Viscous Pressure in the 14-moment approximation", Phys. Rev. **C90**, 024912 (2014), arXiv:1403.0962 [nucl-th] (page 73).

[253] J. S. Moreland and R. A. Soltz, "Hydrodynamic simulations of relativistic heavy-ion collisions with different lattice quantum chromodynamics calculations of the equation of state", Phys. Rev. **C93**, 044913 (2016), arXiv:1512.02189 [nucl-th] (page 73).

[254] B. Schenke, P. Tribedy, and R. Venugopalan, "Fluctuating Glasma initial conditions and flow in heavy ion collisions", Phys. Rev. Lett. **108**, 252301 (2012), arXiv:1202.6646 [nucl-th] (page 73).

[255] H.-J. Drescher, A. Dumitru, A. Hayashigaki, and Y. Nara, "The Eccentricity in heavy-ion collisions from color glass condensate initial conditions", Phys. Rev. **C74**, 044905 (2006), arXiv:nucl-th/0605012 [nucl-th] (page 73).

[256] M. L. Miller, K. Reygers, S. J. Sanders, and P. Steinberg, "Glauber modeling in high energy nuclear collisions", Ann. Rev. Nucl. Part. Sci. **57**, 205–243 (2007), arXiv:nucl-ex/0701025 [nucl-ex] (page 73).

[257] J. S. Moreland, J. E. Bernhard, and S. A. Bass, "Alternative ansatz to wounded nucleon and binary collision scaling in high-energy nuclear collisions", Phys. Rev. **C92**, 011901 (2015), arXiv:1412.4708 [nucl-th] (page 73).

[258] V. P. Konchakovski, W. Cassing, and V. D. Toneev, "Impact of the initial size of spatial fluctuations on the collective flow in Pb-Pb collisions at $\sqrt{s_{NN}} = 2.76$ TeV", J. Phys. **G42**, 055106 (2015), arXiv:1411.5534 [nucl-th] (page 74).

[259] V. P. Konchakovski, E. L. Bratkovskaya, W. Cassing, V. D. Toneev, S. A. Voloshin, and V. Voronyuk, "Azimuthal anisotropies for Au+Au collisions in the parton-hadron transient energy range", Phys. Rev. **C85**, 044922 (2012), arXiv:1201.3320 [nucl-th] (page 74).

[260] V. P. Konchakovski, E. L. Bratkovskaya, W. Cassing, V. D. Toneev, and V. Voronyuk, "Rise of azimuthal anisotropies as a signature of the Quark-Gluon-Plasma in relativistic heavy-ion collisions", Phys. Rev. **C85**, 011902 (2012), arXiv:1109.3039 [nucl-th] (page 74).

[261] V. P. Konchakovski, W. Cassing, Yu. B. Ivanov, and V. D. Toneev, "Examination of the directed flow puzzle in heavy-ion collisions", Phys. Rev. **C90**, 014903 (2014), arXiv:1404.2765 [nucl-th] (page 74).

[262] V. Ozvenchuk, O. Linnyk, M. I. Gorenstein, E. L. Bratkovskaya, and W. Cassing, "Shear and bulk viscosities of strongly interacting "infinite" parton-hadron matter within the parton-hadron-string dynamics transport approach", Phys. Rev. **C87**, 064903 (2013), arXiv:1212.5393 [hep-ph] (pages 77, 78, 154).

[263] J. E. Bernhard, J. S. Moreland, and S. A. Bass, "Characterization of the initial state and QGP medium from a combined Bayesian analysis of LHC data at 2.76 and 5.02 TeV", Nucl. Phys. **A967**, 293–296 (2017), arXiv:1704.04462 [nucl-th] (page 78).

[264] G. Policastro, D. T. Son, and A. O. Starinets, "The Shear viscosity of strongly coupled N=4 supersymmetric Yang-Mills plasma", Phys. Rev. Lett. **87**, 081601 (2001), arXiv:hep-th/0104066 [hep-th] (pages 78, 156).

[265] P. Kovtun, D. T. Son, and A. O. Starinets, "Viscosity in strongly interacting quantum field theories from black hole physics", Phys. Rev. Lett. **94**, 111601 (2005), arXiv:hep-th/0405231 [hep-th] (pages 78, 156).

[266] S. Mattiello and W. Cassing, "Shear viscosity of the Quark-Gluon Plasma from a virial expansion", Eur. Phys. J. **C70**, 243–249 (2010), arXiv:0911.4647 [hep-ph] (page 78).

[267] M. Bluhm, B. Kämpfer, and K. Redlich, "Bulk and shear viscosities of the gluon plasma in a quasiparticle description", Phys. Rev. **C84**, 025201 (2011), arXiv:1011.5634 [hep-ph] (pages 78, 155).

[268] C. Sasaki and K. Redlich, "Bulk viscosity in quasi particle models", Phys. Rev. **C79**, 055207 (2009), arXiv:0806.4745 [hep-ph] (pages 78, 155).

[269] Z. Qiu and U. W. Heinz, "Event-by-event shape and flow fluctuations of relativistic heavy-ion collision fireballs", Phys. Rev. **C84**, 024911 (2011), arXiv:1104.0650 [nucl-th] (page 90).

[270] M. Miller and R. Snellings, "Eccentricity fluctuations and its possible effect on elliptic flow measurements", (2003), arXiv:nucl-ex/0312008 [nucl-ex] (page 90).

[271] B. Alver et al., "System size, energy, pseudorapidity, and centrality dependence of elliptic flow", Phys. Rev. Lett. **98**, 242302 (2007), arXiv:nucl-ex/0610037 [nucl-ex] (page 90).

[272] B. Alver and G. Roland, "Collision geometry fluctuations and triangular flow in heavy-ion collisions", Phys. Rev. **C81**, [Erratum: Phys. Rev.C82,039903(2010)], 054905 (2010), arXiv:1003.0194 [nucl-th] (page 90).

[273] P. F. Kolb and U. W. Heinz, "Hydrodynamic description of ultrarelativistic heavy ion collisions", 634–714 (2003), arXiv:nucl-th/0305084 [nucl-th] (pages 91, 95).

[274] P. Huovinen, P. F. Kolb, U. W. Heinz, P. V. Ruuskanen, and S. A. Voloshin, "Radial and elliptic flow at RHIC: Further predictions", Phys. Lett. **B503**, 58–64 (2001), arXiv:hep-ph/0101136 [hep-ph] (page 95).

[275] P. F. Kolb, P. Huovinen, U. W. Heinz, and H. Heiselberg, "Elliptic flow at SPS and RHIC: From kinetic transport to hydrodynamics", Phys. Lett. **B500**, 232–240 (2001), arXiv:hep-ph/0012137 [hep-ph] (page 95).

[276] T. Hirano and K. Tsuda, "Collective flow and two pion correlations from a relativistic hydrodynamic model with early chemical freezeout", Phys. Rev. **C66**, 054905 (2002), arXiv:nucl-th/0205043 [nucl-th] (page 95).

[277] P. F. Kolb and R. Rapp, "Transverse flow and hadrochemistry in Au+Au collisions at (S(NN))**(1/2) = 200-GeV", Phys. Rev. **C67**, 044903 (2003), arXiv:hep-ph/0210222 [hep-ph] (page 95).

[278] P. Huovinen, "Hydrodynamical description of collective flow. Chapter 1.", 600–633 (2003), arXiv:nucl-th/0305064 [nucl-th] (page 95).

[279] P. Romatschke and U. Romatschke, "Viscosity Information from Relativistic Nuclear Collisions: How Perfect is the Fluid Observed at RHIC?", Phys. Rev. Lett. **99**, 172301 (2007), arXiv:0706.1522 [nucl-th] (page 95).

[280] M. Luzum and P. Romatschke, "Conformal Relativistic Viscous Hydrodynamics: Applications to RHIC results at s(NN)**(1/2) = 200-GeV", Phys. Rev. **C78**, [Erratum: Phys. Rev.C79,039903(2009)], 034915 (2008), arXiv:0804.4015 [nucl-th] (page 95).

[281] B. Schenke, S. Jeon, and C. Gale, "(3+1)D hydrodynamic simulation of relativistic heavy-ion collisions", Phys. Rev. **C82**, 014903 (2010), arXiv:1004.1408 [hep-ph] (page 95).

[282] K. Geiger and B. Muller, "Dynamics of parton cascades in highly relativistic nuclear collisions", Nucl. Phys. **B369**, 600–654 (1992) (page 95).

[283] D. Molnar and M. Gyulassy, "New solutions to covariant nonequilibrium dynamics", Phys. Rev. **C62**, 054907 (2000), arXiv:nucl-th/0005051 [nucl-th] (page 95).

[284] S. A. Bass, B. Muller, and D. K. Srivastava, "Parton rescattering and screening in Au+Au collisions at RHIC", Phys. Lett. **B551**, 277–283 (2003), arXiv:nucl-th/0207042 [nucl-th] (page 95).

[285] I. C. Arsene, L. V. Bravina, W. Cassing, Yu. B. Ivanov, A. Larionov, J. Randrup, V. N. Russkikh, V. D. Toneev, G. Zeeb, and D. Zschiesche, "Dynamical phase trajectories for relativistic nuclear collisions", Phys. Rev. **C75**, 034902 (2007), arXiv:nucl-th/0609042 [nucl-th] (page 95).

[286] S. Plumari, A. Puglisi, F. Scardina, and V. Greco, "Shear Viscosity of a strongly interacting system: Green-Kubo vs. Chapman-Enskog and Relaxation Time Approximation", Phys. Rev. **C86**, 054902 (2012), arXiv:1208.0481 [nucl-th] (page 95).

[287] S. A. Bass et al., "Microscopic models for ultrarelativistic heavy ion collisions", Prog. Part. Nucl. Phys. **41**, [Prog. Part. Nucl. Phys.41,225(1998)], 255–369 (1998), arXiv:nucl-th/9803035 [nucl-th] (page 95).

[288] Z. Xu and C. Greiner, "Thermalization of gluons in ultrarelativistic heavy ion collisions by including three-body interactions in a parton cascade", Phys. Rev. **C71**, 064901 (2005), arXiv:hep-ph/0406278 [hep-ph] (pages 95, 97).

[289] Z. Xu and C. Greiner, "Transport rates and momentum isotropization of gluon matter in ultrarelativistic heavy-ion collisions", Phys. Rev. **C76**, 024911 (2007), arXiv:hep-ph/0703233 [hep-ph] (pages 95, 97).

[290] Z. Xu and C. Greiner, "Dependence of elliptic flow on number of parton degrees of freedom", Phys. Rev. **C81**, 054901 (2010), arXiv:1001.2912 [hep-ph] (pages 95, 97).

[291] C. Nonaka and S. A. Bass, "Space-time evolution of bulk QCD matter", Phys. Rev. **C75**, 014902 (2007), arXiv:nucl-th/0607018 [nucl-th] (page 95).

[292] H. Petersen and M. Bleicher, "Eccentricity fluctuations in an integrated hybrid approach: Influence on elliptic flow", Phys. Rev. **C81**, 044906 (2010), arXiv:1002.1003 [nucl-th] (page 95).

[293] G.-Y. Qin, H. Petersen, S. A. Bass, and B. Muller, "Translation of collision geometry fluctuations into momentum anisotropies in relativistic heavy-ion collisions", Phys. Rev. **C82**, 064903 (2010), arXiv:1009.1847 [nucl-th] (page 95).

[294] H. Song, S. A. Bass, and U. Heinz, "Viscous QCD matter in a hybrid hydrodynamic+Boltzmann approach", Phys. Rev. **C83**, 024912 (2011), arXiv:1012.0555 [nucl-th] (page 95).

[295] H. Petersen, C. Coleman-Smith, S. A. Bass, and R. Wolpert, "Constraining the initial state granularity with bulk observables in Au+Au collisions at $\sqrt{s_{\rm NN}} = 200$ GeV", J. Phys. **G38**, 045102 (2011), arXiv:1012.4629 [nucl-th] (page 95).

[296] H. Petersen, V. Bhattacharya, S. A. Bass, and C. Greiner, "Longitudinal correlation of the triangular flow event plane in a hybrid approach with hadron and parton cascade initial conditions", Phys. Rev. **C84**, 054908 (2011), arXiv:1105.0340 [nucl-th] (page 95).

[297] H. Petersen, R. La Placa, and S. A. Bass, "A systematic study of the sensitivity of triangular flow to the initial state fluctuations in relativistic heavy-ion collisions", J. Phys. **G39**, 055102 (2012), arXiv:1201.1881 [nucl-th] (page 95).

[298] H. Song, S. A. Bass, U. Heinz, T. Hirano, and C. Shen, "200 A GeV Au+Au collisions serve a nearly perfect quark-gluon liquid", Phys. Rev. Lett. **106**, [Erratum: Phys. Rev. Lett.109,139904(2012)], 192301 (2011), arXiv:1011.2783 [nucl-th] (page 95).

[299] B. Schenke, P. Tribedy, and R. Venugopalan, "Event-by-event gluon multiplicity, energy density, and eccentricities in ultrarelativistic heavy-ion collisions", Phys. Rev. **C86**, 034908 (2012), arXiv:1206.6805 [hep-ph] (page 95).

[300] C. Gale, S. Jeon, B. Schenke, P. Tribedy, and R. Venugopalan, "Event-by-event anisotropic flow in heavy-ion collisions from combined Yang-Mills and viscous fluid dynamics", Phys. Rev. Lett. **110**, 012302 (2013), arXiv:1209.6330 [nucl-th] (page 95).

[301] F. Gelis, E. Iancu, J. Jalilian-Marian, and R. Venugopalan, "The Color Glass Condensate", Ann. Rev. Nucl. Part. Sci. **60**, 463–489 (2010), arXiv:1002.0333 [hep-ph] (page 95).

[302] E. Iancu and R. Venugopalan, "The Color glass condensate and high-energy scattering in QCD", in *Quark-gluon plasma 4*, edited by R. C. Hwa and X.-N. Wang (2003), pp. 249–3363, arXiv:hep-ph/0303204 [hep-ph] (page 95).

[303] H. Weigert, "Evolution at small x(bj): The Color glass condensate", Prog. Part. Nucl. Phys. **55**, 461–565 (2005), arXiv:hep-ph/0501087 [hep-ph] (page 95).

[304] J. Alam, B. Sinha, and S. Raha, "Successive equilibration in quark - gluon plasma", Phys. Rev. Lett. **73**, 1895–1898 (1994) (page 96).

[305] B. Kämpfer and O. P. Pavlenko, "Photon production in an expanding and chemically equilibrating gluon enriched plasma", Z. Phys. **C62**, 491–497 (1994) (page 96).

[306] T. S. Biro, E. van Doorn, B. Muller, M. H. Thoma, and X. N. Wang, "Parton equilibration in relativistic heavy ion collisions", Phys. Rev. **C48**, 1275–1284 (1993), arXiv:nucl-th/9303004 [nucl-th] (page 96).

[307] M. Strickland, "Thermal photons and dileptons from nonequilibrium quark - gluon plasma", Phys. Lett. **B331**, 245–250 (1994) (page 96).

[308] H. Stoecker et al., "Glueballs amass at RHIC and LHC Colliders! - The early quarkless 1st order phase transition at $T = 270$ MeV - from pure Yang-Mills glue plasma to GlueBall-Hagedorn states", J. Phys. **G43**, 015105 (2016), arXiv:1509.00160 [hep-ph] (page 96).

[309] V. Vovchenko, I. A. Karpenko, M. I. Gorenstein, L. M. Satarov, I. N. Mishustin, B. Kämpfer, and H. Stoecker, "Electromagnetic probes of a pure-glue initial state in nucleus-nucleus collisions at energies available at the CERN Large Hadron Collider", Phys. Rev. **C94**, 024906 (2016), arXiv:1604.06346 [nucl-th] (page 96).

[310] I. G. Bearden et al., "Charged meson rapidity distributions in central Au+Au collisions at s(NN)**(1/2) = 200-GeV", Phys. Rev. Lett. **94**, 162301 (2005), arXiv:nucl-ex/0403050 [nucl-ex] (pages 99, 100, 175).

[311] S. S. Adler et al., "Identified charged particle spectra and yields in Au+Au collisions at S(NN)**1/2 = 200-GeV", Phys. Rev. **C69**, 034909 (2004), arXiv:nucl-ex/0307022 [nucl-ex] (pages 99, 100, 174–176).

[312] I. Arsene et al., "Centrality dependent particle production at y=0 and y 1 in Au + Au collisions at s(NN)**(1/2) = 200-GeV", Phys. Rev. **C72**, 014908 (2005), arXiv:nucl-ex/0503010 [nucl-ex] (pages 100, 175).

[313] J. Adams et al., "Azimuthal anisotropy in Au+Au collisions at s(NN)**(1/2) = 200-GeV", Phys. Rev. **C72**, 014904 (2005), arXiv:nucl-ex/0409033 [nucl-ex] (page 101).

[314] B. B. Back et al., "Centrality and pseudorapidity dependence of elliptic flow for charged hadrons in Au+Au collisions at s(NN)**(1/2) = 200-GeV", Phys. Rev. **C72**, 051901 (2005), arXiv:nucl-ex/0407012 [nucl-ex] (page 101).

[315] V. Voronyuk, V. D. Toneev, S. A. Voloshin, and W. Cassing, "Charge-dependent directed flow in asymmetric nuclear collisions", Phys. Rev. **C90**, 064903 (2014), arXiv:1410.1402 [nucl-th] (page 101).

[316] B. Kämpfer, O. P. Pavlenko, A. Peshier, and G. Soff, "Dilepton production in a chemically equilibrating, expanding, and hadronizing quark - gluon plasma", Phys. Rev. **C52**, 2704–2713 (1995) (page 101).

[317] C. T. Traxler, H. Vija, and M. H. Thoma, "Hard photon production rate of a quark - gluon plasma at finite quark chemical potential", Phys. Lett. **B346**, 329–334 (1995), arXiv:hep-ph/9410309 [hep-ph] (page 101).

[318] O. Linnyk, W. Cassing, J. Manninen, E. L. Bratkovskaya, and C. M. Ko, "Analysis of dilepton production in Au+Au collisions at $\sqrt{s_{NN}} = 200$ GeV within the Parton-Hadron-String Dynamics (PHSD) transport approach", Phys. Rev. **C85**, 024910 (2012), arXiv:1111.2975 [nucl-th] (pages 101, 102).

[319] O. Linnyk, E. L. Bratkovskaya, V. Ozvenchuk, W. Cassing, and C. M. Ko, "Dilepton production in nucleus-nucleus collisions at top SPS energy within the Parton-Hadron-String

Dynamics (PHSD) transport approach", Phys. Rev. **C84**, 054917 (2011), arXiv:1107.3402 [nucl-th] (pages 101, 102).

[320] T. Song, W. Cassing, P. Moreau, and E. Bratkovskaya, "Open charm and dileptons from relativistic heavy-ion collisions", Phys. Rev. **C97**, 064907 (2018), arXiv:1803.02698 [nucl-th] (page 102).

[321] A. Adare et al., "Enhanced production of direct photons in Au+Au collisions at $\sqrt{s_{NN}} =$ 200 GeV and implications for the initial temperature", Phys. Rev. Lett. **104**, 132301 (2010), arXiv:0804.4168 [nucl-ex] (pages 102, 103).

[322] A. Adare et al., "Centrality dependence of low-momentum direct-photon production in Au+Au collisions at $\sqrt{s_{NN}} = 200$ GeV", Phys. Rev. **C91**, 064904 (2015), arXiv:1405.3940 [nucl-ex] (pages 102, 103).

[323] O. Linnyk, V. Konchakovski, T. Steinert, W. Cassing, and E. L. Bratkovskaya, "Hadronic and partonic sources of direct photons in relativistic heavy-ion collisions", Phys. Rev. **C92**, 054914 (2015), arXiv:1504.05699 [nucl-th] (page 102).

[324] O. Linnyk, W. Cassing, and E. L. Bratkovskaya, "Centrality dependence of the direct photon yield and elliptic flow in heavy-ion collisions at $\sqrt{s_{NN}} = 200$ GeV", Phys. Rev. **C89**, 034908 (2014), arXiv:1311.0279 [nucl-th] (page 102).

[325] O. Linnyk, V. P. Konchakovski, W. Cassing, and E. L. Bratkovskaya, "Photon elliptic flow in relativistic heavy-ion collisions: hadronic versus partonic sources", Phys. Rev. **C88**, 034904 (2013), arXiv:1304.7030 [nucl-th] (page 102).

[326] J. Zhao, "Dielectron continuum production from $\sqrt{s_{NN}}$ = 200 GeV p + p and Au + Au collisions at STAR", J. Phys. **G38**, 124134 (2011), arXiv:1106.6146 [nucl-ex] (page 104).

[327] L. Adamczyk et al., "Measurements of Dielectron Production in Au+Au Collisions at $\sqrt{s_{\mathrm{NN}}} = 200$ GeV from the STAR Experiment", Phys. Rev. **C92**, 024912 (2015), arXiv:1504.01317 [hep-ex] (page 104).

[328] L. Adamczyk et al., "Dielectron Mass Spectra from Au+Au Collisions at $\sqrt{s_{\mathrm{NN}}}$ = 200 GeV", Phys. Rev. Lett. **113**, [Addendum: Phys. Rev. Lett.113,no.4,049903(2014)], 022301 (2014), arXiv:1312.7397 [hep-ex] (page 104).

[329] A. Adare et al., "Detailed measurement of the e^+e^- pair continuum in $p+p$ and Au+Au collisions at $\sqrt{s_{NN}} = 200$ GeV and implications for direct photon production", Phys. Rev. **C81**, 034911 (2010), arXiv:0912.0244 [nucl-ex] (page 104).

[330] S. Afanasiev et al., "Enhancement of the dielectron continuum in s(NN)**(1/2) = 200-geV Au+Au collisions", (2007), arXiv:0706.3034 [nucl-ex] (page 104).

[331] A. Toia, "Measurement of low mass dielectron continuum in s(NN)**(1/2) = 200-GeV Au+Au collisions with the PHENIX experiment at RHIC", Nucl. Phys. **A774**, 743–746 (2006), arXiv:nucl-ex/0510006 [nucl-ex] (page 104).

[332] A. Toia, "Measurement of low mass dielectron continuum in (S(NN))**(1/2) = 200-GeV Au + Au collisions in the PHENIX Experiment at RHIC", Eur. Phys. J. **C49**, 243–247 (2007), arXiv:nucl-ex/0608010 [nucl-ex] (page 104).

[333] J. Seixas et al., "NA60 results on p(T) spectra and the rho spectral function in In-In collisions", J. Phys. **G34**, S1023–1028 (2007), arXiv:0705.3138 [nucl-ex] (page 105).

[334] R. Stock, "Strange quarks in matter", J. Phys. **G28**, 1517–1526 (2002) (page 107).

[335] M. Gazdzicki and M. I. Gorenstein, "On the early stage of nucleus-nucleus collisions", Acta Phys. Polon. **B30**, 2705 (1999), arXiv:hep-ph/9803462 [hep-ph] (page 107).

[336] J. Cleymans, H. Oeschler, K. Redlich, and S. Wheaton, "Transition from baryonic to mesonic freeze-out", Phys. Lett. **B615**, 50–54 (2005), arXiv:hep-ph/0411187 [hep-ph] (page 107).

[337] A. Andronic, P. Braun-Munzinger, and J. Stachel, "Hadron production in central nucleus-nucleus collisions at chemical freeze-out", Nucl. Phys. **A772**, 167–199 (2006), arXiv:nucl-th/0511071 [nucl-th] (page 107).

[338] A. Andronic, P. Braun-Munzinger, and J. Stachel, "Thermal hadron production in relativistic nuclear collisions: The Hadron mass spectrum, the horn, and the QCD phase transition", Phys. Lett. **B673**, [Erratum: Phys. Lett.B678,516(2009)], 142–145 (2009), arXiv:0812.1186 [nucl-th] (page 107).

[339] K. A. Bugaev, D. R. Oliinychenko, J. Cleymans, A. I. Ivanytskyi, I. N. Mishustin, E. G. Nikonov, and V. V. Sagun, "Chemical Freeze-out of Strange Particles and Possible Root of Strangeness Suppression", EPL **104**, 22002 (2013), arXiv:1308.3594 [hep-ph] (page 107).

[340] E. L. Bratkovskaya, M. Bleicher, M. Reiter, S. Soff, H. Stoecker, M. van Leeuwen, S. A. Bass, and W. Cassing, "Strangeness dynamics and transverse pressure in relativistic nucleus-nucleus collisions", Phys. Rev. **C69**, 054907 (2004), arXiv:nucl-th/0402026 [nucl-th] (page 107).

[341] H. Weber, E. L. Bratkovskaya, W. Cassing, and H. Stoecker, "Hadronic observables from SIS to SPS energies: Anything strange with strangeness?", Phys. Rev. **C67**, 014904 (2003), arXiv:nucl-th/0209079 [nucl-th] (page 107).

[342] E. L. Bratkovskaya, W. Cassing, C. Greiner, M. Effenberger, U. Mosel, and A. Sibirtsev, "Aspects of thermal and chemical equilibration of hadronic matter", Nucl. Phys. **A675**, 661–691 (2000), arXiv:nucl-th/0001008 [nucl-th] (page 107).

[343] H. Petersen, J. Steinheimer, G. Burau, M. Bleicher, and H. Stöcker, "A Fully Integrated Transport Approach to Heavy Ion Reactions with an Intermediate Hydrodynamic Stage", Phys. Rev. **C78**, 044901 (2008), arXiv:0806.1695 [nucl-th] (pages 107, 130).

[344] Yu. B. Ivanov, V. N. Russkikh, and V. D. Toneev, "Relativistic heavy-ion collisions within 3-fluid hydrodynamics: Hadronic scenario", Phys. Rev. **C73**, 044904 (2006), arXiv:nucl-th/0503088 [nucl-th] (pages 107, 130).

[345] Yu. B. Ivanov and D. Blaschke, "Robustness of the Baryon-Stopping Signal for the Onset of Deconfinement in Relativistic Heavy-Ion Collisions", Phys. Rev. **C92**, 024916 (2015), arXiv:1504.03992 [nucl-th] (pages 107, 130).

[346] R. Rapp, "Dilepton Spectroscopy of QCD Matter at Collider Energies", Adv. High Energy Phys. **2013**, 148253 (2013), arXiv:1304.2309 [hep-ph] (page 108).

[347] R. Rapp, "Update on Chiral Symmetry Restoration in the Context of Dilepton Data", [J. Phys. Conf. Ser.420,012017(2013)] (2012) 10.1088/1742-6596/420/1/012017, arXiv:1210.3660 [hep-ph] (page 108).

[348] U. Vogl and W. Weise, "The Nambu and Jona Lasinio model: Its implications for hadrons and nuclei", Prog. Part. Nucl. Phys. **27**, 195–272 (1991) (page 108).

[349] M. C. Birse, "Chiral symmetry in nuclei: Partial restoration and its consequences", J. Phys. **G20**, 1537–1576 (1994), arXiv:nucl-th/9406029 [nucl-th] (page 108).

[350] J. Randrup and J. Cleymans, "Maximum freeze-out baryon density in nuclear collisions", Phys. Rev. **C74**, 047901 (2006), arXiv:hep-ph/0607065 [hep-ph] (page 108).

[351] T. D. Cohen, R. J. Furnstahl, and D. K. Griegel, "Quark and gluon condensates in nuclear matter", Phys. Rev. **C45**, 1881–1893 (1992) (pages 109, 111).

[352] H. Hellmann, "Einführung in die quantenchemie", in *Hans hellmann: einführung in die quantenchemie: mit biografischen notizen von hans hellmann jr.* Edited by D. Andrae (Springer Berlin Heidelberg, Berlin, Heidelberg, 2015), pp. 19–376 (page 109).

[353] R. P. Feynman, "Forces in Molecules", Phys. Rev. **56**, 340–343 (1939) (page 109).

[354] M. Gell-Mann, R. J. Oakes, and B. Renner, "Behavior of current divergences under SU(3) x SU(3)", Phys. Rev. **175**, 2195–2199 (1968) (page 110).

[355] M. Bando, T. Kugo, and K. Yamawaki, "Nonlinear Realization and Hidden Local Symmetries", Phys. Rept. **164**, 217–314 (1988) (page 110).

[356] T. D. Cohen, R. J. Furnstahl, D. K. Griegel, and X.-m. Jin, "QCD sum rules and applications to nuclear physics", Prog. Part. Nucl. Phys. **35**, [,221(1994)], 221–298 (1995), arXiv:hep-ph/9503315 [hep-ph] (page 110).

[357] B. Friman, W. Norenberg, and V. D. Toneev, "The Quark condensate in relativistic nucleus-nucleus collisions", Eur. Phys. J. **A3**, 165–170 (1998), arXiv:nucl-th/9711065 [nucl-th] (pages 110, 111).

[358] J. M. Alarcon, J. Martin Camalich, and J. A. Oller, "The chiral representation of the πN scattering amplitude and the pion-nucleon sigma term", Phys. Rev. **D85**, 051503 (2012), arXiv:1110.3797 [hep-ph] (page 111).

[359] M. Hoferichter, J. Ruiz de Elvira, B. Kubis, and U.-G. Meißner, "High-Precision Determination of the Pion-Nucleon σ Term from Roy-Steiner Equations", Phys. Rev. Lett. **115**, 092301 (2015), arXiv:1506.04142 [hep-ph] (page 111).

[360] G. S. Bali, S. Collins, D. Richtmann, A. Schäfer, W. Söldner, and A. Sternbeck, "Direct determinations of the nucleon and pion σ terms at nearly physical quark masses", Phys. Rev. **D93**, 094504 (2016), arXiv:1603.00827 [hep-lat] (page 111).

[361] Y.-B. Yang, A. Alexandru, T. Draper, J. Liang, and K.-F. Liu, "πN and strangeness sigma terms at the physical point with chiral fermions", Phys. Rev. **D94**, 054503 (2016), arXiv:1511.09089 [hep-lat] (page 111).

[362] J. Bordes, C. A. Dominguez, P. Moodley, J. Penarrocha, and K. Schilcher, "Corrections to the $\mathbf{SU(3)} \times \mathbf{SU(3)}$ Gell-Mann-Oakes-Renner relation and chiral couplings L_8^r and H_2^r", JHEP **10**, 102 (2012), arXiv:1208.1159 [hep-ph] (page 111).

[363] M. Hoferichter, J. Ruiz de Elvira, B. Kubis, and U.-G. Meißner, "Remarks on the pion–nucleon σ-term", Phys. Lett. **B760**, 74–78 (2016), arXiv:1602.07688 [hep-lat] (page 111).

[364] J. Boguta and A. R. Bodmer, "Relativistic Calculation of Nuclear Matter and the Nuclear Surface", Nucl. Phys. **A292**, 413–428 (1977) (page 112).

[365] A. Lang, B. Blaettel, W. Cassing, V. Koch, U. Mosel, and K. Weber, "Dynamical and thermal aspects of relativistic heavy ion collisions", Z. Phys. **A340**, 287–295 (1991) (pages 112, 113).

[366] Y. Akiba et al., "Particle production in Au + Au collisions from BNL E866", Nucl. Phys. **A610**, 139C–152C (1996) (pages 120, 171).

[367] R. Lacasse et al., "Hadron yields and spectra in Au + Au collisions at the AGS", Nucl. Phys. **A610**, 153C–164C (1996), arXiv:nucl-ex/9609001 [nucl-ex] (pages 120, 171).

[368] S. Ahmad et al., "Lambda production by 11.6-A/GeV/c Au beam on Au target", Phys. Lett. **B382**, [Erratum: Phys. Lett.B386,496(1996)], 35–39 (1996) (pages 120, 171).

[369] J. Barrette et al., "Lambda production and flow in Au + Au collisions at 11.5-A-GeV/c", Phys. Rev. **C63**, 014902 (2001), arXiv:nucl-ex/0007007 [nucl-ex] (pages 120, 171).

[370] T. Anticic et al., "Lambda and anti-Lambda production in central Pb - Pb collisions at 40-A-GeV, 80-A-GeV and 158-A-GeV", Phys. Rev. Lett. **93**, 022302 (2004), arXiv:nucl-ex/0311024 [nucl-ex] (pages 120, 172–174).

[371] T. Anticic et al., "Centrality dependence of proton and antiproton spectra in Pb+Pb collisions at 40A GeV and 158A GeV measured at the CERN SPS", Phys. Rev. **C83**, 014901 (2011), arXiv:1009.1747 [nucl-ex] (pages 120, 172–174).

[372] T. Anticic et al., "System-size and centrality dependence of charged kaon and pion production in nucleus-nucleus collisions at 40A GeV and158A GeV beam energy", Phys. Rev. **C86**, 054903 (2012), arXiv:1207.0348 [nucl-ex] (pages 120, 173).

[373] B. I. Abelev et al., "Identified particle production, azimuthal anisotropy, and interferometry measurements in Au+Au collisions at s(NN)**(1/2) = 9.2- GeV", Phys. Rev. **C81**, 024911 (2010), arXiv:0909.4131 [nucl-ex] (page 122).

[374] J. Cleymans, B. Hippolyte, H. Oeschler, K. Redlich, and N. Sharma, "Thermal Model Description of Collisions of Small Nuclei", (2016), arXiv:1603.09553 [hep-ph] (page 124).

[375] P. Steinbrecher, "The QCD crossover at zero and non-zero baryon densities from Lattice QCD", Nucl. Phys. **A982**, 847–850 (2019), arXiv:1807.05607 [hep-lat] (page 129).

[376] C. S. Fischer and J. Luecker, "Propagators and phase structure of Nf=2 and Nf=2+1 QCD", Phys. Lett. **B718**, 1036–1043 (2013), arXiv:1206.5191 [hep-ph] (page 129).

[377] P. Senger, E. Bratkovskaya, A. Andronic, R. Averbeck, R. Bellwied, V. Friese, C. Fuchs, J. Knoll, J. Randrup, and J. Steinheimer, "Observables and predictions", Lect. Notes Phys. **814**, 681–847 (2011) (page 129).

[378] H. Berrehrah, W. Cassing, E. Bratkovskaya, and T. Steinert, "Quark susceptibility in a generalized dynamical quasiparticle model", Phys. Rev. **C93**, 044914 (2016), arXiv:1512.06909 [hep-ph] (pages 130, 132, 140, 156).

[379] C. Shen and B. Schenke, "Dynamical initialization and hydrodynamic modeling of relativistic heavy-ion collisions", Nucl. Phys. **A982**, 411–414 (2019), arXiv:1807.05141 [nucl-th] (page 130).

[380] M. Li and C. Shen, "Longitudinal Dynamics of High Baryon Density Matter in High Energy Heavy-Ion Collisions", Phys. Rev. **C98**, 064908 (2018), arXiv:1809.04034 [nucl-th] (page 130).

[381] I. Karpenko, "Rapidity scan in heavy ion collisions at $\sqrt{s_{\mathrm{NN}}} = 72$ GeV using a viscous hydro + cascade model", Acta Phys. Polon. **B50**, 141–148 (2019), arXiv:1805.11998 [nucl-th] (page 130).

[382] M. Li and J. I. Kapusta, "Large Baryon Densities Achievable in High Energy Heavy Ion Collisions Outside the Central Rapidity Region", Phys. Rev. **C99**, 014906 (2019), arXiv:1808.05751 [nucl-th] (pages 130, 164).

[383] S. S. Adler et al., "Elliptic flow of identified hadrons in Au+Au collisions at s(NN)**(1/2) = 200-GeV", Phys. Rev. Lett. **91**, 182301 (2003), arXiv:nucl-ex/0305013 [nucl-ex] (page 131).

[384] A. Peshier, "Hard gluon damping in hot QCD", Phys. Rev. **D70**, 034016 (2004), arXiv:hep-ph/0403225 [hep-ph] (pages 131, 194).

[385] A. Peshier, "Hard parton damping in hot QCD", J. Phys. **G31**, S371–S378 (2005), arXiv:hep-ph/0409270 [hep-ph] (pages 131, 194).

[386] M. H. Thoma, "Parton interaction rates in the quark - gluon plasma", Phys. Rev. **D49**, 451–459 (1994), arXiv:hep-ph/9308257 [hep-ph] (pages 131, 147).

[387] S. Y. F. Liu and R. Rapp, "T-matrix Approach to Quark-Gluon Plasma", Phys. Rev. **C97**, 034918 (2018), arXiv:1711.03282 [nucl-th] (page 131).

[388] B. Vanderheyden and G. Baym, "Selfconsistent approximations in relativistic plasmas: Quasiparticle analysis of the thermodynamic properties", J. Stat. Phys., [J. Statist. Phys.93,843(1998)] (1998) 10.1023/B:JOSS.0000033166.37520.ae, arXiv:hep-ph/9803300 [hep-ph] (pages 131, 137).

[389] H. Berrehrah, E. Bratkovskaya, W. Cassing, P. B. Gossiaux, J. Aichelin, and M. Bleicher, "Collisional processes of on-shell and off-shell heavy quarks in vacuum and in the Quark-Gluon-Plasma", Phys. Rev. **C89**, 054901 (2014), arXiv:1308.5148 [hep-ph] (pages 132, 143, 144, 194).

[390] H. Berrehrah, E. Bratkovskaya, W. Cassing, and R. Marty, "Transport properties of the hot and dense sQGP", J. Phys. Conf. Ser. **612**, 012050 (2015), arXiv:1412.1017 [hep-ph] (page 132).

[391] H. Berrehrah, E. Bratkovskaya, W. Cassing, P. B. Gossiaux, and J. Aichelin, "Heavy quark scattering and quenching in a QCD medium at finite temperature and chemical potential", Phys. Rev. **C91**, 054902 (2015), arXiv:1502.01700 [hep-ph] (page 132).

[392] S. Borsanyi, G. Endrodi, Z. Fodor, S. D. Katz, S. Krieg, C. Ratti, and K. K. Szabo, "QCD equation of state at nonzero chemical potential: continuum results with physical quark masses at order mu^2", JHEP **08**, 053 (2012), arXiv:1204.6710 [hep-lat] (pages 132, 139, 140).

[393] F. Karsch, "The last word(s) on CPOD 2013", PoS **CPOD2013**, 046 (2013), arXiv:1307.3978 [hep-ph] (page 132).

[394] A. Peshier, B. Kämpfer, and G. Soff, "The Equation of state of deconfined matter at finite chemical potential in a quasiparticle description", Phys. Rev. **C61**, 045203 (2000), arXiv:hep-ph/9911474 [hep-ph] (page 133).

[395] T. Steinert and W. Cassing, "Quark susceptibilities in a generalized quasiparticle model", J. Phys. Conf. Ser. **1024**, 012029 (2018) (page 133).

[396] O. Kaczmarek, F. Karsch, F. Zantow, and P. Petreczky, "Static quark anti-quark free energy and the running coupling at finite temperature", Phys. Rev. **D70**, [Erratum: Phys. Rev.D72,059903(2005)], 074505 (2004), arXiv:hep-lat/0406036 [hep-lat] (pages 133, 134).

[397] M. L. Bellac, *Thermal Field Theory*, Cambridge Monographs on Mathematical Physics (Cambridge University Press, 2011) (pages 133, 193, 194).

[398] R. D. Pisarski, "Renormalized Gauge Propagator in Hot Gauge Theories", Physica **A158**, 146–157 (1989) (page 136).

[399] J. P. Blaizot, E. Iancu, and A. Rebhan, "Approximately selfconsistent resummations for the thermodynamics of the quark gluon plasma. 1. Entropy and density", Phys. Rev. **D63**, 065003 (2001), arXiv:hep-ph/0005003 [hep-ph] (pages 137, 193, 194).

[400] E. Braaten and M. H. Thoma, "Energy loss of a heavy fermion in a hot plasma", Phys. Rev. **D44**, 1298–1310 (1991) (page 147).

[401] P. Chakraborty and J. I. Kapusta, "Quasi-Particle Theory of Shear and Bulk Viscosities of Hadronic Matter", Phys. Rev. **C83**, 014906 (2011), arXiv:1006.0257 [nucl-th] (page 147).

[402] D. Zubarev, V. Morozov, and G. Röpke, *Statistical mechanics of nonequilibrium processes: relaxation and hydrodynamic processes*, Statistical Mechanics of Nonequilibrium Processes (Akademie Verlag, 1996) (page 154).

[403] G. Aarts and J. M. Martinez Resco, "Transport coefficients, spectral functions and the lattice", JHEP **04**, 053 (2002), arXiv:hep-ph/0203177 [hep-ph] (page 154).

[404] M. Iwasaki, H. Ohnishi, and T. Fukutome, "Shear viscosity of the quark matter", J. Phys. **G35**, 035003 (2008), arXiv:hep-ph/0703271 [hep-ph] (page 154).

[405] R. Lang, N. Kaiser, and W. Weise, "Shear Viscosity of a Hot Pion Gas", Eur. Phys. J. **A48**, 109 (2012), arXiv:1205.6648 [hep-ph] (pages 154, 155).

[406] R. Lang and W. Weise, "Shear viscosity from Kubo formalism: NJL model study", Eur. Phys. J. **A50**, 63 (2014), arXiv:1311.4628 [hep-ph] (page 154).

[407] M. Haas, L. Fister, and J. M. Pawlowski, "Gluon spectral functions and transport coefficients in Yang–Mills theory", Phys. Rev. **D90**, 091501 (2014), arXiv:1308.4960 [hep-ph] (page 154).

[408] N. Christiansen, M. Haas, J. M. Pawlowski, and N. Strodthoff, "Transport Coefficients in Yang–Mills Theory and QCD", Phys. Rev. Lett. **115**, 112002 (2015), arXiv:1411.7986 [hep-ph] (page 154).

[409] C. Sasaki and K. Redlich, "Transport coefficients near chiral phase transition", Nucl. Phys. **A832**, 62–75 (2010), arXiv:0811.4708 [hep-ph] (page 155).

[410] M. Bluhm, B. Kämpfer, and K. Redlich, "Viscosities in the Gluon-Plasma within a Quasiparticle Model", Nucl. Phys. **A830**, 737C–740C (2009), arXiv:0907.3841 [hep-ph] (page 155).

[411] M. Albright and J. I. Kapusta, "Quasiparticle Theory of Transport Coefficients for Hadronic Matter at Finite Temperature and Baryon Density", Phys. Rev. **C93**, 014903 (2016), arXiv:1508.02696 [nucl-th] (pages 155, 157).

[412] N. Astrakhantsev, V. Braguta, and A. Kotov, "Temperature dependence of shear viscosity of $SU(3)$–gluodynamics within lattice simulation", JHEP **04**, 101 (2017), arXiv:1701.02266 [hep-lat] (pages 155, 156).

[413] J. E. Bernhard, J. S. Moreland, S. A. Bass, J. Liu, and U. Heinz, "Applying Bayesian parameter estimation to relativistic heavy-ion collisions: simultaneous characterization of the initial state and quark-gluon plasma medium", Phys. Rev. **C94**, 024907 (2016), arXiv:1605.03954 [nucl-th] (page 156).

[414] H. B. Meyer, "A Calculation of the bulk viscosity in SU(3) gluodynamics", Phys. Rev. Lett. **100**, 162001 (2008), arXiv:0710.3717 [hep-lat] (page 158).

[415] S. Sakai and A. Nakamura, "Lattice calculation of the QGP viscosities: Present results and next project", PoS **LATTICE2007**, [AIP Conf. Proc.893,5(2007)], 221 (2007), arXiv:0710.3625 [hep-lat] (page 158).

[416] J. Günther, R. Bellwied, S. Borsanyi, Z. Fodor, S. D. Katz, A. Pasztor, and C. Ratti, "The QCD equation of state at finite density from analytical continuation", EPJ Web Conf. **137**, 07008 (2017) (pages 158–161, 179).

[417] S. Ejiri, F. Karsch, E. Laermann, and C. Schmidt, "The Isentropic equation of state of 2-flavor QCD", Phys. Rev. **D73**, 054506 (2006), arXiv:hep-lat/0512040 [hep-lat] (page 160).

[418] C. Eckart, "The Thermodynamics of irreversible processes. 3.. Relativistic theory of the simple fluid", Phys. Rev. **58**, 919–924 (1940) (page 161).

[419] R. Ryblewski and W. Florkowski, "Highly-anisotropic hydrodynamics in 3+1 space-time dimensions", Phys. Rev. **C85**, 064901 (2012), arXiv:1204.2624 [nucl-th] (page 163).

[420] I. Newton and J. Colson, *The method of fluxions and infinite series;: with its application to the geometry of curve-lines* (London:: Printed by Henry Woodfall; and sold by John Nourse, 1736) (page 164).

[421] J. Raphson, *Analysis aequationum universalis seu ad aequationes algebraicas resolvendas methodus generalis, & expedita, ex nova infinitarum serierum methodo, deducta ac demonstrata* (1967) (page 164).

[422] J. Cleymans, H. Oeschler, K. Redlich, and S. Wheaton, "Comparison of chemical freeze-out criteria in heavy-ion collisions", Phys. Rev. **C73**, 034905 (2006), arXiv:hep-ph/0511094 [hep-ph] (pages 168, 169).

[423] M. Reiter, A. Dumitru, J. Brachmann, J. A. Maruhn, H. Stoecker, and W. Greiner, "Entropy production in collisions of relativistic heavy ions: A Signal for quark gluon plasma phase transition?", Nucl. Phys. **A643**, 99–112 (1998), arXiv:nucl-th/9806010 [nucl-th] (page 168).

[424] A. Andronic, P. Braun-Munzinger, and J. Stachel, "The Horn, the hadron mass spectrum and the QCD phase diagram: The Statistical model of hadron production in central nucleus-nucleus collisions", Nucl. Phys. **A834**, 237C–240C (2010), arXiv:0911.4931 [nucl-th] (page 169).

[425] G. Agakishiev et al., "Strangeness Enhancement in Cu+Cu and Au+Au Collisions at $\sqrt{s_{NN}} = 200$ GeV", Phys. Rev. Lett. **108**, 072301 (2012), arXiv:1107.2955 [nucl-ex] (pages 174–176).

[426] M. McNelis, D. Bazow, and U. Heinz, "(3+1)-dimensional anisotropic fluid dynamics with a lattice QCD equation of state", Phys. Rev. **C97**, 054912 (2018), arXiv:1803.01810 [nucl-th] (page 182).

[427] J. Hansen and I. McDonald, *Theory of Simple Liquids* (Elsevier Science, 2006) (page 187).

[428] N. N. Bogolyubov, J. Phys. (U.S.S.R.) **10**, 256 (1946) (page 188).

[429] H. S. G. M. Born F. R. S., "A general kinetic theory of liquids I. The molecular distribution functions", Proceedings of the Royal Society of London A: Mathematical, Physical and Engineering Sciences **188**, 10–18 (1946), eprint: http://rspa.royalsocietypublishing.org/content/188/1012/10.full.pdf (page 188).

[430] J. G. Kirkwood, "The Statistical Mechanical Theory of Transport Processes I. General Theory", The Journal of Chemical Physics **14**, 180–201 (1946), eprint: https://doi.org/10.1063/1.1724117 (page 188).

[431] J. G. Kirkwood, "The Statistical Mechanical Theory of Transport Processes II. Transport in Gases", The Journal of Chemical Physics **15**, 72–76 (1947), eprint: https://doi.org/10.1063/1.1746292 (page 188).

[432] J. Yvon, *La théorie statistique des fluides et l'équation d'état*, Actualités scientifiques et industrielles (Hermann & cie, 1935) (page 188).

[433] D. M. Jamil and P. J. T. Rhee, "Quark–Gluon Plasma, by K. Yagi, T. Hatsuda and Y. Miake", Contemporary Physics **50**, 665–666 (2009), eprint: https://doi.org/10.1080/00107510902978246 (page 189).

[434] A. A. Vlasov, "On the vibrational properties of an electron gas", J. Exp. Theor. Phys. **93**, 444–470 (1967), eprint: https://ufn.ru/ru/articles/1967/11/f/ (page 190).

[435] A. Peshier, B. Kampfer, O. P. Pavlenko, and G. Soff, "A Massive quasiparticle model of the SU(3) gluon plasma", Phys. Rev. **D54**, 2399–2402 (1996) (page 193).

[436] P. Levai and U. W. Heinz, "Massive gluons and quarks and the equation of state obtained from SU(3) lattice QCD", Phys. Rev. **C57**, 1879–1890 (1998), arXiv:hep-ph/9710463 [hep-ph] (page 193).

[437] A. Peshier, "HTL resummation of the thermodynamic potential", Phys. Rev. **D63**, 105004 (2001), arXiv:hep-ph/0011250 [hep-ph] (pages 193, 194).

[438] R. Cutler and D. W. Sivers, "Quantum Chromodynamic Gluon Contributions to Large p(T) Reactions", Phys. Rev. **D17**, 196 (1978) (pages 194, 207).

[439] H. U. Bengtsson and G. Ingelman, "The Lund Monte Carlo for High p_T Physics", Comput. Phys. Commun. **34**, 251 (1985) (pages 194, 207).

[440] R. Mertig, M. Böhm, and A. Denner, "Feyn calc - computer-algebraic calculation of feynman amplitudes", Computer Physics Communications **64**, 345 –359 (1991) (page 194).

[441] V. Shtabovenko, R. Mertig, and F. Orellana, "New developments in feyncalc 9.0", Computer Physics Communications **207**, 432 –444 (2016) (page 194).

[442] G. Wolf, G. Batko, W. Cassing, U. Mosel, K. Niita, and M. Schaefer, "Dilepton production in heavy ion collisions", Nucl. Phys. **A517**, 615–638 (1990) (page 219).

[443] S. Teis, "Transporttheoretische Beschreibung von relativistischen Schwerionenkollisionen bei SIS-Energien", PhD thesis (Giessen U., 1996) (page 219).

[444] K. Okamoto, Y. Akamatsu, and C. Nonaka, "A new relativistic hydrodynamics code for high-energy heavy-ion collisions", Eur. Phys. J. **C76**, 579 (2016), arXiv:1607.03630 [nucl-th] (page 224).

[445] S. R. De Groot, *Relativistic Kinetic Theory. Principles and Applications*, edited by W. A. Van Leeuwen and C. G. Van Weert (1980) (page 226).

[446] N. G. Van Kampen, "Lorentz-invariance of the distribution in phase space", Physica **43**, 244–262 (1969) (pages 227, 228).

[447] F. Debbasch, J.-P. Rivet, and W. Van Leeuwen, "Invariance of the relativistic one-particle distribution function", Physica **A301**, 181 (2001), arXiv:0707.2499 [astro-ph] (pages 227, 228).

[448] L. LANDAU and E. LIFSHITZ, eds., *The Classical Theory of Fields (Fourth Edition)*, Vol. 2, Course of Theoretical Physics (Pergamon, Amsterdam, 1975) (page 227).